Development of refill friction stir spot welding (RFSSW) for lightweight applications

de Sousa Santos, Pedro Miguel

Award date:
2021

Awarding institution:
Coventry University

Development of Refill Friction Stir Spot Welding (RFSSW) for lightweight applications

By

Pedro Miguel de Sousa Santos

PhD

October 2020

Development of Refill Friction Stir Spot Welding (RFSSW) for lightweight applications

By

Pedro Miguel de Sousa Santos

A thesis submitted in partial fulfilment of the University's requirements for the Degree of Doctor of Philosophy

October 2020

Certificate of Ethical Approval

Applicant:

Pedro De Sousa Santos

Project Title:

Influence of tool material and geometrical features on the mechanical and microstructure properties of RFSSW of aerospace aluminium alloys.

This is to certify that the above named applicant has completed the Coventry University Ethical Approval process and their project has been confirmed and approved as Low Risk

Date of approval:

05 September 2019

Project Reference Number:

P94077

This thesis is dedicated to my parents, António and Susana and my sister Margarida.

"Yesterday's faults, become today's lessons.

Today's dreams, become tomorrow's reality."

(B.J. Neblett)

Abstract

Refill friction stir spot welding (RFSSW) is a novel solid-state joining technology being developed primary as a replacement of mass-adding mechanical fastening processes. The appropriate choice of tool material and geometry can influence the tool life-expectancy and may impact the mechanical properties of the joint. Despite the extensive research, there is a lack of publicly available experimental data regarding the effect of different tool designs and tool materials on the microstructural and mechanical properties of RFSSW lapped joints.

The aim of this research is to further understand the relationship between RFSSW tool design and material with the mechanical performance and microstructural features of the joint produced. The main objectives are: 1) to quantify the influence of process parameters on the mechanical performance; 2) to select and benchmark the most promising tool material candidates for RFSSW based on industrially relevant criteria (e.g. process repeatability, tool life, joint mechanical properties); 3) to characterise the effect of different tool materials and geometries on the mechanical performance of the weld; 4) to compare the material flow and microstructural features of welds produced with tools with different geometries.

The key findings are summarised as follows. Firstly, the influence of RFSSW process parameters on the weld mechanical strength was determined for various aluminium alloys using a standard RFSSW tool. This allowed determining the most effective process parameter combination for each alloy. Plunge depth had the greatest impact on mechanical strength, while welding conditions promoting lower heat input tended to improve the shear strength. Furthermore, residual stress measurements on RFSSW specimens with multiple spot-weld were performed using the contour method. The results suggest that the increasing number of spot-welds translates into lower peak stress values. RFSSW in the presence of aerospace grade sealant was also investigated. The results showed an increase in mechanical performance, which was attributed to the adhesiveness of the sealant at preventing secondary bending of the specimen.

Secondly, the tool material benchmarking investigation suggests that surface treated specimens produced intermetallic compounds at the internal surface of the tool specimen per plunge, which lead to persistent clogging. M42 high speed steel showed to be the most suitable tool material for RFSSW with the best cost-benefit ratio.

Finally, the impact of different tool materials and geometries in the microstructure and mechanical performance of the weld was determined. The main findings from this investigation suggest that the left-handed features present on the surface of the plunging component enhanced the stirring action, accentuating downward material flow and enlarging the welded area. Welds made with a conventional design RFSSW tool and made from M42 high speed steel, exhibited decreased mechanical performance. This can be attributed to the use of a tool material with a lower thermal conductivity coefficient, producing a weld with a higher peak temperature and promoting softening of the base material.

This thesis contributed to the further development of RFSSW, establishing both a theoretical and technical basis for new researchers or industrial users searching for alternative single point joining methods. Technological strong points and limitations are discussed, aiming to identify the most promising fields of application.

Disclaimer

Coventry University PhD Thesis in Materials and Manufacturing Engineering.

I hereby declare that the work submitted in this PhD thesis entitled "Development of Refill Friction Stir Spot Welding (RFSSW) for lightweight applications", is my own original work except where otherwise indicated and have referenced all sources of information. In the event of any work performed jointly, contributions of collaborators and myself have been stated clearly in the text.

The attached thesis has not been and will not be, submitted in whole or in part to another university for the award of any other degree.

Content removed on data protection grounds

Preface

This thesis is submitted for the degree of Doctor of Philosophy at Coventry University. This research project was based at the National Structural Integrity Research Centre (NSIRC) in TWI Ltd, sponsored by the Industrial Members of TWI as part of the Core Research Programme and Coventry University. The research work was carried out under the supervision of Professor Xiang Zhang (Director of Studies) and Dr Bilal Ahmad from Coventry University and Dr João Gandra (Industrial Supervisor) from TWI Ltd, for the period of May 2017 to September 2020.

A significant portion of the work performed during this PhD research has already been disseminated in an international conference and many local conferences/events as listed below:

International Conferences

- De Sousa Santos, Pedro; McAndrew, Anthony; Gandra, João; Zhang, Xiang. 'Refill Friction Stir Spot Welding parameter optimisation for transport industry aluminium alloys', 6th International Conference on Scientific and Technical Advances on Friction Stir Welding & Processing (FSWP 2019), Louvain-la-Neuve, Belgium, 11-13th September 2019 (Abstract plus Oral presentation)

Local Conferences/Presentations

- De Sousa Santos, Pedro; McAndrew, Anthony; Gandra, João; Zhang, Xiang. 'Development of Refill friction stir spot welding for aerospace applications', *NSIRC Annual Conference 2018*, TWI Ltd, Cambridge, 3-4th of July 2018. (Poster presentation)
- De Sousa Santos, Pedro; McAndrew, Anthony 'Development of Refill friction stir spot welding for aerospace applications', *TWI research board yearly review,* TWI Ltd, 13th November 2018 (Oral presentation)
- De Sousa Santos, Pedro; McAndrew, Anthony; Gandra, João; Zhang, Xiang. 'RFSSW parameter optimisation for transport industry aluminium alloys', *NSIRC Annual Conference 2019*, TWI Ltd, Cambridge, 2-3rd July 2019. (Extended abstract plus oral presentation)
- De Sousa Santos, Pedro; McAndrew, Anthony. 'RFSSW parameter optimisation for transport industry aluminium alloys', *TWI research board yearly review,* TWI Ltd, 8th November 2019 (Oral presentation)

- De Sousa Santos, Pedro; McAndrew, Anthony; Gandra, João; Zhang, Xiang. 'Influence of tool material and design on the mechanical and microstructural properties of refill friction stir spot welds', *NSIRC Annual Conference 2020*, TWI Ltd, Cambridge, 23rd July 2020. (Extended abstract plus oral presentation)

The author's contribution to the research performed and that of others is given below:

Specimen preparation: All specimens were manufactured by TWI Ltd using TWI's Kawasaki RFSSW C-frame system as specified by the author and with support from TWI technicians Simon Walford and Ian Jeakins.

Residual stress evaluation: The contour measurements were performed by Dr Bilal Ahmad at Coventry University as requested by the author.

Mechanical testing and metallographic characterisation: Lap shear, cross tension and fatigue testing was performed by laboratory technicians at TWI under the direction of the author. Metallographic specimen preparation and characterisation and fractography were performed by the author using the facilities at TWI Ltd. The experimental methodology, specimen design, coordination of all mechanical testing performed by technicians, and finally analysis and interpretation of test results presented in this thesis was carried out by the author.

Acknowledgements

The work presented in this document represents the outcome of one of the most exciting chapters of my academic life, truly a unique experience that has shaped me at a professional as well as a personal level. However, I could not have achieved this goal without the help, support and conviction from crucial people and organisations.

First and foremost, I would like to thank my academic supervisors Prof. Xiang Zhang and Dr Bilal Ahmad for their guidance and continuous support. I would also like to acknowledge Dr Bilal Ahmad for performing residual stress measurements using the contour method and for his input on the analysis of data.

It is with a great deal of appreciation that I thank my industrial supervisor, Dr João Gandra, for his everlasting patience, guidance and constructive feedback, as well as his dedication. In addition to his cornerstone teachings, I am thankful for his friendship.

I would also like to thank my colleagues at the Friction and Forge Processes at TWI. Special thanks to Dr Steve Dodds, for his friendship and invaluable dedication towards my professional development; Dr Anthony McAndrew, for his continuous enthusiasm, guidance and crucial support; Mr Bertrand Flipo and Mr Richard Andrews, for their insightful conversations and valuable advices; Mr Stuart Page, for his educational insights; Mrs Helen Everson, for her support and readiness to help; Mr Ian Jeakins and Mr Simon Walford for their support during the many welding activities.

This research was conducted as part of a Core Research project co-funded by the Industrial Members of TWI, Coventry University and the National Structural Integrity Research Centre (NSIRC). I would like to acknowledge the importance of the granted funding that enabled this research.

I would like to thank all the staff members at TWI, whose teachings and insights are present in this work or have allowed me to contribute in various scientific outreach activities. Thank you for your contribution to this research and for the opportunities to develop new skills.

To the friends that I've made through the NSIRC PhD program, thank you for your friendship and for the unforgettable moments we shared. A special thank you to the members of the NSIRC Student Committee and the "cake office".

It is with great deal of appreciation that I express my indebtedness to my family. Their constant encouragement and never-ending love have always been my driving forces to face greater challenges and achieve greater milestones. A special thanks to my parents, who incentivise me to pursue this opportunity and start my doctorate.

To my Kochanie, Berenika Syrek-Gerstenkorn, I would like to express my gratitude for her patience, support, dedication and love throughout this journey. Thank you for believing in me, for making me a better and happier person and for the good times we had and that are yet to come.

In loving memory of my grandmother - Fernanda Gabriel Marques Duarte dos Santos, a true-life example, who always believed in me and to who I will be forever grateful for all the love, care and dedication she gave me throughout my life.

Table of Contents

List of Figures

List of Tables

List of Abbreviations

Abbreviation	*Definition*
AISI	The American Iron and Steel Institute
ALE	Arbitrary Lagrangian-Eulerian formulation
ANOVA	Analysis of variance
AWS	American welding society
BS	Bottom sheet
CF-PPS	Carbon fibre polyphenylene sulphide
CFRP	Carbon fibre reinforced polymer
CMM	Coordinate measuring machine
CNC	Computer numerical control
DF	Degrees of freedom
FEM	Finite element method
FFDoE	Full-factorial design of experiments
FSpW	Friction spot welding
FSSW	Friction stir spot welding
FSW	Friction stir welding
GKSS	Gesellschaft für Kernenergieverwertung in Schiffbau und Schiffahrt gmbh
H&W	Harms & wende
HAZ	Heat affected zone
HZG	Helmholtz-zentrum geesthacht
KHI	Kawasaki heavy industries
LSS	Lap shear strength
PCBN	Polycrystalline cubic boron nitride
PD	Plunge depth
PMMA	Polymethyl methacrylate
PPO	Plug pull out
RFSSW	Refill friction stir spot welding
RS	Rotation speed
SEM	Scaning electron microscope
SEM	Scanning electron microscopy
SF-TI	Shear fracture through the interface
STP	Shear fracture through the plug

SZ	Stir zone
SZ_P	Probe stir zone
SZ_S	Shoulder stir zone
TI	Through the interface
TMAZ	Thermo-mechanically affected zone
TS	Top sheet
TTS	Through the Sheet
TWI	The welding institute

Chapter 1

Introduction

This chapter describes the motivation and the objectives for this work, as well as, the structure of this document. The chapter sequence is explained, complemented by a short description of the topics addressed and a flowchart diagram linking the chapters together.

1.1 Motivation

The increasing number of vehicles, such as cars and aeroplanes, have contributed to an increase in greenhouse gas emissions. To address this situation, governments enforce progressively stricter limits on carbon dioxide and nitrogen oxide emissions. All transport sectors are being challenged to develop innovative solutions that satisfy new regulations and the customer-driven demand for more efficient vehicles. In addition to the potential efficiency gains by improved powertrain designs, lowering the weight of a vehicle is a common solution to increase its efficiency and performance. The use of lighter materials and innovative structural designs reduces the vehicle's propulsion energy requirements. For vehicles powered by fossil fuel powertrains, weight reduction also lessens the polluting emissions.

Vehicle body structures are commonly assembled using single-point lap joints, especially when considering aerospace and automotive platforms. In addition to be a cost-effective route for fabricating large structures, this approach also minimises the total heat input into the component, reducing distortion and residual stresses. Most manufacturers rely on mechanical fastening or fusion welding processes like resistance spot welding or laser spot welding as summarised by Briskham et al. (2006). The use of an autogenous fusion-based processes will mitigate the weight additions and galvanic corrosion considerations linked to the use of external fasteners. However, specific issues may arise from locally melting and solidifying the material as reviewed by Padmanabhan et al. (2011). In the case of resistance spot welding, the progressive contamination and degradation of the electrode tip will also affect the weld quality, as identified by Zhou et al. (2004). Mechanical fastening has been the most popular joining solution for aerospace. Fasteners, such as flush head solid rivets, are extensively used in load-bearing aircraft joints as they are fit for purpose and have well-established standards and specifications. However, pre-joining operations like drilling and deburring, as well as the need for galvanic protections, are some of the drawbacks associated with this joining method.

Refill friction stir spot welding (RFSSW) has clear advantages compared to other mainstream single-point joining or mechanical fastening processes. As a solid-state process, the RFSSW avoids many of the defects associated with fusion welding of lightweight metals, typically caused during melting and solidification (e.g. porosity and solidification cracking). The lower peak temperatures also offer advantages when controlling shrinkage and distortion, which is critical on large assemblies with multiple spot welds. The process can also weld different thicknesses with the

same tool setup, reducing cycle time and costs on equipment in a production environment. RFSSW does not require the addition of a third element to produce a joint, meaning that there is no added weight to the final assembly. Moreover, there is no need for pre- or post-joining operations such as hole drilling and cleaning or sealant coating. The absence of a third material element to produce a joint also means that the electrochemical potential of the welded material remains unaltered, providing higher corrosion resistance. Due to the independent vertical motion of the rotating components during the weld cycle, the RFSSW process produces a flush surface finish as shown in Figure 1.1. This offers an improved surface finish for applications where aerodynamics and air-flow management are critical factors.

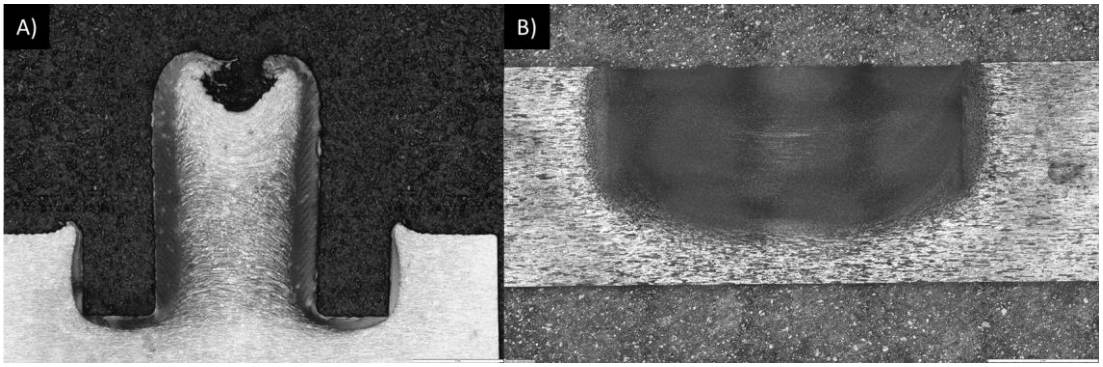

Figure 1.1 – Cross-section of RFSSW weld A) mid-process and B) a completed weldment.

Extensive research focused on the effect of process parameters on joint mechanical performance, microstructural features and defect formation has been reported by Boldsaikhan et al. (2019), Da Silva et al. (2007-A) and Pieta et al. (2014). However, as emphasised in the work of Montag et al. (2014) and recently highlighted by Feng et al. (2019), the effect of different tool external geometrical features and tool materials on the microstructural and mechanical properties of RFSSW joints has not been widely studied. This lack of experimental data publicly available regarding the RFSSW tool design has been identified as one of the reasons for the limited industrial implementation of the RFSSW process. As in its parent process, friction stir welding, the tool plays a vital part in the RFSSW process. As an external-tool based friction welding process, the correct choice of tool geometry and features can influence heat generation and the material flow around the tool. In addition, when welding high strength and abrasive materials, the choice of tool material can have a significant impact on the tool life-expectancy and wear. The importance of this topic has been highlighted by the research work of Barnes et al. (2012), Buffa et al. (2012), Seighalani et al. (2010) and Singarapu, Adepu and Arumalle (2015).

1.2 Aim and Objectives

The present thesis was developed within the framework of a 3-year research program at The Welding Institute (TWI) funded by the Industrial Members of TWI. The aim of this project was to gather impartial data on the properties of RFSSW on aluminium alloys used in the automotive and aerospace industries. This involved the determination of optimal process parameters, as well as the assessment of mechanical performance and microstructural characterisation of the joints.

Within this broad scope, the aim of this thesis is to further understand the relationship between RFSSW tool design and material with the mechanical performance and microstructural features of the joint produced.

The primary objectives are as follows:

- Quantify the influence of process parameters on the mechanical performance.
- Select and benchmark the most promising tool material candidates for RFSSW based on industrially relevant criteria (e.g. process repeatability, tool life, joint mechanical properties).
- Characterise the effect of different tool materials and geometries on the mechanical performance.
- Compare the material flow and microstructural features of welds produced with tools with different geometries.

1.3 Thesis Structure

This thesis is comprised of 6 chapters as follows.

Chapter 2 presents a comprehensive literature review, with special emphasis on the RFSSW process. The main objective of this review was to identify the remaining “knowledge gaps” in the available literature, so that a relevant research project could be formulated. Based on the conclusions from this chapter, the aim and objectives of this thesis were chosen as detailed in the previous section.

Chapters 3 to 5 describe the experimental work developed in this thesis along with an analysis of the findings and a summary of the conclusions gathered. Figure 1.2 presents a flowchart of the thesis structure.

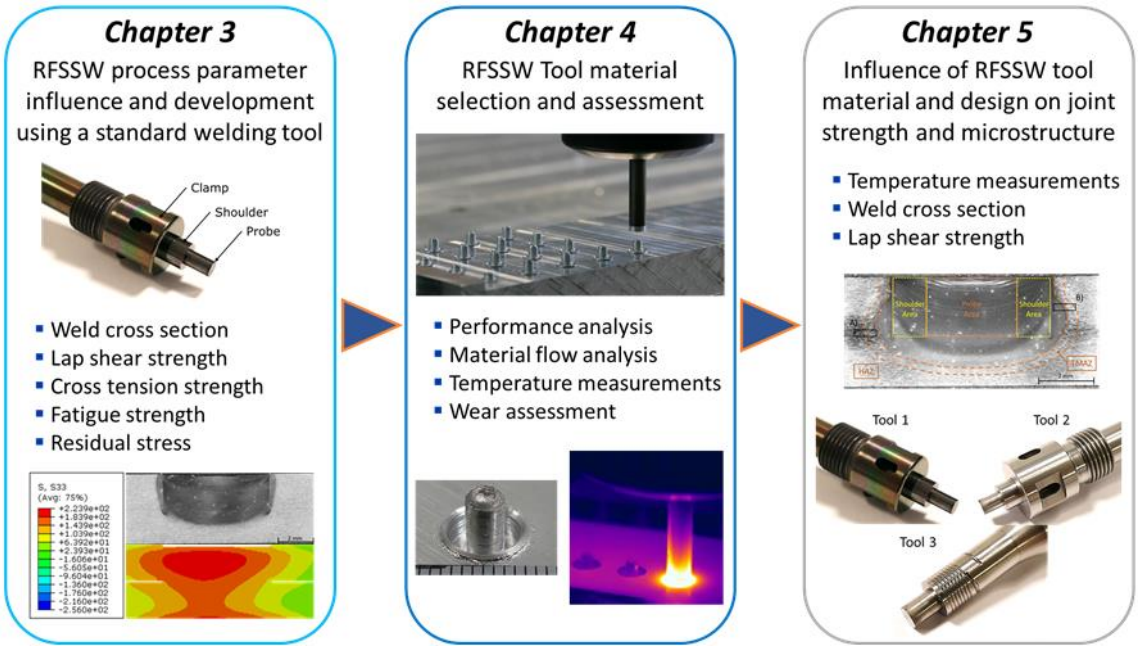

Figure 1.2 - Thesis structure.

Chapter 3 focuses on the on the design and analysis of experimental refill friction stir spot welds on AA2024-T3, AA5754-H24 and AA7075-T6. In this chapter, a process parameter window was defined for each alloy using a RFSSW tool provided by the equipment manufacturer. The most promising process parameter combination was determined by lap shear strength and weld cross-section examination. An empirical-based analytical model was developed to predict the shear strength of a single-spot weld specimen. The effect of an interfacial sealant on the weld properties was investigated for AA2024-T3 and AA7075-T6. Lastly, Fatigue testing and residual stress measurements were performed on specimens with the most promising process parameter combination.

Chapter 4 focuses on the assessment of various material candidates to be used as RFSSW tool materials. In this chapter, five different material and surface modification combinations were tested under RFSSW service conditions. A candidate material was chosen based on relevant selection criteria for tool materials, as well as its performance in service and specimen life-expectancy.

Chapter 5 focuses on the impact of different tool materials and geometrical features in the weld mechanical performance and microstructure. In this chapter, three RFSSW tools made from different materials and with different designs were used: one RFSSW tool provided by the equipment manufacturer and two RFSSW tools produced from the tool material selected from

Chapter 4 with different designs. Welds were produced with all tools using the base materials and the strongest process parameter combination from Chapter 3. The lap shear strength of the weldments was assessed and the cross-section of the welds was characterised. Finally, tool failure was analysed using SEM fractography.

Chapter 6 presents recommendations for further research based on industrially relevant topics as well as the limitations of the work presented in this thesis.

Chapter 2

Literature review

The present chapter provides a broad overview throughout to the fundamentals of the RFSSW process, applications and the most relevant developments of this technology

2.1 Friction Stir Welding

Friction stir welding (FSW) is a solid-state joining process pioneered at TWI in 1991 (Thomas et al. 1991). The development of this process represented a significant breakthrough in the metal joining technology by producing high integrity joints in materials that were difficult or even deemed non-weldable by conventional fusion joining processes. Figure 2.1 demonstrates the operating principles of FSW. The process uses a non-consumable rotating tool (typically featuring a shoulder and a probe) which is plunged into the abutting edges of components to join. As the tool penetrates the material, frictional heat is developed creating a boundary layer of viscoplastic material. It is common practice to dwell the tool at the plunge location for a period until suitable temperature and viscoplasticity conditions are developed. The tool is then traversed along the joint line producing a forged joint where both materials have been mechanically mixed. At the end of the joint, the tool is extracted from the components, leaving an exit hole (Colligan 2010 and Threadgill et al. 2009).

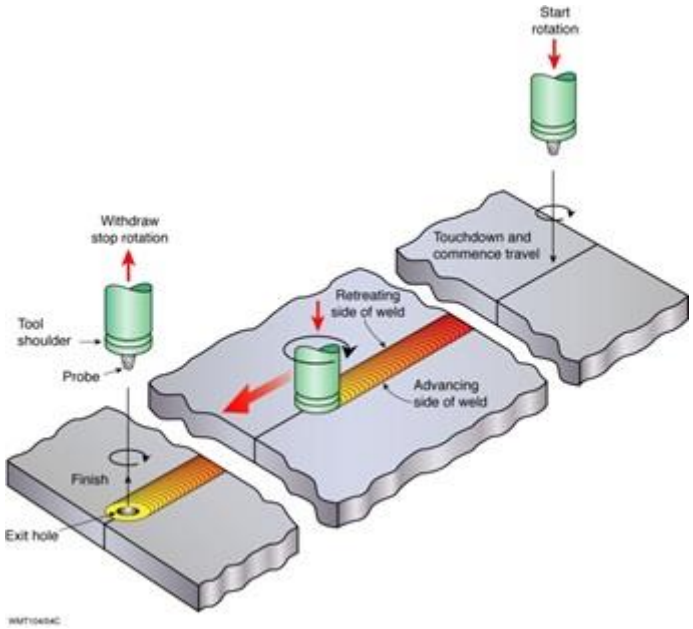

Figure 2.1 - Schematic representation of the FSW process phases (Threadgill et al, 2009).

Since its first commercial application to produce hollow aluminium panels for the fishing industry, products manufactured using FSW can be found in a myriad of applications across various sectors. From joining frames for high-fidelity speakers to more critical applications such as aerospace and aviation applications, FSW has established itself as the joining process of reference (Amini, Asadi and Zolghadr 2014). With the growing trend of vehicle electrification, FSW has found its way into

the automotive industry in the production of housings for batteries and thermal management components (Klender 2020; TRA-C 2020)

2.2 Friction stir spot welding

Friction Stir Spot Welding (FSSW) is a single spot joining process developed as a variant of FSW and patented by Mazda Motor Corporation in 2003 (Iwashita 2003). In FSSW, the non-consumable tool is used to produce a localised joint without any linear movement across the workpiece material. Figure 2.2 shows the main steps of the FSSW process. The process begins by plunging the rotating tool through the upper sheet to a depth that allows interaction with the sheet underneath. The tool is dwelled for a set time to generate sufficient frictional heat and viscoplastic deformation around the tool probe. After the tool is extracted from the material, the joint between the upper and lower sheets is completed in the area where the plastic flow occurred (Yang et al. 2014).

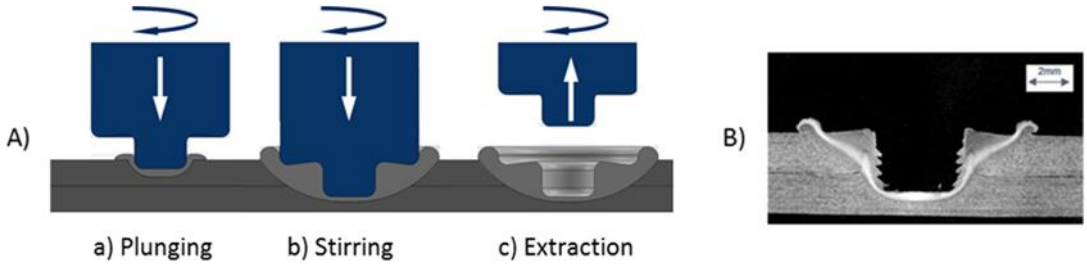

Figure 2.2 - A) Schematic drawing of the conventional FSSW process and B) correspondent cross-section.

Compared to other single-point fusion welding techniques, FSSW produces no fumes or spatter, while offering a high energy efficient process. As a solid-state process, FSSW produces welds with good mechanical and metallurgical properties, especially in materials that would suffer degradation when subjected to melting and subsequent solidification. This translates into lower processing temperatures which allows to minimise distortion and residual stresses (Ojo, Taban, and Kaluc 2015).

These advantages allowed FSSW to be used in large scale production of components for the automotive industry. The first industrial application was in 2003 on the Mazda RX-8 rear doors, bonnet and boot, as a replacement for resistance spot welding (Da Silva et al. 2007-B). The shift in joining processes enabled an energy reduction of 99 % and 80 % when joining aluminium and steel, respectively, in comparison with that of resistance spot welding. Later on, the company

used FSSW on its MX-5 model to reduce weight on the boot lid by joining aluminium to steel (Automation 2005). Toyota also used FSSW to produce the boot lid and bonnet of its Prius model (Pan 2007). For the rolling stock industry, railcar prototypes for the next-generation Shinkansen and Maglev have been produced by Kawasaki Heavy Industries. The company has proposed the use of FSSW to join aluminium reinforcement ribs to sheet panels (Pan 2007).

The limitation on the materials and thicknesses that the process is capable of welding are some of the disadvantages of the FSSW process. Furthermore, the inherent exit hole feature after welding have limited its industrial application. This feature causes stress concentration at the centre of the joint, as well as a reduction of the effective joined area. Finally, this feature is prone to localised fouling and corrosion even in applications where corrosion protective coating are used due to the complex shape (Chen, Liu and Ni 2017)

To mitigate the issues associated with feature, researchers attempted to develop new variants that would minimise or eliminate the exit hole feature. Venukumar et al. (2014) attempted to refill the exit hole by applying a secondary operation using a flat rotating tool and a filler plate. In this study, the author was able to eliminate the exit hole and increase static strength. Another approach was investigated by Chen, Liu and Ni (2017) while welding aluminium to steel. The authors proposed a methodology in which the welding cycle consisted of a regular FSSW cycle along with a refilling operation by traveling the tool along a circular path. The welding cycle finished leaving an exit hole on the aluminium top sheet at a shallower plunge depth. Despite some surface cracks, the authors observed an increase in static strength in comparison to conventional FSSW. A hybrid approach was adopted by Deng et al. (2019) while welding AA2024-T4. In this study, the authors devised a welding process consisting of a conventional FSSW cycle followed by a resistance spot welding cycle with a plug to refill the exit hole. This methodology was able to refill the exit hole and produced a combination of plastically deformed and fusion microstructure. In the study conducted by Uematsu et al. (2008), the authors used a flat shoulder tool with a retractable probe to eliminate the FSSW exit hole. In this approach, the cycle began by plunging the probe to a pre-defined depth, followed by retraction of the probe and a final plunge of both the probe and shoulder components into the weld area. This plunging action forged and consolidated the weld area prior to the extraction of the tool, as shown in Figure 2.3. The outcome of this study showed that the proposed methodology was able to refill the exit hole and improved the static strength of the weld. However, lack of fill at the centre of the weld area was observed.

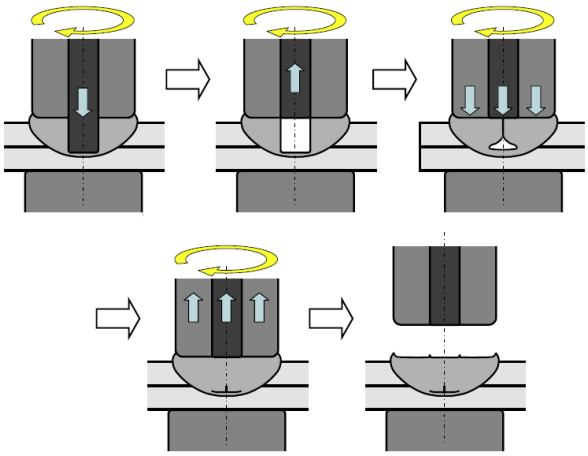

Figure 2.3 - Schematic illustration of the FSSW process with refilling stage. (Uematsu et al. 2008)

Despite the best attempts, the shortcomings of these methodologies are that they either require a secondary operation, increasing weld cycle time, or produce a secondary exit hole.

2.3 Refill friction stir spot welding

Refill friction stir spot welding (RFSSW) or Friction spot welding (FSpW) is the newest variant of the FSSW processes. Developed and patented by HZG (former GKSS) in 2004 (Schilling and dos Santos, 2004), RFSSW produces a single spot solid-state weld between adjacent materials in an overlap configuration. The process uses a non-consumable tool as shown in Figure 2.4. The tool is comprised of two concentric rotating components named as the probe and shoulder, encompassed by an outer static clamp ring. The main difference of RFSSW compared to FSSW tools is that the rotating components have vertical independent motion allowing to create a nugget of plastic material without leaving an exit hole, as shown in Figure 2.5 and Figure 2.6.

Figure 2.4 - RFSSW tool.

The operating process of the Refill FSSW system consists of four stages (Boldsaikban et al. 2017; Campanelli et al. 2011; Padhy et al. 2017):

Stage 1 (sheet clamping and frictional heating) – the clamp presses the sheets against the anvil to prevent plate separation. The rotating probe and shoulder contact the top sheet to soften the workpiece material by frictional heating.

Stage 2 (plunge) – the shoulder is plunged into the material to a set depth at a predetermined constant speed or load. At the same time, the probe moves in the opposite vertical direction at a different speed than the shoulder, creating a chamber between the probe and shoulder, that allows the softened material to flow into this space. To increase the stirring time and heat generation, the shoulder remains at the targeted depth for some time, defined as the wait time.

This process variant is commonly described as shoulder plunge. Because of the aforementioned vertical independent movement of the rotating components, a probe plunge variant can also be performed by changing the plunging and retracting components. Due to the smaller diameter of the probe, the volume of processed material is smaller which leads to a lower heat input that may be beneficial for some applications. However, the weld size is smaller and narrower in this variant, typically producing a weaker joint.

Stage 3 (re-plunge or refill) – whilst rotating, the shoulder and probe return to the surface of the top of the material to refill the weld nugget. To ensure proper consolidation of the processed material, the probe is plunged slightly into the material during this stage.

The same principle is applied for the probe plunge, but in this variant, the probe remains at the surface of the top sheet material while the shoulder produces the final consolidating plunging action.

Stage 4 (retract or removal) - the rotating probe and shoulder are retracted to the original position. The process is then completed, and the tools are released from the surface material.

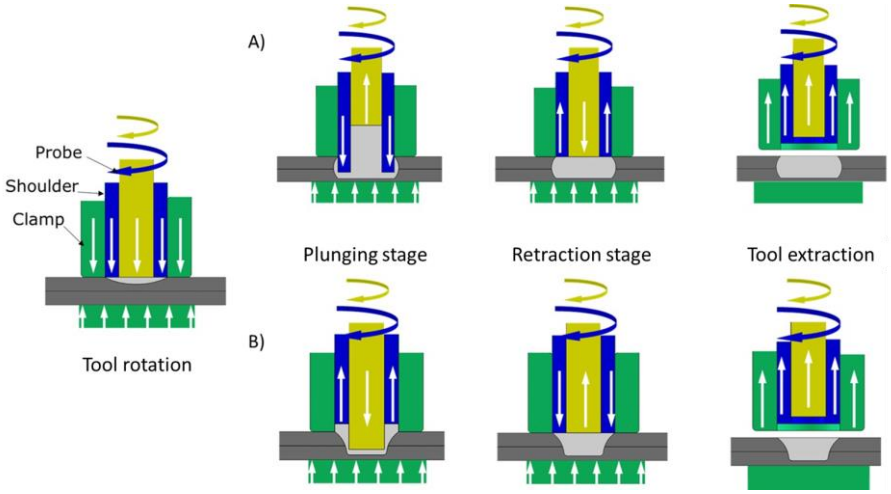

Figure 2.5 - Schematic drawing of the RFSSW process for A) shoulder-plunge and B) probe-plunge variant.

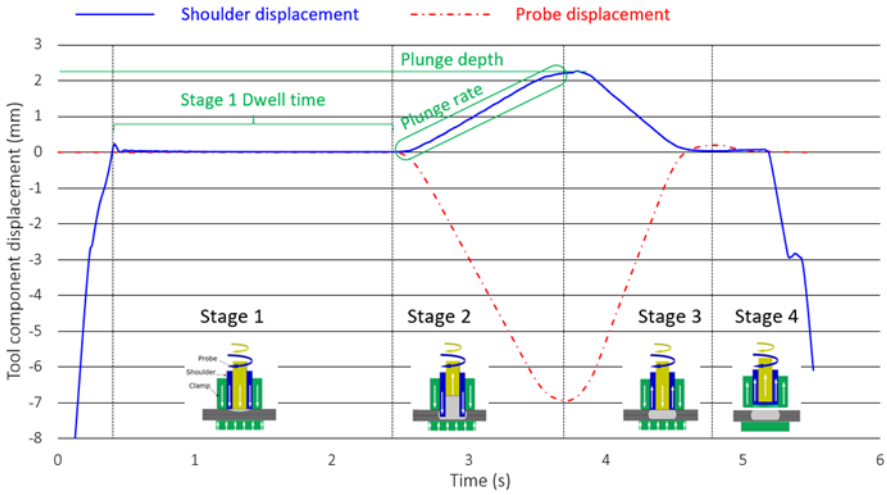

Figure 2.6 - Displacement of tool components during a RFSSW weld cycle (positive values of displacement represent a plunge of the tool component in the weld material).

2.3.1. Process parameters

In RFSSW, the quality of the welds is strongly dependent on the appropriate selection of process parameters. Depending on the type and thickness of material to weld, these parameters need to be adjusted to meet the requirements of the application. The main process parameters are described herein.

2.3.1.1. Tool rotation speed [rev/min]

The rotational speed of the probe and shoulder plays a major part on the material mixing and the heat input of the process. However, excessive rotational speeds may overheat the material contributing to a detrimental effect on the metallurgical properties of the weld. The effect of different rotational speed values on the microstructure and the mechanical strength was

investigated by Zhou et al. (2017). When welding overlapped AA6061-T6 plates at tool rotation speeds from 1100 to 1700 rev/min, the author observed that the grains in the Heat Affected Zone (HAZ) became coarser with the increase of the tool rotation speed. This was most likely associated with the higher thermal cycle. The maximum ultimate shear strength values were achieved for a rotational speed value of 1500 rev/min (Figure 2.7). Furthermore, the rotational speed also influenced the type of failure mode observed.

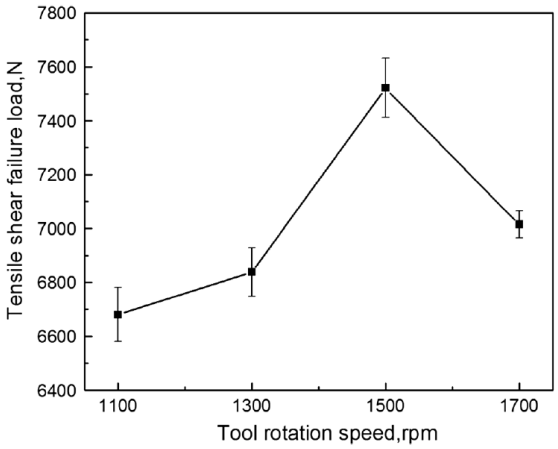

Figure 2.7 - Shear test results for the different tool rotation speeds (Zhou et al., 2017).

Similar conclusions were also reported by Shi et al. (2018) when welding AA2198-T8. For a range of rotational speed values between 1200 and 1800 rev/min, a maximum failure load of 9298 N was registered for a rotational speed of 1600 rev/min. Also, the weld cross-section presented voids for a rotational speed of 1200 rev/min, most likely due to poor material consolidation. Santana et al. (2017) performed a process parameter optimisation study when joining a 3-mm thick Al-Mg-Si alloy to maximise mechanical strength. Based on the statistical analysis, the rotational speed was the factor with the largest influence on the shear strength of the joints (36.6%).

2.3.1.2. Plunge depth [mm]

The plunge depth corresponds to the depth of penetration of the plunging tool element into the workpiece material. In RFSSW, the plunge depth affects the volume of stirred material during the welding cycle, influencing the weld nugget size. Pieta et al. (2014) conducted a parameter optimisation study on overlapped AA2198-T8 plates, with 3.18 mm thickness, using a shoulder plunge variant. The effects of different rotational speed, plunge depth and welding times on the mechanical and microstructural properties were investigated. For a constant rotational speed value of 2000 rev/min and a plunge depth range between 3.7 to 5.2 mm, the maximum shear

strength of 14.73 kN was obtained for a plunge depth of 4.7 mm. Zhao et al. (2014) investigated the effect of the plunge depth of the shoulder on the microstructure and mechanical properties of Alclad 7B04-T74 aluminium alloy sheets. As demonstrated in Figure 2.8, a maximum shear strength was achieved with a plunge depth of 3mm, 1.1 mm into the bottom sheet. Increasing the plunge depth altered the geometry and height of the hook feature resulting in a detrimental effect on joint strength.

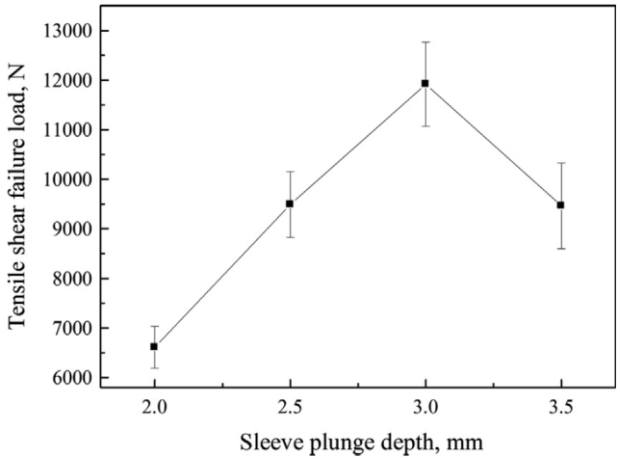

Figure 2.8 - Shear test results for the different tool plunge depths (Zhao et al., 2014).

2.3.1.3. Plunge rate [mm/s]

The plunge rate, along with the rotation speed, also plays a major part on the total heat input and the material strain rate during RFSSW. The ratio between these two process parameters provides the number of tool revolutions per unit of distance during the plunge or retract stage, as shown in equation 1.

$$revolutions\ per\ plunge/retract\ (rev/mm) = \frac{Rotation\ speed\ (rev/min)}{Plunge/retract\ rate\ (mm/min)} \quad [1]$$

The heat input in RFSSW is proportional to this ratio, as demonstrated by Reimann et al. (2017a). In this investigation, the microstructure and mechanical properties of through-hole repair welds on AA7075-T651 using RFSSW were investigated. The thermal cycle analysis was based on the input process parameters correlated with the data from thermocouples imbedded in the aluminium plate at a set distance. As shown in Figure 2.9, it was observed that an increase of the revolutions per plunge distance increased the energy supplied to the weld, leading to higher peak temperatures. This led to the formation of a larger layer of material undergoing viscoplastic deformation, taking place ahead of the shoulder during the plunge state. It was also noted that

the frictional conditions between the tool and the workpiece have a linear relationship without significant change within the process parameters tested.

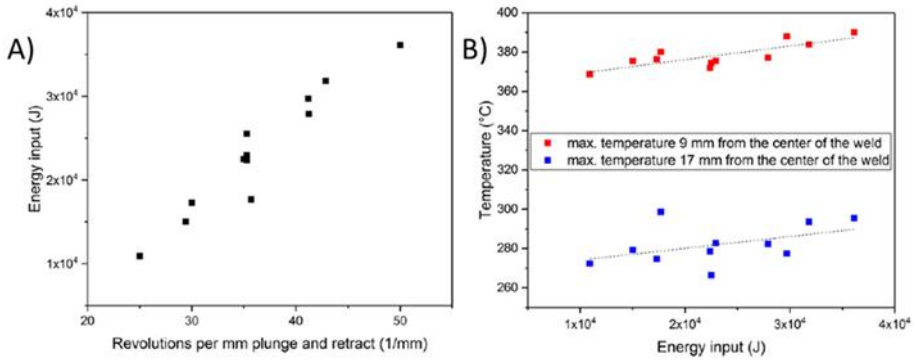

Figure 2.9 - Correlation between the A) revolutions per plunge depth and retract with the Energy input during the weld cycle and B) with the peak temperature measured (Reimann et al., 2017a).

Rosendo et al. (2011) investigated the effect of different rotational speed values and joining times on the mechanical and microstructural properties of AA6181-T4 plates. Defects associated with material flow located on the path of the shoulder were observed for excessive plunge rates (short joining times). Different microstructure of the thermo-mechanically affected zone (TMAZ) was also observed depending on the maximum process temperature and faster plunge rates lead to consistently lower shear strength for the same rotation speed. Tier et al. (2013) studied the influence of different values of rotation speed, plunge depth, plunge rate and cycle times on the microstructure and shear strength on AA5042 plates. Based on the results obtained in this study, plunge rate was not a critical process parameter for shear strength as joining time. Plunge depth was the parameter that had the greatest influence on the shear strength, followed by the tool rotation speed.

2.3.1.4. Joining time [s]

The joining time is a combination of three separate phases such as:

- **Plunging time:** the time to achieve the target depth.
- **Dwell time**: the period that the tool remains at target depth.
- **Retraction time**: the time to retract the tool from the workpiece material.

Joining time can also be related to the plunge rate and therefore can affect the heat input of the process. Amancio-Filho et al. (2011-B) studied the influence of the process parameters on the microstructure and mechanical performance of AA2024-T3 plates. The results showed that

joining time had a greater effect on the shear strength compared to that of the rotation speed. Also, the first-order interaction between rotation speed and joining time demonstrated a maximum value of shear strength for the middle range values that were experimented, which can be explained by different efficiencies in the frictional heating.

Effertz et al. (2017) performed a process parameter optimisation when joining AA7050-T76 plates using a Taguchi orthogonal array. This is a highly fractional orthogonal design type of factorial designs which allows to consider a selected subset of combinations of multiple factors at multiple levels. Different values for plunge depth, plunging time and rotational speed were experimented in an L9 orthogonal array and an Analysis of variance (ANOVA) was performed to determine the influence of each parameter on the shear strength. The ANOVA test is used in statistics to determine the influence that independent variables have on the dependent variable in a regression study. The parameter with the greatest influence was the plunge depth (43.6%) followed by the plunging time (29.7%) and the rotational speed (16.0%).

2.3.1.5. Clamp force [kN]

The clamp force prevents the separation of the workpiece plates during the welding cycle. In some applications, it can constrain the workpiece material after the welding cycle to prevent joint detachment while cooling. This parameter is of special importance when joining dissimilar material combinations without plunging into the lower sheet (joining aluminium to Zn-coated steel or aluminium to polymers are some examples). It prevents the processed material from deforming towards the interface between the two sheets, leading to incomplete refill of the spot. However, an excessive clamp force can leave an indent on the top surface due to local material softening.

In the study performed by Esteves et al. (2015) on the dissimilar joining of AA6181-T4 and carbon fibre reinforced polymer (CFRP), the clamp force had a minimal effect on the joint shear strength. However, the hydrostatic forces created by the clamp, controlled the flow of the molten polymer and promote the filling of microscopic grooves on the surface of the aluminium. Increasing the clamping force promoted bonding between the polymer and the aluminium, but excessive values decreased the thickness of the molten polymer.

When studying the influence of RFSSW process parameters on AA2024-T3 and CFRP, Goushegir et al. (2015) observed that the rotational speed was the most important parameter affecting the shear strength, followed by the clamping force. On a pre-treated aluminium surface,

higher values of clamp force promoted the flow of molten polymer into the pores and crevices which increased the micro-mechanical interlocking between the joining parts.

2.3.1.6. Tool temperature

During multiple weld cycles, the heat from the process can build-up within the tool components, which can lead to premature failure of the tool due to thermal fatigue (Persson, Hogmark and Bergström, 2005). To increase weld efficiency and reduce scattering of results, it is important to prevent the tool from overheating. Excessive accumulated heat in the tool promotes wear reducing the tool life and weld quality. Several authors applied a cooling cycle after each weld using compressed air- or water-cooling blocks to improve the mechanical strength (Seaman et al., 2016; Shen et al., 2016 and Shen et al., 2017).

2.3.1.7. Tool material and profile

The selection of an appropriate tool material is critical to ensure good weld quality as well as a long tool life expectancy. This choice, however, is strongly dependent on the application and the physical properties of the tool material. The essential tool materials requirement for FSW and its variants, as described by Fuller (2007), Infante and Vidal (2014) and Rai et al. (2011), can be summarised as follows:

- High compressive and shear strength, both in ambient and elevated temperature conditions;
- High thermal fatigue strength and dimensional stability when in use;
- Low coefficient of thermal expansion, especially for bimetal tools;
- Be inert with the environment and the workpiece material;
- Good fracture toughness and wear resistance;
- Must be machinable, readily procurable and cost-effective;

Similar requirements can be defined for RFSSW tools, since the main difference to an FSW cycle is the absence of the bending moment produced the traverse motion of the tool across the joint. The plunge is the stage of the process which generates more load on the tool, with most of the wear and tool fractures being observed during this stage. In the start of the plunge stage, high flow stresses arise from processing the workpiece material at room temperature. This loads the tool with the maximum axial force and torque experienced during the cycle. This is due to the

cold conditions the workpiece material requires of the workpiece material which leads to greater flow stress and axial load (Thomas et al., 1999 and Lienert et al., 2003).

Although it has not been the primary focus for most of the published research work, this section presents some of the tool materials used for RFSSW and the conclusions from various researchers. Tool steel is the most common choice when manufacturing tools for joining combinations of aluminium alloys or joining aluminium to other engineering materials. In particular, the AISI H13 alloy (a chromium-molybdenum tool steel for hot working applications) has been the most widely used due to its low cost, commercial availability, machinability and good wear resistance when a surface hardening coating is applied. From published work, several authors have reported fully consolidated welds with high joint strengths (in both shear and cross tension loading conditions) and good fatigue life (Ding et al., 2017; Plaine et al., 2016 and 2017; Reimann et al., 2016; and Yue et al., 2017). This is the tool material of choice for most of the research work conducted when using an RFSSW system supplied by Harms & Wende.

Montag et al. (2014) investigated the influence of the tool wear on quality criteria such as the lap shear strength (LSS) and the surface quality of AA6082-T6 RFSSW lap welds. After 3,500 welding points made with an AISI H13 tool, the study showed no dependence between tool wear and lap shear strength. However, the increasing wear of the tool components led to loss of welding material and increase of spindle current. A premature failure on 2 sets of AISI H13 tools was recorded by Nasiri et al. (2018) while welding 1 mm thick sheets of AA2099-T83. The failure mechanism was identical on both toolsets and it was attributed to liquid metal embrittlement from permeation of lithium-rich film into the tool surfaces.

Oliveira et al. (2011 and 2012) studied the influence of the tool material on the weld properties of Polymethyl methacrylate (PMMA) resin RFSSW joints. In their study, stainless steel TS30000 and titanium Ti-6Al-4V were selected as tool material candidates. Both materials have good mechanical properties and low thermal conductivity coefficients, which minimised heat losses through the tool body. The lower thermal conductivity coefficient of the titanium tool produced better quality welds with higher shear strengths than the welds performed with the stainless steel. However, the titanium tool had a life expectancy of about 50 welds before the features on the outside of the shoulder were completely eroded. Further developments to the joining of PMMA and carbon-fibre-reinforced polyamide 66 laminate were presented by Gonçalves et al. (2015a and 2015b). A titanium Ti-6Al-4V RFSSW tool with a nitriding hardened surface was tested.

The addition of the nitriding process extended the tool life expectancy to about 200 welds without major material loss or complete erosion of the features of the shoulder. Figure 2.10 presents the graphs from the profilometer measurements before welding trials and after 200 welds.

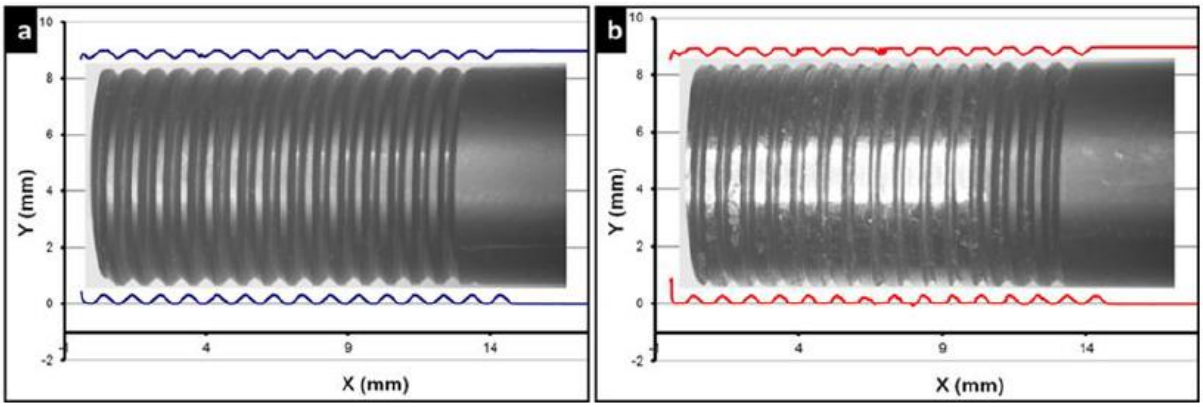

Figure 2.10 - Wear analysis on titanium Ti-6Al-4V RFSSW tool (Gonçalves et al., 2015).

Like in the FSW process and its variants, the tool geometry and profile have a significant influence on the quality and properties of the welds. Different features and groves on the surface of the tool generate affect the heat generation process and the material flow behaviour. This will ultimately influence the weld microstructure as well as the mechanical properties. The most common tool profile is the simple left-hand threaded shoulder, as shown in Figure 2.11. This tool profile has been extensively used in RFSSW to join different materials and is the typical design of the Harms & Wende system.

Figure 2.11 - RFSSW tool with a threaded shoulder from H&W (Nasiri et al. 2018).

However, despite the knowledge from other FSW variants, the influence of the RFSSW tool profile on the weld properties is still not fully understood. Limited studies have been conducted to determine which of the various geometrical parameters of the tool profile influence the weld

quality and what is the impact on mechanical performance. Ji et al. (2017-B) studied the effect of different tool geometries on the material flow based on a three-dimensional model. The different shoulder geometries are depicted in Figure 2.12, with the model validation being performed for the threaded shoulder [Figure 2.12.A)], rotating in a clockwise motion.

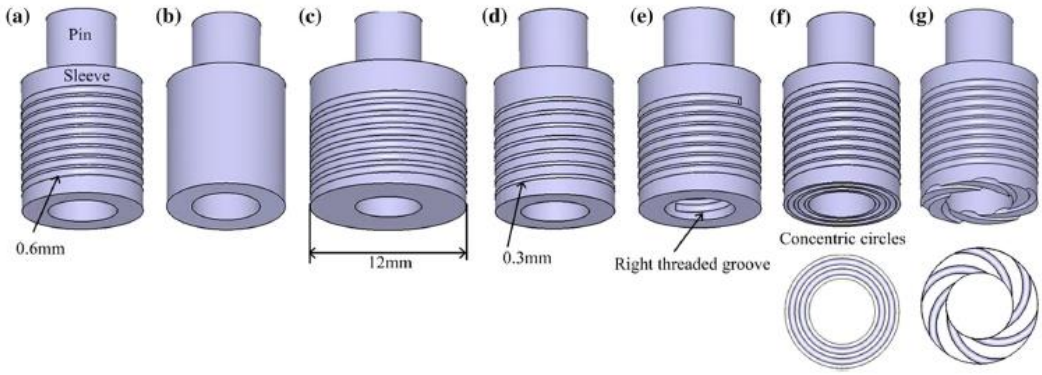

Figure 2.12 - Shoulder designs used to simulate the material flow in (Ji et al. 2017-B).

The results from the simulation work suggested that the absence of features on the outer surface of the shoulder may have contributed to the reduction of the hook height. However, the maximum velocity of the material flow on this area is lower than that enabled by the conventional threaded shoulder tool design. The results for the inner thread shoulder design promoted the mixing of material at the interface, decreasing the bonding ligament thickness. Regarding bottom shoulder profiles, the scrolled design performed better than the concentric circle design by promoting a higher flow of material in the vertical direction.

Further developments on the effect of modifying the bottom surface of the shoulder on weld properties were achieved by Łogin et al. (2019). In this study, the authors used three designs for the bottom shoulder surface to determine the impact on the process temperature as well as weld mechanical and microstructural properties. The tools used in this study are shown in Figure 2.13. The outcome from this study confirmed that lower process temperatures and better mechanical performances can be achieved with modifications to the bottom surface of the shoulder. In this study, the single-spiral design [Figure 2.13.A) and B)] produced the strongest welds with the best surface finish and lower process temperatures. This result confirmed one of hypothesis from the study conducted by Ji et al. (2017-B).

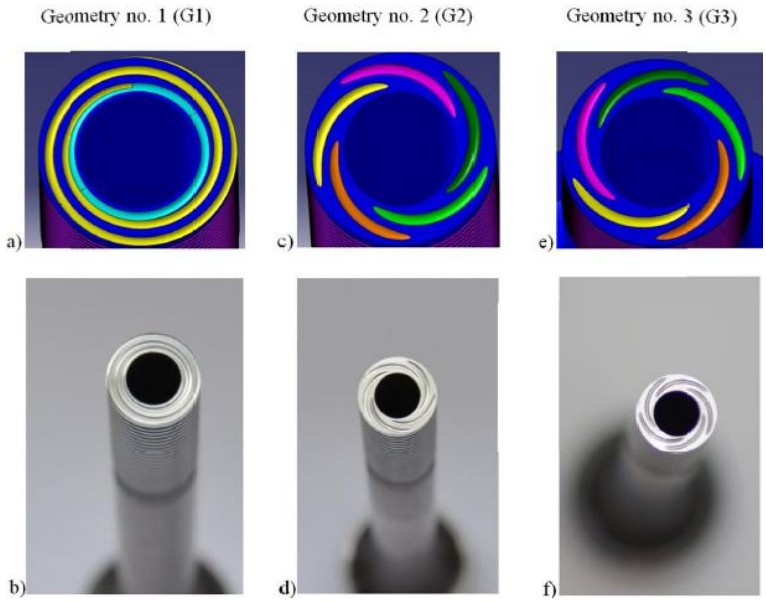

Figure 2.13 - RFSSW shoulder designs (Łogin et al. 2019)

Shen et al. (2018) compared the mechanical and microstructural properties of welds performed with a standard threaded RFSSW shoulder and a modified version. The tools used in this study are shown in Figure 2.14. The welds made with the modified tool displayed improved metallurgical bond and intermixing between both materials. As a result, a more consistent lap shear strength was observed for all the process parameter combinations tested.

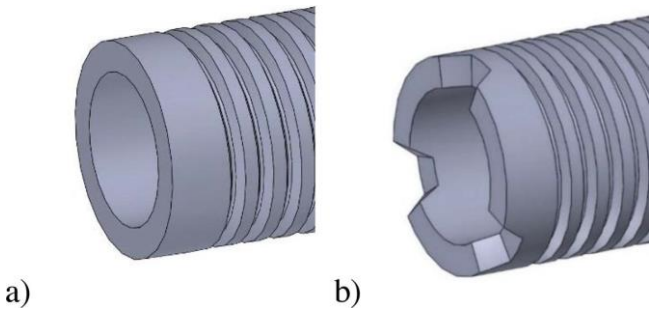

Figure 2.14 - A) Standard left-hand threaded RFSSW shoulder and B) modified version with groves on the bottom surface. (Shen et al. 2018)

2.3.2. Microstructural regions and flaws

The heat and pressures generated during the process affect the base material microstructure, grain size and orientation. The cross-section of an RFSSW weld is shown in Figure 2.15.A), where the characteristic regions are delimited and are symmetric concerning the tool axis.

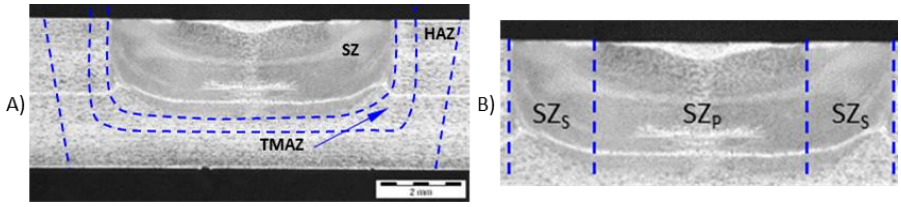

Figure 2.15 - A) Optical microscope macrograph of a typical RFSSW connection cross-section showing the weld regions and B) detailed view of the Stir Zone.

The Stir Zone (SZ), consists in the region of the weld where the base material has been in direct contact with the rotating tool. This submits the base material to intense plastic deformation and high temperatures due to the frictional heating, promoting the dynamic recrystallization of the grains in this region. The microstructure consists of equiaxed grains, with an order of magnitude smaller than the grains in the base material region and a stochastic grain orientation. Because of the self-regulating nature of the frictional heat generation in the RFSSW process, the temperatures in this area typically reach the 80% of the melting temperature (Campanelli et al. 2013-B). However, for some alloys, local grain boundaries can reach their eutectic melting temperature. As a result, liquation cracks can occur, as showed by Zhao et al (2018-B). The stir zone can be further divided into the Shoulder Stir Zone (SZ_S) and the Probe Stir Zone (SZ_P) located, respectively, on the outer side and at the centre of the stir zone [Figure 2.15B)]. This is particularly noticeable in the shoulder plunge variant due to the different rate of plastic deformation experienced in these two zones, producing distinct grain sizes and orientation.

The TMAZ is the area of the material located at the vicinity of the tool. In this area, due to the plunge and retracting shoulder motion, the material generally experiences moderate plastic deformation and thermal cycle. This leads to microstructural changes and vertical upward flowing pattern without grain recrystallisation. In the region closer to the stir zone, inhomogeneous grains can also be present due to partial recrystallisation (Yue et al. 2017)

With a grain orientation similar to that of the base material, the HAZ only experiences a thermal cycle caused by dissipation of the heat generated at the stir zone. This leads to the coalescence of the grains and a decrease in hardness values in this region. In heat-treatable alloys, coarsening of the incoherent particles also leads to a deterioration in strength due to over ageing. The extent of the TMAZ and HAZ is influenced by the process parameters, such as rotation speed, and the boundary between these two areas can be challenging to observe by optical microscopy. In the work published by Rosendo et al. (2011) of RFSSW AA6181-T4, the transition between these two

regions can be defined as the area of minimum hardness value between the stir zone and the base material, as showed in Figure 2.16.

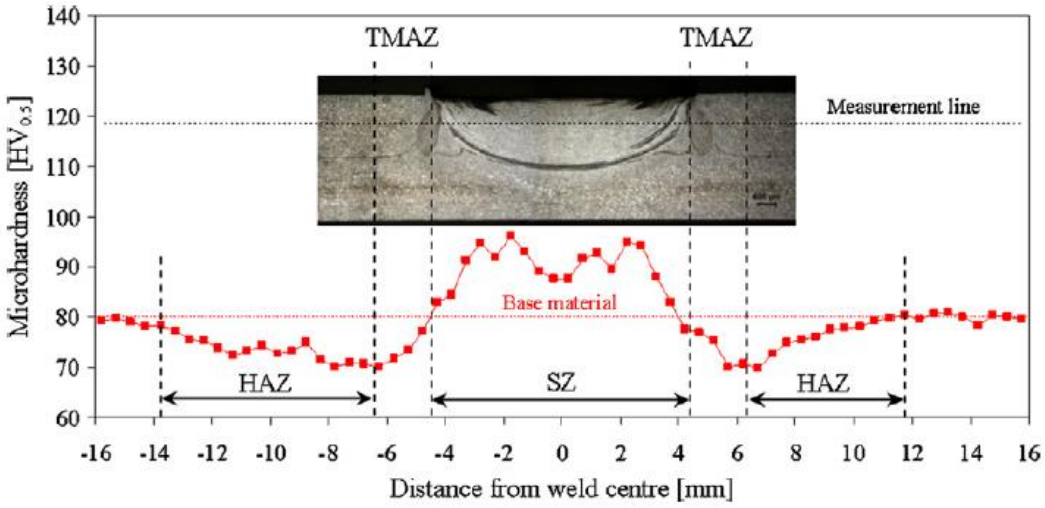

Figure 2.16 - Microhardness profile along an RFSSW weld on a heat-treatable aluminium alloy (Rosendo et al. 2011)

An appropriate selection of process parameters has a great impact on the quality and mechanical strength of the weld. Most of the flaws or defects are caused by either incorrect process parameters or excessive wear of components (Schmal, Meschut and Buhl 2019).

Voids can be described as an internal discontinuity between the plasticised material and the weld region. This defect is usually associated with insufficient heat and consolidation of the plasticised material. Kubit et al. (2019-A) studied the effects of structural defects on the fatigue strength of RFSSW joints. The authors observed that, although these defects did not have a detrimental effect on the static shear strength, a significant reduction in fatigue life was measured. By performing C-scan analysis on the welds the authors also revealed that, despite the asymmetry of process, the voids do not present a continuous form along the perimeter of the weld.

The incomplete refill defect is shown in Figure 2.17.A and can be defined as a consolidation defect from the top surface of the weld material relative to the original sheet surface. As explained by Adamus, K. and Adamus, J. (2019), this defect is caused by loss of plasticised material in the form of superficial chips of flash during welding. However, this feature can also be caused by insufficient pressure from the probe component during the refill stage, leading to the formation of a discontinuity at the centre of the weld [Figure 2.17.B)].

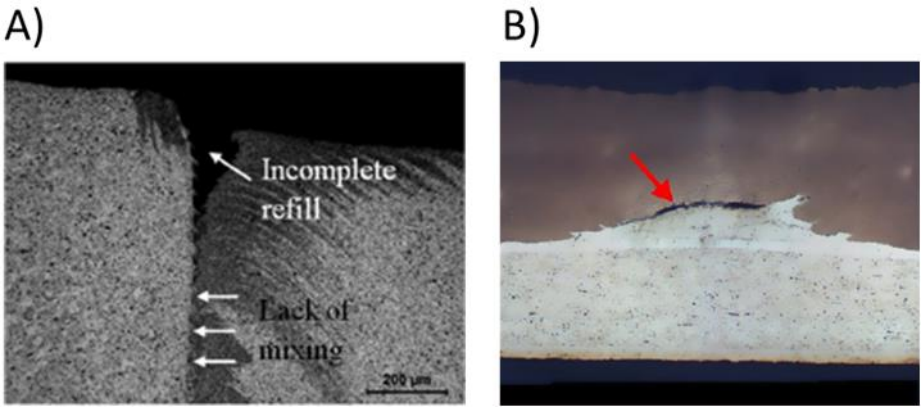

Figure 2.17 - A) Incomplete refill and B) discontinuity at the centre of the weld.

The joint line remnant is located along the width of the stir zone and is characterised by an alignment of oxide from the original base material interface. This feature can be more or less noticeable depending on the process parameters and the base material used. Also, due to the intense shearing action from the shoulder surface, the joint line remnant is generally more dispersed at the corner regions of the weld. As observed in the study performed by Shen et al. (2013), this feature provides the path for crack propagation of shear fracture failure modes.

The hook feature is described as the transition between the bonded area of the stir zone and the unbonded regions of the thermomechanical affected zone. This is an inherent feature to overlap welding configurations that can act as a stress concentration point and provide a location for crack initiation. The hook profile can present various geometries depending on the material flow during the plunge and refill stage, as seen in Figure 2.18. The hook height is measured from the original interface level to the highest point the feature (hook tip). Cao et al. (2016) examined the effect of process parameters on the hook formation and shear strength. Three different hook profiles were identified by varying the rotation speed, joining time and plunge depth. A positive correlation between these process parameters and the hook height was observed, leading to weaker welds. Similar findings were observed by Santana et al. (2017).

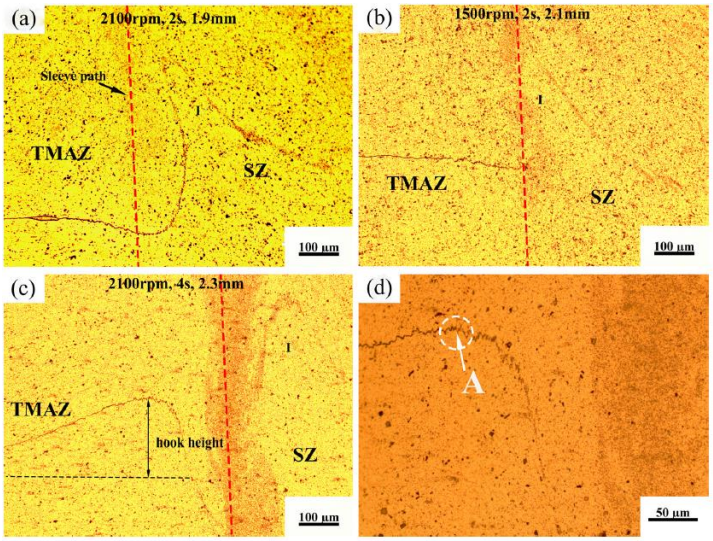

Figure 2.18 - Example of different hook profiles (Cao et al. 2016):
A) Upward curved;
B) Flat;
C) Upwards and downwards.
D) Hook tip.

The presence of surface contaminants or protective coatings (e.g. Alclad or primer paint), have also been shown to have a detrimental effect on joint strength. Kubit et al. (2018-B) analysed the microstructure and mechanical properties of RFSSW AA7075-T6 Alclad sheets. In their study, the authors observed an increase in grain size near the Alclad swirl inside the stir zone, suggesting that these heterogeneities have a detrimental effect on the recrystallisation process. To address this issue, Cao et al. (2020) proposed an initial plunge of the probe component prior to the RFSSW cycle, as shown in Figure 2.5. Despite the increase in cycle time, stronger welds without consolidation defects at the centre of the stir zone were produced.

2.3.3. Material combinations

As a relatively new technology compared to other spot-welding processes, the full extent of industrial and academic research topics is far from being explored. Currently, most of the published research regarding the RFSSW technology is focused on similar and dissimilar material welding or joining and process parameters experimentation based on the optimisation of mechanical properties (Montag et al. 2014). The characterisation of the microstructural areas as well as defects are also areas of current research (Silva et al. 2020). The materials addressed in literature have been selected based on the current or future application requirements from the aerospace or the automotive industry as well as, current RFSSW system's capability. Table A1

presents a non-extensive list of the similar material joining combinations addressed so far along with the lap shear strength values.

The introduction of new lighter weight alloys in current design structures has provided a short-to-medium term solution to the continuous demand for more efficient and less pollutant means of transportation. As a result, designs that include hybrid material structures have become more common due to the greater design freedoms and weight-to-strength ratios that can be achieved. Several authors have published their findings regarding the use of RFSSW to join various combinations of lightweight alloys, proving it to be a versatile technology. Table A2 presents a non-extensive list of the dissimilar material joining combinations addressed so far.

2.3.4. Modelling of RFSSW

In general, computational models and numerical simulations greatly promote a better understanding of the operating principles of many manufacturing processes, often providing an insight of parameter inter-dependencies. Several challenges arise when numerical modelling RFSSW, mainly associated with the complex material deformation developed over a short weld cycle. The viscoplastic flow of material close to the plunging component and the elastic-plastic behaviour of the workpiece material, require a hybrid simulation model based on fluid and solid dynamics (Santos et al. 2009). The heat generation is also highly dependent on the thermo-mechanical properties of the workpiece material as well as the tool geometry, material and features. The latter affects the friction coefficient which varies throughout the process.

During the first decade after the RFSSW process was patented, a relatively low number of research papers were published concerning the numerical modelling. Some authors proposed schematic models based on experimental studies, grain morphology and orientation to describe the material flow during RFSSW (Kalagara et al., 2010 and Suhuddin et al., 2011). However, the information provided by these representations is limited when compared to computational models.

Both variants of the RFSSW process have been analysed with a currently greater focus on the shoulder plunge variant due to the higher weld strengths achieved in this variant.

2.3.4.1. Probe plunge

Muci-Küchler et al. (2005a) developed a three-dimensional isothermal model using Finite Element Method (FEM) for the initial plunge stage. In this study, the author developed two

models in Abaqus/Explicit© with physical properties of AA7075-T6 and AA2024-T3. His findings were confirmed with experimental trials, using aluminium foil to trace the material flow. Following the work of Muci-Küchler et al. (2005b) on the visualisation of the material flow in AA7075-T6 using AA1100 markers, Itapu and Muci-Küchler (2006) performed a similar analysis using a three-dimensional isothermal FEM model of the plunge stage using an arbitrary Lagrangian-Eulerian (ALE) formulation, together with an adaptive meshing strategy. In this study, the author used virtual tracers to visualise the material flow near the tool. Despite the simplifications in the model, the results showed reasonable agreement with experimental results reported in the literature. A preliminary attempt to add the thermal phenomenon to the previous model was presented by Kalagara and Muci-Küchler (2007). A fully coupled thermo-mechanical model was used to explore the effect of the stick/slip condition between the tool and the workpiece material on the process temperature, stress and strain distribution predicted by the model. Further development of this model was presented by Muci-Küchler et al. (2010). This study compared the results obtained between the fully thermo-mechanical FEM model with an ALE formulation and an adaptive mesh algorithm and experimental results. The model showed good agreement with the process temperature, flash height and other process outputs. Stress and equivalent plastic strain distributions were consistent with the expected for the RFSSW, as shown in Figure 2.19.

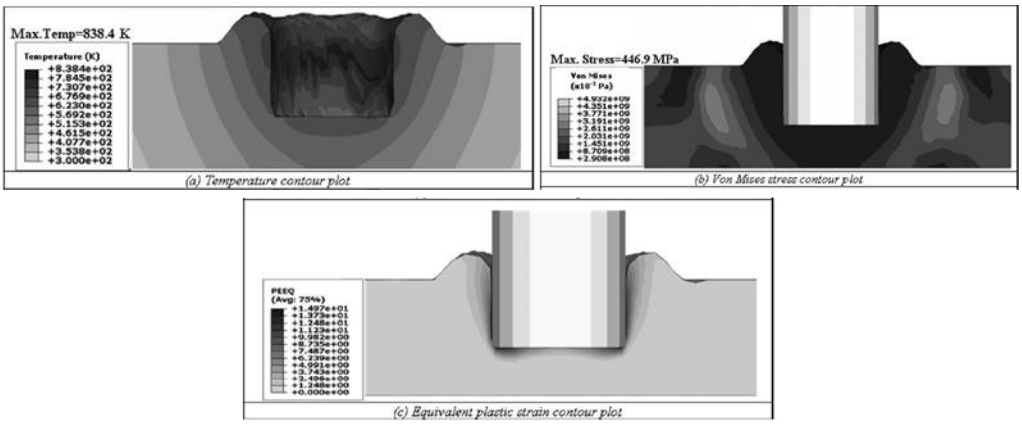

Figure 2.19 - Temperature, stress and strain distribution plots (Muci-Küchler et al., 2010).

2.3.4.2. Shoulder plunge

Zhao et al. (2016 and 2018-A) presented the first computational model to describe the temperature distribution and material flow on the shoulder plunge variant. A FEM model using DEFORM-3DTM© with an ALE formulation and adaptive re-mesh algorithm was developed to simulate the welding of Alclad 7B04 (Figure 2.20) using a threaded shoulder. The results obtained

from the numerical model were compared against temperature measurement trials and microstructural morphology analysis. Overall, the simulated results showed good agreement with the experimental trials.

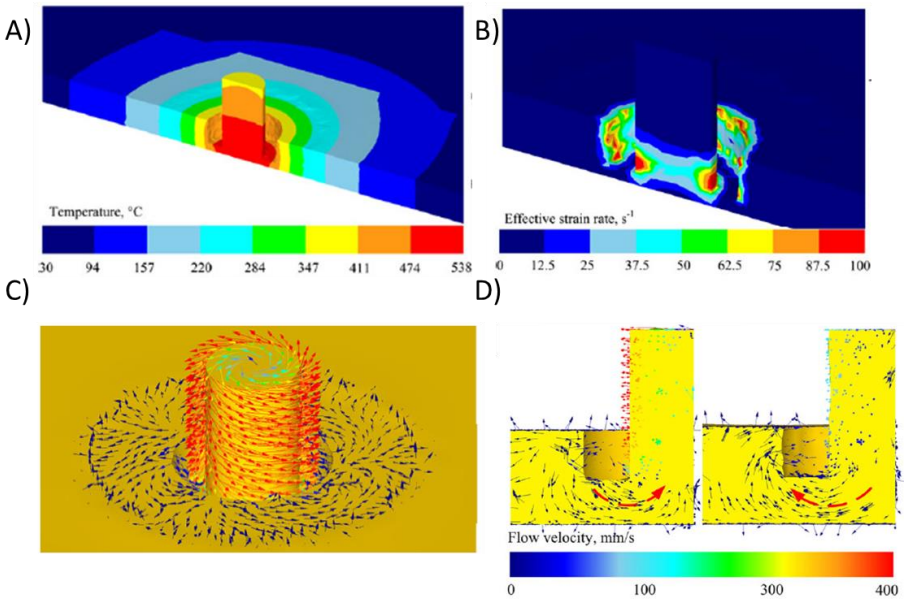

Figure 2.20 - Numerical simulation results for the A) process temperature, B) strain distribution and C) and D) material flow during the plunge (left) and the retracting (right) stage (Zhao et al., 2016).

Ji et al. (2017-A) studied the material flow of the RFSSW process using a threaded shoulder on an aluminium alloy LY12. For this simulation, a Re-normalisation group (RNG) k-ε numerical model was developed in the fluid dynamic software ANSYS FLUENT©. The model was first verified by experimental studies, followed by an analysis on the effect of different plunge depths, rotation speeds and plunge rates on the material flow. Results showed that, for the shoulder outer and inner wall, the maximum flow velocity is located near the contact area and this value decreases as the distance from this point increases. All process parameters that were experimented had a positive influence on the material flow maximum velocity being the rotation speed the parameter with the greatest influence. Higher flow velocities provided more deformation promoting the mixing between Alclad and the workpiece material.

2.3.4.3. Mechanical performance

The possibility of determining the mechanical performance of a weld is of great importance and value when designing structures. A reliable numerical model of the weld properties could predict failure loads and locations, fracture modes and stress distributions as well as, the plastic deformation of small and large assemblies under service conditions. This can lead to savings in

costs and time by minimising the number of experimental trials and iterations when developing new components.

Some authors have published their best efforts to model the mechanical response of an RFSSW joint. Mazzaferro et al. (2009) developed a numerical model of a single RFSSW joint coupon using a combination of the commercial packages Solidworks© and Abaqus©. The welds were produced of similar material AA2024-T3 and loading conditions representing lap-shear and cross-tensile were simulated and compared to experimental data. The results showed good agreement between the maximum force obtained via simulation and experimental data, but the loading curve profile was different due to the absence of a failure criterion. Campanelli et al. (2013-A) investigate the stress distribution on different nugget and hook shapes for lap shear test of single-spot RFSSW AZ31 magnesium alloy. The analysis of the finite element model showed that the presence of the hook defect, regardless of the nugget distinction, produces a degree of uncertainty regarding the failure mode and stress distribution in the vicinity of the weld area, where tensile and compressive stresses are concentrated. Lacki and Derlatka (2016) addressed the numerical model of similar AA6061-T6 RFSSW welds to determine the crack location under tensile loading. In this study, coupons with four and five spot welds were used and assessed regarding maximum shear strength as well as stress and strain distributions. The model results showed good agreement with the experimental results obtained using a digital image correlation software. Recently, Kubit et al. (2019-B) conducted numerical and experimental analysis on the stability under compressive loading of an aircraft skin model produced using RFSSW and riveting. This study also investigated the influence of different spacing between the welds on local buckling of the panel. The results between both analyses show good agreement up to 75% of the maximum load, with the panel with equal spacing displaying similar ultimate load.

A numerical model to simulate the mechanical performance of RFSSW joints between AA2024-T3 and CF-PPS was presented by Paz et al. (2014) and Goushegir, dos Santos and Amancio-Filho (2016). The model was produced a combination of the commercial packages Solidworks© and Abaqus© and the results were compared with experimental data obtained using a digital image correlation software. Good agreement between the load-displacement curve from the model and the experimental data was obtained as showed in Figure 2.21.

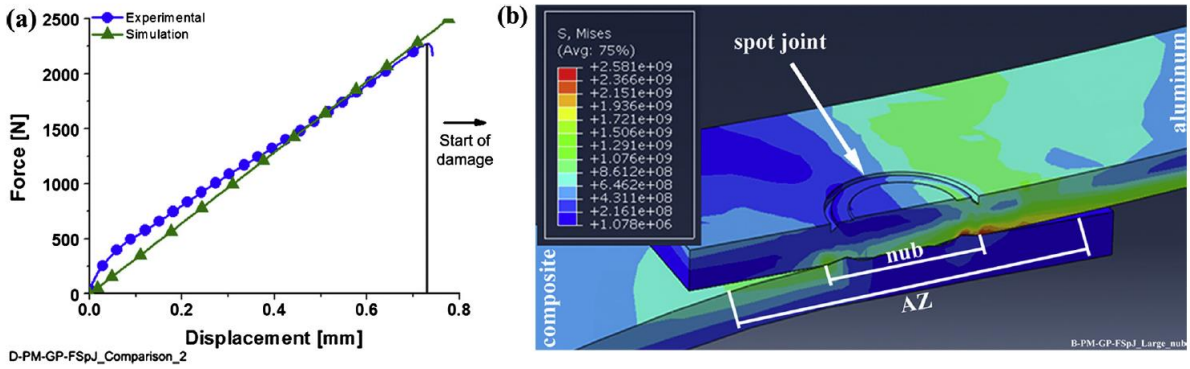

Figure 2.21 - (a) Load-displacement curves obtained from experimental data and numerical simulation and (b) cross-section of the finite element model analysis (Goushegir, dos Santos and Amancio-Filho 2016).

2.3.5. Applications

With the increasing use of lightweight alloys in the transport industry, RFSSW can provide an alternative solution to applications where established fusion welding and mechanical fastening process may not be suitable. Although most of the published research presents the microstructural and mechanical characterisation of test coupons, some studies present the development of prototype demonstrators as well as the development of new applications like FSW exit hole closure.

2.3.5.1. Technology demonstrators

Traditional riveting is still the technique of choice for aluminium sheet joining in the aerospace industry due to its reliability and extensive knowledge on the process. However, the process is not easily automated, requires complex pre-joining operations and adds extra weight to the aircraft (Hameister, 2013). Preliminary data and proof of concept research work using RFSSW has been published regarding the production of aerospace closures and structural components. However, further development is required until the process can achieve the same level of strength and reliability as the established techniques.

Patnaik et al. (2006) studied the microstructural and mechanical properties of RFSSW skin stiffened panels. In this work, RFSSW process parameters were optimised to produce AA2024-T3 T-joint stiffener panels for compression testing (Figure 2.22). The panels produced in the study behaved as expected, with a failure mode attributed to the excessive crippling of the stiffener and a 9% lower buckling load compared to design equations for rivets. Nevertheless, the stiffener

and skin behaved as a single unit and exhibited an adequate performance under buckling characteristics.

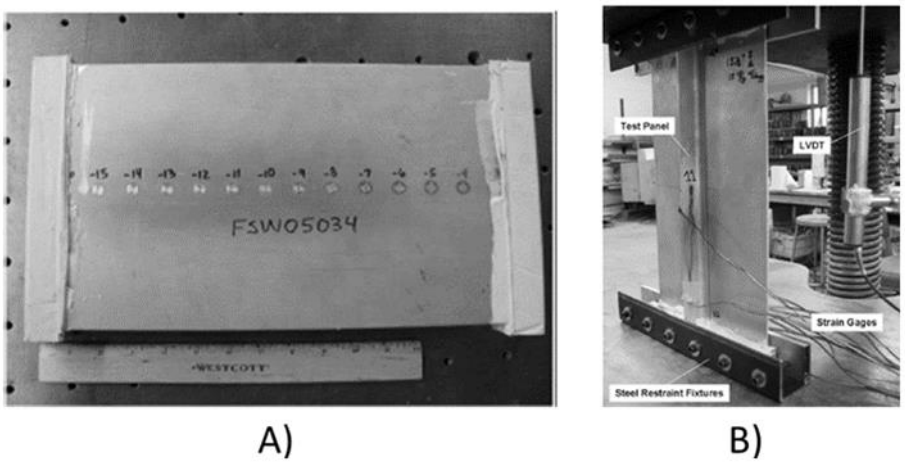

Figure 2.22 - A) RFSSW Skin stiffened panel as welded and B) in compression testing (Patnaik et al., 2006).

Cellular beams can be used to produce aircraft structures such as floor sections (Figure 2.23). Their major advantage is the reduction of material volume without compromising structural integrity

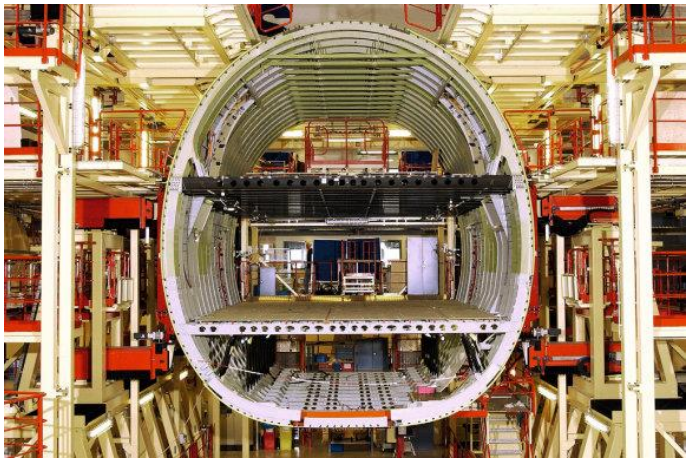

Figure 2.23 - Airbus A380 cross-section (FLUG REVUE 02/2013).

Derlatka and Kasza (2014a) presented a numerical analysis of aluminium cellular beams produced using RFSSW. The beam components were modelled from two AA6061-T6 cold-bent C-section and two flat bars, joined together by RFSSW. The effect of different cell diameters on the bending strength of the beam was analysed via three-point bending test simulation. The effect of different cell spacings was also analysed by Derlatka and Kasza (2014b). The results showed that these factors affect the stress distribution across the beam as well as the location of the maximum and

minimum stresses. Furthermore, increasing the diameter and reducing the spacing between the cells was found to produce higher stresses and Z-displacements.

Further experimental work on composite cell beams was conducted by Lacki and Derlatka (2017). In this study, a comparison between the load-bearing capacity of an aluminium-titanium and an aluminium-fibreglass cell beam is presented. Three-point bending tests were performed on both composite beams and a numerical analysis was performed for the aluminium-titanium. The load-bearing capacity was reported to be similar for both composite beams with an economical and physical advantage for the aluminium fibreglass combination. However, lateral-torsional buckling appeared in the webs due to lower stiffness when compared to the flanges. The addition of polyurethane (PU) foam as a measure to increase the buckling resistance was explored by Lacki and Derlatka (2018). This produced an increase of the load-bearing capacity of the beam by 200% and limited lateral-torsional buckling without a significant addition of weight to the structure.

Okada et al. (2013) performed a parameter optimisation study to produce helicopter closures. The materials joined were AA6061-T6 and AA2024C-T3 which are used, respectively, for skin panels and stiffeners in the aerospace industry. Prototype doors and frames were produced without any spring back, almost no distortion and with a flushed surface without defects (Figure 2.24). These results suggest that RFSSW has the potential to replace conventional rivets to produce aerospace closures. Further work and research are needed before the full application of these components in-service conditions.

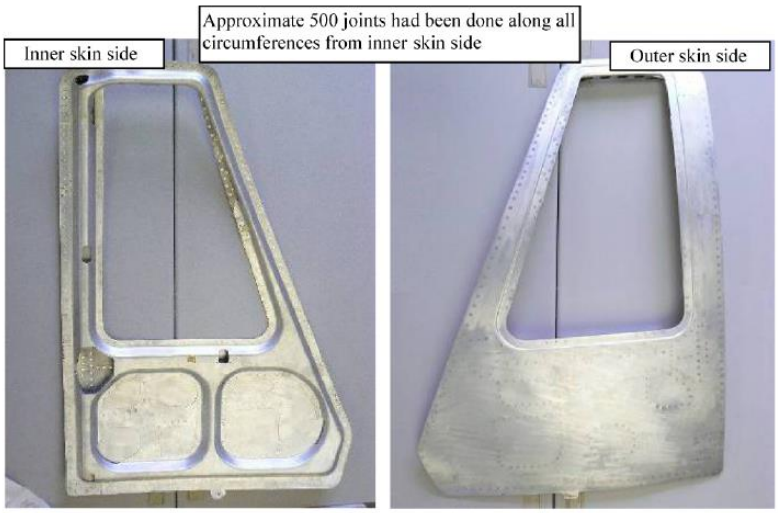

Figure 2.24 - RFSSW prototype door for a helicopter (Okada et al., 2013).

2.3.5.2. Exit hole and crack closure

A novel application for the RFSSW process was presented by Reimann et al. (2016; 2017-A; 2017-B; 2018) for the closure of weld exit holes and borehole sealing. With a different approach to the conventional use of RFSSW, this solution was developed to repair through holes in aluminium components and to refill exit holes produced during welding processes such as FSW. This is a convenient solution for applications that require high-quality seal standards where runoff tabs are challenging due to geometrical and metallurgical factors. Examples of such applications are housings and pressurized tanks for aerospace applications.

As a solid-state process, this solution can be applied to aluminium grades that are not weldable by fusion welding processes. The process stages are schematically shown in Figure 2.25 This technique uses a cylindrical plug of material, identical to the workpiece material, to fill the hole in the workpiece. The RFSSW process is performed, promoting the mixing between the plug and the workpiece material, producing a sealed joint.

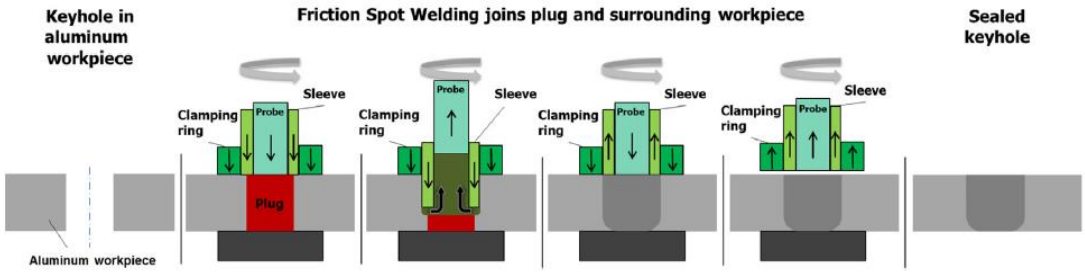

Figure 2.25 - Schematic drawing of the RFSSW exit hole closure process (Reimann et al. 2016).

2.3.6. Equipment suppliers

To the best of the author's knowledge, Harms & Wende (H&W, Germany), Kawasaki Heavy Industries (KHI, Japan) and Bond technologies are the only machine suppliers offering RFSSW commercial solutions. On a basic level, the RFSSW machines possess three independent servo motors that control the vertical movement of the shoulder, probe and the rotation speed during the weld cycle, as described in Section 2.3. The clamping force can be generated mechanically (using an assembly with a set of calibrated springs) or hydraulically (by using a hydraulic cylinder to move the welding head into position). The clamp force is them recorded via load cell under the backing support.

2.3.6.1. H&W

The first commercially available system was produced by H&W which was developed in a technology transfer project with the participation of HZG, H&W and RIFTEC (Camilo et al. 2014). The process control system is based on position/displacement control of the plunging component and time for each of the four-welding stages. On the plunging stage, the plunge rate of the plunging component can be defined as linear (constant plunge rate) or sinusoidal (variable plunge rate).

Figure 2.26.A) shows the first welding head prototype launched by the company, the RPS 100 SK. This is a modular system that can be assembled as a pedestal system or coupled with a robot for production operations, requiring external backing support to react the welding forces. The RPS 100 ZA is the C-frame version as shown in Figure 2.26.B). This assembly provides the necessary backing support and records the reaction forces via loadcell.

The RPS 200 is a custom-built system, designed to withstand high process loads from high strength materials and larger thickness components. Figure 2.26.C) shows an RPS 200 system installed at HZG, GmbH. This is a gantry type machine meaning that the movement of the welding head is restricted to the Z-direction. The travelling worktable enables the movement in the (X, Y) direction using electric ball screw actuators. This allows the system to weld multiple spots on the same component in different locations without the need to readjust the component between spots. This system is also capable of bi-rotational speed of the components, meaning that the shoulder and probe can rotate at different speeds and directions. This can increase the viscoplastic flow in the weld area, leading to an increase in lap shear strength as observed by Fu (2019).

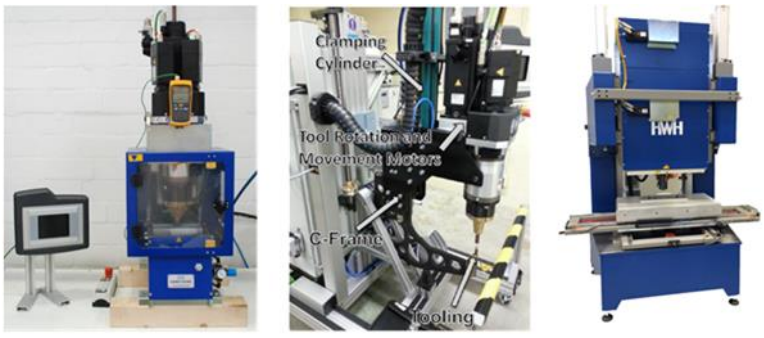

Figure 2.26 - Harms & Wende RFSSW systems A) RPS 100 SK, B) RPS 100 ZA and C) RPS 200 (Courtesy of HZG, GmbH and Nasiri et al., 2018)

2.3.6.2. KHI

KHI patented a different process control variant (Okada et al. 2015) and developed an RFSSW system which is currently considered a research prototype machine. As such, it is not as readily commercially available as the H&W machines. In this system, a reactive force limit experienced by the shoulder during the plunge stage is predefined as an input process parameter. This means that the plunge rate will be continuously adjusted until the shoulder reaches the predefined plunge depth. Another difference between the KHI system and the H&W systems is the way the clamp force is applied during the welding cycle. H&W relies on a clamping cylinder to apply the clamp force while the KHI system uses an assembly of calibrated springs to apply a constant force. An example of this system has been installed at TWI (Figure 2.27).

Figure 2.27 - KHI RFSSW system (Courtesy of TWI, Ltd).

2.3.6.3. Bond technologies

Bond technologies currently provides the most robust commercially available system. With a maximum rotation speed range of 6000 rev/min and maximum torque 16.9 N.m, this system enables the production of sub-one second weld. In the study performed by Larsen and Hovanski (2020), RFSSW AA5052-H36 sheets with 2mm were produced under one second using optimised process parameters. Both tool components can be operated under force or position control, providing great versatility to the system. Similar to the KHI system, the bond technologies machine can be coupled with a 6-axis robot or a gantry type system.

Figure 2.28 - Bond technologies RFSSW system (Bond technologies 2018)

2.4 Residual Stresses

The characterisation of residual stress fields in engineering components and welded assemblies is important to ensure their structural integrity in safety-critical applications. The presence of residual stresses can have a detrimental effect on the mechanical performance of the component and its assembly during service. As explained by Leggatt (2008), the development of residual stresses in welded assemblies can be attributed to the following factors:

- The fabrication operations prior to/after joining (manufacturing and machining);
- The geometry of the parts to be joined;
- The restraints applied to the parts during and after welding;
- The welding process and procedure;
- The thermal or mechanical loading of components during service life;

During welding, residual stresses arise due to the restricted thermal expansion of the weld material by the cold materials in its vicinity. In fusion welding, residual stress levels are often at, or very close to, parent material or weld metal yield strength. Even though FSW is a solid-state joining technology, during which melting and solidification of the materials is avoided, formation of residual stresses is inevitable. As summarised by Staron, Kocak and Williams (2002) and

Threadgill et al. (2009), residual stresses in FSW present an "M" shape distribution, as shown in Figure 2.29. The tensile stress region encompass the nugget and TMAZ to the extent of the hot region beneath the shoulder, with a peak value usually located between HAZ and TMAZ. This "M" shape is produced by the non-uniform temperature field in the transverse section as explained by Peel et al. (2006). Lower level compressive residual stresses are produced away from the weld region, to balance the tensile stress.

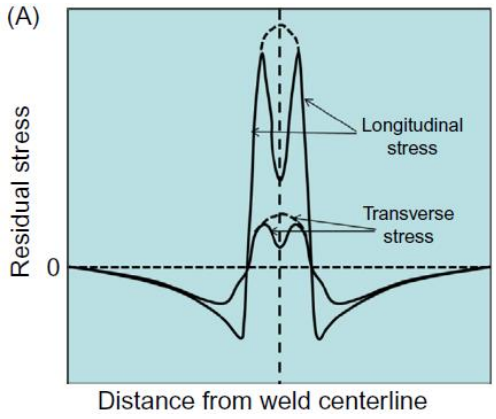

Figure 2.29 - Typical distribution of residual stress in FSW of similar material.

To the best of the authors knowledge, residual stresses measurements and distribution in a RFSSW joint has not been addressed in any publicly available source. With the advantages of this technology for the transport sector, further research in this topic is recommended.

2.5 Conclusions

RFSSW has clear advantages compared to other mainstream single-point joining or mechanical fastening processes. As a solid-state joining process, the RFSSW avoids many of the defects commonly associated with fusion welding of lightweight metals (e.g. porosity formation and solidification cracking). Involving peak temperatures below melting also offers advantages when controlling shrinkage and distortion, which is critical on large assemblies with multiple spot welds. It is also an energy-efficient process without the need for special shielding or cooling units. It is readily automated making it suitable for a production environment. The process can also weld different thicknesses without the need to exchange the design of tool design (riveting and clinching for instance, would require a bespoke tooling for each thickness/material combination).

This reduces the cycle time and costs on equipment in a production environment, especially when joining assemblies comprising various plate arrangements

Unlike conventional mechanical fastening processes such as bolting or riveting, RFSSW does not require the addition of a third element to produce a joint. This means that there is no added weight to the final assembly and no need for pre- or post-joining operations such as hole pre-drilling and cleaning, nor the application of sealants or coatings (Hameister and Bock 2011). When welding similar materials, the absence of a third element to produce a joint also means that the electrochemical potential of the welded material stays unaltered, providing higher corrosion resistance. The dynamic recrystallisation of the material in the stirred zone leads to a higher corrosion protection as observed in FSW (Maggiolino and Schmid 2008). Due to the independent vertical movement of the rotating components during the weld cycle, the RFSSW process produces a flush surface finish. This offers an improved surface finish compared to FSSW, riveted or resistance spot-welded joints. This is a valuable feature for applications where aerodynamics and air-flow management are critical factors.

However, several factors are limiting the industrial application of the process for mass production, namely:

- The limited number of suppliers that commercialise the RFSSW system.
- The increased complexity of the system compared to a conventional FSSW machine.

Despite the growing research in the RFSSW technology, some areas of industrial and academic relevance need to be further developed, namely:

- Modelling of the RFSSW process

As previously discussed in this review, the material movement is quite complex due to the thermal and mechanical nature of the RFSSW process. Most of the published research work regarding the modelling of the material flow during the RFSSW is mainly based on similar material combinations, in particular AA7xxx series alloys. Some authors proposed material flow models for RFSSW of dissimilar material combinations based on experimental studies. However, the development of numerical models would be a valuable contribution to further improve the optimisation of process parameter and augment the understanding of the material flow in similar and dissimilar material welding/joining.

- Process development

RFSSW is a relatively new technology with a significant contribution to offer to improve the joining operations that are currently used in various industry sectors. However, the process still possesses great potential for improvement and development that could enable to overcome its current limitations.

Topics that have been explored for other friction technologies include the effect of using a pre-heating method to reduce the overall process force and weld cycle times (especially relevant for joining materials like steel). Another topic that can enhance the mixing of material in the stir zone is the use of opposite rotating tool components as explored by Fu (2019). The encouraging results from this study highlight the need for further research.

The heat input during the weld cycle is mainly governed by the selected process parameters and influences the mechanical performance of the weld and the metallurgical regions. The use of a temperature control system as proposed by de Backer and Bolmsjö (2013) and Silva, de Backer and Bolmsjö (2017) in combination with an online control system can be a very useful process feedback control tool, with minimum workpiece instrumentation.

- RFSSW tool data

The tool geometry and material are both main process parameters in the RFSSW process and its influences in the heat generation, material flow and deformation during the weld cycle are unquestionable. A better understanding of the effect of different tool designs and tool materials on the weld quality and mechanical performance of the joint would allow to optimise the tool design for various applications based on its requirements.

Also, a greater knowledge of the tool life and a more intuitive indicator of the tool wear during its service life would be beneficial to develop preventive maintenance plans and reduce costs caused by catastrophic failures. The investigation on different tool materials already used on other processes such as FSW and FSSW could enlarge the process capability to weld high strength materials such as steels and titanium alloys.

- Residual stress investigation

Although the peak temperature reached during RFSSW is substantially lower when compared to that of other fusion spot-welding processes, the impact of the heat accumulation by various spot

welds on the development and intensity of residual stresses has not been addressed in any publication. This is probably due to most of the research work that was conducted performed analysis only at a coupon level with a limited number of spots. Further research needs to consider how this phenomenon can affect the mechanical performance of the component.

Chapter 3

RFSSW process parameter influence and development using a standard welding tool

This chapter addresses the effect of process parameters on the mechanical performance of RFSSW joints between lapped sheets of AA2024-T3, AA5754-H24 and AA7075-T6. The research reported in this chapter was performed using a standard tool provided by the equipment manufacturer.

3.1 Introduction

Despite the relative infancy of the RFSSW process, several authors have published their results on the feasibility of RFSSW for joining similar and dissimilar materials, frequently reporting on the influence of key process parameters on joint static mechanical performance and microstructure (de Castro et al. 2018-B; Effertz et al. 2017; Tier et al. 2013 and Xu et al. 2018). However, as shown in the previous chapter, there is a lack of experimental data publicly available regarding the effect of tool material and geometrical features on joint microstructure and mechanical properties. The experimental work reported in this chapter aimed at understanding the effect of process parameters on the mechanical performance of RFSSW joints using a standard tool provided by the equipment manufacturer.

3.2 Materials and methods

3.2.1. Materials

In this investigation, AA2024-T3, AA5754-H24 and AA7075-T6 sheets were used as base materials, all with a thickness of 2 mm and supplied as bare. AA2024-T3 and AA7075-T6 are high strength heat treatable aluminium alloys used in the aerospace industry. As explained by Mouritz (2012), the AA2024-T3 aluminium alloy is commonly used in fuselage and structural applications due to its fatigue resistance and improved toughness, while AA7075-T6 is mainly used as reinforcement for higher load-bearing structures for its higher strength. AA5754-H24 is a non-heat treatable aluminium alloy generally used for formed parts in the automotive industry, namely body-in-white structures, body closure panels and internal door stiffeners, as described by Senkara and Zhang (2000). The chemical compositions and mechanical properties of the alloys, obtained from experimental testing at TWI and from the mill certificates for this material and thickness, are presented in Table 3.1 and Table 3.2, respectively.

Table 3.1 - Chemical composition of the base material.

Element [Weight %]	Si	Fe	Cu	Mn	Mg	Zn	Cr	Ti	Al
AA5754-H24	0.1	0.4	0.02	0.30	2.73	< 1.00	0.05	0.01	remainder
AA2024-T3	0.9	0.11	4.3	0.52	1.5	0.1	0.01	0.04	
AA7075-T6	0.07	0.17	1.5	0.03	2.4	5.9	0.2	0.03	

Table 3.2 - Mechanical properties of the base material.

	Yield stress $\sigma_{0.2\%}$ [MPa]	Ultimate tensile stress σ_{UTS} [MPa]	Elasticity modulus [GPa]	Poisson ratio [ν]	Elongation [%]	Hardness [HV0.2]
AA5754-H24	206.0 ± 2.4	264.1 ± 2.7	73	0.33	11.7 ± 0.6	77 ± 1.9
AA2024-T3	343 ± 3.0	473 ± 5.0			18.0 ± 1.0	137 ± 4.9
AA7075-T6	512 ± 2.0	580 ± 1.0			13.0 ± 0.7	177 ± 4.3

3.2.2. Welding equipment

The work was carried out using TWI's RFSSW system, shown in Figure 3.1. This system consists of a 6-axis articulated robot with a 300kg payload capacity manufactured by Kawasaki Heavy Industries Ltd (KHI), which has been fitted with a C-frame RFSSW gun. In contrast to other systems in the market relying purely on position control, KHI's system incorporates force control capability on the shoulder component. This means that the plunge rate of the shoulder is determined by the input force applied to this component during the welding cycle. The C-frame gun is instrumented to monitor process parameters in real time, namely rotation speed, Z-position for each tool component, shoulder force and probe vertical speed.

Figure 3.1 - TWI's FW-35 KHI RFSSW system.

This information was recorded with the manufacturer's data acquisition system and processed using a dedicated macro. The RFSSW equipment specifications are provided in Table 3.3.

Table 3.3 - TWI RFSSW system specifications

Robot System	
Gun Mounting	6 axis articulating arm
Gun specifications	
Drive Method	AC servomotor drive (Shoulder axis/rotating axis/probe axis)
Force Range	1,470 to 14,700 N (150 to 1,500 kgf)
RPM Range	0 to 2,160 rev/min
Pressure Shaft Stroke	Max. 180 mm
Mass	Approx. 190 kg

3.2.3. Tool design

The RFSSW tool used for the welding trials was provided by KHI and it is shown in Figure 3.2. The tool material of all components was a metal matrix composite of tungsten carbide particles imbedded in a cobalt binder and coated with a low friction diamond-like carbon coating. This tool material has been used for FSW and FSSW to weld steel and titanium alloys due to its high toughness and hardness as well as its dimensional stability under service conditions.

Figure 3.2 - KHI RFSSW tool components.

The geometry of the tools was cylindrical without any superficial features, unlike the conventional FSW or FSSW tools. The dimensions of the components are provided in Table 3.4.

Table 3.4 - RFSSW tool dimensions

	Probe	Shoulder	Clamp
External diameter [mm]	Ø 4	Ø 7	Ø 16
Internal diameter [mm]	n/a	Ø 4	Ø 7

3.2.4. Welding sequence

Interface surfaces were manually cleaned with acetone prior to welding to remove contaminants. Similar material and single spot RFSSW specimens were produced using the shoulder-plunge variant of RFSSW [Figure 2.5.A)], operating in force-control mode. A full-factorial design of experiments (FFDoE) with 2 factors and 3 levels was performed to determine the optimised

weldability range of the selected alloys. The best performing process parameter combination was determined based on lap shear strength and cross-section analysis. Table 3.5 presents the range of the process parameters varied in the present investigation. An Analysis of Variance (ANOVA) was conducted to quantify the influence of each process parameter as well as their interaction on the shear strength. All the statistical analysis in this work was performed using the software MINITAB® 17.

Table 3.5 - RFSSW process parameters

Factor	Level 1	Level 2	Level 3
Rotation Speed [RS] [rev/min]	1000	1580	2160
Plunge Depth [PD] [mm]			
AA5754-H24	1.8	2.0	2.2
AA2024-T3 and AA7075-T6	2.0	2.2	2.4
Stage 1 Dwell time [s]			
AA5754-H24		1.0	
AA2024-T3 and AA7075-T6		2.0	
Shoulder plunge force [kN]			
AA5754-H24		13.5	
AA2024-T3 and AA7075-T6		14.5	
Clamp force [kN]		7.0	

The process parameter optimisation on AA5754-H24 was initially performed followed by the higher strength alloys, AA2024-T3 and AA7075-T6. The plunge depth range was increased for the higher strength alloys following the findings from the mechanical testing of AA5754-H24. Dwell times and shoulder plunge forces were adjusted to the higher strength alloys due to the increase of hardness.

The geometry of the testing specimens is shown in Figure 3.3 and Figure 3.4. Specimens for lap shear and fatigue testing were produced in accordance with BS EN ISO 18785-4:2018 and BS EN ISO 14324:2003, respectively. Sheet rolling direction was perpendicular to the loading direction on both geometries. Specimens for cross tension testing were produced in accordance with BS EN ISO 18785-4:2018.

The use of interfacial sealants in assembly joints is a common practice in the aerospace industry to protect against corrosion in extremely variable conditions. Therefore, once the most promising process parameter combination was identified, RFSSW with an interfacial aerospace sealant was performed to investigate its effect on the mechanical strength and microstructural properties of the weld. This was performed for the AA2024-T3 and AA7075-T6 alloys. A high temperature resistant manganese dioxide-based polysulphide polymer sealant was used in this investigation

in accordance with industrial practices. The sealant was applied on the overlapping area of the top and bottom sheets with a layer thickness of approximately 0.15mm. The lap shear strength of the cured sealant specimen without a weld was also evaluated under shear loading conditions. The welding cycle was performed with the sealant in the uncured state followed by natural curing at ambient temperature. The sealant properties are shown in Table 3.6.

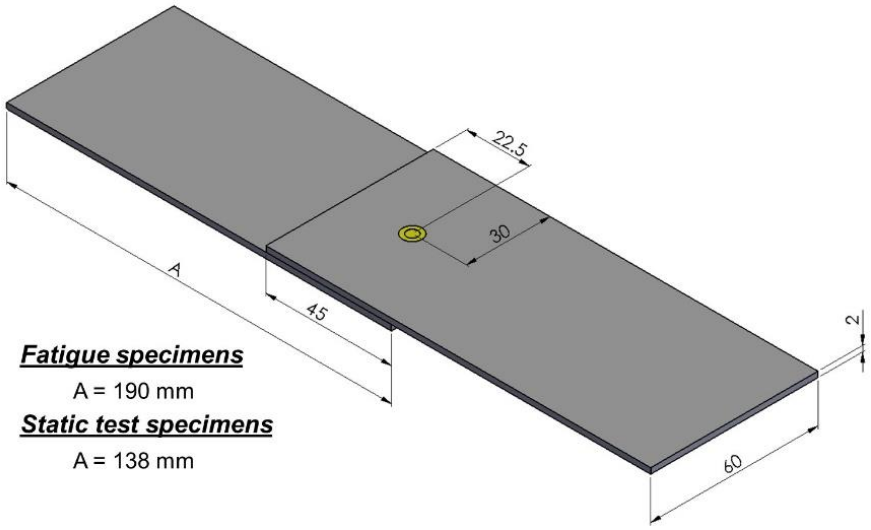

Figure 3.3 - Lap shear and fatigues test specimen geometries.

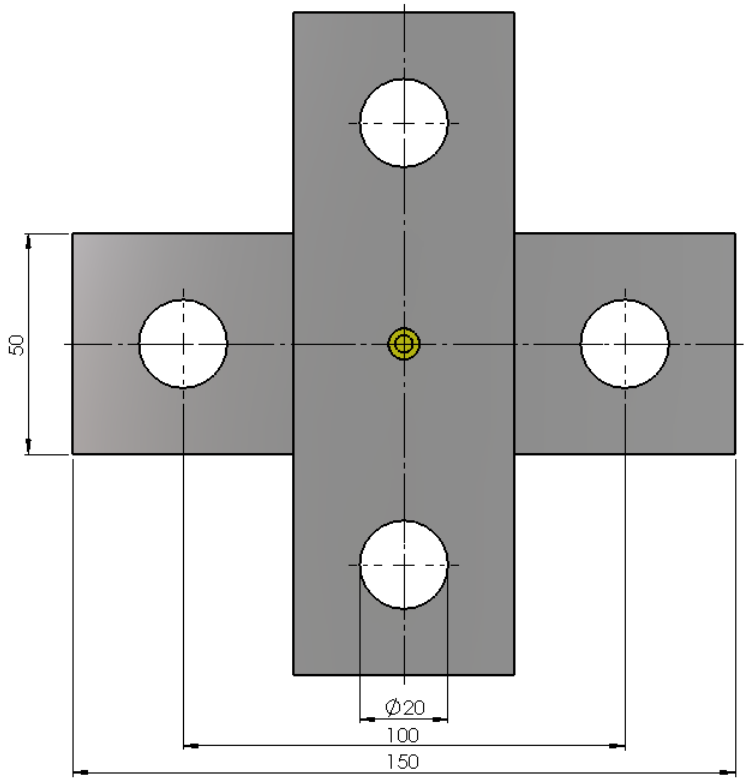

Figure 3.4 - Cross tension test specimens.

Table 3.6 - Interfacial sealant properties

Sealant type	PR-1770 class C-12 faying surface sealant
Viscosity of base compound [poise]	280
Application timeframe [hours]	12
Temperature range [°C]	- 55 to + 180

3.2.5. Microstructural and mechanical characterisation

Metallographic specimens were sectioned, polished and etched with Keller reagent for microstructural analysis. Optical microscopy was conducted using an OLYMPUS GX71 inverted geometry optical microscope with a Colorview III camera. As previously mentioned, AA2024-T3 and AA7075-T6 alloys are heat-treatable alloys, meaning that changes in distribution of the main strengthening precipitates, during and after welding, will affect the mechanical properties of the weld. Also, the sealant used in this investigation requires a minimum of 14 days to be fully cured. Therefore, mechanical characterisation was performed seven weeks after welding, ensuring the consistency between the testing of bare aluminium specimens and specimens with interfacial sealant. Weld static strength was evaluated via lap shear and cross-tension testing in accordance with BS EN ISO 18785-4:2018. Both tests were performed using an INSTRON 8502 tensile machine with a displacement rate of 1 mm/min at room temperature. Three specimens of each process parameter combination were tested.

Fatigue testing was performed for the most promising process parameter combination in accordance with BS EN ISO 14324:2003. A stress ratio of R = 0.1 was set under a sinusoidal axial tensile with constant amplitude load and a frequency of 3 Hz. Loading conditions of 20, 35, 55 and 70% of lap shear strength were tested, with three specimens per loading condition and a stopping criterion of 10^6 cycles or complete failure of the specimen was defined. The tests on AA5754-H24 were ceased after a maximum amplitude of ± 1 mm was reached while the tests on AA2024-T3 and AA7075-T6 were ceased after complete specimen failure. Fracture surfaces from selected conditions were inspected under scanning electron microscopy (SEM) using a Zeiss EVO LS15.

Residual stress measurements were performed using the contour method. The contour method is a destructive residual stress measurement technique based on the stress relaxation. As described by Prime (2001), the displacement profile of the cut surface is measured with a coordinate measuring machine (CMM) and postprocessed to input in a 3D Finite Element model (FEM). A linear elastic finite element analysis is finally used to calculate the residual stress in the

sample. This method is a quick and cost-effective that has been used previously for other welding technologies (Frankel et al. 2009; Liu and Yi 2013 and Thibault et al. 2010).

Measurements were performed for the most promising process parameter combination on a bare multiple spot-weld specimen as shown in Figure 3.5. A spacing between spot-welds and each row was set to approximately three times the spot size diameter, which is consistent with the best practices for aerospace riveted joints (Skoruba and Skoruba, 2012). The arrangement of the spot-welds within the specimen aims to replicate the typical design of riveted fuselage panels found in aeroplanes. For comparison, measurements on bare RFSSW single spot-weld specimen were also performed. The single spot-weld specimen analysis of the AA2024-T3 and AA7075-T6 specimens was produced using two overlapped 136 x 60 x 2 mm sheets with a spot-weld in the centre of the sheet, while the single-spot specimen analysis of AA5754-H24, was performed on a specimen produced in a lap-shear configuration, as shown in Figure 3.3. Samples were cut on a Fanuc Robocut α-C600i wire electric discharge machine with 0.25 mm diameter brass wire. The samples were symmetrically clamped while cutting along the A-A and B-B plane through the sample thickness at a speed of 0.7 mm/min without wire breakage. Cutting direction for A-A and B-B plane was, respectively, from weld nr 5 to nr 6 and from weld nr 2 to nr 10. To improve the surface finish and reduce the magnitude of cutting artefacts, the low power cutting settings were select, as reported by Ahmad et al. (2018). Surface displacement profile was measured with a Zeiss Contura g2 CMM with a resolution of 0.2 µm and an accuracy of 1.5 µm (Carl Zeiss AG 2013). A 3 mm diameter touch trigger probe was used to measure two profiles at mid-thickness of the top sheet and the bottom sheet, with a spacing between individual measurement points of 0.1 mm. The displacement data was post-processed for data aligning, cleaning, flattening and smoothing using the software Matlab®. Spline knot spacing was selected based on the good fit of the averaged displacement data. The data smoothing of sample was performed with a cubic spline with knot spacing of 2.5 mm along both X and Y-directions. The finite element model of the cut sample was built using an 8-node brick element (C3D8R) from the software Abaqus® with a mesh size of approximately 0.2 mm.

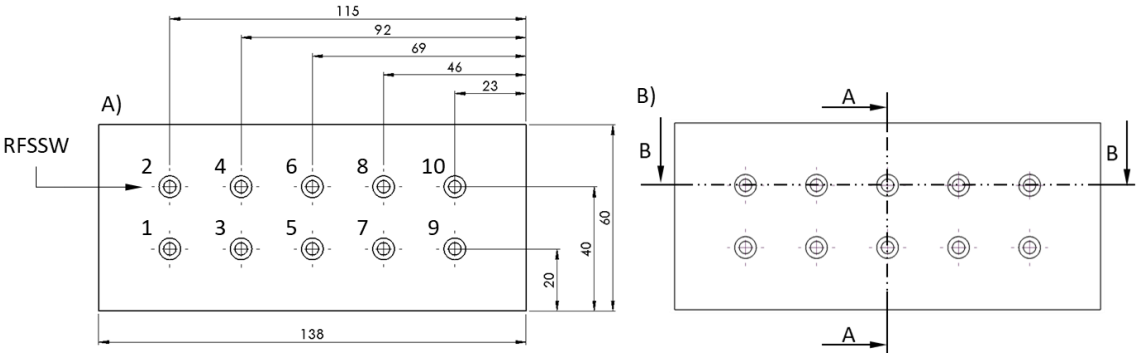

Figure 3.5 - Schematic drawing of the A) RFSSW residual stress measurement specimen and B) sectioning planes at mid length (A-A) and along the length (B-B).

3.3 Results and discussion

3.3.1. Lap shear strength analysis

3.3.1.1. AA2024-T3

Table 3.7 shows the lap shear testing results for the weld conditions obtained from the FFDoE. Within the explored process parameter window, lap shear strength values ranged between 5.56 ± 0.21 kN and 8.59 ± 0.10 kN. In general, standard deviation values varied between 0.8 to 4.6 % of the lap shear strength value, supporting the consistency and repeatability of the results. Shear strength values improved as plunge depth values increased and rotation speed values decreased. The strength gain with the increase of plunge depth can be attributed to an increase of welded area and improved bonding at the weld interface. The lower rotation speed values contribute to a lower heat input and more effective stirring action preventing frictional slip between the tool and the weld material, as observed in friction stir welding (Reilly et al. 2015; Schneider, Beshears and Nunes Jr 2006). Based on a “maximum strength” criteria, the optimised process parameter combination was obtained for 1000 rev/min and 2.4 mm, corresponding to condition W3. This process parameter combination will be used later in this section to determine the effect of an interfacial sealant on the static and fatigue strength, as well as the microstructural characteristics.

Table 3.7 - Lap shear strength results of RFSSW AA2024-T3

Welding Condition	Rotation Speed [rev/min]	Plunge Depth [mm]	Lap Shear Strength [kN]	Failure Mode
W1	1000	2.0	6.97 ± 0.29	Shear fracture through the weld nugget
W2		2.2	8.01 ± 0.20	
W3		2.4	8.59 ± 0.10	
W4	1580	2.0	6.00 ± 0.13	
W5		2.2	7.88 ± 0.36	
W6		2.4	8.52 ± 0.26	
W7	2160	2.0	5.56 ± 0.21	
W8		2.2	7.47 ± 0.06	
W9		2.4	8.27 ± 0.08	

As a potential replacement for resistance spot welding and riveting, lap shear strength values of RFSSW should be compared with the strength requirements for these joining methods. Based on the thickness and material properties of the alloys used in this investigation, the AWS D17.2/D17.2M:2019 standard specifies for resistance spot welding a minimum lap shear strength of 4.56 kN per spot. All conditions tested in this investigation exceeded this value, confirming that the RFSSW process is a suitable replacement technology. The shear strength design for a 1/4" MS20426DD (AA2024-T31) solid rivet is 8.99 kN for AA2024-T3 joints, as specified by MMPDS-04 (2008). The shear strength of W3 did not exceeded the strength requirements of an equivalent riveted joint, with a value of 95.5% of the strength requirement. However, the negligible difference between the strength values demonstrate the potential of RFSSW as a suitable joining technology for aerospace applications.

The ANOVA of the acquired lap shear strength data from RFSSW AA2024-T3 is presented in Table 3.8. For this analysis, a confidence interval of 95% ($\alpha = 0.05$) was used. A process parameter is considered relevant to the output if its contribution is higher than the associated error. The results suggest that PD was the factor with the greatest influence on lap shear strength values with a contribution of 78.93%. The interaction between factors and the second order factors presented a negligible effect on the shear strength values. Within the process parameter window tested, RS has relatively low influence on the mechanical properties of the weld. As previously mentioned, the alloys used in this investigation are designated as heat treatable, i.e. their mechanical properties can be influenced by thermal cycles. Since rotation speed is one of the process parameters that controls the heat input, the minor influence of rotation speed to the weld shear strength is a somewhat contradictory result. A possible explanation for this conclusion is that in the RFSSW process, due to high plunge and retraction speeds, a variation on the rotation

speed value does not translate into a significant increase or decrease of the total number of rotations of the tool during the welding cycle.

Table 3.8 - ANOVA for the shear strength output of RFSSW AA2024-T3.

Source	DF	Sum of Squares	Mean Square	F Value	P Value	Contribution [%]
RS	1	2.57	0.78	11.04	0.003	8.62
RS^2	1	0.00	0.00	0.01	0.908	0.00
PD	1	23.51	0.01	0.20	0.000	78.93
PD^2	1	1.33	1.33	18.66	0.000	4.45
RS x PD	1	0.89	0.89	12.51	0.002	2.98
Error	21	1.49	0.07			5.01
Total	26	29.79				100.00

To predict the shear strength of the joint within the process parameter window explored, a second order regression model was developed (Equation 1). Table 3.9 presents the second order regression model equation with the correspondent coefficient of correlation, R^2. It should be noted that, the R^2 is considerably high (> 0.95). This is an indication that there is good agreement between the experimental results and the results from the model.

Table 3.9 - Second order regression equation for RFSSW AA2024-T3.

	Equation [kN]	R^2 Value
Equation 1	$\mathrm{LSS_{ST}} = -52.4 - 5.93 \times 10^{-3} \times \mathrm{RS} + 53.7 \times \mathrm{PD} - 11.75 \times \mathrm{PD}^2 + 2.346 \times 10^{-3} \times \mathrm{RS} \times \mathrm{PD}$	0.997

The contour plot of Equation 1 is presented in Figure 3.13. The dominant effect of plunge depth compared to the rotation speed on the shear strength can be observed by the higher variation of shear strength along the X-axis compared to the Y-axis.

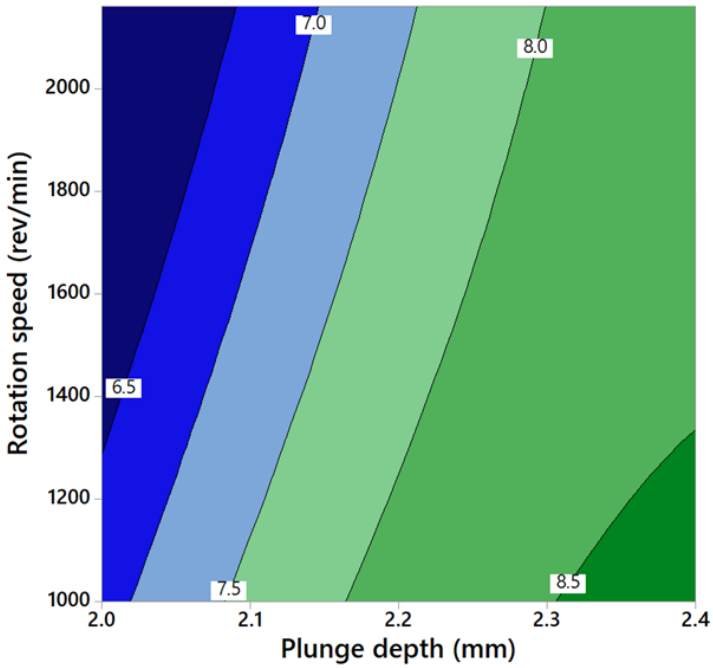

Figure 3.6 - Contour plot of lap shear strength as function of process parameters for RFSSW AA2024-T3.

To determine the accuracy of the model, specimens with process parameters from within the explored process parameter window were performed and tested to compare the experimental shear strength value (LSS Actual) against the predicted shear strength value from the model (LSS Predicted). The results are presented in Table 3.10. Considering that the discrepancy between the values is small and within the confidence interval, the results confirm the accuracy of the model.

Table 3.10 - Comparison between experimental shear strength and predicted shear strength from Equation 1.

Rotation Speed [rev/min]	Plunge Depth [mm]	LSS Predicted [kN]	LSS Actual [kN]	Error [%]
1280	2.4	8.51 ± 0.60	8.27 ± 0.09	2.80

Figure 3.7 shows the fracture surface of condition W3 with magnified regions obtained by SEM of RFSSW AA2024-T3. All specimens fractured through the nugget region.

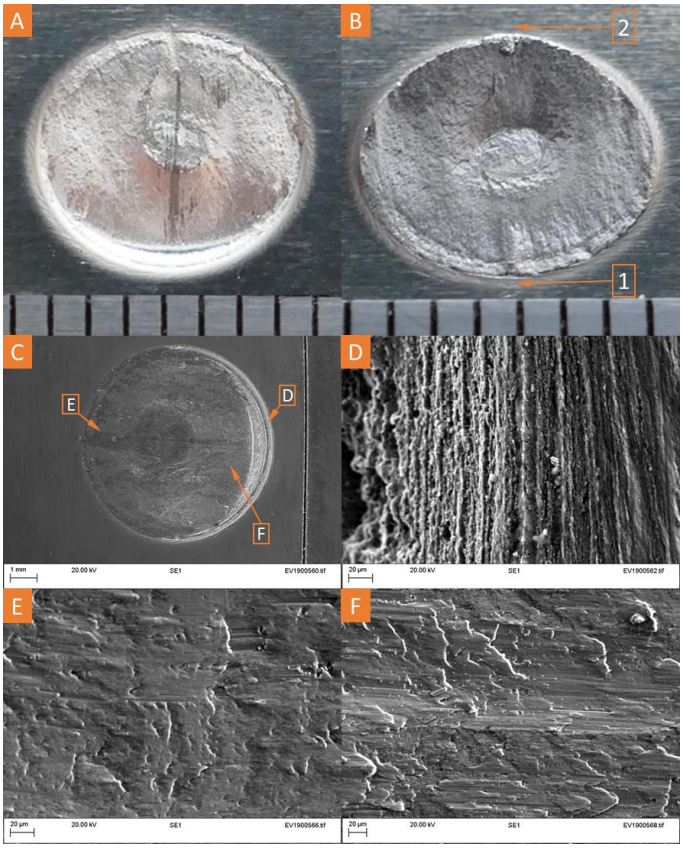

Figure 3.7 - Fracture surfaces of RFSSW AA2024-T3 weld condition W3 (RS = 1000 rev/min; PD = 2.4mm):
A) Top sheet;
B) Bottom sheet;
C) SEM fractography;
D) High magnification region – location shown in Figure 3.7.C);
E) High magnification region – location shown in Figure 3.7.C);
F) High magnification region – location shown in Figure 3.7.C).

Figure 3.7.B) shows the fracture surface on the bottom sheet of RFSSW AA2024-T3. Overlapped joining configurations generally possess a transition region between the bonded weld area and the unbonded interface, designated as the hook, which is prone to stress concentration. A full description of this feature will be presented in Section 3.3.4.1. In this investigation, two types of cracks developed on opposite sides of the weld: an initial crack initiated by the nucleation of annular cracks at the tip of the hook (Figure 3.7.B)-1) and a circumferential crack, originating at the hook from the opposite side (Figure 3.7.B)-2) propagating perpendicular to the loading direction. These crack initiating sites and the type of cracks are closely related to the type of stresses that are generated on the edges of the spot-weld. As shown in Figure 3.8, due to the asymmetric design of the overlapped configuration, the location from Figure 3.7.B)-1) on the bottom sheet relate to areas of tensile stresses while the location from Figure 3.7.B)-2 on the

bottom sheet relate to areas of compressive stresses. For the top sheet, the same locations on the specimen have stresses of opposite nature.

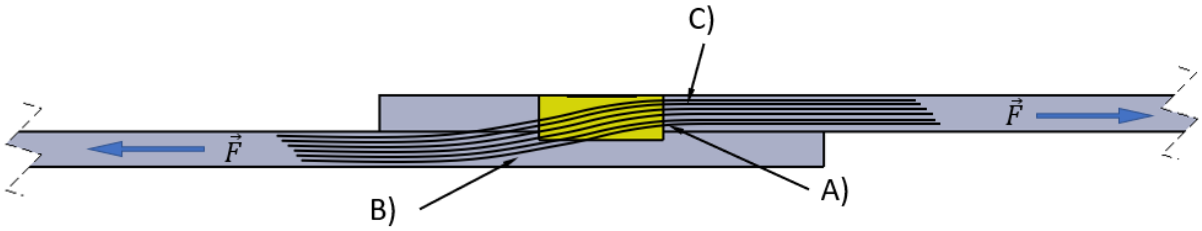

Figure 3.8 - Stress regions caused by asymmetric loading on lap joints:
A) tensile-stressed side of top sheet;
B) tensile-stressed side of bottom sheet;
C) load paths.

Due to the asymmetry of the forces being applied to the specimen under unguided shear loading conditions, the weld nugget is forced to rotate and deform to a certain angle. This rotation generates a perpendicular load component on the load vector that is perpendicular to the sheet surface, ($\overrightarrow{F_N}$), forcing the crack to propagate at an angle with the loading direction. Figure 3.9 shows a schematic drawing of this phenomenon at an extreme stage. The deformation angle before failure will mainly depend on the ductility of the joint. This phenomenon, although of small effect, can be seen in Figure 3.7.B) by the inclined fracture surfaces and by the striation pattern present in Figure 3.7.F). Complete specimen fracture occurred with the interception of both cracks at the periphery of the weld nugget.

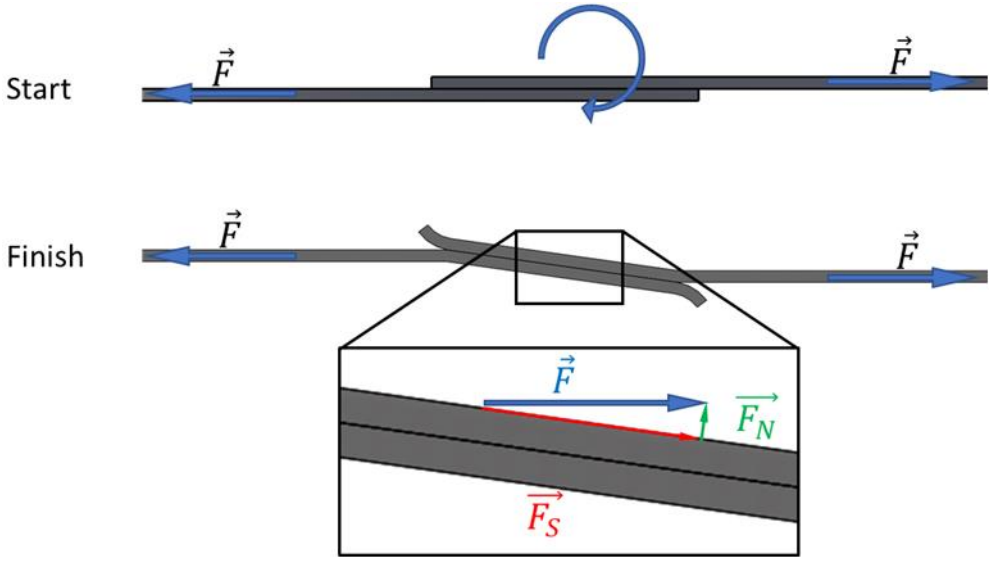

Figure 3.9 - Rotation of the nugget due to unguided asymmetric loading.

Figure 3.10 presents the load-displacement curve for the strongest and the weakest conditions, W3 and W7 respectively, of RFSSW AA2024-T3 under shear loading conditions. The minimum strength requirement for AWS D17.2/D17.2M:2019 and MMPDS-04 are also shown on each graph. For the strongest and weakest weld condition, the behaviour under shear loading conditions is very similar. Specimens exhibited low deformation during the plastic deformation stage, which is coherent with a brittle fracture of the weld.

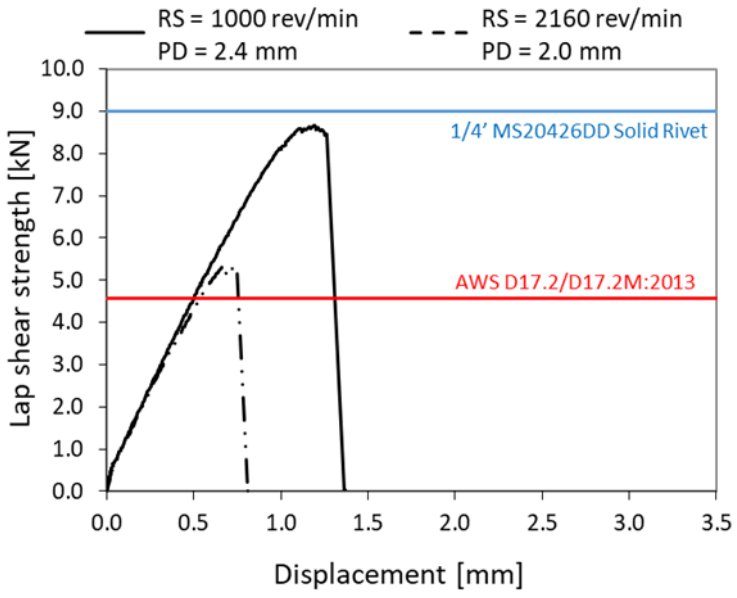

Figure 3.10 - Lap shear test load-displacement curve of RFSSW AA2024-T3 weld conditions W3 (RS = 1000 rev/min; PD = 2.4 mm) and W7 (RS = 2160 rev/min; PD = 2.0 mm).

Table 3.11 shows the strength comparison between RFSSW in the bare condition and in the presence of an interfacial sealant. The use of sealants on overlapped configurations typically has a detrimental effect on the weld mechanical properties, since the sealant layer acts both as a thermal insulator and barrier to material stirring leading to sealant entrapment in the weld area. In this investigation, the presence of the interfacial sealant improved the lap shear strength with an increase of 51% compared to the bare material condition.

Table 3.11 - RFSSW AA2024-T3 weld conditions W3 lap shear strength comparison between the bare and sealant condition

Welding Condition	Rotation Speed [rev/min]	Plunge Depth [mm]	Lap Shear Strength [kN]	Failure Mode
AA2024-T3 Bare	1000	2.40	8.59 ± 0.10	Shear through the weld nugget
AA2024-T3 Sealant			12.98 ± 1.15	Shear through the weld interface

Figure 3.11 presents the load-displacement curve for weld condition W3 of RFSSW AA2024-T3 specimens in the bare and with interfacial sealant condition. The minimum strength requirement from both AWS D17.2/D17.2M:2019 and MMPDS-04 are also shown. Considering that low rotation speed values reduce the heat input and improves the shear strength of the weld, it is likely that this increase in strength comes from an even lower peak temperature due to the energy absorption by the sealant during volatilisation of the solvent.

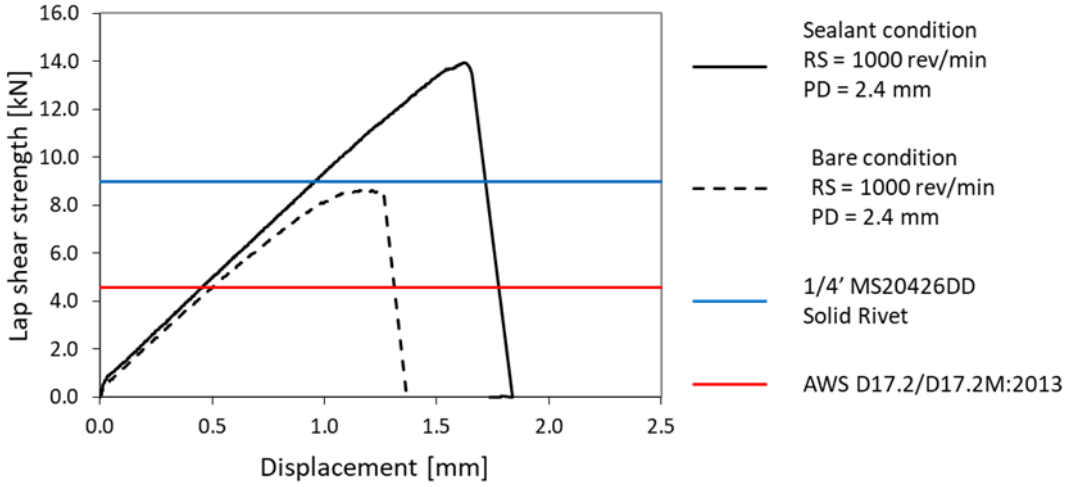

Figure 3.11 - Lap shear test load-displacement curve of RFSSW AA2024-T3 weld condition W3 (RS = 1000 rev/min; PD = 2.4 mm) in bare and with sealant condition.

Figure 3.12 shows the fracture surface of RFSSW AA2024-T3 welding condition W3 with sealant with magnified regions obtained by SEM. Similar fracture mechanism to the one observed in the bare specimen condition was recorded, however the crack propagated through the joint line

remnant on RFSSW AA2024-T3, as opposed to what was observed in the bare condition. Poor bonding and material stirring at the weld centre can be observed in Figure 3.12.C) and E), which can be the cause for the different fracture path. Away from the weld area and on the sealant side, a predominant cohesive failure can be observed. Despite not using any sealant squeeze-out technique before the welding cycle, most of the sealant was displaced away from the weld area as observed in Figure 3.12.A), B) and F). Microscopic analysis will provide further indication of any sealant remnants within in the weld region.

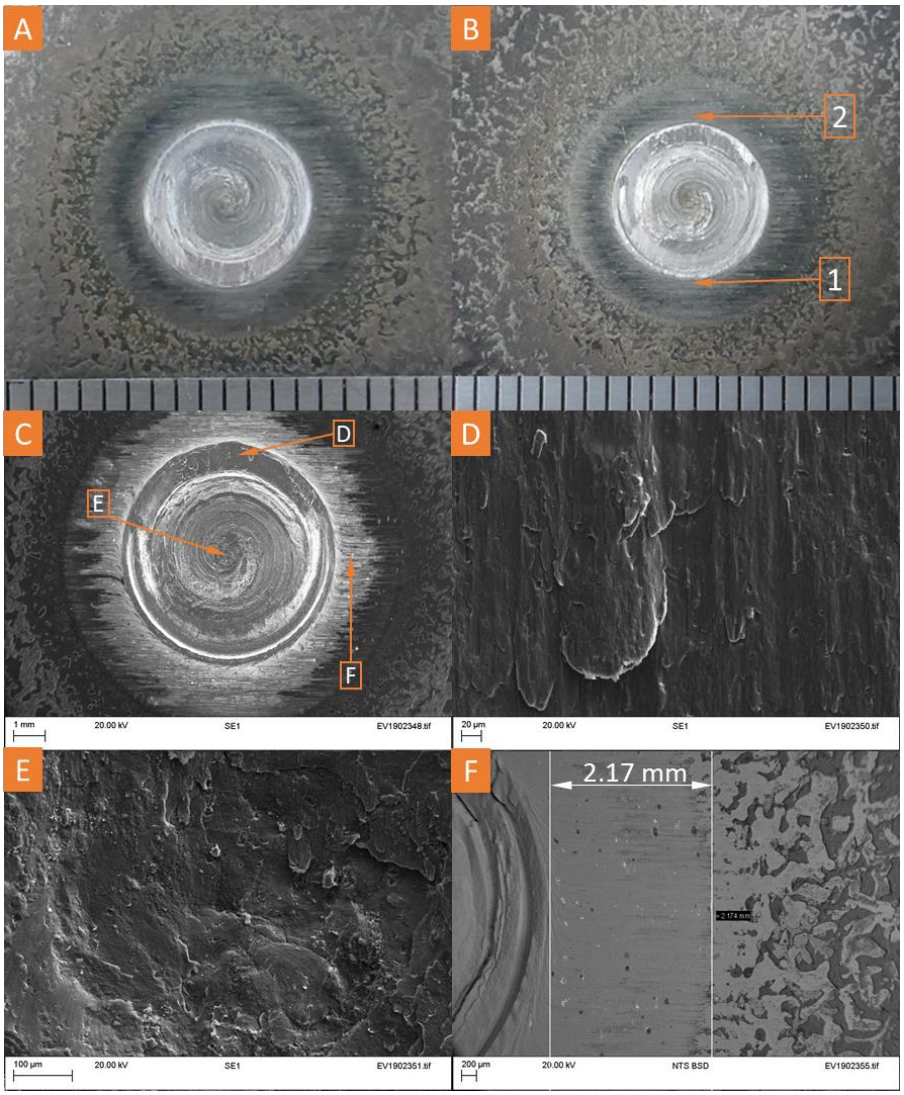

Figure 3.12 - Fracture surfaces of RFSSW AA2024-T3 weld condition W3 with sealant (RS = 1000 rev/min; PD = 2.4 mm):
A) Top sheet;
B) Bottom sheet;
C) SEM fractography;
D) High magnification region – location shown in Figure 3.12.C);
E) High magnification region – location shown in Figure 3.12.C);
F) High magnification region – location shown in Figure 3.12.C).

As mentioned before, an increase in the shear strength values for the RFSSW with sealant specimens was observed. Another possible explanation for this phenomenon can be the adhering layer of sealant at the vicinity of the spot-weld. Once fully cured, specimens only bonded with sealant were also tested under shear loading conditions producing an average shear strength value of 2 kN. Therefore, the load distribution through this area further prevented nugget rotation. As observed in the work of Amâncio-Filho et al. (2011-B), one of the main bonding mechanisms for joining of AZ31 magnesium alloy and carbon fibre reinforced poly (phenylene sulphide) was the interfacial chemical adhesion between the polymer and the alloy.

3.3.1.2. AA5754-H24

Table 3.12 shows the lap shear testing results for the weld conditions selected based on the FFDoE. Shear strength load varied between 4.93 ± 0.08 kN and 7.16 ± 0.02 kN, within the explored process parameter window. The standard deviation vales for all process parameter combinations varied between 0.28 % and 1.62 % of the shear strength, supporting the consistency and repeatability of the results and the joining process. As previously observed, the shear strength values improved as plunge depth values increased and rotation speed values decreased. This strength gain with the increase of plunge depth can be attributed to an increase of the welded area and better bonding at the weld interface. Although this alloy group is considered as non-heat treatable, the lower rotation speed values contribute to a lower heat input, reducing material overaging and grain growth.

Table 3.12 – Lap shear strength results of AA5754-H24.

Welding Condition	Rotation Speed [rev/min]	Plunge Depth [mm]	Lap Shear Strength [kN]	Failure Mode
W10	1000	1.8	5.87 ± 0.07	Shear fracture through the weld interface
W11		2.0	6.85 ± 0.04	
W12		2.2	7.16 ± 0.02	
W13	1580	1.8	4.99 ± 0.02	
W14		2.0	6.37 ± 0.06	
W15		2.2	6.76 ± 0.09	
W16	2160	1.8	4.93 ± 0.08	
W17		2.0	5.91 ± 0.05	
W18		2.2	6.16 ± 0.06	

The optimised process parameter settings for this study, based on a “maximum strength” criteria, was obtained for condition W12 with a rotation speed value of 1000 rev/min and a plunge depth of 2.2 mm. As a potential replacement for resistance spot welding, strength values were

compared against the strength requirements set by the relevant standard. Based on the AWS D17.2/D17.2M:2019 standard for spot-welding strength requirements, a minimum lap shear strength value of 3.80 kN per spot is specified for this alloy. All conditions tested in this investigation exceeded this value, supporting the suitability of the RFSSW process as a joining process for lightweight automotive applications.

Table 3.13 presents the ANOVA of the acquired lap shear strength data from RFSSW AA5754-H24. A standard 95 % confidence interval was used, similar to what was used in the previous section. In this study, PD was the factor with the greatest influence on the shear strength values with a contribution of 62%, followed by RS with a contribution of 28%. The low contribution of the RS x PD suggests that there is a negligible effect of the process parameter interaction on the shear strength. Considering that AA5754-H24 belongs to a strain hardened alloy group, the higher contribution value of RS compared to the value obtained for AA2024-T3 is an interesting result. This could be attributed to the influence of the rotation speed to the thermal softening of the work-hardened treatment.

Table 3.13 - ANOVA for the shear strength output of RFSSW AA5754-H24.

Source	DF	Sum of Squares	Mean Square	F Value	P Value	Contribution [%]
RS	1	4.13	0.06	12.48	0.00	28.02
RS^2	1	0.07	0.07	42.87	0.00	0.47
PD	1	9.19	1.14	7.29	0.01	62.32
PD^2	1	0.97	0.96	9.86	0.01	6.54
RS x PD	1	0.00	0.01	3.92	0.06	0.02
Error	21	0.39	0.02			2.62
Total	26	14.75				100.00

A second-order model was developed to predict the shear strength value within the process parameter window explored. Table 3.14 presents the second order model equation (Equation 2), along with the correspondent coefficient of correlation, R^2. The large value of R^2 suggests a good fit between the model and the results obtained experimentally.

Table 3.14 - Second order regression equation for RFSSW AA5754-H24

	Equation [kN]	R^2 Value
Equation 2	$\mathrm{LSS_{ST}} = -39.28 - 1.56 \times 10^{-3} \times \mathrm{RS} + 43.9 \times \mathrm{PD} - 10 \times \mathrm{PD}^2 + 1.40 \times 10^{-4} \times \mathrm{RS} \times \mathrm{PD}$	0.994

The response surface plot from Equation 2 is presented in Figure 3.13. As observed in the previous section and by the ANOVA table, the surface plot shows the dominant effect of plunge depth

compared to the rotation speed on the shear strength by the higher variation of shear strength values along the X-axis compared to the Y-axis. The strongest process parameter combination can be found for high plunge depth and low rotation speed values, as observed in Table 3.12. However, it should be noted that significantly lower rotation speed and higher plunge depth values than the ones tested could lead to process parameter combinations unsuitable for welding. These conditions may not generate enough frictional heat to plasticise the material. For such low values of rotation speed, Kubit et al. (2018-A) have reported internal and volumetric defects and de Castro et al. (2018-A) considered to be unsuitable for welding due to low heat input.

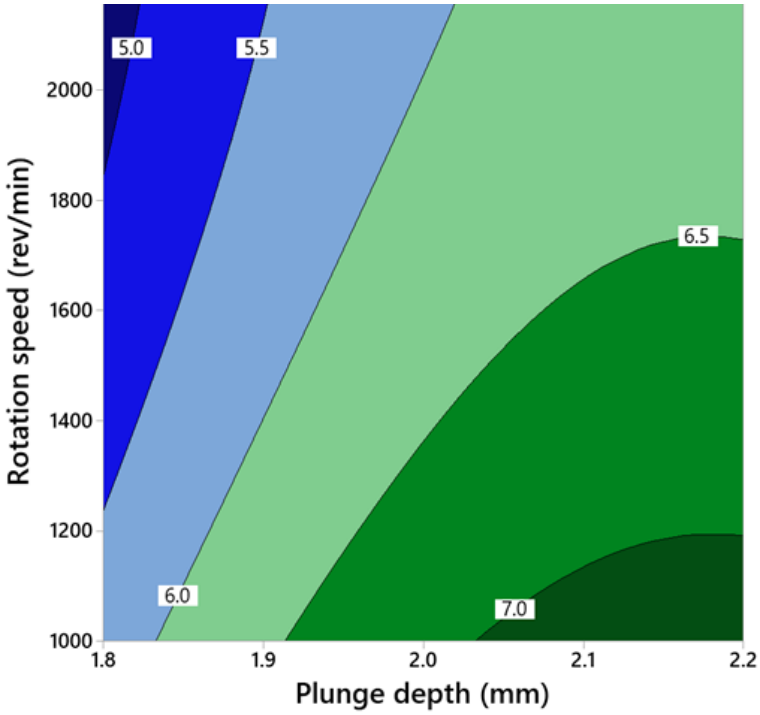

Figure 3.13 - Contour plot of lap shear strength as function of process parameters for RFSSW AA5754-H24.

To determine the accuracy of the model, specimens with process parameters from within the explored process parameter window were produced and tested to compare the experimental shear strength value (LSS Actual) against the predicted shear strength value from the model (LSS Predicted). The results are presented in Table 3.15 and it can be observed that the discrepancy between the values is negligible, confirming the accuracy of the model.

Table 3.15 - Comparison between experimental shear strength and predicted shear strength from Equation 2.

Rotation Speed [rev/min]	Plunge Depth [mm]	LSS Predicted [kN]	LSS Actual [kN]	Error [%]
1280	2.2	6.905 ± 0.310	6.909 ± 0.024	0.06

Figure 3.14 presents the shear testing load-displacement curve for the strongest and the weakest conditions, W12 and W16 respectively. Both welding conditions exhibited similar load-displacement behaviour and fractured under the same failure mode, designated by shear fracture through the interface. The stronger welding condition, W12, has experienced significantly more plastic deformation which is consistent with the higher displacement values recorded for this sample. This deformation comes from the nugget rotation phenomenon explained in Section 3.3.1.1 before failure and can be clearly seen in Figure 3.15.A).

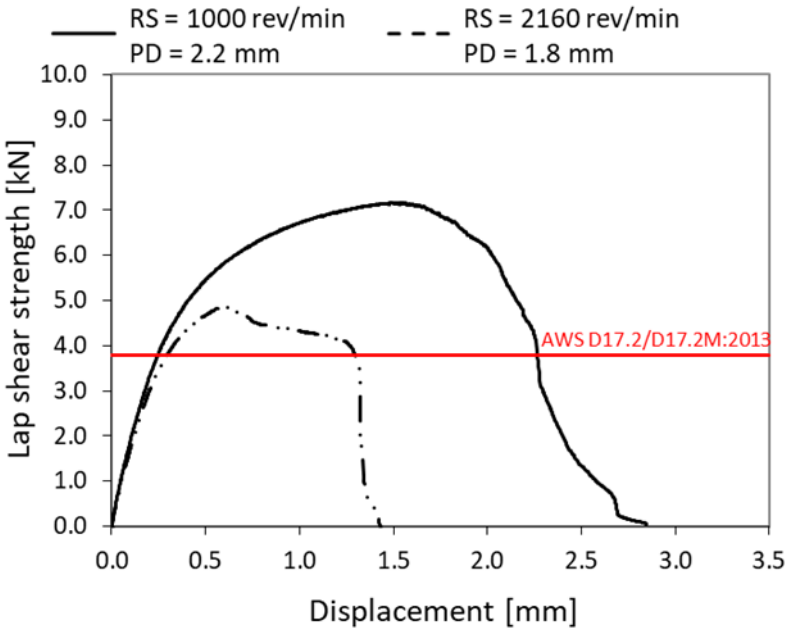

Figure 3.14 - Lap shear test load-displacement curve of RFSSW AA5754-H24 weld conditions W12 (RS = 1000 rev/min; PD = 2.2 mm) and W16 (RS = 2160 rev/min; PD = 1.8 mm).

Figure 3.15 shows the fracture surface for condition W12 and magnified regions obtained by SEM. The fracture mode is similar to the one observed and described in Section 3.3.1.1, with the crack propagating along the joint line remnant. The principle of crack initiation and propagation was the same for both the strongest and weakest weld conditions. However, the extent of the plastic deformation from the rotation of the nugget experienced by the stir zone region was higher on the strongest conditions, as shown in Figure 3.15.A), suggesting better bonding conditions. The presence of microscopic voids (commonly designated as dimples) throughout the surface is consistent with a predominantly ductile fracture mode. Different dimple formations and shapes can be seen between Figure 3.15.D) and E) which can be attributed to different crack propagation rates and microstructure gradients.

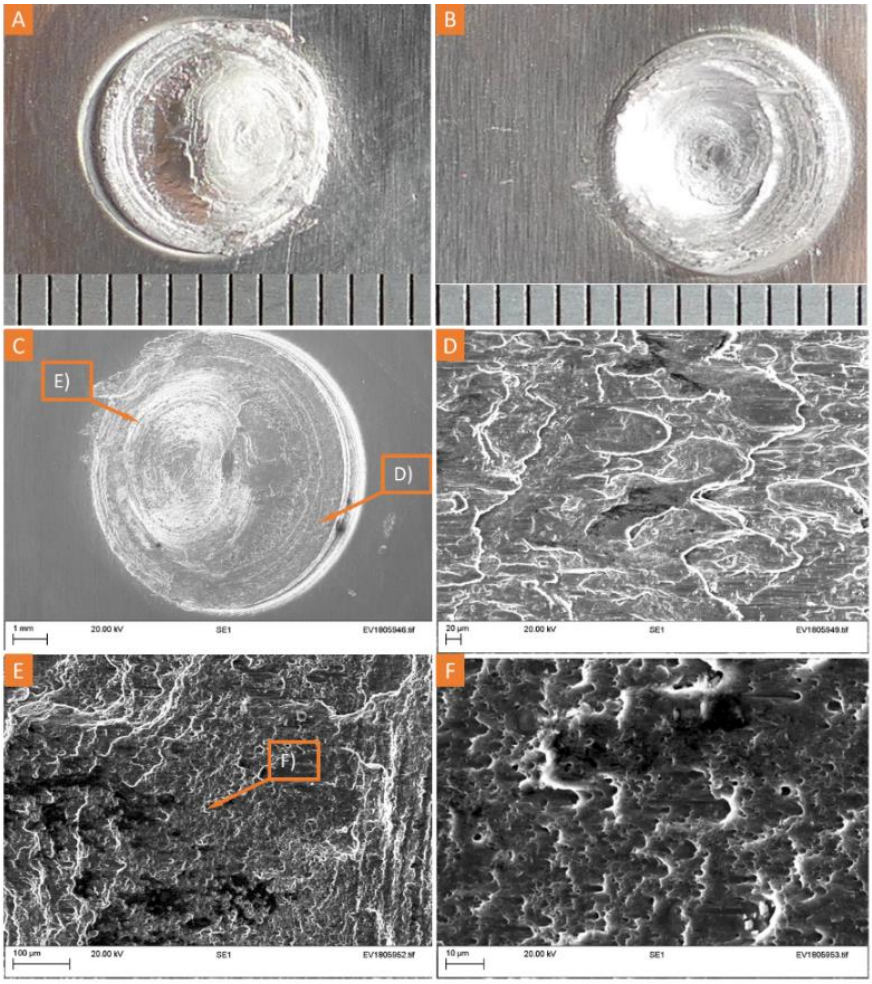

Figure 3.15 – Fracture surfaces of condition W12 (RS = 1000 rev/min; PD = 2.2 mm):
A) Top sheet;
B) Bottom sheet;
C) SEM fractography;
D) High magnification region – location shown in Figure 3.15.C);
E) High magnification region – location shown in Figure 3.15.C);
F) High magnification region – location shown in Figure 3.15.C).

3.3.1.3. AA7075-T6

Table 3.16 shows the lap shear testing results for the weld conditions obtained from the FFDoE. Within the explored process parameter window, shear strength values of RFSSW AA7075-T6 varied between 6.03 ± 0.04 kN and 9.10 ± 0.08 kN. The results obtained were consistent and repeatable with standard deviation values ranging between 0.66 % and 2.53 % of the shear strength value. Similar trend to the previous alloys was observed with the shear strength values improving as plunge depth values increased and rotation speed values decreased. Considering the properties of this alloy, the explanation for the increase of strength is similar to the one presented for the AA2024-T3. The optimised process parameter combination within the explored

process parameter range, based on a "maximum strength" criteria, was obtained for 1000 rev/min and 2.4 mm, corresponding to condition W21 and it will be used later in this section to determine the impact of an interfacial sealant on the weld microstructure and mechanical properties.

Table 3.16 - Lap shear strength results of RFSSW AA7075-T6.

Welding Condition	Rotation Speed [rev/min]	Plunge Depth [mm]	Lap Shear Strength [kN]	Failure Mode
W19	1000	2.0	7.06 ± 0.17	Shear fracture through the weld interface
W20		2.2	8.68 ± 0.19	
W21		2.4	9.10 ± 0.08	
W22	1580	2.0	7.17 ± 0.06	
W23		2.2	8.34 ± 0.06	
W24		2.4	9.09 ± 0.11	
W25	2160	2.0	6.03 ± 0.04	
W26		2.2	7.52 ± 0.19	
W27		2.4	8.31 ± 0.07	

As performed for the previous sections, shear strength values of RFSSW were compared with the shear strength standards for resistance spot welding and riveting. Based on the thickness and material properties of the alloys used in this investigation, the AWS D17.2/D17.2M:2019 standard specifies for resistance spot welding a minimum lap shear strength of 4.56 kN per spot. All conditions tested in this investigation exceeded this value, confirming that the RFSSW process is a suitable resistance spot welding replacement technology. The shear strength design for a 1/4" MS20426DD AA2024-T31 solid rivet, according to MMPDS-04 (2008), is 9.43 kN for AA7075-T6. In this investigation, with a shear strength value of 96.5% of the shear strength of an equivalent rivet, the maximum lap shear strength did not exceed the strength requirements. However, the negligible difference between the strength values demonstrate the potential of RFSSW as a suitable joining technology for aerospace applications.

The ANOVA of the acquired shear strength data from RFSSW AA7075-T6 is presented in Table 3.17. For this analysis, a standard confidence interval of 95% ($\alpha = 0.05$) was used. The results suggest that PD was the factor with the greatest influence on lap shear strength values with a contribution of 73.54 %. Similar to what was observed for AA2024-T3, the rotation speed has small influence on the weld shear strength. Considering the influence of this parameter on the process heat input, this is a non-intuitive result for this heat treatable alloy.

Table 3.17 - ANOVA for the shear strength output of RFSSW AA7075-T6.

Source	DF	Sum of Squares	Mean Square	F Value	P Value	Contribution [%]
RS	1	4.42	0.08	2.84	0.106	16.68
RS^2	1	1.04	1.04	35.58	0.000	3.94
PD	1	19.48	1.07	38.46	0.000	73.54
PD^2	1	0.89	0.89	30.18	0.000	3.34
RS x PD	1	0.04	0.04	1.45	0.242	0.16
Error	21	0.67	0.03			2.33
Total	26	26.49				100.00

A second order regression model to predict the shear strength of the weld within the process window explored was developed. Table 3.18 shows the model equation, Equation 3, along with the coefficient of correlation, R^2. The R^2 is considerably high (> 0.95), which indicates good agreement between the experimental results and the results from the model.

Table 3.18 - Second order regression equation for RFSSW AA7075-T6

	Equation [kN]	R^2 Value
Equation 3	$\mathrm{LSS_{ST}} = -49.45 + 1.94 \times 10^{-3} \times \mathrm{RS} + 1 \times 10^{-6} \times \mathrm{RS}^2 + 46.66 \times \mathrm{PD} - 9.61 \times \mathrm{PD}^2 + 5.14 \times 10^{-4} \times \mathrm{RS} \times \mathrm{PD}$	0.977

The contour plot of Equation 3 is presented in Figure 3.16. The dominant effect of plunge depth compared to the rotation speed on the shear strength is further supported by the higher variation of shear strength along the X-axis compared to the Y-axis.

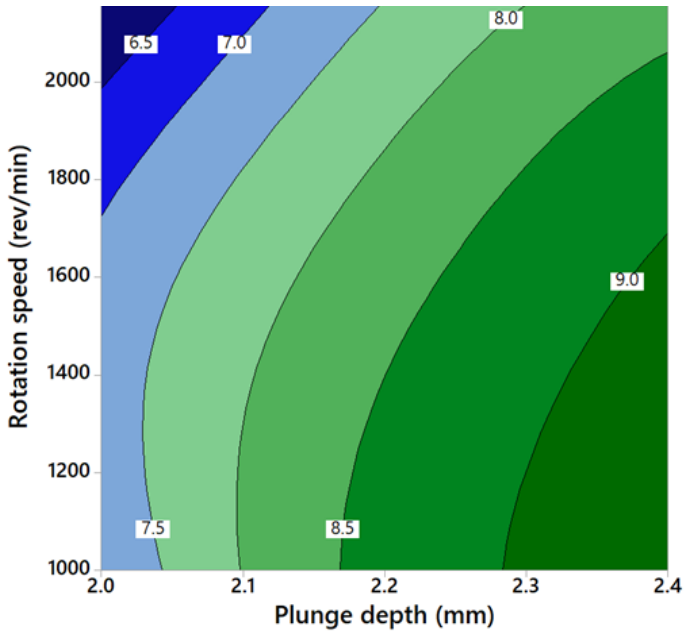

Figure 3.16 - Contour plot of lap shear strength as function of process parameters for RFSSW AA7075-T6.

To determine the accuracy of the model, specimens with process parameters from within the explored process parameter window were performed and tested to compare the experimental shear strength value (LSS Actual) against the shear strength predicted by Equation 3 (LSS Predicted). The results are presented in Table 3.19 and it can be observed that the discrepancy between the predicted and the experimental shear strength value is negligible, confirming the accuracy of the model.

Table 3.19 - Comparison between experimental shear strength and predicted shear strength from Equation 3

Rotation Speed [rev/min]	Plunge Depth [mm]	LSS Predicted [kN]	LSS Actual [kN]	Error [%]
1280	2.4	9.22 ± 0.39	8.96 ± 0.06	2.94

Figure 3.17 shows the fracture surface of condition W21 with magnified regions obtained by SEM of RFSSW AA7075-T6. In this investigation, both AA2024-T3 and AA7075-T6 joint samples presented similar fracture mechanisms, described as shear through the interface, with different fracture propagation paths. For RFSSW AA2024-T3, the initial crack propagated through the weld nugget, while on the RFSSW AA7075-T6 the initial crack propagated along the joint line remnant leading to the separation of the top sheet from the bottom sheet. An extensive explanation of this fracture mechanism and particularities of an unguided shear test has been previously presented in Section 3.3.1.1.

Figure 3.18 presents the load-displacement curve for the strongest and the weakest conditions, W21 and W25 respectively, of RFSSW AA2024-T3 under shear loading conditions. The minimum strength requirement for AWS D17.2/D17.2M:2019 and MMPDS-04 (2008) are also shown on each graph. For the strongest and weakest weld condition, the behaviour under shear loading conditions is very similar, with the specimens presenting poor elongation during the plastic deformation stage. This is coherent with the brittle fracture surface observed in Figure 3.17.

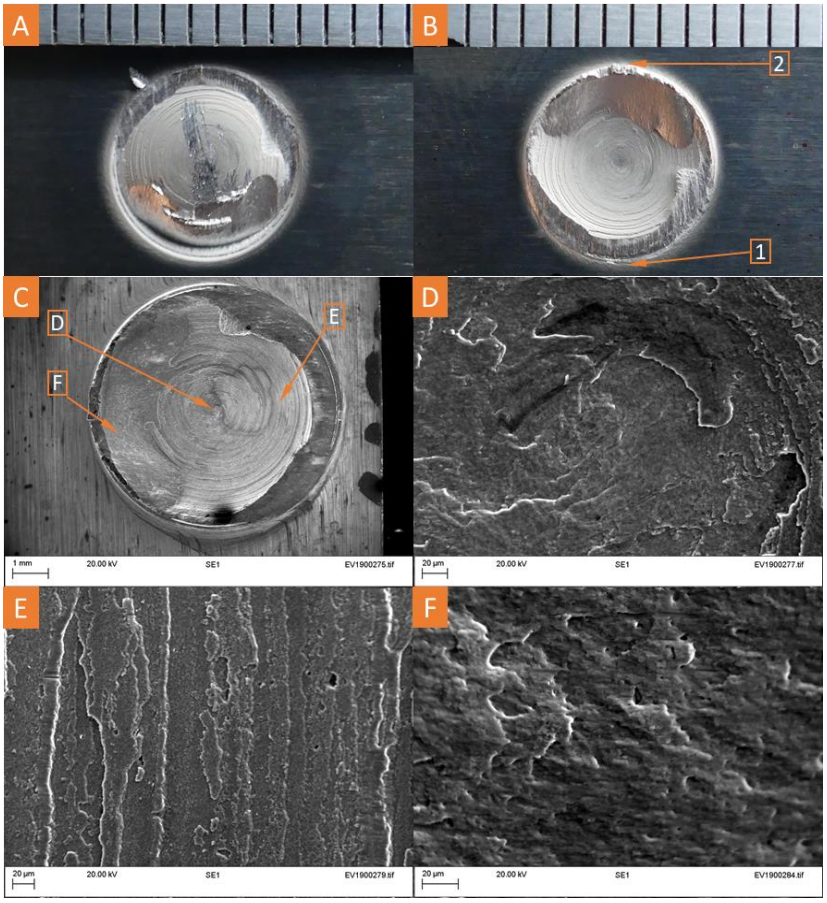

Figure 3.17 - Fracture surfaces of RFSSW AA7075-T6 condition W21 (RS = 1000rev/min; PD = 2.4mm):
A) Top sheet;
B) Bottom sheet;
C) SEM fractography;
D) High magnification region – location shown in Figure 3.17.C);
E) High magnification region – location shown in Figure 3.17.C);
F) High magnification region – location shown in Figure 3.17.C).

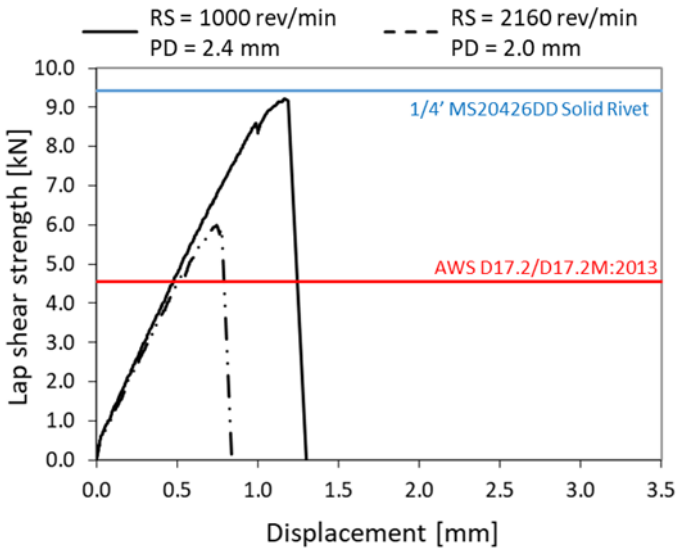

Figure 3.18 - Lap shear test load-displacement curve of RFSSW AA7075-T6 weld condition W21 (RS = 1000 rev/min; PD = 2.4 mm) and W25 (RS = 2160 rev/min; PD = 2.0 mm).

Table 3.20 shows the strength comparison between RFSSW in the bare condition and in the presence of interfacial sealant. Similar to what was observed for AA2024-T3, the presence of the interfacial sealant improved the lap shear strength, with an increase of 44 % compared to the bare material condition.

Table 3.20 - RFSSW AA7075-T6 Lap shear strength comparison between the bare and sealant condition.

Welding Condition	Rotation Speed [rev/min]	Plunge Depth [mm]	Lap Shear Strength [kN]	Failure Mode
AA7075-T6 Bare	1000	2.40	9.10 ± 0.08	Shear fracture through the weld Interface
AA7075-T6 Sealant			13.10 ± 0.78	Shear fracture through the weld nugget

Figure 3.19 presents the load-displacement curve for weld condition W21 of RFSSW AA7075-T6 specimens in the bare and with interfacial sealant condition. The minimum strength requirement from both AWS D17.2/D17.2M:2019 and MMPDS-04 (2008) are also shown on each graph. The adhesion of the interfacial sealant near the joint limited nugget rotation and cleavage stress concentration at the hook. Considering the similarity of trends between the AA2024-T3 and AA7075-T6, the heat absorption from the sealant during volatilisation of solvent is likely to have caused the increase in strength on both alloys.

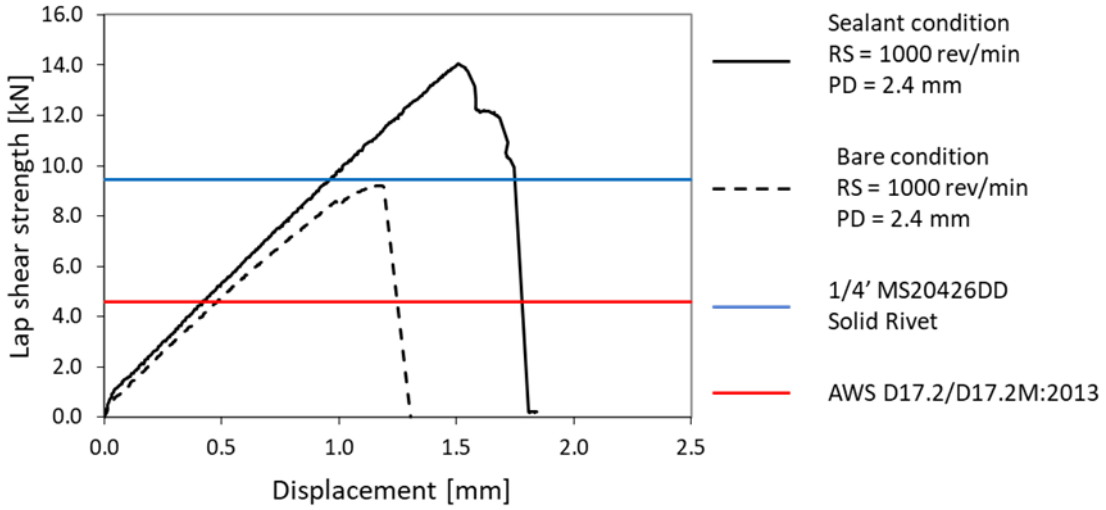

Figure 3.19 - Lap shear test load-displacement curve of RFSSW AA7075-T6 weld condition W21 (RS = 1000 rev/min; PD = 2.4 mm) in bare and with sealant condition.

Figure 3.20 shows the fracture surface of condition W21 with sealant with magnified regions obtained by SEM of RFSSW AA7075-T6. As seen for the AA2024-T3 analysis, similar fracture mechanism to the one observed in the bare specimen condition was recorded, with the crack propagating through the weld nugget, as opposed to what was observed in the bare condition. Tearing of the probe stir zone at the centre of the weld can be observed in Figure 3.20.A) and E). Away from the weld area, a predominant cohesive failure of the sealant can be observed. Most of the sealant was displaced away from the weld area as observed in Figure 3.20.A) and B). Microscopic analysis will provide further indication of any sealant present in the weld region.

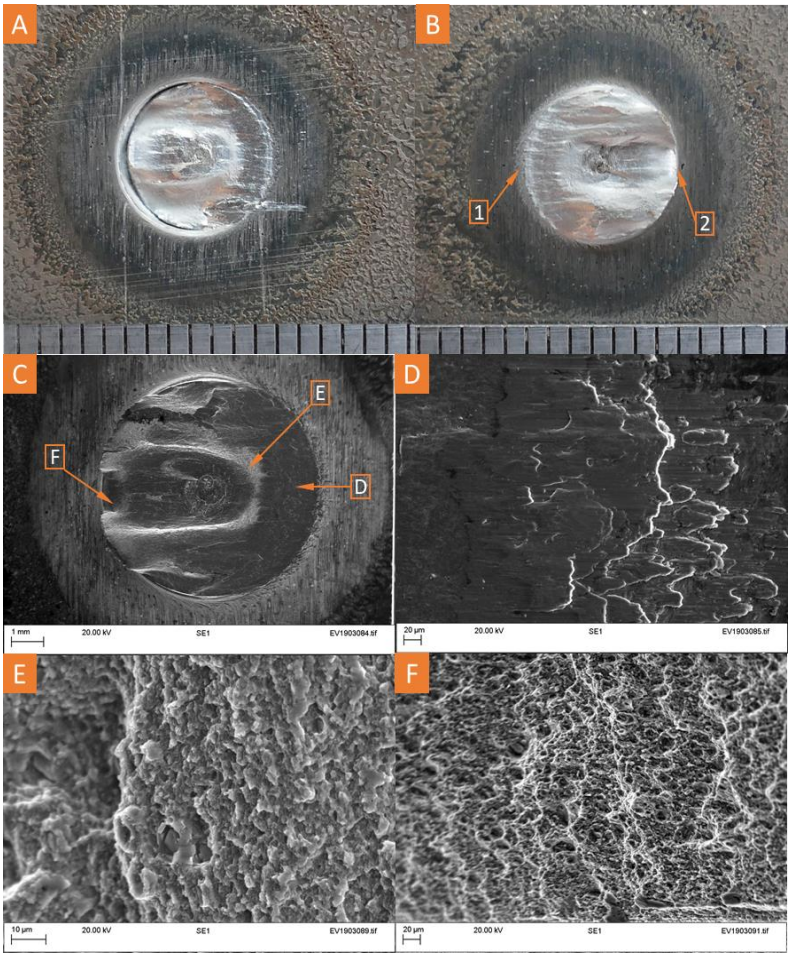

Figure 3.20 - Fracture surfaces of RFSSW AA7075-T6 condition W21 with sealant (RS = 1000 rev/min; PD = 2.4 mm):
A) Top sheet;
B) Bottom sheet;
C) SEM fractography;
D) High magnification region – location shown in Figure 3.20.C);
E) High magnification region – location shown in Figure 3.20.C);
F) High magnification region – location shown in Figure 3.20.C).

3.3.2. Cross-tension strength analysis

3.3.2.1. AA2024-T3

Table 3.21 shows the cross-tension testing results for the weld conditions obtained from the FFDoE. Within the explored process parameter window, cross tension strength values ranged between 2.18 ± 0.45 kN and 3.19 ± 0.11 kN. Lower strength values compared to the lap shear strength performance were expected, as overlap joints tend to have poorer performance under cross tension conditions. This can be attributed to the peeling stress concentration at the hook region, which promotes premature crack initiation. Figure 3.21 shows a schematic representation of the loading direction during cross-tension testing and the stresses generated at the edge of the weld area. In this study, two different failure modes were observed: Through interface (TI)

and Plug Pull Out (PPO). The plug pull out failure mode was observed on the top sheet (TS) and the bottom sheet (BS).

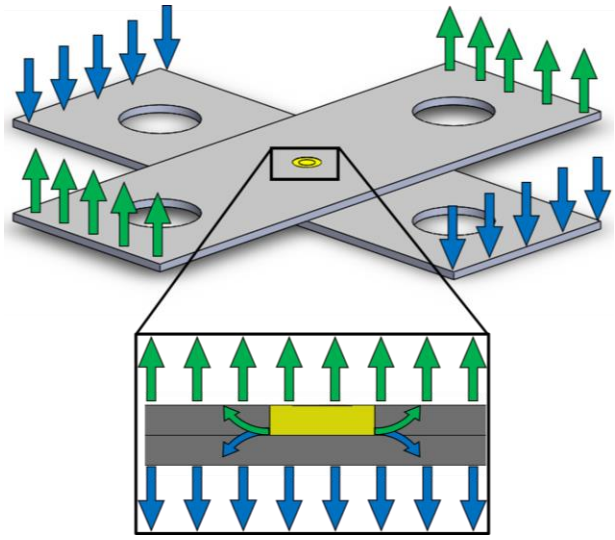

Figure 3.21 - Schematic representation of the loading directions during cross-tension testing and the stresses produced on the weld.

A significant increase in standard deviation and reasonable decrease in the overall strength values was observed for welding conditions with high rotation speed values. This can be explained by the increase in the heat input conditions leading to higher degree of material softening and different failure modes within the same welding condition. The decrease in strength at low rotation speed values and deeper plunge depth values can be attributed to the increase in hook height at relatively low heat input conditions. For rotation speed values of 1000 and 1580 rev/min and plunge depth values higher than the sheet thickness, the standard deviation was smaller due to the consistent failure modes observed. This supports the consistency and repeatability of the results within a smaller operating window.

Table 3.21 - RFSSW cross tension strength results of AA2024-T3.

Welding Condition	Rotation Speed [rev/min]	Plunge Depth [mm]	Cross Tension Strength [kN]	Failure Mode
W1	1000	2.0	3.19 ± 0.11	Mixed failures
W2		2.2	3.13 ± 0.04	PPO - TS
W3		2.4	2.91 ± 0.04	
W4	1580	2.0	2.89 ± 0.14	Mixed failures
W5		2.2	3.02 ± 0.08	PPO - BS
W6		2.4	2.99 ± 0.01	
W7	2160	2.0	2.18 ± 0.45	Mixed failures
W8		2.2	2.71 ± 0.25	
W9		2.4	2.76 ± 0.39	

The ANOVA table and regression models for this study are not presented in this section due to the poor fitting of the model with the experimental results. This can be attributed to the overall higher standard deviation values. Due to the mixed failures observed in the specimens within the same welding condition, it is not clear which failure mode is indication of an effective process parameter combination. However, specimens that failed by plug pull out provided the most consistent results and stronger values within the same welding condition. Based on a "maximum strength" criteria, the optimised process parameter combination was obtained for 1000 rev/min and 2.0 mm, corresponding to condition W1. However, considering the overall mechanical performance, the welding condition W3 will be used later in this section to determine the effect of an interfacial sealant on the static cross tension strength.

Figure 3.22 shows a fracture surface of the through interface failure mode along with SEM micrographs of regions of interest. Similar to the shear fracture through the interface failure mode described in Section 3.3.1.1, the fracture starts at the hook along the weld periphery. The initial crack then progresses through the weld interface along the joint line remnant until complete failure occurs as the crack reaches the centre of the weld or tears through the stir zone. Poor bonding at the centre of the weld can be observed in Figure 3.22.D) and .F), which relates to the stir zone affected by the probe motion. This area possesses less plastic deformation and consolidation in comparison with other regions of the weld.

Figure 3.23 presents the fracture surface of a plug pull out failure mode along with SEM fractography of high-magnification areas. The fracture starts at the hook in various locations of the weld periphery and progresses up to the surface along the interface between the stir zone and thermo-mechanically affected zone, as observed by the striation patterns in Figure 3.23.E). Different crack propagation rates can be observed by the difference in surface morphology between Figure 3.23.D) and. E). Complete plug failure occurs once all the cracks meet and reach the surface of the plug. This failure mode was predominantly observed on the top sheet, with the nugget being partially stuck to the bottom sheet. The crack propagation mechanism is identical for the bottom sheet failure variant, as observed by Figure 3.23.F).

Table 3.22 shows the cross-tension strength comparison between RFSSW AA2024-T3 in the bare condition and in the presence of interfacial sealant. As opposed to what was observed under lap shear conditions, cross-tension strength did not improve with the presence of the interfacial sealant. In fact, a reduction of 19% of the cross-tension strength along with an increase of an

order of magnitude on standard deviation was observed when compared to the bare specimen results. This outcome can be explained by the generation of cleavage stresses at the edge of the specimen, which represent the most severe form of loading for sealants and adhesives. The concentration of these stresses led to a premature failure of the bonded edge of the sealant, without any improvement to the cross-tension strength.

Mixed failure modes were observed for the three specimens tested, with a plug pull out failure mode being related to a best performing weld. A description of this failure mode has been previously presented in this section. Sealant failure is predominantly cohesive, showing good adhesion to the substrate. Due to the initial pressure applied by the clamp, a considerable portion of the sealant on the overlapped area was expelled away from the weld area.

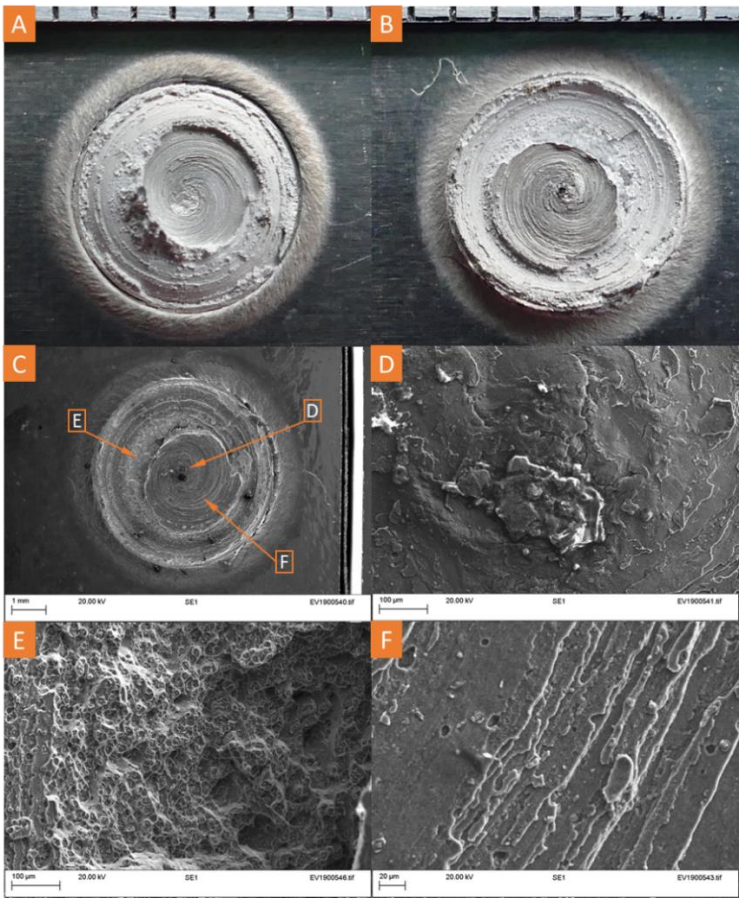

Figure 3.22 - Fracture surfaces of a through interface failure mode of RFSSW AA2024-T3 condition W1 (RS = 1000 rev/min; PD = 2.0 mm):
A) Top sheet;
B) Bottom sheet;
C) SEM fractography;
D) High magnification region – location shown in Figure 3.22.C);
E) High magnification region – location shown in Figure 3.22.C);
F) High magnification region – location shown in Figure 3.22.C).

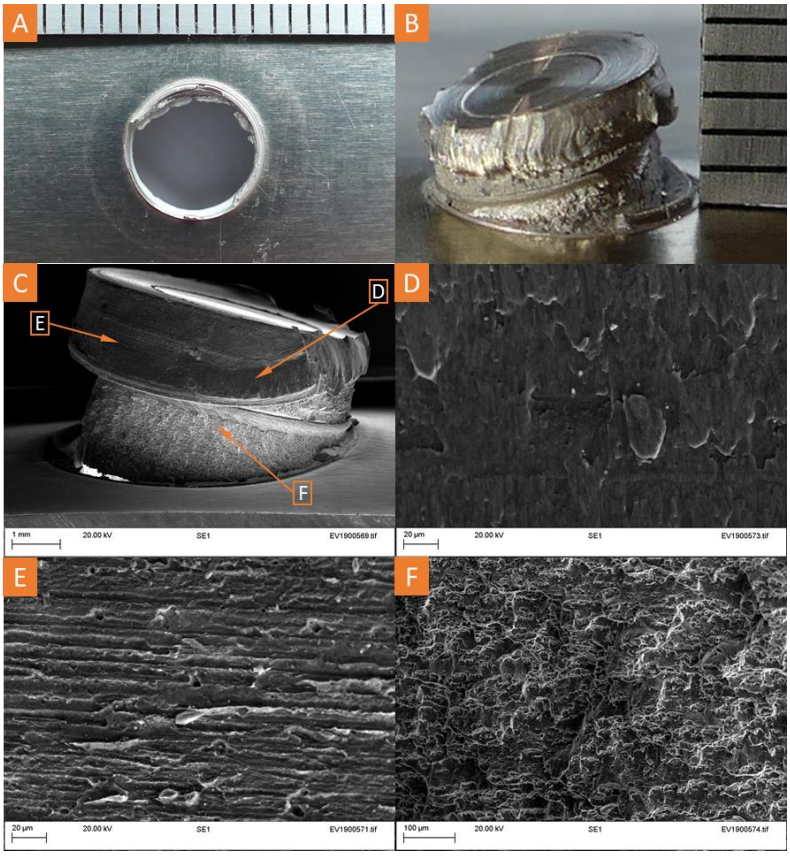

Figure 3.23 - Fracture surfaces of a plug pull out top sheet failure mode of RFSSW AA2024-T3 condition W1 (RS = 1000 rev/min; PD = 2.0 mm):
A) Top sheet;
B) Bottom sheet;
C) SEM fractography;
D) High magnification region – location shown in Figure 3.23.C);
E) High magnification region – location shown in Figure 3.23.C);
F) High magnification region – location shown in Figure 3.23.C).

Table 3.22 - RFSSW cross tension strength of 2 mm thick AA2024-T3 in the bare and with sealant conditions.

Welding Condition	Rotation Speed [rev/min]	Plunge Depth [mm]	Cross Tension Strength [kN]	Failure Mode
AA2024-T3 Bare	1000	2.4	2.91 ± 0.04	Plug pull out Top sheet
AA2024-T3 Sealant			2.34 ± 0.40	Mixed failures

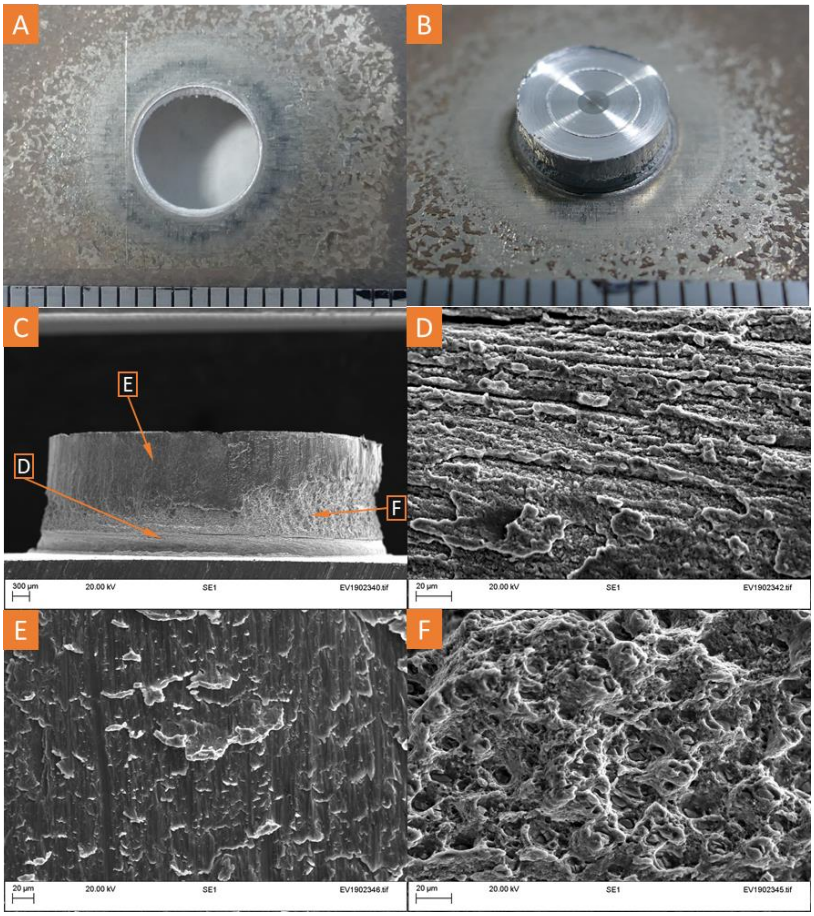

Figure 3.24 - Fracture surfaces of a plug pull out top sheet failure mode of RFSSW AA2024-T3 condition W3 (RS = 1000 rev/min; PD = 2.4 mm) with sealant:
A) Top sheet;
B) Bottom sheet;
C) SEM fractography;
D) High magnification region – location shown in Figure 3.24.C);
E) High magnification region – location shown in. Figure 3.24C);
F) High magnification region – location shown in. Figure 3.24C).

3.3.2.2. AA5754-H24

Table 3.23 presents the cross-tension testing results for the weld conditions selected based on the FFDoE. The cross-tension strength values varied between 2.27 ± 0.84 kN and 3.88 ± 0.29 kN, for conditions W16 and W10, respectively. Higher standard deviation across the results was observed, compared to the values observed in the lap shear tests. This is particularly true for welding conditions with low plunge depth values and increasing rotation speed values. As observed in Section 3.3.2.1, an explanation for the scatter in the results can be attributed to the inconsistent failure modes between replicates observed for the same welding condition. As the plunge depth increases, the observed failure modes become more consistent within the parameter combination, leading to a decrease in the standard deviation values.

Table 3.23 - Cross-tension testing results of RFSSW AA5754-H24.

Welding Condition	Rotation Speed [rev/min]	Plunge Depth [mm]	Cross-Tension Strength [kN]	Failure Mode
W10	1000	1.8	3.88 ± 0.29	PPO - TS
W11		2.0	3.56 ± 0.03	
W12		2.2	3.35 ± 0.13	
W13	1580	1.8	2.93 ± 0.66	Mixed failure
W14		2.0	3.71 ± 0.15	PPO - TS
W15		2.2	3.39 ± 0.09	
W16	2160	1.8	2.27 ± 0.84	Mixed failure
W17		2.0	3.06 ± 0.53	
W18		2.2	3.17 ± 0.11	PPO - TS

A clear trend regarding the mechanical performance was not observed in this investigation. However, for lower rotation speed values, increasing the plunge depth value tends to decrease the strength of the joint. This can be explained by the increasing size of the hook at relatively low heat input conditions. The overall higher standard deviation values compromised the validity of the ANOVA table and regression models for this study due to the poor fitting of the model with the experimental results. Therefore, this analysis is not presented in this section. Similar failure modes as observed in the previous section were observed, with plug pull out failure modes producing the highest cross-tension strength values.

Figure 3.25 presents the fracture surface of a RFSSW AA5754-H24 plug pull out failure along with SEM fractography of high-magnification areas. The fracture propagation mechanism has been covered in Section 3.3.2.1. In Figure 3.25.D) and .E), striation patterns can be observed which demonstrates the development and propagation of circumferential cracks up to the surface and along the weld periphery, respectively.

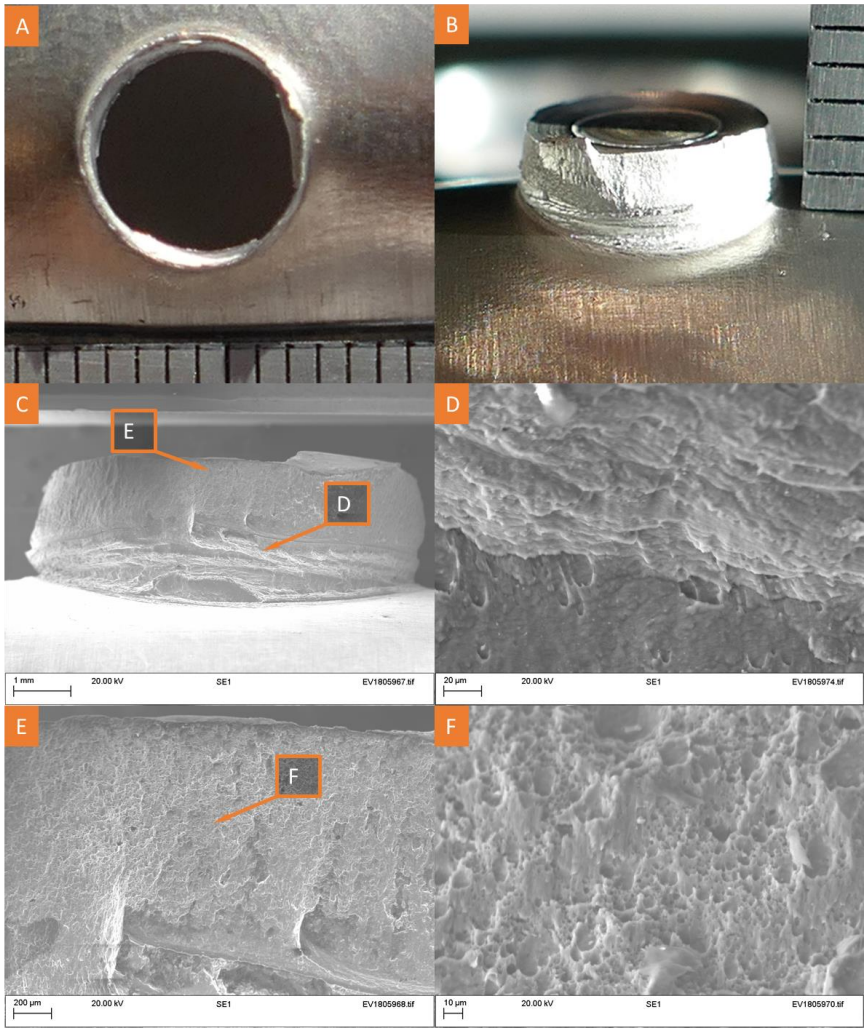

Figure 3.25 - Fracture surfaces of a plug pull out top sheet failure mode of RFSSW AA5754-H24 condition W10 (RS = 1000 rev/min; PD = 1.8 mm):
A) Top sheet;
B) Bottom sheet;
C) SEM fractography;
D) High magnification region – location shown in Figure 3.25.C);
E) High magnification region – location shown in Figure 3.25.C);
F) High magnification region – location shown in Figure 3.25.C).

Figure 3.26 presents the fracture surface of a RFSSW AA5754-H24 through the interface failure along with SEM fractography of high-magnification areas. This failure mode has been previously described in Section 3.3.2.1. Tearing of the stir zone began much prematurely (halfway the shoulder diameter) and was the main cause of failure.

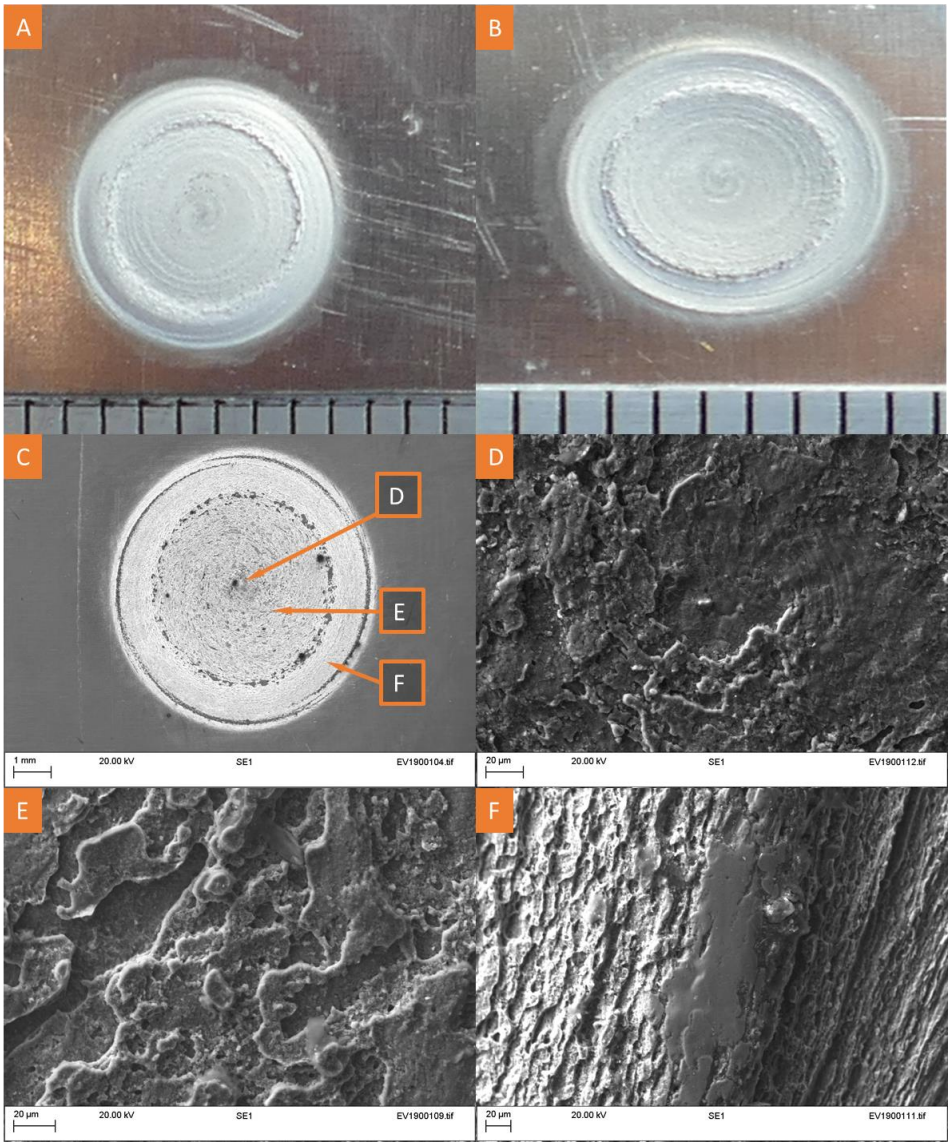

Figure 3.26 - Fracture surfaces of a through interface failure mode of RFSSW AA5754-H24 condition W16 (RS = 2160 rev/min; PD = 1.8 mm):
A) Top sheet;
B) Bottom sheet;
C) SEM fractography;
D) High magnification region – location shown in Figure 3.26.C);
E) High magnification region – location shown in Figure 3.26.C);
F) High magnification region – location shown in Figure 3.26.C).

3.3.2.3. AA7075-T6

Table 3.24 shows the cross-tension testing results for the weld conditions obtained from the FFDoE. Cross-tension strength values ranged between 1.46 ± 0.27 kN and 3.43 ± 0.05 kN within the process parameter window explored. In this study, no clear trend regarding mechanical strength could be identified, however the more successful process parameter window, in terms of strength and consistency of results, were the ones with highest plunge depth values. This could

be attributed to more consistent failure modes, in particular when specimens failed via plug pull out. As opposed to what was previously observed in this investigation, increasing the rotation speed value for the shallowest and deepest plunge depth values improved the cross-tension strength.

Table 3.24 - Cross tension strength results of 2 mm thick RFSSW AA7075-T6 in bare condition.

Welding Condition	Rotation Speed [rev/min]	Plunge Depth [mm]	Cross Tension Strength [kN]	Failure Mode
W19	1000	2.0	1.46 ± 0.27	TI
W20		2.2	3.41 ± 0.12	PPO - TS
W21		2.4	3.36 ± 0.05	
W22	1580	2.0	2.20 ± 0.26	TI
W23		2.2	3.39 ± 0.07	Mixed failures
W24		2.4	3.38 ± 0.05	PPO - BS
W25	2160	2.0	2.90 ± 0.49	Mixed failures
W26		2.2	3.18 ± 0.08	PPO - BS
W27		2.4	3.43 ± 0.05	

Similar to what was observed in the previous sections, the accuracy of the ANOVA table and regression models for this study were low due to a poor fitting of the model with the experimental results. This was caused by the mixed failures observed in this study, leading to an increase in scatter of the results. In this study, plug pull out and through interface failure modes were observed as well as a combination of failure modes within the same welding condition. Figure 3.27 and Figure 3.28 present, respectively, examples of plug pull out and through interface failure modes. Plug pull out failures were observed in the top sheet as well as the bottom sheet and were an indication of an effective process parameter combination, presenting the strongest results. A detailed explanation on the fracture mechanism of these failure modes has been presented in Section 3.3.2.1.

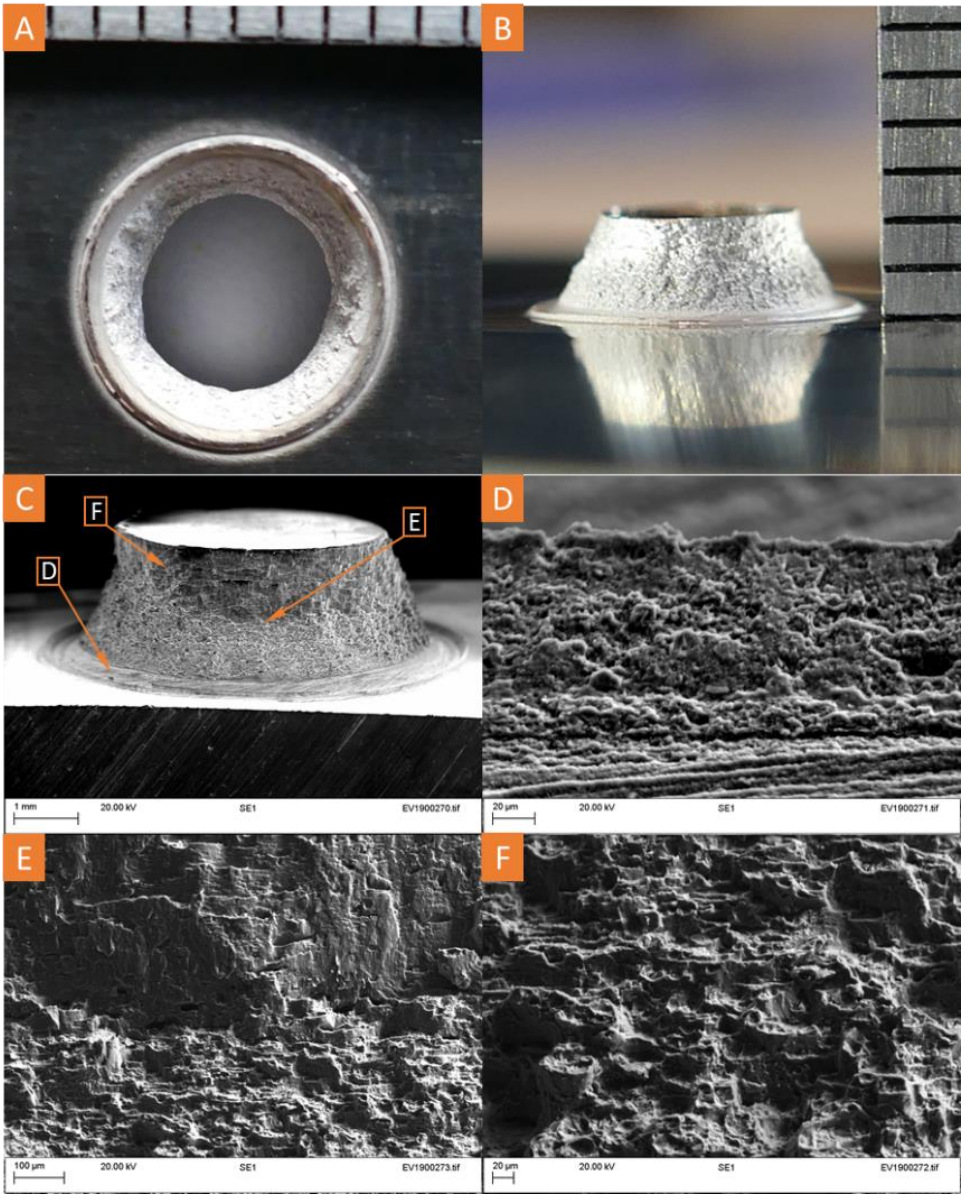

Figure 3.27 - Fracture surfaces of a plug pull out bottom sheet failure mode of RFSSW AA7075-T6 condition W27 (RS = 2160 rev/min; PD = 2.4 mm):
A) Top sheet;
B) Bottom sheet;
C) SEM fractography;
D) High magnification region – location shown in Figure 3.27.C);
E) High magnification region – location shown in Figure 3.27.C);
F) High magnification region – location shown in Figure 3.27.C).

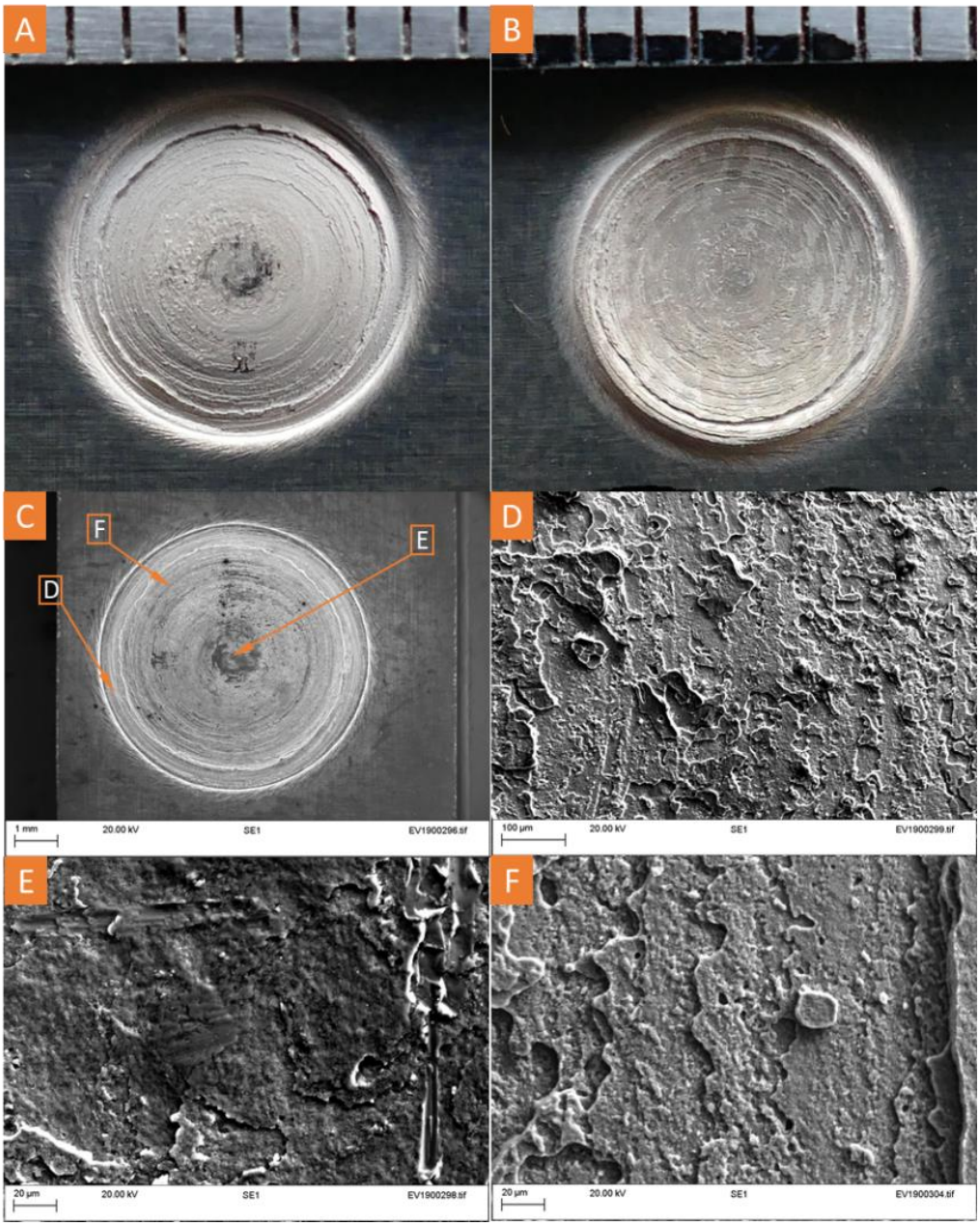

Figure 3.28 - Fracture surfaces of a through interface failure mode of RFSSW AA7075-T6 condition W19 (RS = 1000 rev/min; PD = 2.0 mm):
A) Top sheet;
B) Bottom sheet;
C) SEM fractography;
D) High magnification region – location shown in Figure 3.28.C);
E) High magnification region – location shown in Figure 3.28.C);
F) High magnification region – location shown in Figure 3.28.C).

Based on "maximum strength" criteria, the optimised process parameter combination was obtained for 2160 rev/min and 2.4 mm, corresponding to condition W27. However, considering the overall mechanical performance, the welding condition W21 will be used later in this section to determine the effect of an interfacial sealant on the static cross tension strength.

Table 3.25 shows the strength comparison between RFSSW AA7075-T6 in the bare condition and in the presence of interfacial sealant. Similar to what was observed in Section 3.3.2.1, a decrease of 4% in the cross-tension strength was observed when compared to the bare specimen results. A plausible explanation for this phenomenon has been given in the same section.

Table 3.25 - RFSSW AA7075-T6 cross tension strength comparison between the bare and sealant condition.

Welding condition	Rotation Speed [rev/min]	Plunge Depth [mm]	Cross tension strength [kN]	Failure mode
AA7075-T6 Bare	1000	2.40	3.36 ± 0.05	Plug Pull Out
AA7075-T6 Sealant			3.24 ± 0.05	Top sheet

Plug pull out failure mode was observed on all tested specimens with sealant, which produced a repeatable and accurate strength result. A detailed explanation of the fracture mechanism has been presented in Section 3.3.2.1.

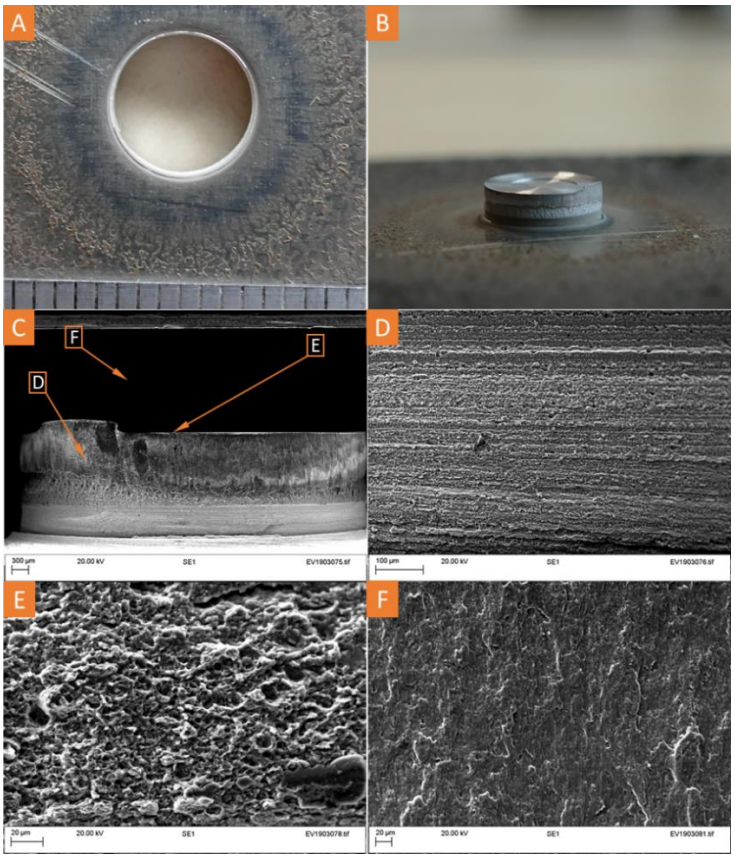

Figure 3.29 - Fracture surfaces of a plug pull out top sheet failure mode of RFSSW AA7075-T6 condition W21 (RS = 1000 rev/min; PD = 2.4 mm) with sealant:
A) Top sheet;
B) Bottom sheet;
C) SEM fractography;
D) High magnification region – location shown in Figure 3.29.C);
E) High magnification region – location shown in Figure 3.29.C);
F) High magnification region – location shown in Figure 3.29.C).

3.3.3. Fatigue life analysis

3.3.3.1. AA2024-T3

Table 3.26 presents the fatigue loading levels with the corresponding number of cycles and failure modes, in bare and with sealant conditions. Fatigue tests were performed using weld condition W3 (RS = 1000 rev/min; PD = 2.4 mm) and maximum stress values (S_{MAX}) were determined as a fraction of the mean lap shear strength ($\%_{LSS}$) and the weld cross-section area (38.5 mm^2). In this investigation, three different fatigue fracture modes were observed: Shear fracture through the interface (SF-TI), Through the Sheet (TTS) and Shear fracture through the plug (STP). TTS and STP failures were observed in the top sheet (TS) and bottom sheet (BS) as well.

Table 3.26 - Fatigue load and results for RFSSW AA2024-T3 specimens in bare and with sealant condition.

S_{MAX}	Bare Specimens		S_{MAX}	Specimens with Sealant	
[$\%_{LSS}$ / MPa]	Cycles [N_f]	Failure Mode	[$\%_{LSS}$ / MPa]	Cycles [N_f]	Failure Mode
20 % / 44.6	577,588	TTS - BS	**20 % / 67.6**	2,398,010	SF-TI
	542,154	TTS - TS		3,929,380	
	506,710			3,039,893	TTS - BS
35 % / 78.1	26,675	STP - BS	**35 % / 178.0**	52,881	SF-TI
	20,389	TTS - TS		165,245	
	20,344	SF-TI		95,440	
55 % / 122.8	2,554	SF-TI	**55 % / 185.5**	5,094	
	3,730			5,329	
	2,924			8,541	
70 % / 156.3	743	SF-TI	**70 % / 235.9**	2,740	
	743	STP - TS		2,069	
	631	STP - BS		593	

The results obtained are consistent with observations from other authors such as Lage et al. (2018) and Effertz et al. (2016), who also obtained high fatigue life values for specimens under low force loading conditions. This outcome suggests that further research into solutions to improving high load cyclic loadings performance is required before progressing into sub-sized component evaluation.

A general fatigue life improvement was registered for the RFSSW specimens with interfacial sealant. Fatigue life was improved by various factors ranging between 2 and 11 times when compared with the bare specimen condition, with the improvement being more noticeable under the loading conditions of 20 and 35 $\%_{LSS}$. The overall fatigue life improvement can be attributed to the adhesion from the sealant at the edge of the specimen, similar to what was observed under shear loading. Figure 3.30 presents the S-N curve plot obtained from the experimental data to

predict the fatigue life of the single RFSSW joint specimen. Using the experimental data to produce stress-life curves means that the initial conditions of as welded components (initial and fabrication induced residual stresses) are influencing parameters that affect the measured cycles to failure for all cases.

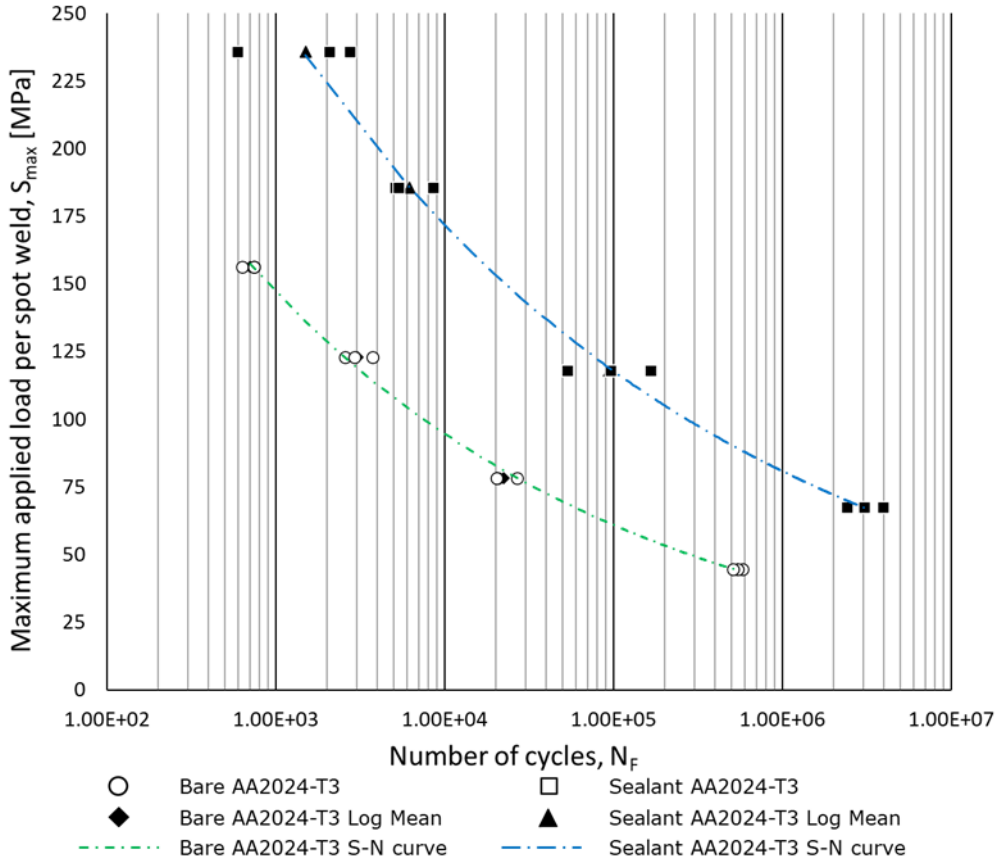

Figure 3.30 - S-N Curve of RFSSW AA2024-T3 welding condition W3 (RS = 1000 rev/min; PD = 2.4 mm) in bare and with sealant condition.

Table 3.27 shows the equations used to predict the fatigue life along with the correspondent coefficient of correlation, R^2. These equations were determined based on the experimental data and it should be noted that the R^2 is high (> 0.95). This means that the model is an adequate fit to the experimental results and therefore suitable for an accurate prediction of the fatigue life within the loading conditions explored. The units for S_{max} are MPa and present the highest stress applied for a cyclic stress ratio of 0.1 and an oscillation frequency of 3 Hz.

Table 3.27 - Equations of RFSSW AA2024-T3 S-N curves with correspondent coefficient of correlation.

Specimen Condition	Equation	R^2 value
AA2024-T3 Bare	$S_{max} = 552.0 \times N_f^{-0.191}$	0.997
AA2024-T3 Sealant	$S_{max} = 777.5 \times N_f^{-0.164}$	0.998

Figure 3.31 shows an example of a through the top sheet failure and SEM micrographs of the fracture surface and regions of interest. The crack initiation and development are reasonably similar between the top sheet and bottom sheet variant, therefore only the top sheet failure will be analysed. This type of failure was commonly observed in specimens that were loaded at 20 $\%_{LSS}$, as in this condition the lower stress concentration on the hook tip has a reduced impact on the early failure of the weld. As seen in Figure 3.31.A) and Figure 3.31.B), a predominant crack initiated on the tensile-stressed side of the spot-weld at the hook tip of the top sheet, propagating along the weld periphery, perpendicular to the loading direction until full specimen fracture at the edge of the sheet. The appearance of a secondary crack on the opposite edge of the weld of the bottom sheet with similar propagation mechanism is common in this failure mode, however it was not observed in this specimen. Figure 3.31.C) presents the SZ/TMAZ interface with multiple subtle striations due to the refined grain microstructure. Figure 3.31.D) shows the centre of the nugget on the top sheet, where the fatigue striations (beach marks) features along the fracture surface show the propagation direction of the circumferential crack along the spot-weld periphery. Figure 3.31.E) presents the interface between the welded and unwelded region at a higher magnification. The longitudinal striation pattern suggests a gradual propagation of the crack from the weld area until the edge of the sheet until complete specimen failure.

Figure 3.32 shows an example of a shear fracture through the interface failure and SEM micrographs of the fracture surface and regions of interest. This type of failure was consistently observed in specimens with sealant that were subjected to loads above 20 $\%_{LSS}$. This can be attributed to the presence of sealant at the weld interface, contributing to poor bonding in this area. The fracture mechanism is comparable to the one observed under lap shear conditions. however, some particularities can be observed due to the cyclic loading. Figure 3.32.A) and. B) present the fracture surface of the bottom sheet. The crack initiated at location 1 from Figure 3.32.A) (tensile-stressed side of the spot-weld at the hook tip of the bottom sheet), propagating along the joint line remnant until full specimen fracture at the opposite edge of the spot-weld. At halfway, circumferential cracks began to develop perpendicular to the loading direction but did not developed up to the surface. A higher magnification of the fracture surface at the centre of the weld is shown in Figure 3.32.D). This is an area of low peripheral velocity and less effective stirring action, leading to a weaker bond and a quicker crack propagation rate. Fatigue striations can be observed in Figure 3.32.E) along the base of the SZ evidencing the gradual propagation of the original crack along the joint line remnant. Complete specimen fracture occurred suddenly as evidence by the smooth surface on Figure 3.32.F).

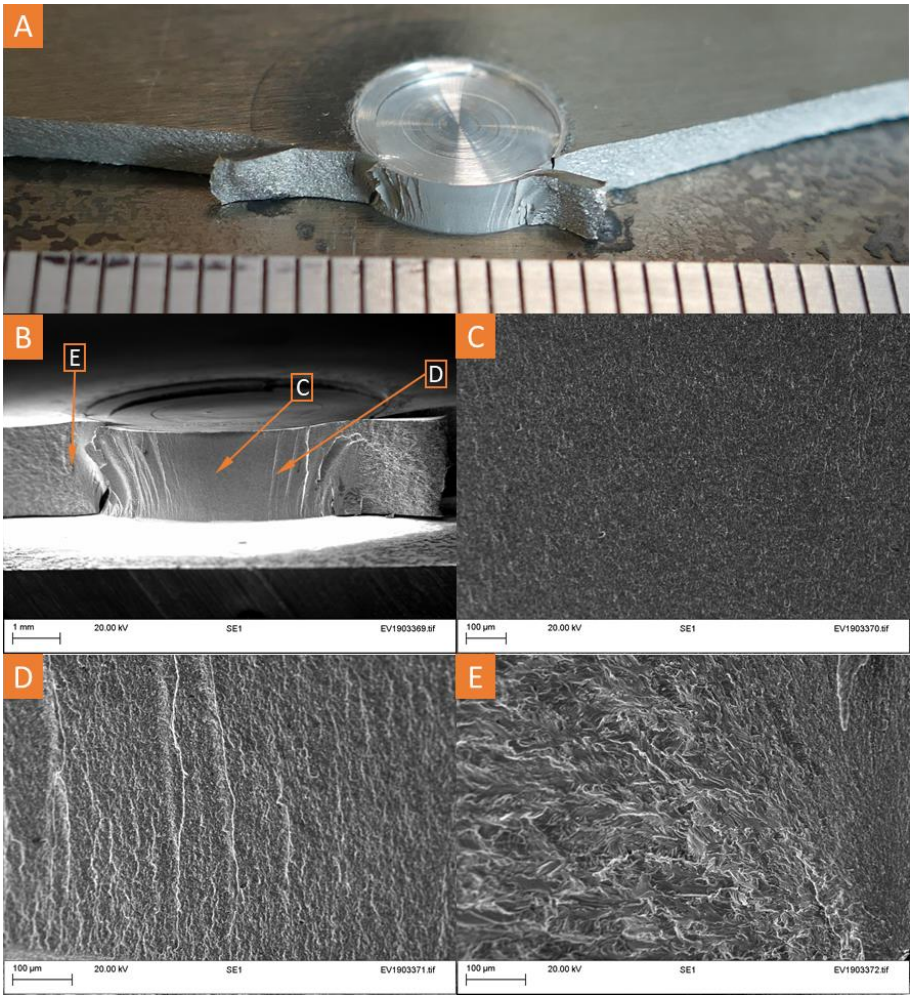

Figure 3.31 - Through the top sheet failure mode of RFSSW AA2024-T3 subjected to cyclic stress of 44.6 MPa:
A) Fracture surface on top sheet;
B) SEM macrograph of fracture surface on top sheet;
C) High magnification region – location shown in Figure 3.31.B);
D) High magnification region – location shown in Figure 3.31.B);
E) High magnification region – location shown in Figure 3.31.B).

Figure 3.33 shows an example of a shear through the plug on the top sheet failure and SEM micrographs of the fracture surface and regions of interest. This type of failure presents a variation from the previous failure mode, since the crack initiation mechanism is identical but not the crack propagation mechanism. In this work, this type of fracture was observed exclusive on bare conditions under different loading conditions. This could be attributed to a better bonding at the weld interface, preventing crack propagation along the joint line remnant. Figure 3.33.A) presents the fracture surface of the bottom sheet. Similar to the shear fracture through the interface failure mode, the crack initiated on the tensile-stressed side of the top sheet at the hook tip, shown in Figure 3.33.D), propagating at an angle with the loading direction up to the surface of the spot-weld. A second crack is formed on location 1 from Figure 3.33.A) (tensile-stressed side

of the bottom sheet at the hook tip), propagating perpendicular to the loading direction. When both cracks reach the surface, full fracture of the specimen occurs. The surface at the centre of the weld is shown in Figure 3.33.C). This area exhibits a smooth surface due to the continuous cyclic loading action, with subtle crack propagation marks along the surface. A change in the crack propagation rate can be observed between the fracture face and the top surface of the spot-weld in Figure 3.33.E).

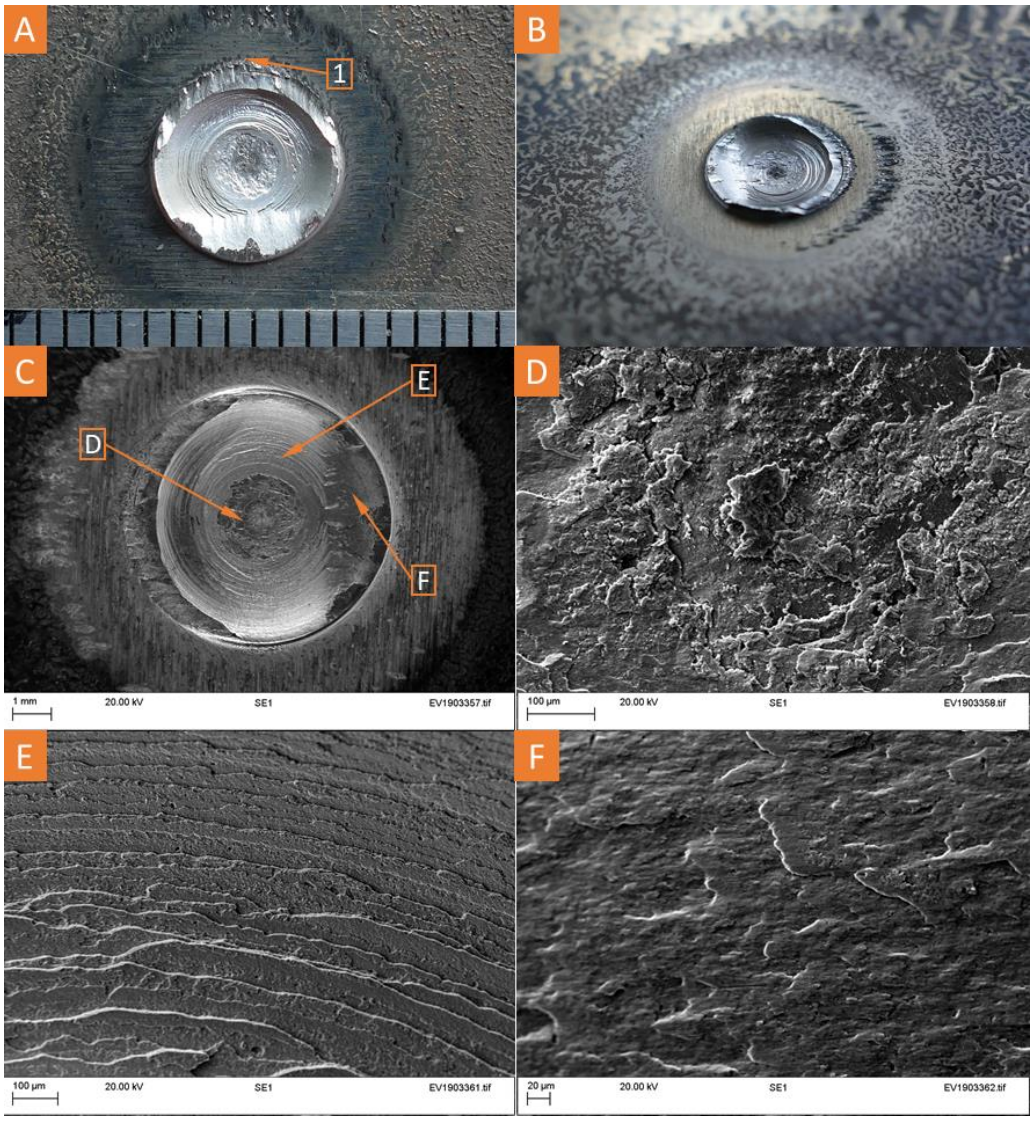

Figure 3.32 - Shear fracture through the interface failure mode of RFSSW AA2024-T3 with sealant subjected to cyclic stress of 185.5 MPa:
A) Fracture surface on top sheet;
B) Fracture surface on top sheet;
C) SEM micrographs of fracture surface on top sheet;
D) High magnification region – location shown in Figure 3.32.C);
E) High magnification region – location shown in Figure 3.32.C);
F) High magnification region – location shown in Figure 3.32.C).

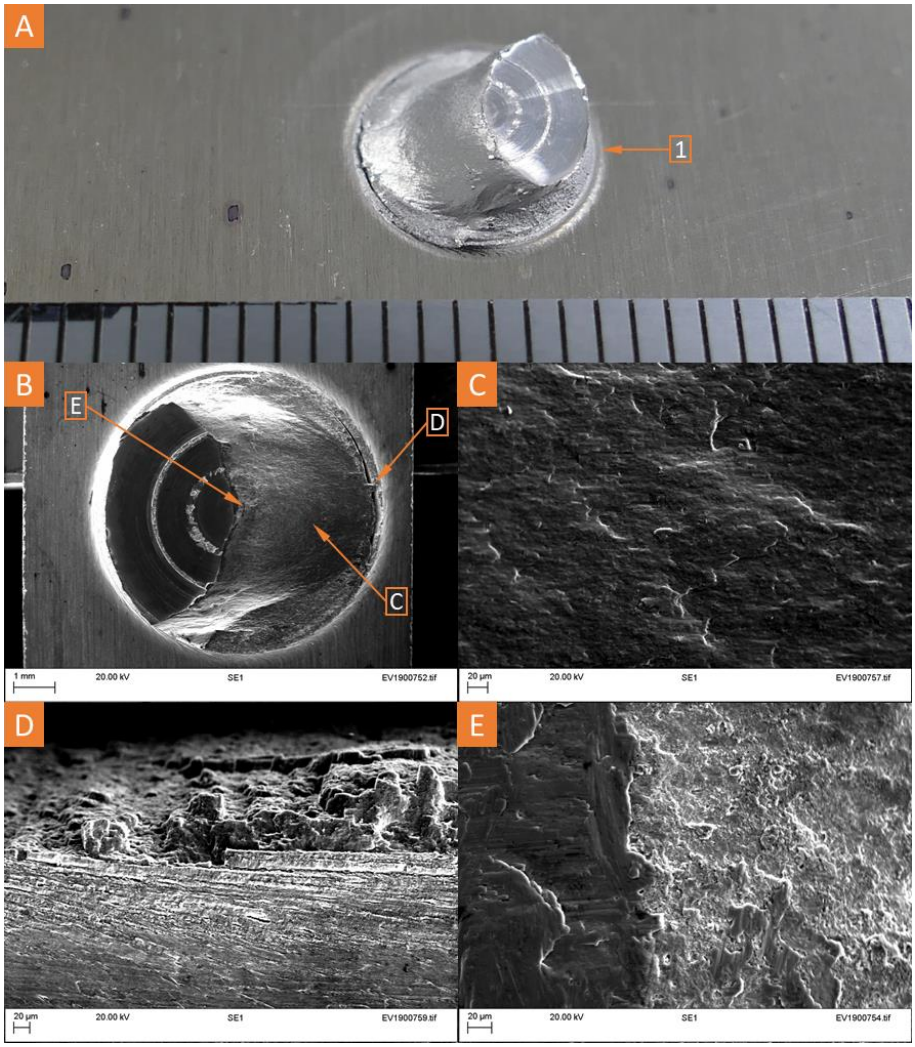

Figure 3.33 - Shear through the plug on the top sheet failure mode of RFSSW AA2024-T3 subjected to cyclic stress of 156.3 MPa:
A) Fracture surface on bottom sheet;
B) Fracture surface on bottom sheet;
C) High magnification region - location shown in Figure 3.33.B);
D) High magnification region - location shown in Figure 3.33.B);
E) High magnification region - location shown in Figure 3.33.B);

3.3.3.2. AA5754-H24

Table 3.28 presents the fatigue loading levels with the corresponding number of cycles and failure modes. Fatigue tests were performed under four different loading conditions, which were determined as a fraction of the mean lap shear strength. For the conditions tested, full fracture of the specimen before triggering the displacement threshold was only observed for maximum stress of 37.2 MPa (20 $\%_{LSS}$). The fracture mode observed is described as through the sheet on the top sheet and a detailed explanation of the fracture mechanism has been presented in Section 3.3.3.1. The remaining conditions presented fracture initiation at the edge of the weld region on

the tension side, leading to the rotation of the nugget. However, full specimen failure did not occur before the imposed displacement limit was triggered. The fatigue life results obtained are similar to the results observed in the previous section, supporting the need for solutions to improve the fatigue performance.

Table 3.28 - Fatigue load amplitudes and results of 2 mm thick RFSSW AA5754-H24.

S_{MAX} [%LSS / MPa]	Cycles [N_f]	Failure mode
20 % / 37.2	716,004	TTS - TS
	736,869	
	640,275	
35 % / 65.1	33,073	Fracture did not occur for these conditions before the displacement threshold was reached
	26,650	
	24,431	
55 % / 102.3	3,549	
	3,207	
	3,143	
70 % / 130.2	935	
	1,046	
	1,190	

Figure 3.34 presents the S-N curve plot obtained from the experimental data to predict the fatigue life of the single RFSSW joint specimen. Using the experimental data to produce stress-life curves means that the initial conditions of as welded components (initial and fabrication induced residual stresses) are influencing parameters that affect the measured cycles to failure for all cases. Table 3.29 presents the S-N equation used to predict the fatigue life of the single RFSSW joint specimen This equation was determined based on the experimental data and it should be noted that the coefficient of determination is considerably high (> 0.95). This means that the model is an adequate fit and therefore suitable for an accurate prediction of the fatigue life based on the loading conditions. The units for S_{max} are MPa and present the highest stress applied for a stress ratio of 0.1 and oscillation frequency of 3Hz.

Table 3.29 - Equation of S-N curve with correspondent coefficient of correlation

Specimen condition	Equation	R^2 value
AA5754-H24	$S_{max} = 488.3 \times N_f^{-0.193}$	0.997

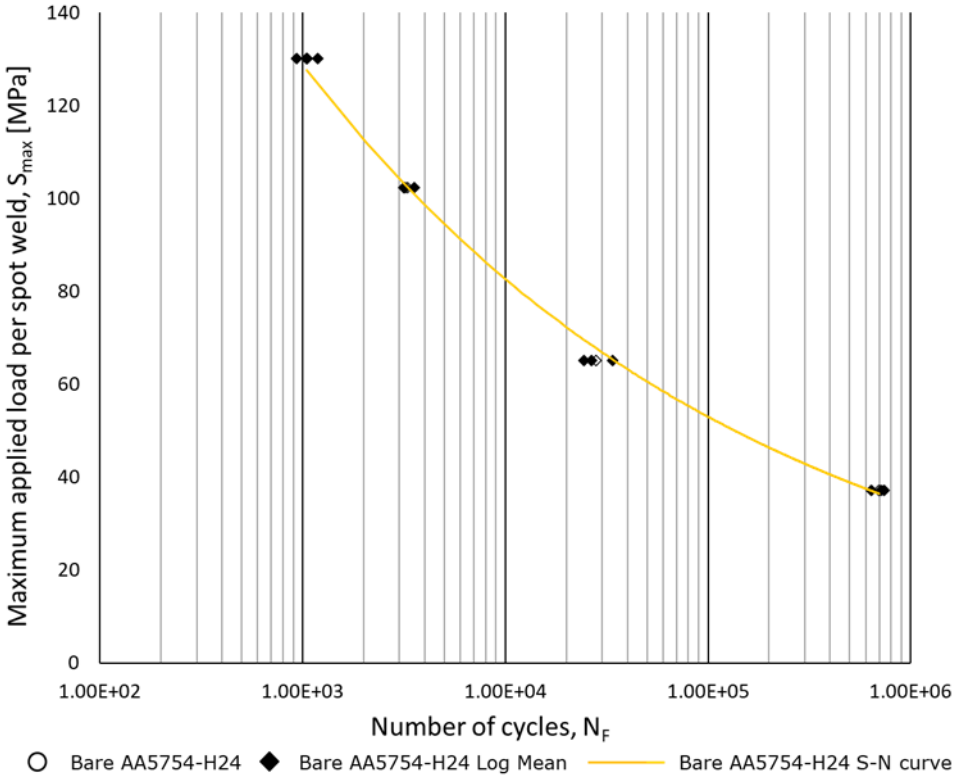

Figure 3.34 - S-N Curve of RFSSW AA5754-H24 welding condition W12 (RS = 1000 rev/min; PD = 2.2 mm).

Figure 3.35 shows visual and SEM imaging of the fracture surface for a specimen loading under 20% $_{LSS}$ loading. An extended description of this failure mode has been presented in Section 3.3.3.1. In this investigation, all specimens developed a secondary crack on the tensile-stressed side of the bottom sheet. However, due to the different crack propagation rate, the fracture occurred consistently on the top sheet.

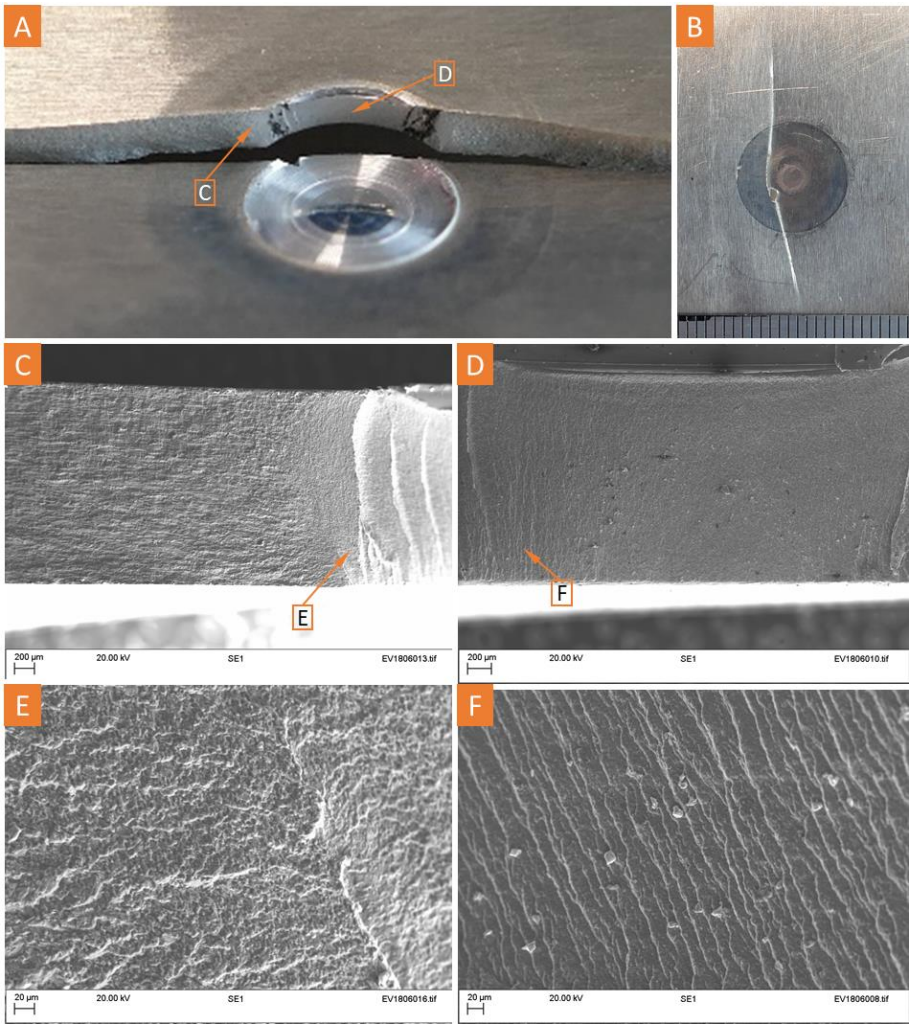

Figure 3.35 - Through the top sheet failure mode of RFSSW AA5754-H24 subjected to cyclic stress of 37.2 MPa:
A) Fracture surface on top sheet;
B) Fracture surface on bottom sheet;
C) SEM micrograph of transition between welded and unwelded regions;
D) SEM micrograph of fatigue striations in the welded region;
E) High magnification region – location shown in Figure 3.35.C);
F) High magnification region – location shown in Figure 3.35.D);

3.3.3.3. AA7075-T6

Table 3.30 presents the loading conditions with the corresponding number of cycles and failure modes in bare and with sealant conditions. Fatigue tests were performed using weld condition W21 (RS = 1000 rev/min; PD = 2.4 mm) and maximum stress values, S_{MAX}, were determined as a ratio of the mean lap shear strength ($\%_{LSS}$) and the weld cross-section area (38.5 mm^2). In this investigation, similar failure modes as seen in Section 3.3.3.1 were observed and an extensive explanation of the crack propagation mechanism along with fractography images have been presented for each failure mode.

Table 3.30 - Fatigue load amplitudes and results for RFSSW AA7075-T6 specimens

S_{MAX}	Bare specimens		S_{MAX}	Specimens with sealant	
[%LSS / MPa]	Cycles [N_f]	Failure mode	[%LSS / MPa]	Cycles [N_f]	Failure mode
20 % / 1.82	183,600	TTS - TS	**20 % / 2.62**	2,268,477	TTS - TS
	193,446			1,851,408	
	203,175	TTS - BS		1,035,882	SF-TI
35 % / 3.19	32,583	SF-TI	**35 % / 4.59**	112,557	SF-TI
	24,678			95,253	
	28,410			51,677	
55 % / 5.01	3,165	SF-TI	**55 % / 7.21**	5,934	
	2,613			5,529	
	2,810			3,044	
70 % / 6.37	745	SF-TI	**70 % / 9.17**	1,444	
	581	STP - TS		887	
	461			465	

For the specimens tested in the bare condition, full fracture was observed before the first million cycle within the load range tested. A general fatigue life improvement was registered for the RFSSW specimens with interfacial sealant. This improvement was more noticeable under lower loading conditions, where the fatigue life improved by various factors ranging between 2 and 11 times when compared with the bare specimen condition.

Figure 3.36 presents the S-N curve plot obtained from the experimental data to predict the fatigue life of the single RFSSW joint specimen. Using the experimental data to produce stress-life curves means that the initial conditions of as welded components (initial and fabrication induced residual stresses) are influencing parameters that affect the measured cycles to failure for all cases. Full fracture at higher loads occurs at similar number of cycles for both specimen conditions. The effect of the adhesion layer from the sealant reduces the stress concentration at the hook as the maximum applied load decreases in value, significantly improving the fatigue life.

Table 3.31 shows the equations used to predict the fatigue life along with the correspondent coefficient of correlation, R^2. These equations were determined based on the experimental data and it should be noted that the coefficient of determination is considerably high (> 0.95). This means that the model is an adequate fit and therefore suitable for an accurate prediction of the fatigue life based on the loading conditions.

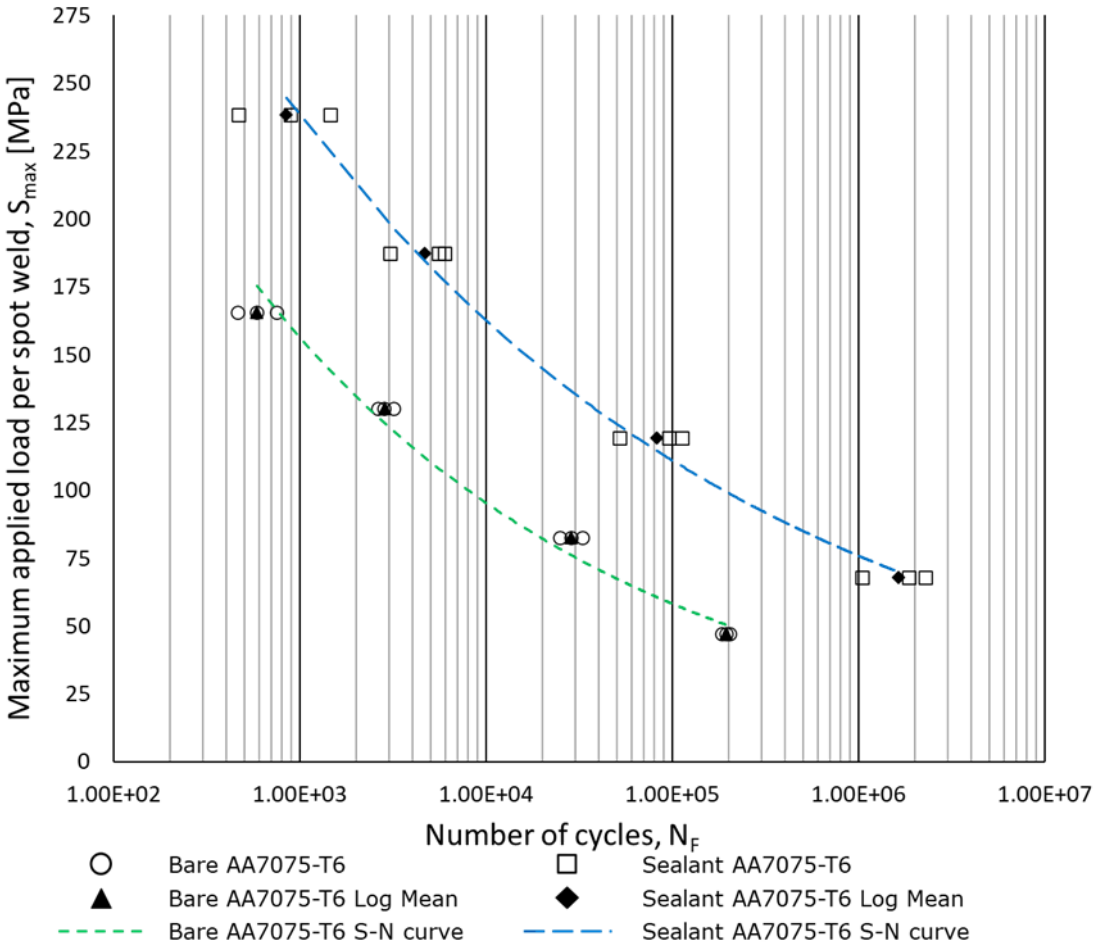

Figure 3.36 - S-N Curve of RFSSW AA7075-T6 welding condition W21 (RS = 1000 rev/min; PD = 2.4 mm) with and without sealant.

Table 3.31 - Equations of S-N curves with correspondent coefficient of correlation

Specimen condition	Equation	R^2 value
AA7075-T6 Bare	$S_{max} = 687.3 \times N_f^{-0.21}$	0.982
AA7075-T6 Sealant	$S_{max} = 746.2 \times N_f^{-0.165}$	0.996

3.3.4. Microstructural analysis

3.3.4.1. AA2024-T3

Figure 3.37 presents the cross-section of RFSSW AA2024-T3 welding condition W3 (RS = 1000rev/min; PD = 2.4mm).

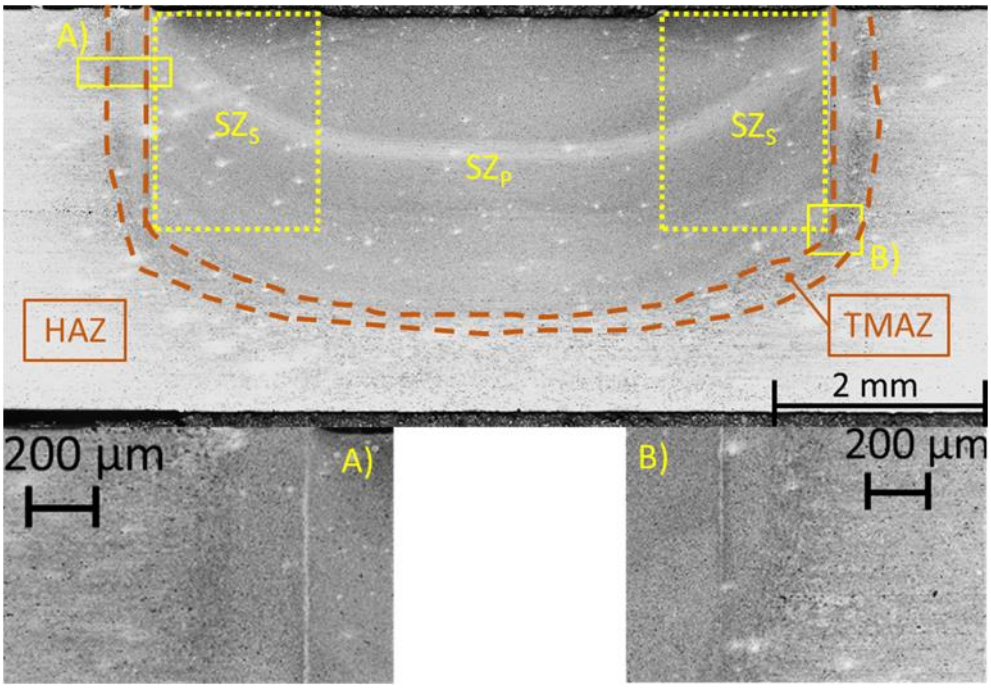

Figure 3.37 - Cross-section of RFSSW AA2024-T3 welding condition W3 (RS = 1000 rev/min; PD = 2.4 mm):
A) SZ/TMAZ interface;
B) Hook region.

The three common weld areas can be identified based on the microstructural changes, namely the stir zone (SZ), the thermo-mechanically affect zone (TMAZ) and the heat affected zone (HAZ). The SZ is an area where the material undergoes extreme plastic deformation and frictional heating driven by the tool action. This combination of heat and deformation leads to dynamic recrystallisation producing a fine and equiaxed microstructure. The SZ is located at the centre of the spot-weld and can be further divided into two areas: (i) the area processed by the shoulder (SZ_S) and (ii) the area processed by the probe (SZ_P). Due to the increase in the peripheral velocity of the tool, the average grain size present in the SZ_S is smaller than the one at the SZ_P. This phenomenon was also observed by Suhuddin et al. (2019). In this study, no visible distinction can be observed between the two sub-areas on AA2024-T3. This suggests an even distribution of frictional heat and material deformation in the SZ, promoting an even degree of dynamic recrystallisation along the whole area.

The interaction between the edge of the rotating tool and the base material in its vicinity produces a narrow area with a refined grain structure, corresponding to the TMAZ. This area does not undergo dynamic recrystallisation, as opposed to the grains in the SZ, due to the moderate strain rate and the lower temperatures. However, grain refinement is observed near the SZ/TMAZ interface and gradually decreases as the stirring action from the tool becomes less prevalent. The

TMAZ presents a deformed structure when compared to the base material rolling direction, as observed in the studies conducted by de Castro et al. (2018-B). This can be explained by the material movement during the different stages of the welding cycle, which can be enhanced by the presence of external geometrical features on the plunging component. The fact that the tool used comprises a featureless shoulder explains the lack of significant grain deformation in the TMAZ. This is consistent with what was reported by Ji et al. (2017-B), as this tool design produces less downward material flow compared to threaded component designs.

The HAZ is located between the TMAZ and the base material that only experiences a thermal cycle due to heat conduction. This promotes growth and coalescence of second phase precipitates, leading to a decrease of the mechanical properties of the weld. Its exact extension is generally estimated by the decrease in hardness values across the weld cross-section.

The joint line remnant is created between the top and bottom sheet in the SZ due to the original aluminium oxide films at the lap interface and its usual curved morphology is a consequence of the material movement during the refilling stage. In this study, the joint line remnant is not evident which suggests an extensive material mixing and breakdown of the oxide film. In parallel, the hook is another feature commonly observed in overlapped joints, produced at the transition between the unwelded and welded interface. The hook feature is shown in Figure 3.37.B), however the extent or height of this feature was not identifiable in this study. Due to the material flow direction in this region, it is common to find voids and internal defects in this area. As explained by Kwee et al. (2019), these internal voids are formed by poor material flow to fill the corners of the weld nugget during the refill stage. The role of the hook in the structural integrity of the weld is not clear, with different authors reporting different outcomes regarding the influence of the hook height (distance between the original interface and the tip of the hook) in mechanical performance. Santana et al. (2017) reported that higher hook heights related to weaker joint strength. However, no correlation between shear values and hook height was found for the study of de Castro et al. (2018-B) for RFSSW of AA2198-T8. In this investigation, although the fracture initiated on the hook, no relationship between the hook height and the shear strength value of a welding condition was found.

No internal voids or volumetric defects can be observed, supporting a correct choice of process parameters. However, as shown in Figure 3.38, internal voids were observed on the bottom edge of the weld nugget for welding condition W1 (low rotation speed and plunge depth values). This

is an indication of unsuitable welding conditions and a process boundary within the parameter window tested. A shallow surface indent on the probe region was observed for this welding condition, which can be attributed to incorrect tool zero level.

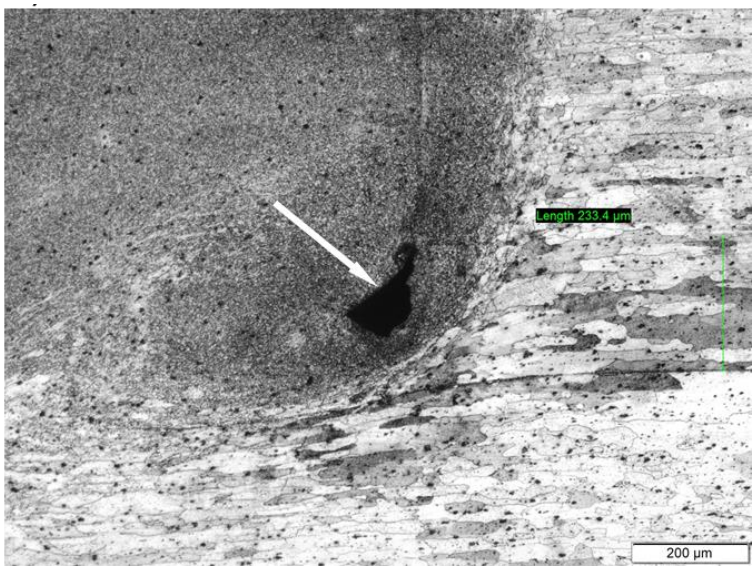

Figure 3.38 - Internal defects on the cross-section of RFSSW AA2024-T3 condition W1 (RS = 1000 rev/min; PD = 2.0 mm).

Figure 3.39 presents the cross-section of RFSSW AA2024-T3 welding condition W3 (RS = 1000rev/min; PD = 2.4mm) with sealant. The weld structure of the RFSSW is, in general, similar for the bare and with sealant specimens. However, a difference in grain morphology can be observed on the top of the SZ_P area, which relates to the lower peripheral velocity produced by the probe. No volumetric or internal defects can be observed, however the joint line remnant in the specimens with sealant is more evident. A possible explanation for this observation is the presence of small amounts of sealant trapped between the weld interface that mix with the oxide films. These sealant remnants display a different colour when etched. Boldsaikhan et al. (2019) also observed this phenomenon, where the use of Keller's reagent reacted with the cured epoxy sealant revealing sealant residue along the joint line remnant.

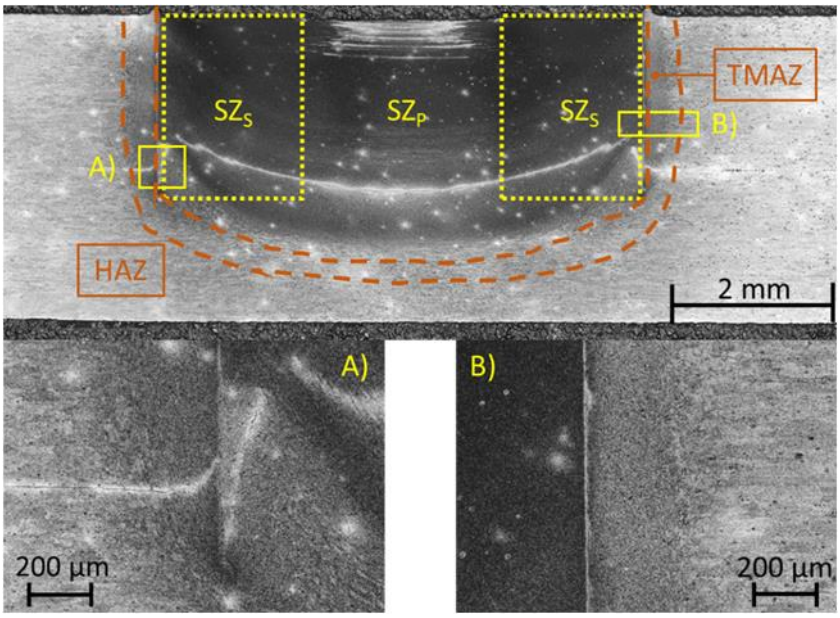

Figure 3.39 - Cross-section of RFSSW AA2024-T3 welding condition W3 (RS = 1000 rev/min; PD = 2.4 mm) with sealant:
A) Hook region;
B) SZ/TMAZ interface.

3.3.4.2. AA5754-H24

Figure 3.40 presents the cross-section of RFSSW AA5754-H24 performed with the parameter combination W12 (RS = 1000 rev/min; PD = 2.2 mm). A general overview of the weld regions has been presented in Section 3.3.4.1.

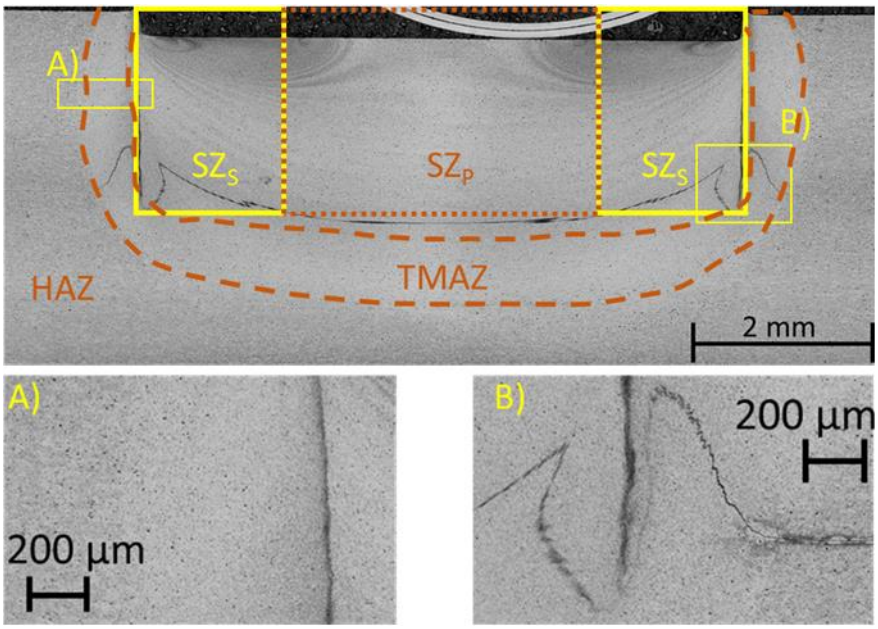

Figure 3.40 - Cross-section of RFSSW AA5754-H24 welding condition W12 (RS = 1000 rev/min; PD = 2.2 mm):
A) SZ/TMAZ interface;
B) Hook region.

No volumetric or internal voids can be observed, confirming an effective selection of weld parameters. A shallow surface indent was produced during the refilling stage to ensure weld consolidation in the stir zone. As observed by Xu et al. (2018), loss of material through the tool clearance fits needs to be compensated with a surface indent to enhance the diffusion bonding at the TMAZ/SZ interface and lap interface. Additionally, insufficient flow of the SZ material at the refilling stage can lead to the formation of voids at the maximum shoulder plunge depth. Due to the increased peripheral velocity of the shoulder, which promotes the dispersion of the original oxide films, the joint line remnant is less noticeable at the edges of the stir zone. The hook feature is visible in Figure 3.40.B). As mentioned in the previously, higher hook heights are generally associated with weaker joint strength values. However, the opposite was true for this work as shown in Table 3.32. No correlation between lap shear strength and hook height was also observed for the study of de Castro et al. (2018-B) for RFSSW of AA2198-T8.

Table 3.32 - Hook height of all experimented process parameter combinations of RFSSW AA5754-H24.

Welding condition	Rotation Speed [rev/min]	Plunge Depth [mm]	Lap shear strength [kN]	Hook height [µm]
W10	1000	1.8	5.87 ± 0.07	44.2
W11		2.0	6.85 ± 0.04	247.5
W12		2.2	7.16 ± 0.02	366.5
W13	1580	1.8	4.99 ± 0.02	24.1
W14		2.0	6.37 ± 0.06	96.8
W15		2.2	6.76 ± 0.09	337.6
W16	2160	1.8	4.93 ± 0.08	21.4
W17		2.0	5.91 ± 0.05	178.2
W18		2.2	6.16 ± 0.06	223.5

The heterogenous nature of the SZ_S on this alloy shows striation bands along the thickness of the sheet. This feature is generated during the refill action, as the shoulder maintains intimate contact with the top layer of the material while retracting in the final stages of the cycle. This creates a gradient of shear layers that become closer to each other as the material is refilled and the retraction rate slows downs. This feature was initially observed for friction stir welding and is known as “onion rings”. Krishnan (2002) explains that this phenomenon occurs due to the combination of frictional heating being generated by the tool rotation and the tool forward motion.

3.3.4.3. AA7075-T6

Figure 3.41 presents the RFSSW AA7075-T6 cross-section of welding condition W21 (RS = 1000 rev/min; PD = 2.4 mm). The three common weld areas can be identified based on the microstructural changes and different etching degrees, which have been extensively described in Section 3.3.4.1.

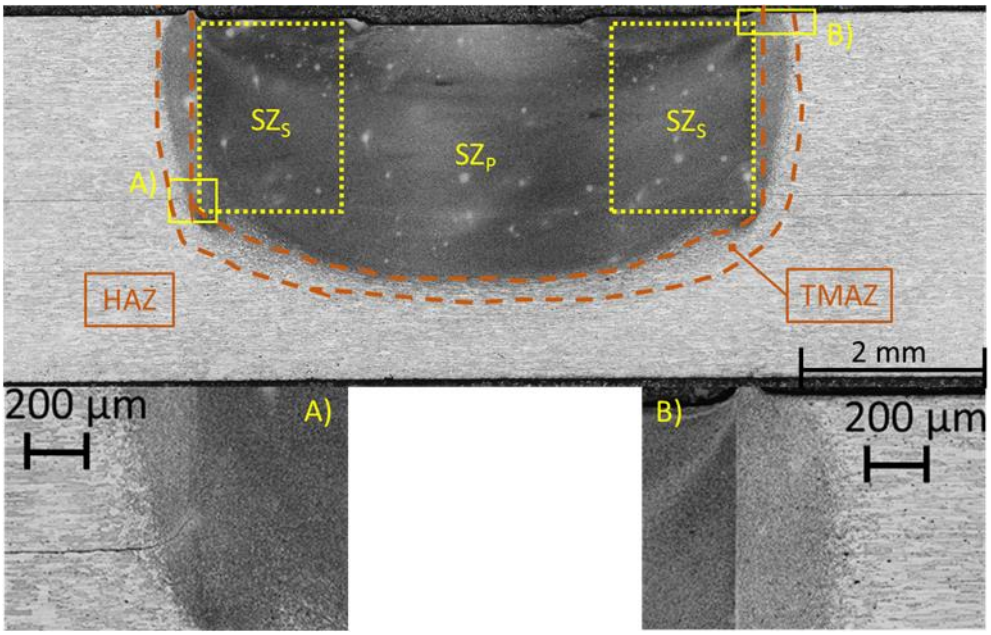

Figure 3.41 - Cross-section of RFSSW AA7075-T6 performed with welding condition W21 (RS = 1000 rev/min; PD = 2.4 mm):
A) Hook region;
B) SZ/TMAZ interface.

No internal voids or volumetric defects can be observed in the cross-section for welding condition W21, confirming the correct choice of process parameters. A shallow surface indent on the probe region was observed for this welding condition, which can be attributed to incorrect tool zero level. The joint line remnant is not evident which suggests an extensive material mixing and breakdown of the oxide film. Similar to what was observed on the AA2024-T3 cross-section, although the fracture initiated on the hook, no relationship between the hook height and the lap shear strength of a welding condition was found.

As observed in Section 3.3.4.1, internal voids were observed on the bottom edge of the weld nugget for welding conditions W1 (low rotation speed and plunge depth values). These voids, of smaller dimensions than the ones observed in Section 3.3.4.1, can be seen in Figure 3.42. This is an indication of a lower process boundary within the parameter window tested. An upper process boundary was not found due to equipment limitation.

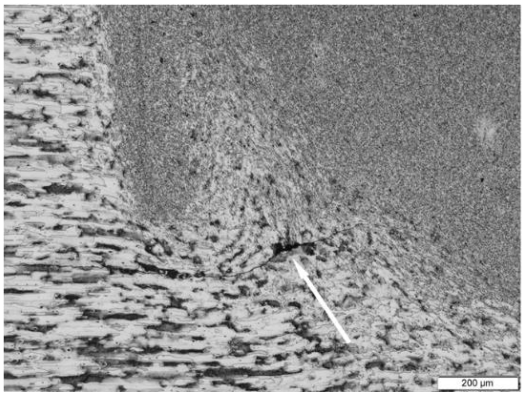

Figure 3.42 - Internal defects on the cross-section of RFSSW AA7075-T6 welding condition W19 (RS = 1000 rev/min; PD = 2.0 mm).

Figure 3.43 present the cross-section of RFSSW AA7075-T6 with sealant performed with welding condition W21 (RS = 1000 rev/min; PD = 2.4mm). The weld structure of the RFSSW is similar for the bare and with sealant specimens, which has been covered in Section 3.3.4.1. A clear difference in grain size and morphology between the SZ_P and SZ_S area can be seen. As covered in Section 3.3.4.1, this can be attributed to the difference in peripheral velocity as well as the smaller interaction between the weld material and the probe. No volumetric or internal defects can be observed, however the joint line remnant in the cross-section with sealant is much more visible. This can be explained by the presence of small amounts of sealant trapped between the weld interface that mix with the oxide films, which display a different colour when etched.

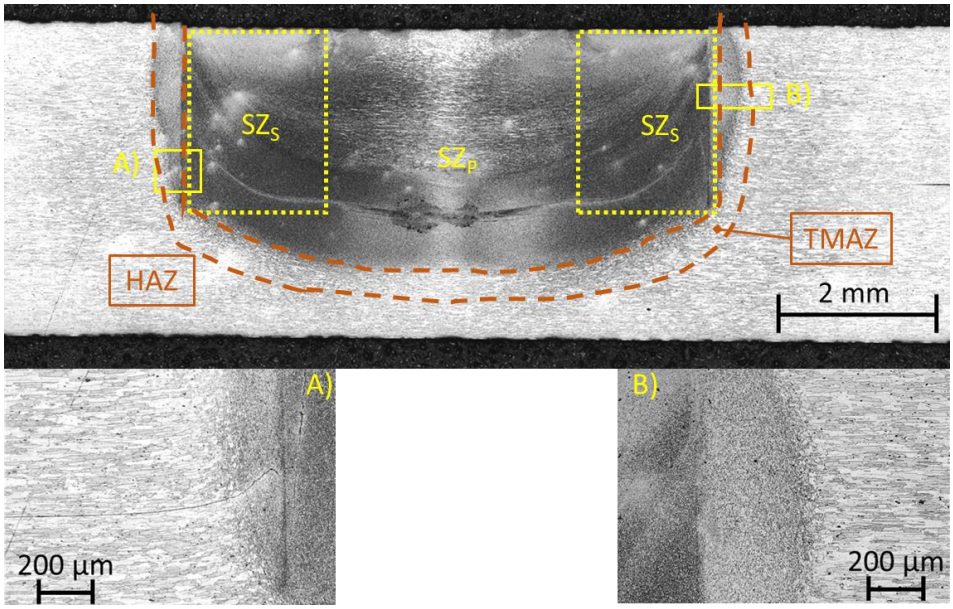

Figure 3.43 - Cross-section of RFSSW AA7075-T6 welding condition W21 (RS = 1000 rev/min; PD = 2.4 mm) with sealant:
A) Hook region;
B) SZ/TMAZ interface

3.3.5. Residual stress measurements

3.3.5.1. AA2024-T3

The longitudinal residual stress distribution across the thickness of a RFSSW AA2024-T3 single spot-weld specimen obtained by the contour method is shown in Figure 3.44. The longitudinal residual stress distribution across the width of the specimen is consistent with what would be expected for a welded specimen, demonstrating the potential of the contour method to map the residual stress field in a RFSSW component. A comparison with other residual stress measurement techniques would fully confirm the accuracy of the results however, such analysis is out of the scope of this investigation and is recommended to be addressed for future work.

From the finite element model, it can be seen that within the weld region and its vicinity, the longitudinal stress distribution is entirely tensile. The same is observed across the thickness of the specimen. This distribution is typical of various welding processes as the free thermal expansion of the weld material during the weld process and subsequent contraction during cooling are restricted by the adjacent parent material. As a result, residual stresses generated by thermal strains are present in this region. Due to the deep plunge depth and thin gauge of the sheets, it was expected that the heat flow from the weld area would produce a uniform residual stress profile. However, an area of higher residual stress values can be observed at the stir zone which is consistent with the temperature profile distribution presented by Zhao et al. (2018-B) and the microstructural transformations present in this area.

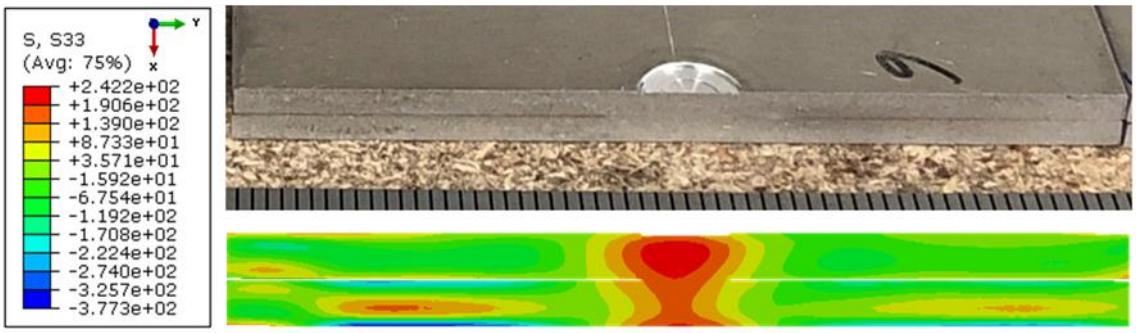

Figure 3.44 - 3D FEM model of the residual stress distribution on an AA2024-T3 single spot-weld specimen (values presented in MPa).

The high value tensile residual stresses on the bottom sheet can be explained by the restrained to the free thermal expansion of the bottom sheet material imposed by the circular anvil when performing the weld cycle. Away from the weld area, the magnitude of the tensile residual stresses decreases as the peak temperatures are lower. A compressive stress state is achieved on

the top sheet parent material that restrains the thermal contraction of the weld material. The opposite state can be observed on the parent material of the bottom sheet and can be attributed to the residual stresses induced in the sheet by rolling during its production. The lower temperature heat flow from the weld area in the bottom sheet compared to the heat flow from the top sheet is less effective at relieving the previous stress state.

Figure 3.45 presents the longitudinal residual stress plot from two measurement lines across the mid-thickness of both sheets. The vertical dash-dotted line marks the centre of the specimen and the spot-weld. For both measurements, the profiles are reasonably symmetrical to the centre line of the spot-weld and follow the same distribution in the weld area and its vicinity. In this investigation, the distinct "M-shaped" distribution generally observed in other friction stir welding technologies (Reynolds et al., 2003; Threadgill et al., 2009) was not observed. This phenomenon can be explained by the different geometry of the plunging component, which leads to a difference in the material flow and the produced microstructure in the stir zone. Although the area with the lowest hardness values, the peak tensile stress value can often be observed at the heat affected zone. However, for both measurement lines, the peak stress values were found at the centre of the stir zone with the highest value observed on the top sheet and a magnitude of 240.77 MPa. This value corresponds to around 70 % of the yield strength of the material.

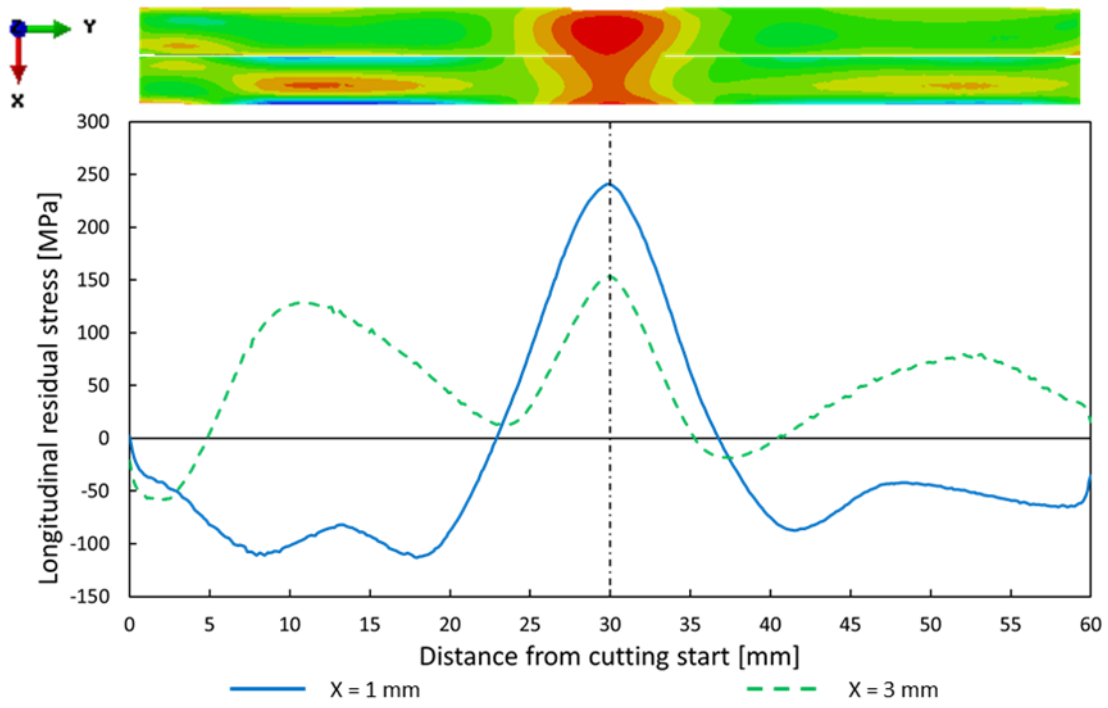

Figure 3.45 - Line plot of residual stress distribution on an AA2024-T3 single spot-weld specimen at specified thicknesses.

Based on the analysis of the single-spot sample, a weld induced affected area can be measured up to 1.5 spot-weld diameters from the centre of the spot. Therefore, the distance of three spot-weld diameters between spot-welds implemented for the multiple spot-weld specimen should minimise the interaction between the residual stresses induced by the multiple spot-welds. The finite element model of the residual stress distribution across the width, as per section 'A' in Figure 3.5, of a multiple spot-weld specimen is depicted in Figure 3.46.

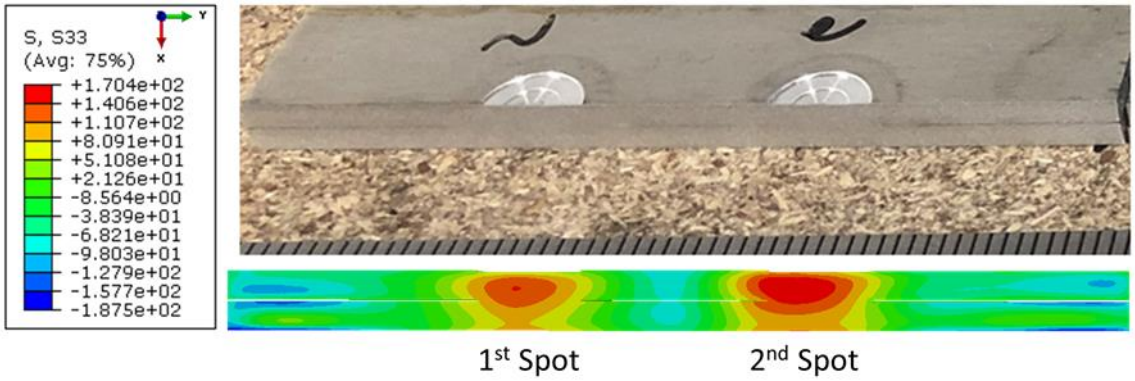

Figure 3.46 -3D FEM model of the residual stress distribution across two rows on an AA2024-T3 multiple spot-weld specimen (values presented in MPa).

Comparing with the stress distribution of a single spot specimen, the type and location of the residual stresses are reasonably similar. The peak stresses were observed at the centre of the spot-weld and were higher on the second spot-weld. This can be explained by a higher peak temperature reached during the weld cycle of the second spot. Since the column of spot-welds in this specimen was performed sequentially, the sheets and tool have more residual heat before the second spot-weld cycle compared to the first one. This phenomenon was also observed by Larsen, Hunt and Hovanski (2020), while producing multi-weld specimens. Away from the spot-weld affected area, compressive stress values are of similar magnitude to the single spot-weld while lower peak tensile stress values were observed.

The longitudinal residual stress plot from two measurement lines across the mid-thickness of both sheets is presented in Figure 3.47. The vertical dash-dotted line indicates the centre of the spot-weld. The stress profiles evidence similar degree of uniformity along the thickness as observed for the single-spot specimen. Peak tensile stresses were measured on the top sheet due to a higher peak temperature and degree of recrystallisation. A decrease of 33.2 % and 36.5 % of the peak tensile value between the top and bottom sheet was determined for the first and second spot-weld, respectively.

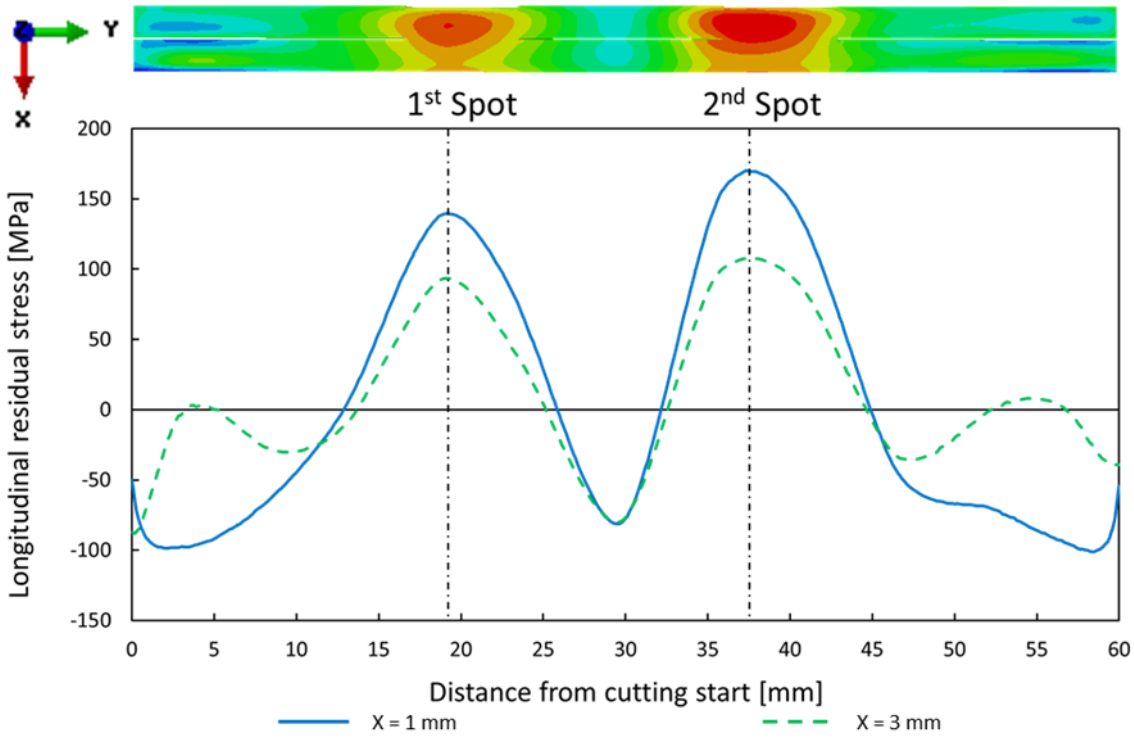

Figure 3.47 - Line plot of residual stress distribution across two rows on an AA2024-T3 multiple spot-weld specimen at specified thicknesses.

Similar weld affected area can be observed for this spot-weld arrangement, with the weld-induced residual stresses shifting from tensile to compressive at the distance of around two spot-weld diameters from the peak point. The peak values of both profiles are slightly offset from the centre of the spot-weld, however this can be attributed to a referencing error while setting up the specimens for welding. The peak tensile stress values for the first and second spot-weld were, respectively, 139.85 and 170.16 MPa, corresponding to 40.7 % and 49.6 % of the base material yield stress. A peak value variation of 17.8 % between the two spot-welds was observed.

The compressive stress value measured between the spot-welds is similar to the expected compressive stress value away from the weld region. This suggests that an appropriate distance between spot-welds was chosen and that there is no truncation of the original stress profile. However, comparing with the single spot-weld specimen, a decrease of 41.9 % and 29.3 % of the peak tensile stress value was measured for the first and second spot-weld, respectively. This observation can be explained by both the influence of the stress distribution of a second spot-weld and the stress relief on the first spot-weld by the heat flow from the second one. This led to an overall balance of the weld-induced residual stress magnitude.

The finite element model of the residual stress distribution across the length, as per section 'B' in Figure 3.5, of a multiple spot-weld specimen is depicted in Figure 3.48. In this analysis, the specimen was cut through the centre of the second spot-weld of each column. As predicted the stress distribution is similar to what was previously observed for the single and double spot-weld specimens, with the peak values being observed at the centre of the spot-weld. For the analysed spot-weld arrangement, similar peak tensile stress values can be observed along the profile. As reported for the double spot-weld specimen, this could be explained by the increase in temperature of the sheets due to the heat flow from the array of spot-welds which leads to a stress relieving action across the specimen.

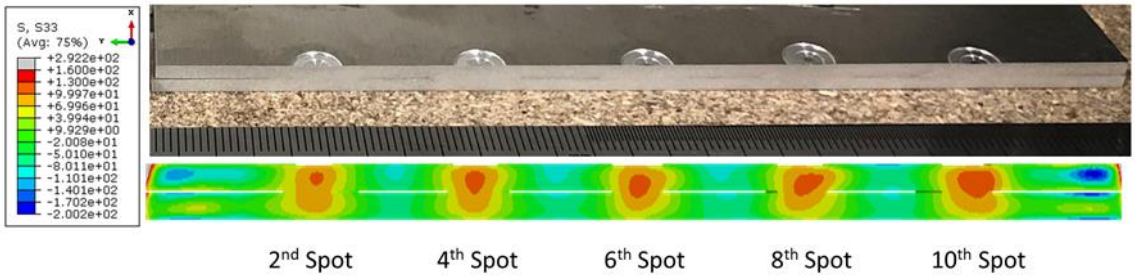

Figure 3.48 - 3D FEM model of the residual stress distribution across the five columns of the top row on an AA2024-T3 multiple spot-weld specimen (values presented in MPa).

When cutting the multiple spot-weld specimen along its length, the rolling direction is aligned with the measurement surface. The increase in value of the compressive stresses observed away from the multiple spot-weld array can be explained by the pre-existing residual stresses due to rolling, which produces an anisotropic behaviour and stress distribution. The longitudinal residual stress plot from the two measurement lines across the mid-thickness of both sheets is presented in Figure 3.49.

It can be seen from the longitudinal stress profiles gathered for the five spot-weld analysis that, similar to what was observed for the single and double spot-weld specimens, the stress profile is fairly uniform along the thickness of the specimen with the peak residual stress values being recorded on the top sheet. An explanation to this phenomenon has been provided previously in this section. Along the length of the specimen, the maximum tensile stress value was registered on the last spot-weld (10^{th} spot), similar to what was observed for the double spot-weld specimen. However, the difference in the peak tensile stress values of the spot-welds was not significant ranging between 105.3 and 124.3 MPa, corresponding to a percentual increase of 15.2 %. These values are equivalent to 30.7 % and 36.2 % of the parent material yield stress,

respectively. Comparing with the peak tensile stress observed on the single spot-weld specimen, a decrease of 56.7 % and 48.3 % was measured for the 2nd and 10th peak tensile stress value.

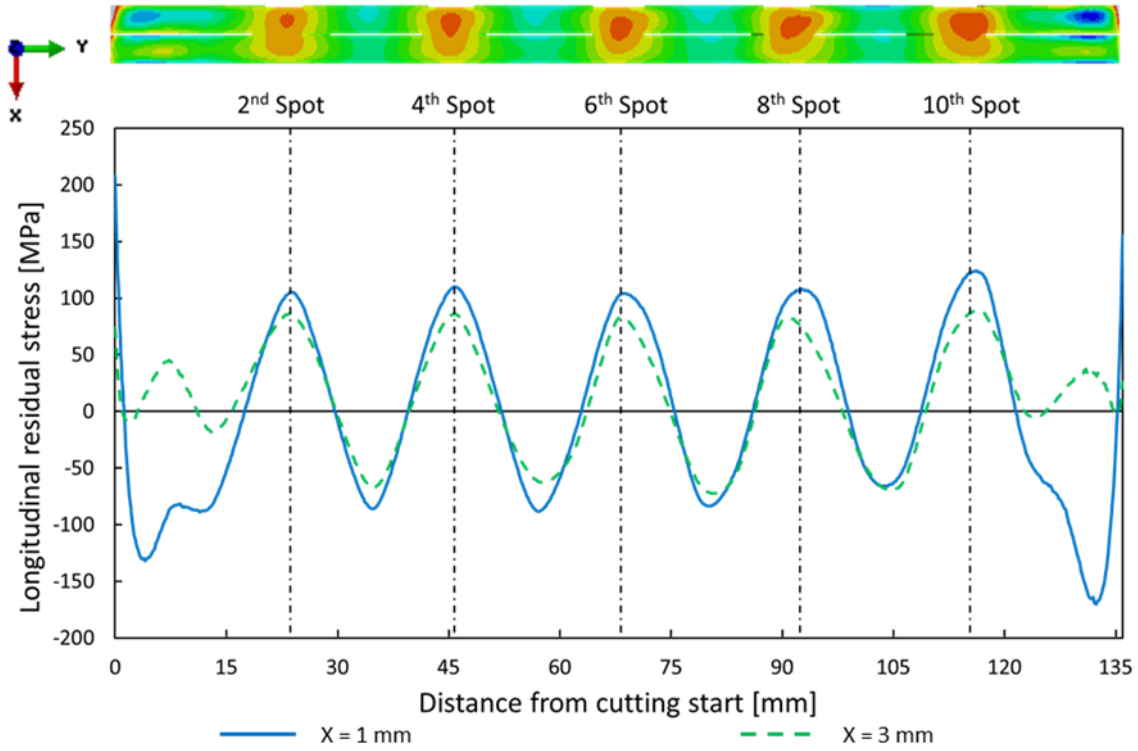

Figure 3.49 - Line plot of residual stress distribution across the five columns on an AA2024-T3 multiple spot-weld specimen at specified thicknesses.

As observed for the double spot-weld specimen, it seems that the increase in number of spot-welds has a detrimental effect on the maximum tensile stress value. However, this is a positive outcome considering that the ideal scenario in an array of multiple spot-welds is to have the lowest residual stress value possible. Due to a smaller thermal expansion and contraction cycle, the peak tensile and compressive stresses on the bottom sheet are fairly uniform along the length of the specimen. The greatest percentual variation between the stress values of the two profiles were measured at the centre of the 10th spot-weld and between the 4th and 6th spot-weld, with a variation of 28.4 % (tensile) and 28.9 % (compressive).

Between the spot-welds, lower compressive stress values were registered compared with the values registered away from the weld area. As already observed in the double spot-weld specimen, this is due to the presence of an adjacent spot-weld that truncates the original stress profile, affecting the stress magnitude and distribution in this area. In fact, since that in this specimen the array of spot-welds is greater than previously analysed, a decrease in the compressive stress values between spot-welds along the profile was observed, with the lowest

value found between the 10th and the 8th spot-weld. This suggests that, as the number of spot-welds increase, the affected area by the weld-induced residual stresses increases and that the original profiles from previous spot-welds are truncated. Although the overall residual stress distribution is significantly below the yield strength of the base material, a bigger spacing between spot-welds might be required to minimise the interaction effects of various spot-welds.

3.3.5.2. AA5754-H24

The longitudinal residual stress distribution across the thickness of a RFSSW AA5754-H24 single spot-weld specimen obtained by the contour method is shown in Figure 3.50. The stress distribution for the single spot-weld specimen of this strain-hardened alloy is fairly similar to the stress distribution observed in the specimen from Section 3.3.5.1, with a tensile stress distribution in the weld area and its immediate vicinity due to the material thermal expansion and contraction experienced in this area. For this specimen, a small indent was observed on the bottom sheet at the anvil region and can explain the higher tensile peak value measured in this region. In comparison with the AA2024-T3 alloy, the inherent physical properties of the AA5754-H24 alloy for stamping applications, such as lower hardness values, allow for further deformation. This deformation can be attributed to the high process forces coupled with local material softening due to the thermal cycle.

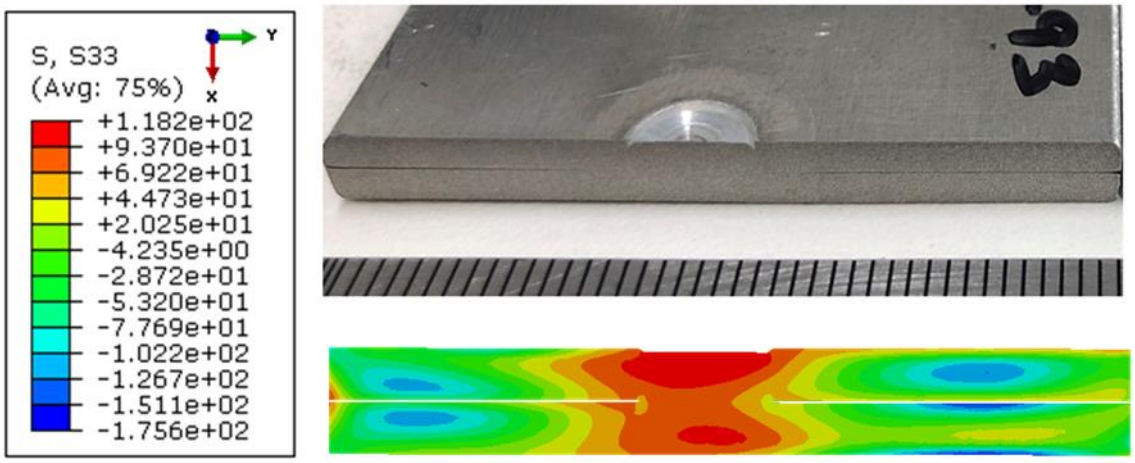

Figure 3.50 - 3D FEM model of the residual stress distribution on an AA5754-H24 single spot-weld specimen (values presented in MPa).

Away from the weld region, a gradient of compressive stresses along the width of the specimen was measured on the top sheet with similar magnitude as the peak tensile stresses found in the stir zone area. A reasonable level of symmetry at the centre line can also be observed with a slight deviation of the residual tensile stresses on the left-hand side of the weld area on the top sheet.

This deviation was also observed on the bottom sheet on the opposite side, which can be explained by the difference in the design of the specimen and the spot-weld location used in this analysis as mentioned in Section 3.2.5. Due to the close proximity of the spot-weld to the edge of the specimen, the heat flow from the weld area is greater at the free edges of the specimen leading to uneven expansion and contraction of the weld material.

Figure 3.51 presents the longitudinal residual stress plot from two measurement lines across the mid-thickness of both sheets. The vertical dash-dotted line indicates the centre of the spot-weld. The same bell curve stress distribution was observed at the weld area for both profiles, as observed in the previous Section. For both measurement profiles, the peak tensile stress values were found at the centre of the stir zone with the highest value observed on the top sheet and a magnitude of 110.78 MPa, corresponding to 53.8 % of the parent material yield stress.

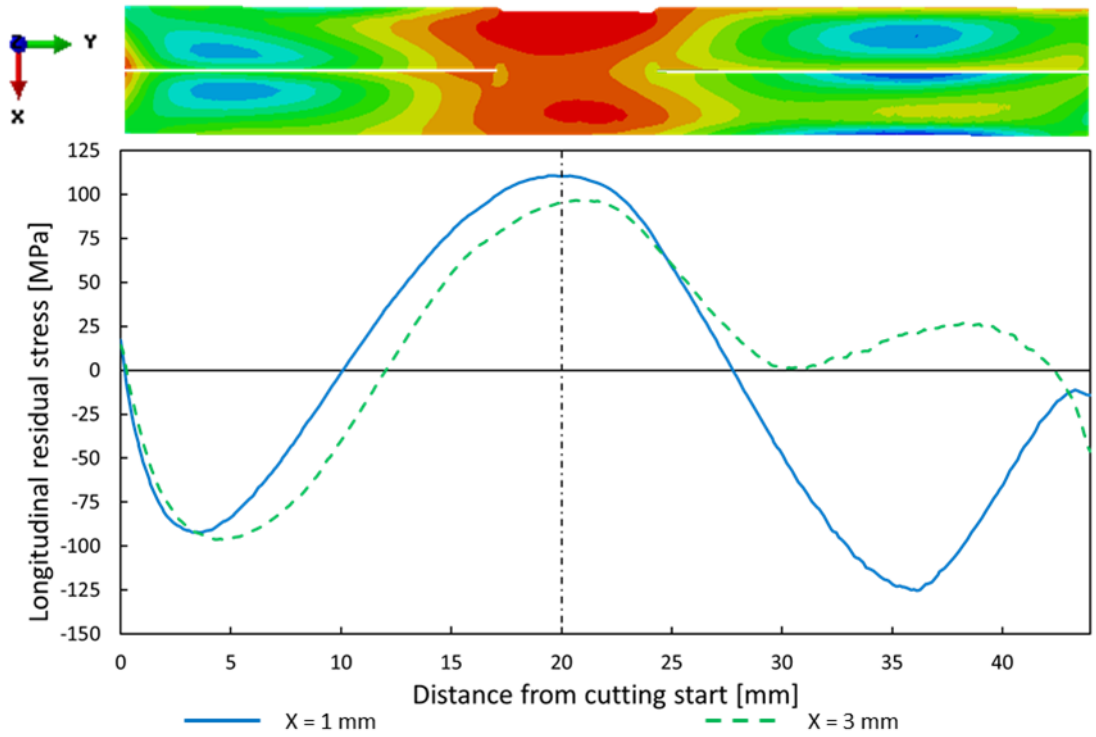

Figure 3.51 - Line plot of residual stress distribution on an AA5754-H24 single spot-weld specimen at specified thicknesses.

The finite element model of the residual stress distribution across the width of the multi spot-weld specimen is shown in Figure 3.52. The residual stress distribution on both spot-welds is consistent with what was observed for the single spot-weld specimen and for the double spot-weld specimen from Section 3.3.5.1. A comprehensive description of the stress distribution has

been presented in that section. Both peak tensile stresses were found at the centre of the spot-weld with a higher value on the second spot-weld.

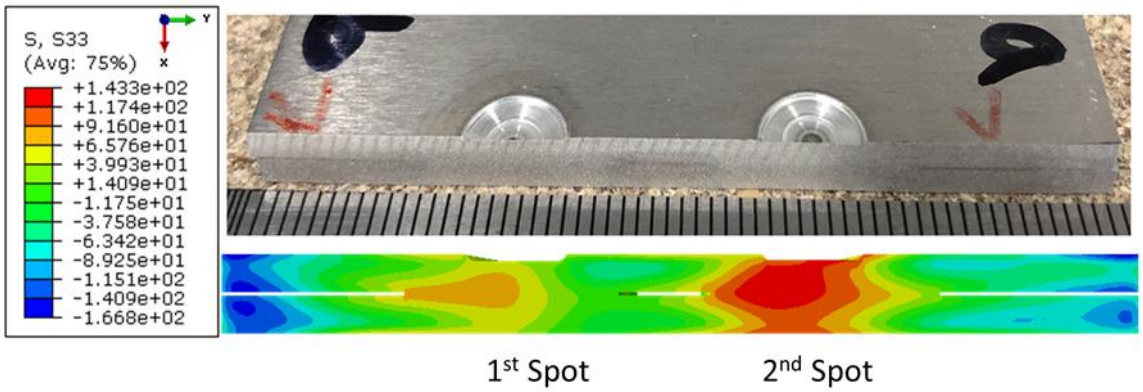

Figure 3.52 - 3D FEM model of the residual stress distribution across two rows on an AA5754-H24 multiple spot-weld specimen (values presented in MPa).

The longitudinal residual stress plot from two measurement lines across the mid-thickness of both sheets is presented in Figure 3.53. The vertical dash-dotted line indicates the centre of the spot-weld. Due to an alignment error while producing the multiple spot-weld specimen, the centre of the first spot-weld was offset by 18 mm from the edge as opposed to the 20 mm distance set in Figure 3.5. The stress profiles evidence similar degree of uniformity along the thickness as observed for the single spot-weld specimen, with the peak stresses being higher on the top sheet. However, a negligible discrepancy between the peak tensile stresses of both profiles was measured on the first spot-weld. Similar weld affected area can be observed for this spot-weld arrangement, with the weld-induced residual stresses shifting from tensile to compressive at the distance of around two spot-weld diameters from the peak value. The peak tensile stress values were 63.82 and 130.79 MPa for the first and second spot-weld, corresponding to 30.9 % and 63.5 % of the base material yield stress, respectively. Comparing with the double spot-weld specimen from Section 3.3.5.1, the stress relieve effect from the second spot-weld on the peak tensile stress value of the first spot-weld was slightly higher, with a reduction of 57.6 % of the peak value obtained from a single spot-weld specimen. However, compared to the peak tensile value of a single spot-weld specimen, an increase of 18 % on the peak tensile stress value (20.01 MPa) was recorded for the second spot-weld, as opposed to the 30 % decrease observed in the specimen from the previous section.

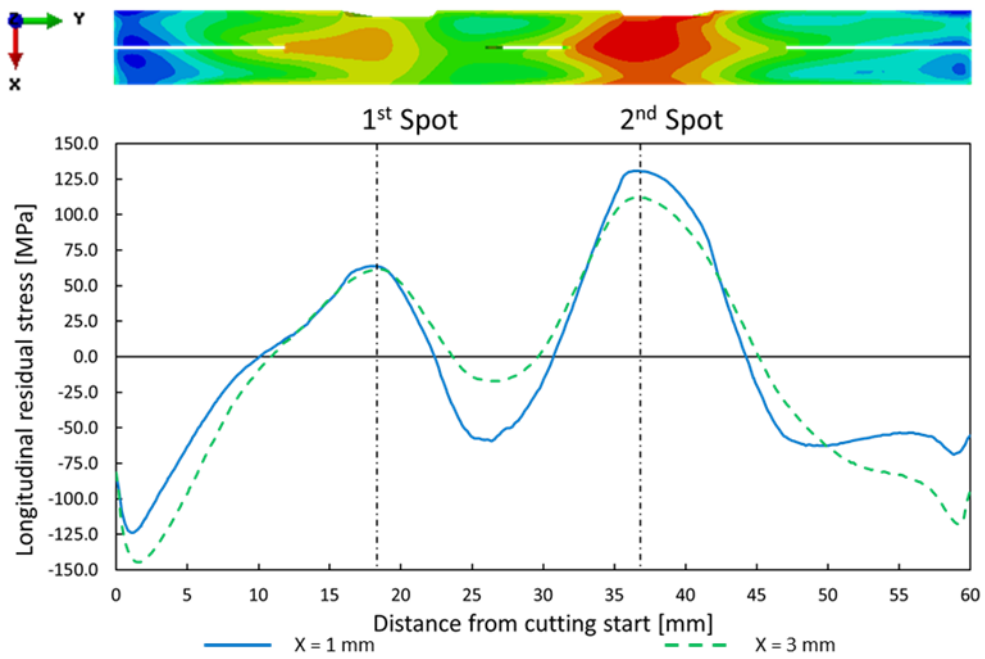

Figure 3.53 - Line plot of residual stress distribution across two rows on an AA5754-H24 multiple spot-weld specimen at specified thicknesses.

Due to the small variation between the two values, an explanation for this phenomenon could be attributed to the machining operations performed to the single spot-weld specimen before the residual stress measurements. As previously mentioned, a lap shear stress specimen (Figure 3.3) was used to measure the residual stress on a single spot-weld in this section. The free edges of this specimen were cut in the guillotine followed by linishing of the corners and edges. These operations could have an impact on the residual stress profile and could have led to stress relieve in the single-spot coupon. Due to the limited budget and time, a new specimen could not be analysed to confirm this hypothesis. As observed in Section 3.3.5.1, a smaller compressive stress value between the spot-welds compared with the values measured for the single spot-weld specimen was registered. An explanation for this phenomenon has been presented in that section.

The finite element model of the residual stress distribution across the length of a multi spot-weld specimen is depicted in Figure 3.54. In this analysis, the specimen was cut through the centre of the second spot-weld of each column. Due to a setup error while welding the specimen, the location of the stresses along the profile length do not fully match the centre of the spot-weld from the 3D model. However, as predicted, the stress distribution is similar to what was previously observed for specimen in Section 3.3.5.1, with the peak stress values being observed at the centre of the spot-weld. In the analysed spot-weld arrangement, similar stress distributions

and magnitudes can be observed from the 2nd to the 8th spot-weld, with a significant increase in tensile stress for the 10th spot-weld.

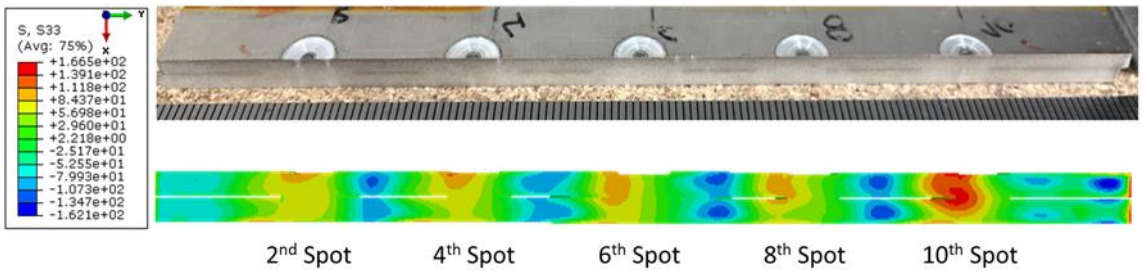

Figure 3.54 - 3D FEM model of the residual stress distribution across the five columns of the top row on an AA5754-H24 multiple spot-weld specimen (values presented in MPa).

The longitudinal residual stress plot from the two measurement lines across the mid-thickness of both sheets is presented in Figure 3.55. The vertical dash-dotted line indicates the centre of each spot-weld. The stress profile is reasonably uniform along the thickness with overall greater residual stress values being recorded on the top sheet. An explanation to this phenomenon has been provided in this section. Similar behaviour to the double spot-weld specimen was observed with a continuous increase in the peak tensile stress value and a maximum registered on the last spot-weld (10th spot). Both profiles evidence a fairly similar peak tensile stress value along the remaining spot-welds.

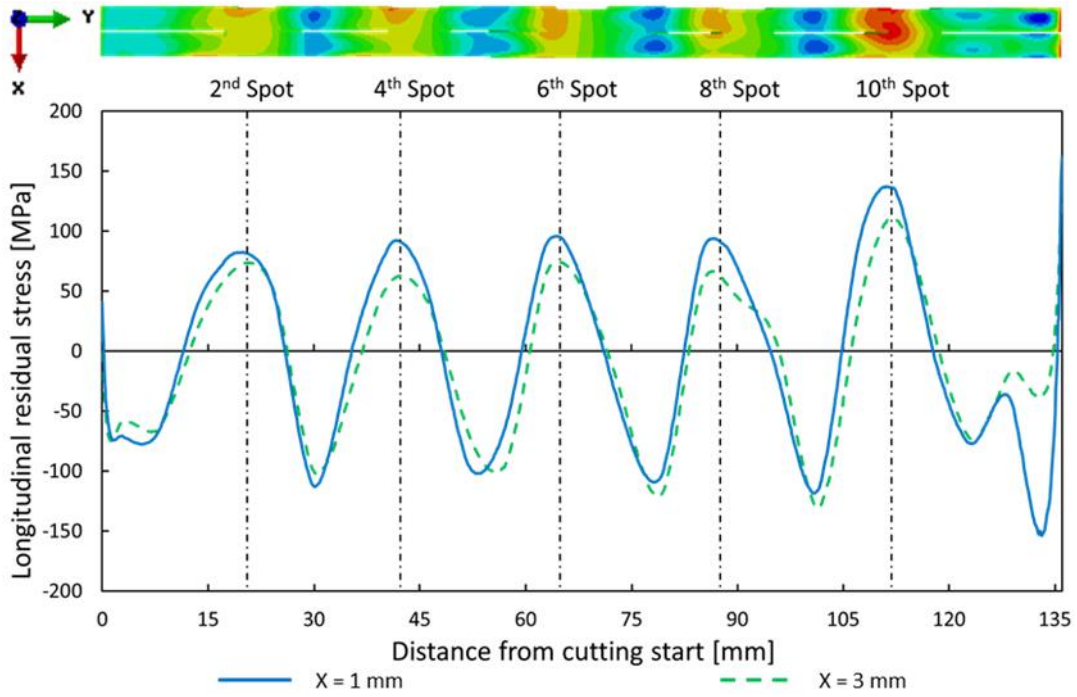

Figure 3.55 - Line plot of residual stress distribution across the five columns on an AA5754-H24 multiple spot-weld specimen at specified thicknesses.

Peak tensile stresses ranged between 82.32 and 136.75 MPa, corresponding to the 2nd and 10th spot-weld, respectively. These values are equivalent to 39.9 % and 66.3 % of the parent material yield stress, respectively. Comparing with the peak tensile stress value observed on the single spot-weld specimen, a decrease of 25.7 % for the 2nd peak tensile spot-weld and, as observed for the double spot-weld specimen, an increase of 23.4 % on the maximum tensile stress was measured. However, similar stress magnitude ranges to the ones observed in the two spot-weld specimen were observed for this specimen, suggesting that the increasing number of spot-welds does not have an impact on the peak tensile stress value. This could be attributed to the non-heat treatable nature of this alloy. However, further testing of this hypothesis is out of the scope of this investigation.

Compressive stress values between the spot-welds tend to increase in magnitude along the length of the specimen. The greatest percentual variations in the stress value between the two profiles were measured between the peak value at the centre of the 4th and 8th spot-weld, with a decrease of 31.8 % and 29.1 %. Between the spot-welds, lower compressive stress values were registered compared with the values registered away from the weld area. The conclusions drawn from the analysis in Section 3.3.5.1 can also be applied to this alloy group.

3.3.5.3. AA7075-T6

The longitudinal residual stress distribution across the thickness of a RFSSW AA7075-T6 single-spot specimen obtained by the contour method is shown in Figure 3.56. The stress distribution for this specimen of this heat treatable alloy is fairly similar to the stress distribution observed in the specimen from Section 3.3.5.1, with a tensile stress distribution in the weld area and its immediate vicinity due to the material thermal expansion and contraction experienced in this area. A small tensile stress region can be observed at the centre of the spot-weld on bottom surface of the bottom sheet. This phenomenon can be attributed to an overheating of the bottom anvil, which generated a localised thermal expansion and contraction cycle of the material in this region. The presence of the anvil to restrict the free movement of the material led to the development of the observed stress state.

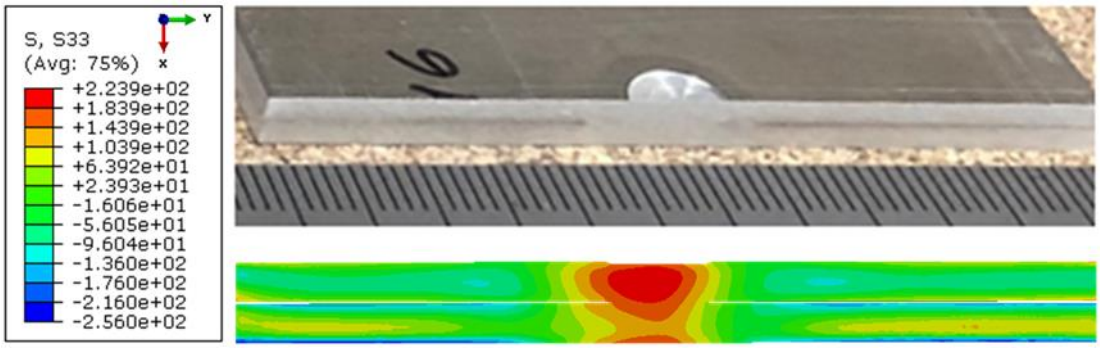

Figure 3.56 - 3D FEM model of the residual stress distribution on an AA7075-T6 single spot-weld specimen (values presented in MPa).

Away from the weld area, the magnitude of the tensile residual stresses decreases as the peak temperatures are lower. A compressive stress state is achieved on the top sheet parent material that restrains the thermal contraction of the weld material during cooling. As observed for the specimen in Section 3.3.5.1, the opposite stress distribution can be observed on the parent material of the bottom sheet. An explanation for this effect has been provided in that section.

Figure 3.57 presents the longitudinal residual stress plot from two measurement lines across the mid-thickness of both sheets. The vertical dash-dotted line indicates the centre of the spot-weld. Due to a minor error on the welding setup, the centre of the spot-weld from the 3D model is not fully aligned with the stress profile. Nevertheless, a reasonable level of symmetry at the centre line can be observed for the stress profile on the top sheet. Comparing with the stress profile from the bottom sheet, it can be seen that away from the weld area the stress profile is not uniform along the thickness. Although the bottom sheet displays an asymmetric stress profile at the weld area, the weld-induced residual stress distribution for both profiles are approximately of the same size. Similar “bell” curve stress distribution was observed at the weld area for both profiles, as observed in the previous sections. For both measurement profiles, the peak tensile stress values were found at the centre of the stir zone with the highest value observed on the top sheet and a magnitude of 222.8 MPa, corresponding to 43.5 % of the parent material yield stress. A decrease of 36.3 % between the peak tensile stresses of the stress profiles from the top and the bottom sheet was measured as observed for the single spot-weld specimen in Section 3.3.5.1.

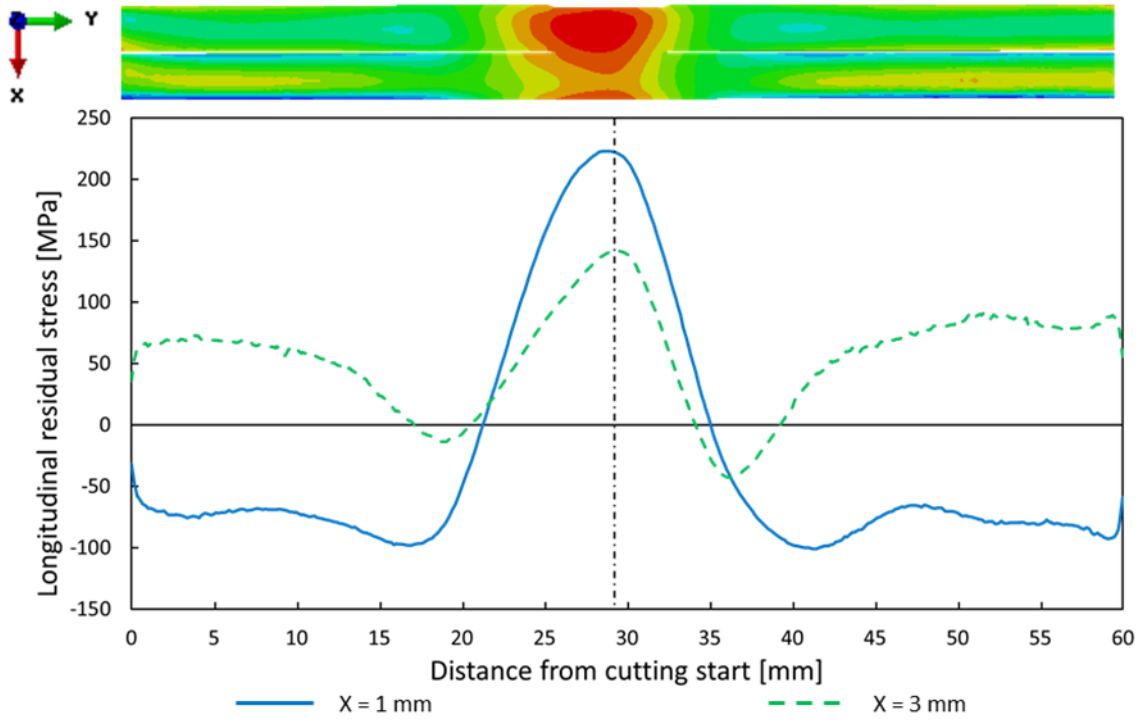

Figure 3.57 - Line plot of residual stress distribution on an AA7075-T6 single spot-weld specimen at specified thicknesses.

The finite element model of the residual stress distribution across the width of the multiple spot-weld specimen is shown in Figure 3.58. Due to a change in the half of the specimen used for the analysis, the 2nd spot is located on the left-hand side of the model. The residual stress distribution on both spot-welds is consistent with what was observed for the single spot-weld specimen and a comprehensive description of the stress distribution has been presented in Section 3.3.5.1. Both peak tensile stresses were found at the centre of the spot-weld with a higher value on the second spot-weld, as observed in the previous specimens. Away from the weld area, a significantly higher compressive stress value was measured on the top sheet. This can be attributed to the restraint to the free thermal contraction of the weld material during cooling. This effect is not as noticeable on the bottom sheet as the peak temperatures and microstructural changes are less intense.

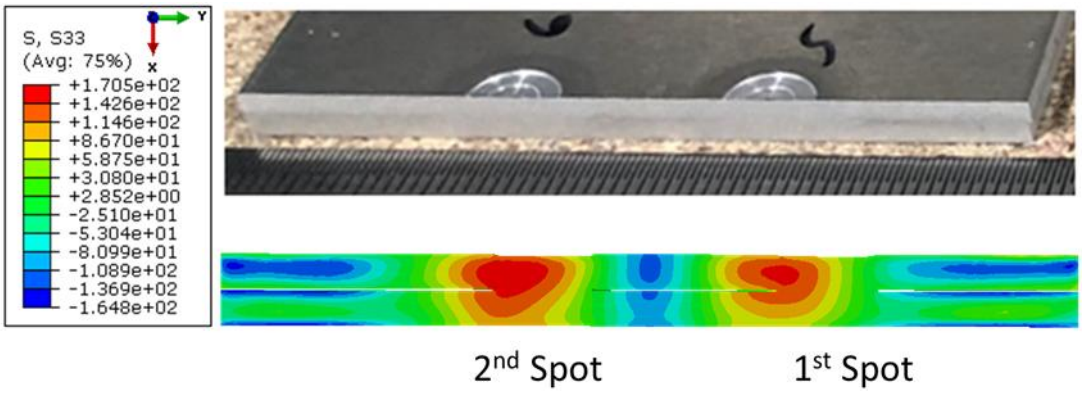

Figure 3.58 - 3D FEM model of the residual stress distribution across two rows on an AA7075-T6 multiple spot-weld specimen (values presented in MPa).

The longitudinal residual stress plot from two measurement lines across the mid-thickness of both sheets is presented in Figure 3.59. The vertical dash-dotted line indicates the centre of the spot-weld. Due to a setup error while welding the specimen, the location of the stresses along the profile length do not fully match the spot-weld centre on the 3D model. Both profiles are fairly symmetrical at the centre of the specimen, as observed on the double spot-weld specimen from Section 3.3.5.1. Similar weld affected area can be observed for this spot-weld arrangement, with the weld-induced residual stresses shifting from tensile to compressive at the distance of around one spot-weld diameter from the peak value. At the weld area, the stress profiles evidence uniformity along the length and thickness, with the peak stresses being higher on the top sheet.

The peak tensile stress values were 149.70 and 170.36 MPa for the first and second spot-weld, respectively, corresponding to 29.2 % and 33.2 % of the base material yield stress. A decrease of 24.3 % and 29.5 % of the peak tensile value between the top and bottom sheet was determined for the first and second spot-weld, respectively. Comparing with the single spot-weld specimen, a decrease of 32.8 % and 23.5 % of the peak tensile stress value was measured for the first and second spot-weld, respectively. As a heat treatable alloy, this stress distribution is similar to the one observed for the specimen in Section 3.3.5.1, which further supports the explanation for the different stress distribution observed for the AA5754-H24 specimen.

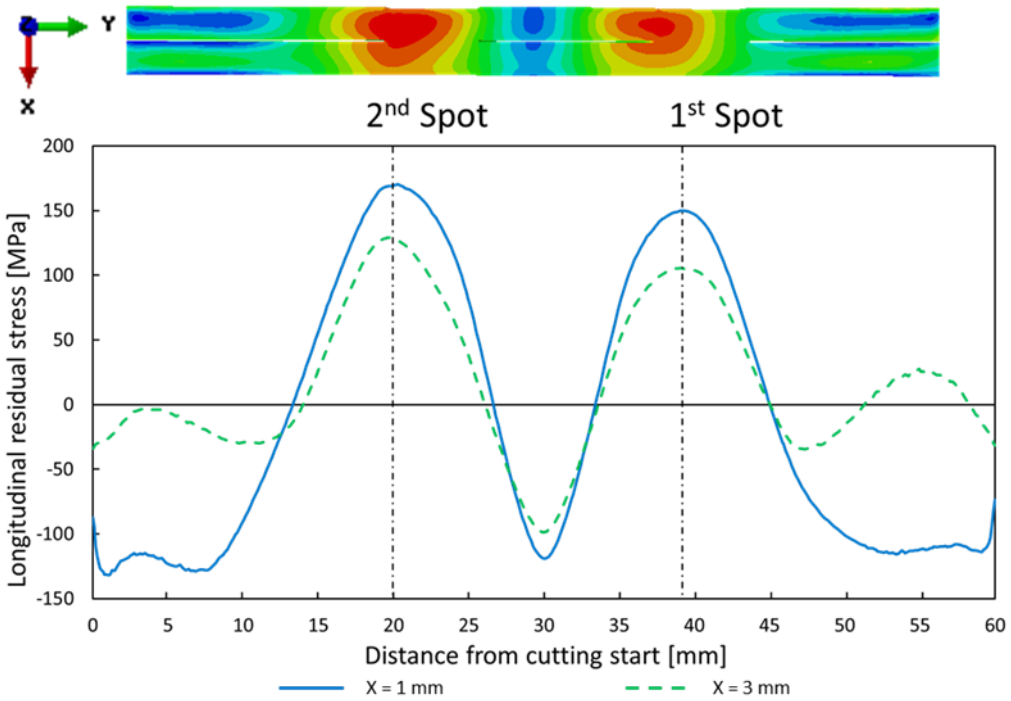

Figure 3.59 - Line plot of residual stress distribution across two rows on an AA7075-T6 multiple spot-weld specimen at specified thicknesses.

Contrary to the previously presented data for the double spot-weld specimens, the compressive stress value between the spot-welds was considerably similar to the value observed for the single spot-weld specimen. This leads to the conclusion that, for this alloy, the selected distance between spot-welds allows for the stress profile to fully stabilise without truncating any of the profiles. The finite element model of the residual stress distribution across the width of a multi spot-weld specimen is depicted in Figure 3.60. As performed in previous sections, the specimen was cut through the centre of the second spot-weld of each column.

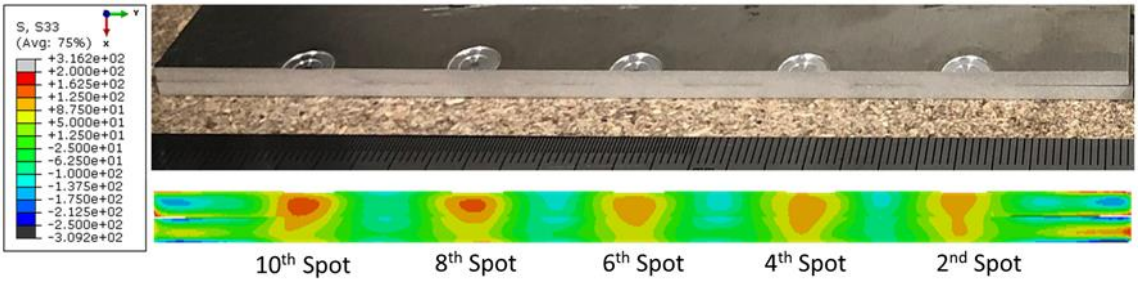

Figure 3.60 - 3D FEM model of the residual stress distribution across the five columns of the top row on an AA7075-T6 multiple spot-weld specimen (values presented in MPa).

The stress distribution is similar to what was previously observed for the specimen in Section 3.3.5.1, with the peak stress values being observed at the centre of the spot-weld on the top sheet. In the analysed spot-weld arrangement, similar stress distributions can be observed across

all spot-welds, with a continuous increase in the peak tensile stress value of each spot-weld. The highest tensile stress value was observed on the 10th spot and an explanation for this phenomenon has been previously presented.

The longitudinal residual stress plot from the two measurement lines across the mid-thickness of both sheets is presented in Figure 3.61. The stress profile is fairly uniform along the thickness and length of the specimen, except at the edges of the specimen where the opposite stress distribution between the two profiles was registered. An overall greater residual stress value was recorded on the top sheet due to a higher peak temperature and degree of recrystallisation. Similar behaviour to the double spot-weld specimen was observed with the peak tensile stress values increasing with the number of spot-welds.

Peak tensile stresses ranged between 107.9 and 142.6 MPa, corresponding to the 2nd and 10th spot-weld, respectively. These values are equivalent to 21.1 % and 27.8 % of the parent material yield stress, respectively. Comparing with the peak tensile stress observed on the single spot-weld specimen, a decrease of 51.5 % and 35.9 % was measured for the 2nd and 10th peak tensile spot-weld, respectively. The greatest percentage variations in the stress value between the two profiles were measured between the 4th and 6th spot-weld and at the centre of the 8th spot-weld, with a variation of 49.9 % (compressive) and 49.2 % (tensile).

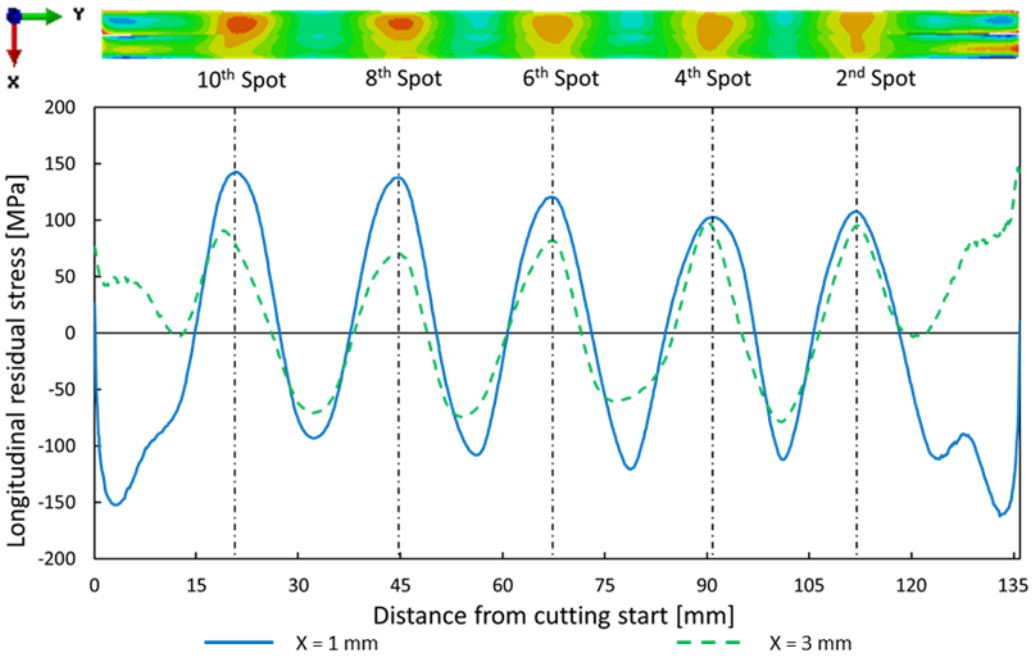

Figure 3.61 - Line plot of residual stress distribution across the five columns on an AA7075-T6 multiple spot-weld specimen at specified thicknesses.

For the first spot-welds, the peak tensile and compressive stresses on the bottom sheet are fairly uniform and aligned with the profile from the top sheet. However, due to an increase in the tool temperature, a significant increase on the tensile stress values of the top sheet was observed. Similar patterns were observed for the peak compressive stress values between the spot-welds, with a continuous decrease in the compressive stress values as the number of spot-welds increases.

3.4 Conclusions

In this investigation, RFSSW of AA2024-T3, AA5754-H24 and AA7075-T6 with a thickness of 2 mm was performed. Rotation speed and plunge depth values were varied to determine the most promising process parameter combination based on lap shear strength, cross tension strength and weld cross-section analysis. Further experiments, such as fatigue testing and residual stress measurements, were carried out on specimens produced using the optimised process parameter combination. The following conclusions can be drawn from the present investigation:

- Within the process window explored, RFSSW lap shear strength values in bare condition varied between 5.56 and 8.59 kN for AA2024-T3 welds, 4.93 to 7.16 kN for AA5754-H24 and between 6.03 and 9.10 kN for AA7075-T6 welds. These results surpassed the minimum strength requirements for resistance spot welding defined by AWS D17.2/D17.2M:2019.
- RFSSW lap shear strength values in bare condition of AA2024-T3 and AA7075-T6 were closely matched with an equivalent AA2024-T31 solid rivet.
- The ANOVA tables allowed to quantify the contribution of the RFSSW process parameters on the lap shear strength of the joints. For both alloys, plunge depth was the dominant process parameter with a contribution between 74 %, 62 % and 79 % for AA2024-T3, AA5754-H24 and AA7075-T6, respectively.
- For the alloys used in this investigation, weld lap shear strength was improved with low rotation speed and high plunge depth values. Increasing plunge depth increases the welded area and promotes better bonding at the weld interface. Lower rotation speed values contribute to a lower heat input weld which reduces coarsening and over aging of the strength precipitates.
- The typical microstructure and metallurgical features of RFSSW were observed on all welds, evidencing a fine and recrystallized grain structure in the centre of the weld. Despite the high

hook height, failure mode under lap shear testing was consistent with effective joining of the SZ/TMAZ interface.

- For the high strength alloys, AA2024-T3 and AA7075-T6, a process parameter boundary was determined for low plunge depth and rotation speed values. These conditions led to the formation of internal voids due to low heat input conditions and poor flowability of the material during the refilling stage.
- Fatigue test results were used to establish an equation for the S-N curve. Good fitting coefficients were correlated for each test condition. Stress concentration from out-of-plane bending promoted crack development at the hook and early failure of the bare specimens.
- Residual stress measurements were performed using the contour method on a bare multiple spot-weld specimen and single spot-weld specimen. Peak tensile stresses were always found at the centre of the spot-weld on the top sheet with values bellow the yield strength of the parent material.
- For heat-treatable alloys, the maximum tensile stress value decreased as the number of spot-welds increased. This trend was not observed for the strain-hardened alloy.

RFSSW of AA2024-T3 and AA7075-T6 in the presence of an aerospace grade sealant was performed to determine the influence of an interfacial sealant on the mechanical properties and weld microstructure. The following conclusions can be drawn from the present investigation:

- Under lap shear conditions, the presence of an interfacial sealant improved the shear strength value by 44 % and 51% for AA7075-T6 and AA2024-T3, respectively.
- The opposite trend was observed under cross tension conditions, where the presence of an interfacial sealant decreased the strength values by 3 % and 19% for AA7075-T6 and AA2024-T3, respectively.
- The presence of an interfacial sealant improved the fatigue life under all loading levels on both alloys, surpassing the first million cycle threshold under the lower load condition.
- The performance improvement observed under shear and fatigue conditions can be attributed to the adhesion from the sealant at the edge of the specimen. The sealant restricts sheet separation, preventing the generation of peeling stress at the hook region and fretting damage.

- The thin layer of sealant at the weld interface influences the stirring efficiency and consolidation of material in this area, decreasing the strength under cross tension loading.

Chapter 4

RFSSW tool material evaluation

This chapter compares a range of relevant materials that could be used to produce RFSSW tool components based on their performance, influence on the microstructure and preliminary wear analysis. The knowledge gathered from this investigation will provide an indication of the most appropriate tool material to use as a replacement for the current WC-Co RFSSW tool material supplied by KHI.

4.1 Introduction

In all third body friction welding technologies, the tool has a significant impact on the performance and efficiency of the joining process (Mehta et al. 2011; Rai et al. 2011). Different tool materials have different physical properties that can influence the heat generation process as well as the heat conduction from the weld area to the tool body. This can lead to changes in the mechanical performance and microstructural properties of the weld. An appropriate material selection considering the stress that the tool will be subjected while in service can ensure its longevity and prevent catastrophic failures (Buffa et al. 2012; Liu et al. 2018).

4.2 Materials and methods

4.2.1. Base material

The base material chosen was AA7050-T7451 which is a high strength heat treatable aluminium alloy used extensively in aerospace structural applications. This alloy is known to have a detrimental effect on the tool life due to the high flow stresses and pressures during friction stir welding. For this study, the base material was provided in plate form with the dimensions 200x400x25 mm. The chemical composition and mechanical properties are shown in Table 4.1 and Table 4.2, respectively.

Table 4.1 - Chemical composition of AA7050-T7451.

Element [Weight %]	Si	Fe	Cu	Mn	Mg	Zn	Cr	Ti	Al
AA7050-T7451	0.12	0.15	2.3	0.1	2.3	6.2	0.04	0.06	remainder

Table 4.2 - Mechanical properties of AA7050-T7451.

Hardness [HV]	162
Ultimate Tensile Stress [MPa]	524
Yield Tensile Stress [MPa]	469
Elongation at Break [%]	11

4.2.2. Tool materials/surface treatment combinations

Like the conventional FSSW, during the RFSSW process the tool is mainly subjected to compression stresses at temperatures reaching approximately 85% of the melting temperature of the base material (Zhao et al. 2016). Also, significant wear and other degradation phenomena can arise due to the continuous friction coupling between the tool and the base material. The essential and desirable properties for a RFSSW tool material are summarised in Table 4.3.

Table 4.3 - Properties of tool materials.

Essential properties	Desirable properties
Sufficient high temperature strength	Oxidation resistance
Wear resistance at ambient and service temperatures	Established material
Fracture toughness at ambient and service temperatures	Low toxicity
Machinability	Affordability
Stable microstructure at service temperature	Availability
Inert to workpiece at service temperature	Thermal fatigue

In this investigation, three different materials were selected based on their physical properties and previous uses in friction stir welding applications:

- M42 High speed tool steel;
- MP159 multiphase alloy; and
- Silicon Nitride (Si_3N_4).

Table 4.4 shows the chemical compositions of the selected materials. The composition of Si_3N_4 is not present since the material is entirely composed of this chemical compound.

Table 4.4 - Chemical composition of metallic tool materials.

Element [Weight %]	Co	Cr	Fe	Mo	C	V	W	Ni	Ti	Cb	Al
M42	8	3.9	remainder	9.4	1.1	1.2	1.5	-----	-----	-----	-----
MP159	35.7	19	9	7	-----	-----	-----	25.5	3	0.6	0.2

M42 belongs to the cobalt molybdenum series of tool steel that is commonly used to produce cutting tools and applications that require hot hardness due to its good balance between toughness and hardness (ASM International, 1989). In its annealed form it is easily machinable material and its extensive use in industry makes it an easily obtainable material at a relatively low cost. MP159 is a Co-Ni-Cr multiphase alloy with ultra-high strength, ductility and corrosion resistance at elevated temperatures (Davis, 2000). It is used in various industries under demanding environments such as high temperature fasteners, components for jet engines and marine applications. It is a reasonably machinable material in the annealed condition with a high relative cost and reasonable market availability. Si_3N_4 is part of the flexible and machinable engineering ceramics branch (AZOM, 2001). Characterised by high strength, toughness and hardness and excellent chemical and thermal stability, the aim was to replace metals with

ceramics in high service temperature applications. Due to its high manufacturing cost, Si_3N_4 is currently used in niche market applications for example in reciprocating engine components and turbochargers, bearings, metal cutting and shaping tools and hot metal handling. Table 4.5 presents the physical properties of the materials used in this investigation.

Table 4.5 - Physical properties of selected tool materials.

	M42	MP159	Si_3N_4
Density [Kg/m^3]	7.9	8.4	3.3
Modulus of Elasticity [kN/mm^2]	200.0	234.0	310.0
Thermal Conductivity [W/m °C]	28.0	11.2	30.0
Coefficient of thermal expansion [10^{-6}/ °C]	11.5	14.9	3.3

To determine if improvements in tool life and overall performance could be gained by the use of surface engineering/coating techniques, surface treatments were applied to M42 and MP159 specimens as shown in Table 4.6. For components where resistance to wear and galling is important, the use of plasma nitriding in high alloyed steels can be beneficial as the release of active nitrogen into the surface of the steel generates a layer that increases the surface hardness of the material. A suitable surface treatment for the MP159 was identified and applied based on previous research conducted by TWI. Consisting on low temperature diffusion of large quantities of carbon and/or nitrogen into the surface, this surface treatment improves wear resistance, strength and resistance to galling. The exact process details are confidential property of the company. The process parameters for both surface treatments were adjusted to treat the material up to a depth of 100 µm.

Table 4.6 - Designations for tool materials and surface treatment combinations

Tool Materials	M42		MP159		Si_3N_4
Surface treatment	Hardened and tempered	Hardened, tempered and Plasma Nitriding (PN)	Hardened	Hardened and Surface engineered	------
Designation	HT	HT+PN	H	H+SE	Si_3N_4

4.2.3. Specimen Geometry

The tool materials were supplied as round bar in annealed condition. This enabled machining to size prior to heat treatment and surface treatments. Tool material test specimen geometry is presented in Figure 4.1. The present design aimed at simplifying the machining operations, while replicating the dimensions of the plunging area of the shoulder (which are the key features governing the stage 1 and 2 of the RFSSW process. To machine Si_3N_4, dedicated tools are required which would increase the total cost of the component. Therefore, to reduce the lead time and

costs of each specimen, only the plunging region was machined to match the dimensions of the shoulder.

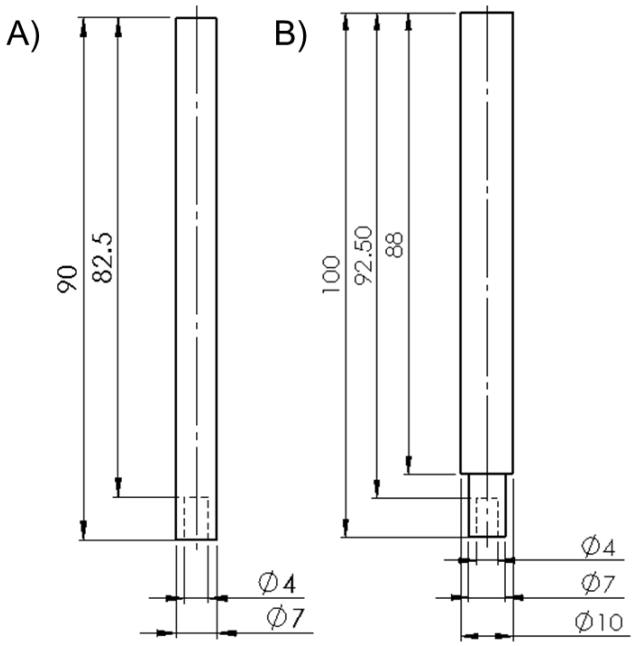

Figure 4.1. Tool material test specimens: A) M42 and MP 159 and B) Si_3N_4.

4.2.4. Plunging procedure

The stage 1 and 2 of the RFSSW, dwell and plunging stage respectively, are the stages that impose the greatest amount of wear and stresses on the tool. As the heat to plasticise the material ahead of the tool has not been generated yet, this leads to higher flow stresses between the tool and the base material. A RFSSW cycle consisting only of the stage 1 and 2 of the process will be hereinafter referred to "plunge cycle" and an array of plunge cycles will be hereinafter referred to "plunge trials". For each plunge cycle, no weld is produced since the process only displaces and processes the material around the tool, creating a protruding feature as shown in Figure 4.2.

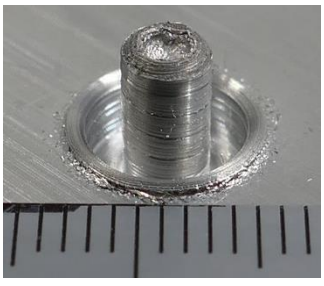

Figure 4.2 - Protruding feature produced during the plunge trials.

Considering the shape of the specimens used in this investigation, a conventional FSW machine without traverse motion is suitable to replicate the stage 1 and 2 of the RFSSW weld cycle.

Figure 4.3 shows the machine used to perform the experiments, TWI's FW-36 AWEA LP 4025Z. This machine is a based on a gantry type CNC milling machine, which has been fitted with recording instruments to monitor rotation speed, plunge speed and depth, as well as tool axial and side force.

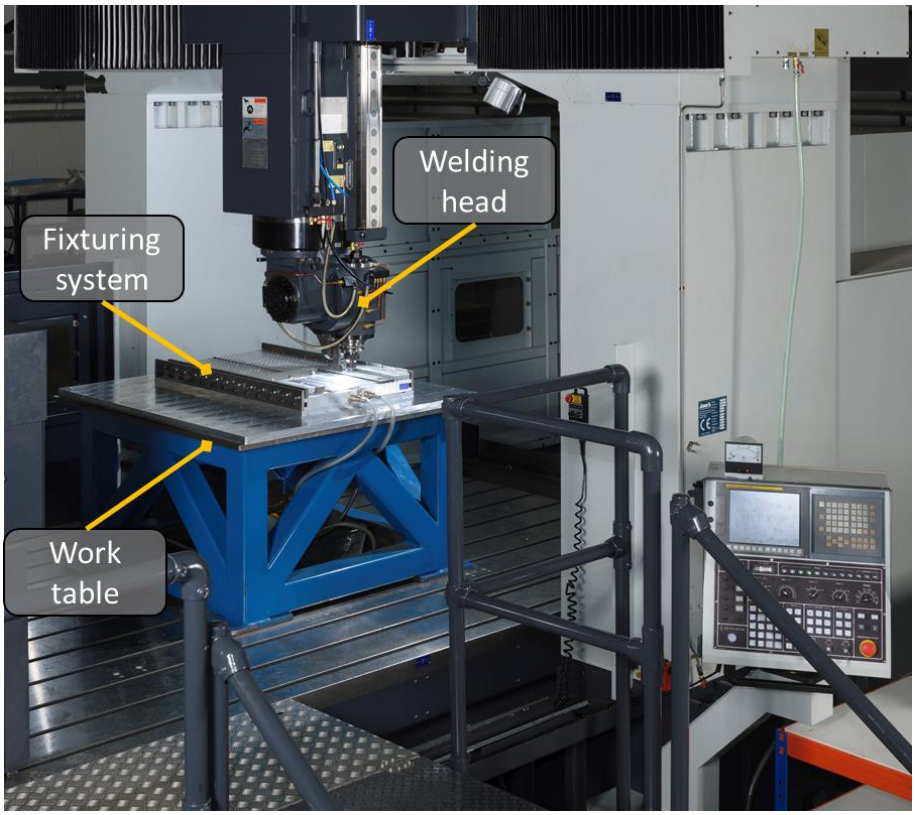

Figure 4.3 - FW-36 AWEA LP 4025Z FSW machine.

Plunge trials were performed in position-control, using the best effort process parameters obtained from Chapter 3. However, due to frequent clogging of material inside the tool, a shallower plunge depth of 2.0 mm was later selected. Clogging was one of the most significant issues found in this investigation and will be addressed in further detail later in this chapter. Table 4.7 presents the process parameter combinations used in this investigation.

Table 4.7 - Process parameters

Rotation speed [Rev/min]	1000.0
Plunge depth [mm]	2.0
Dwell time [s]	2.0
Plunge rate [mm/min]	54.0
Retraction rate [mm/min]	750.0

Before initiating the first plunge trial sequence, the top surface of the base material plate was skimmed to remove surface oxides and contaminants. Plunge trials consisted of 9 plunge cycles

in a row along the width of the plate, with the first plunge being located 15 mm from the edges and the subsequent plunges being separated by 20 mm intervals. In order to maintain a stable tool temperature and minimise the likelihood of clogging, three consecutive rows were performed followed by rapid water cooling to ambient temperature. This procedure was repeated up to the end of the plate, in a total of 16 rows, until a tool inspection milestone was reached or until the tool became clogged.

After the 16th row was completed, a 2.2 mm layer of material was milled from the base material plate to remove the previous features and level the base material sample. This was performed until a minimum plate thickness of 12 mm was reached or excessive bowing of the plate was observed due to the thermal and machining stresses generated on the top side of the plate.

Once the tool became clogged, plunge trials were ceased and the tool was removed. This was to ensure that no premature failure of the tool specimen would occur as a result of the excess material inside the tool and to continue to replicate the material movement around the tool observed during RFSSW in every plunge. The clog was removed from the specimen using a 3.8 mm diameter drill and a 4 mm rimer on a manual lathe, endeavouring to preserve the external surfaces of the tool. The tool inspection procedure will be described later in the following section.

4.2.5. Characterisation techniques

Prior to conduct an inspection of the tool external surfaces, the specimens were dipped in a solution of sodium hydroxide (NaOH) for a maximum period of 4 hours. This was performed to remove the aluminium layer that adheres to the tool contact surfaces. To determine the wear of the tool throughout the plunge trials, tool test specimens were measured using an Alicona InfiniteFocus SL 3D surface profilometer. Analysis was performed using the associated IF Measure Suite software. This procedure was initially performed every 150 plunges up to 450 plunges, following an analysis at 750 plunges and at 2000 plunges. The affected surface of the tool was also inspected for cracks using a Zeiss EVO LS15 SEM.

Metallographic specimens of the protruding features were sectioned, polished and etched with Keller's reagent for microstructural analysis. Optical microscopy was conducted using an OLYMPUS GX71 inverted geometry optical microscope with a Colorview III camera.

Thermal measurements on single and nine-consecutive plunges specimens were performed to understand the variation of peak weld temperature across multiple spots. To record the thermal

cycle during the plunge cycle and measure the maximum temperature at the vicinity of the plunge zone, two Type-K thermocouples were embedded in the aluminium plate at a depth of 2 mm and a distance of 1 mm from the edge of the tool. Temperature measurements were recorded at 100Hz using a calibrated Ni 9213 digital acquisition module and processed using Ni Express 2015 software.

4.3 Results and discussion

4.3.1. Performance

Si_3N_4 has been used previously in friction stir welding for high temperature applications. Ahn et al. (2012) examined the microstructural and mechanical properties of 409L stainless steel with a thickness of 3 mm when friction stir welded using a Si_3N_4 tool. Sound welds were produced with similar mechanical strength to the base material. Kim et al. (2014) compared the performance of a high cost polycrystalline cubic boron nitride (PCBN) tool with a lower cost Si_3N_4 tool for friction stir welding of 1.4mm DP590 steel sheets. Despite the similar weld mechanical performance to the base material, the Si_3N_4 tool life was around 5 m (half of the PCBN tool) with possible tool life improvements after welding conditions and tool design optimisation.

During the plunge trials, the two Si_3N_4 tool specimens presented significantly shorter lives than the other tool material candidates, registering only 92 and 2 plunges. Furthermore, a catastrophic and predominantly brittle fracture surface was observed on both specimens. The fracture surface of a Si_3N_4 tool specimen after 92 plunges is presented in Figure 4.4.

Figure 4.4 - Fracture surface of a Si_3N_4 tool after 92 plunges.

Considering the poor performance and reliability issues allied with its relative high cost and special machining requirements, Si_3N_4 was not considered a viable tool material alternative for RFSSW shoulder designs. No further testing or analysis was performed for this tool material.

A fundamental RFSSW tool material requirement to prevent unexpected tool failures is to minimise material adhesion to the tool surface, which can lead to clogging. The stages leading to the clogging of the tool specimens are shown in Figure 4.5. Like the formation of a built-up edge in cutting tools, as described by Song et al. (2017), clogging is promoted by the high temperatures and strain rates. These conditions lead to the interdiffusion between aluminium and the tool material, generating a thin layer of intermetallic compounds. These compounds on the inside wall of the tool specimen provide a nucleation site for additional layers of base material, promoting the continuous entrapment of the processed material. This could lead to the restriction of motion of the tool components during the welding process as well as liquid metal embrittlement of alloying elements as observed by Nasiri et al. (2018), causing catastrophic failures.

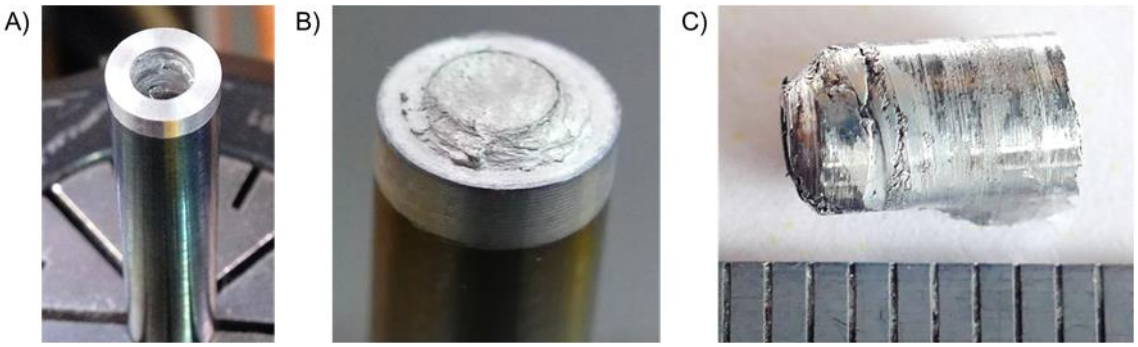

Figure 4.5 - Tool clogging stages: A) base material accumulation on the inside surface of tool specimen, B) fully clogged tool with a C) slug of material.

The performance of each tool material and surface treatment combination was evaluated based on the maximum number of consecutive plunges without clogging or chemical cleaning. The results from this analysis are presented in Table 4.8. The high temperature and pressure experienced by the tool material test specimens during the plunge trials can be compared to other manufacturing processes, such as extrusion of aluminium. Due to the high friction and wear of the die associated with this process, the extrusion dies, usually manufactured from tool steels such as AISI H13, undergo a nitriding process to increase their wear resistance. As described by Akhtar, Arif and Tilbas (2012), this process is repeated several times during the service life of the dies due to gradual decrease in thickness of the surface nitride layer. Once this layer decreases and exposes the hardened layer of the material, the affinity with aluminium increases.

Table 4.8 - Maximum number of plunges before clogging for each tool material and surface treatment combination.

Tool Material Surface treatment	Tool performance [*Maximum number of plunges before clogging*]
M42 HSS	
HT	508
HT + PN	150
MP159	
H	494
H + SE	100

As previously mentioned, clogging was observed in various occasions with all metallic tool materials used in this investigation. As shown in Table 4.8, a greater propensity for clothing was observed in both tool materials with surface treatment, when compared to the simple heat treated variant. This was an unexpected result considering that the purpose of the surface treatment was to produce the opposite outcome. An explanation for this phenomenon might be related to differences in surface energy or surface roughness between the specimen variants, which increased the affinity between the tool material and the base material.

4.3.2. Metallography

A typical cross-section of a protruding feature produced during the plunge trials is shown in Figure 4.6. Due to the similarity in microstructure and geometry, only the feature produced using a M42 HT tool specimen will be analysed. The hole on the bottom right-hand side of the picture shows the location where the thermocouple was inserted. The analysis of this feature can provide a greater understanding of the material microstructural changes and flow patterns at the end of the plunging stage of the RFSSW process. Other researchers have employed "stop-action" procedures to further understand the material flow at each stage as well as the formation of intermetallic compounds at the interface of dissimilar material welds (Reimann, Goebel and Dos Santos 2017; Suhuddin, Fischer and Dos Santos 2013 and Suhuddin et al. 2017). These procedures consist in stopping the weld cycle during or once the plunging stage has been completed and analyse the joint produced.

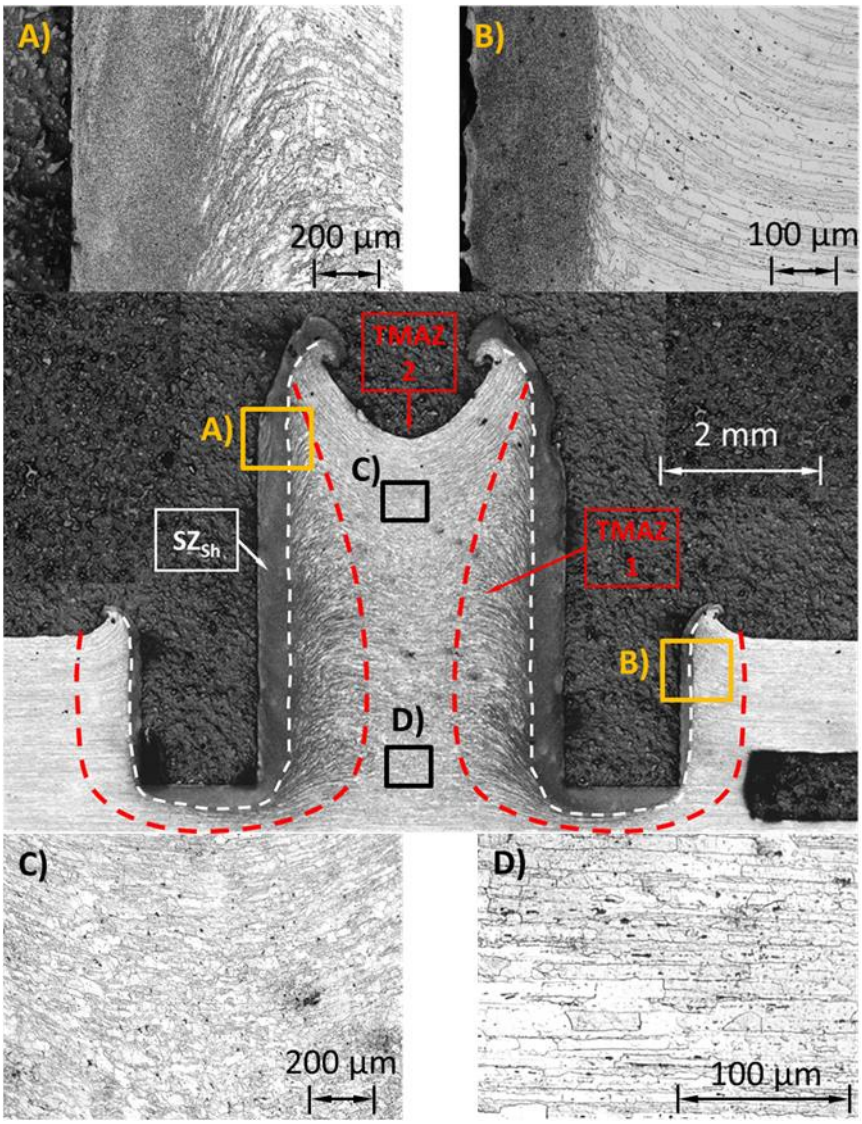

Figure 4.6 - Cross-section of a protruding feature produced with a M42 high speed steel hardened and tempered
A) SZ_{SH}/TMAZ 1 interface in protruding feature;
B) SZ_{SH} /TMAZ 1 interface in base material;
C) Top TMAZ 2;
D) Bottom TMAZ 2.

In this simplified scenario however, limited or no interaction between the surface of the tool specimen and the centre region of the protruding feature has occurred due to the absence of the probe element of the RFSSW tool. Also, due to the absence of a clamp ring, part of the displaced material by the shoulder was pushed outwards. This highlights the need for the clamping ring component in order to contain the displaced material within the weld area and promote a confined material flow during the plunge stage of the RFSSW cycle, thereby minimising material losses. Based on the microstructural changes, four different weld regions can be identified: the stir zone produced by the shoulder (SZ_{SH}), the thermo-mechanically affected zone 1 (TMAZ 1), the

thermo-mechanically affected zone 2 (TMAZ 2) and the unaffected base material. The SZ_{SH} is the volume of material in direct contact with the rotating surface of the shoulder, which is located at the periphery of the protruding feature, side and bottom of the indent mark left by the shoulder. Some of the simulation work carried out by Zhao et al. (2016) is shown in Figure 4.7. The outcome of their investigation shows that this area, during the plunge stage, exhibits both the highest temperature and peripheral velocity. The combination of intense heat and plastic deformation leads to dynamic recrystallisation producing a fine and equiaxed microstructure, as shown in Figure 4.6.A) and B).

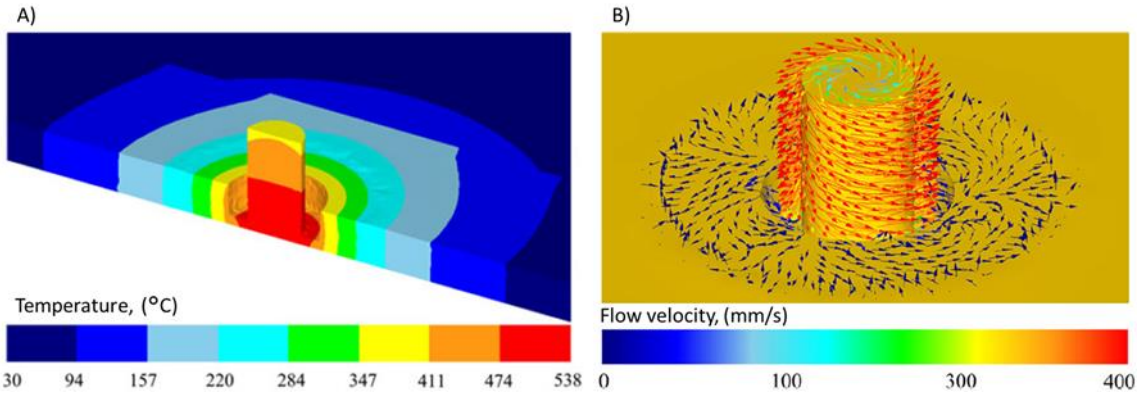

Figure 4.7 - A) Temperature and B) Material flow velocity simulations during the plunging stage of the RFSSW (Zhao et al. 2016).

As observed in Figure 4.7.B), the peripheral velocity naturally decreases towards the centre as the influence from the contact area is less noticeable. This leads to a gradient of microstructural changes, producing two TMAZ regions with different grain sizes and orientation. The TMAZ 1 is the region adjacent to the SZ_{SH} which, due to the lower temperature and plastic deformation, does not undergo dynamic recrystallisation. The TMAZ 2 is the region of material at the centre of the protruding feature that has been pushed upwards as a reaction to the plunging motion of the shoulder.

The TMAZ 1 is characterised by distorted grains due to the upward viscoplastic flow during the plunge stage. The grain alignments observed in Figure 4.6.A) and B) are consistent with the material flow model proposed by Shen et al. (2020). The material from the bottom surface of the shoulder progresses predominantly inwards and upwards while the shoulder moves downwards. This symmetrical movement of material generates a concave surface at the top of the protruding feature, like the joint line remnant shape observed in the study conducted by Shen et al. (2018). In their study, the authors proposed that the explanation for this phenomenon was the

compression effect from the probe. However, in this investigation the material was not restricted by any surface during the plunge of the shoulder and similar results were observed. This seems to suggest that the shape of the joint line remnant is predominantly, if not exclusively, dictated by the motion of the shoulder and could possibly be influenced by different shoulder geometries and features.

Within the TMAZ 2 different grain sizes and alignments can be observed, caused by the temperature and plastic deformation gradients. The upper and lower regions of the core of the protruding feature are shown in Figure 4.6.C) and D), respectively. The grain morphology and alignment from the lower regions of the TMAZ 2 are similar to the base material, as shown is Figure 4.6.D), due to the negligible interaction between the tool and the base material. Internal voids of small scale can be observed in Figure 4.6.C), which can be explained by the absence of the probe element of the RFSSW tooling (which would, in nominal conditions, contribute to ensure the consolidation of material as its being extruded). Smaller size and distorted grains can be observed at the upper regions of the feature due to the increased influence of the upward peripheral material flow.

4.3.3. Temperature measurements

The peak temperatures recorded for each tool material candidate for a single spot and a multiple spot specimen are shown in Table 4.9. The temperatures recorded for all settings are substantially lower than the tempering temperature of both tool materials. However, the measurements were taken 1 mm away from the tool/base material interface where the temperature values are significantly higher and local melting of secondary phase particles and eutectic films is likely to occur as observed by other authors (Gerlich, Yamamoto and North 2008; Horie et al. 2010 and Zhao et al. 2018-B). The long exposure of the tool materials to these temperatures can lead to over-tempering and reduce the hardness as observed by Nasiri et al. (2018).

Table 4.9 - Peak temperature values registered for each tool material and surface treatment combination for the single and multiple spot specimens.

Tool material	Single spot	Multiple spot 1st	Multiple spot 9th
Surface treatment	Peak temperature [°C]	Peak temperature [°C]	Peak temperature [°C]
M42			
HT	190.39	187.09	261.33
HT + PN	215.79	176.94	241.57
MP159			
H	189.86	178.11	243.88
H + SE	186.42	186.73	276.05

From an energetic balance point of view, there are various variables that can influence the temperature during the welding process as explained by Su et al. (2006). In their work, the authors suggest that the effective energy released from the tool rotation is the difference between the heat generated by the tool and the associated heat losses. Heat dissipation sources include energy losses to the surrounding atmosphere, to the clamping and fixturing system, conductive heat loss through the sheets as well as through the tooling components. Consequently, the choice of tool material can have a direct impact on the weld mechanical performance and microstructural changes. The tool materials chosen for this experiment have both low values of thermal conductivity, with MP159 being the least thermally conductive of the two, as shown in Table 4.5.

The thermal profiles for the single spot and multiple spot are presented in Figure 4.8 and Figure 4.9, respectively. The heat propagation from the various plunge cycles can be seen by the multiple peaks observed in Figure 4.9. Based on the data gathered from Table 4.9, Figure 4.8 and Figure 4.9, no correlation between the thermal conductivity coefficients of the various tool materials and the peak temperature values can be observed. In fact, the thermal behaviour is similar across all tool materials apart from the temperature profile for the M42 HT+PN single spot specimen. However, upon analysis of the cross-section, this difference in profile is explained by the collapse of the thermocouple hole, as seen in Figure 4.10.

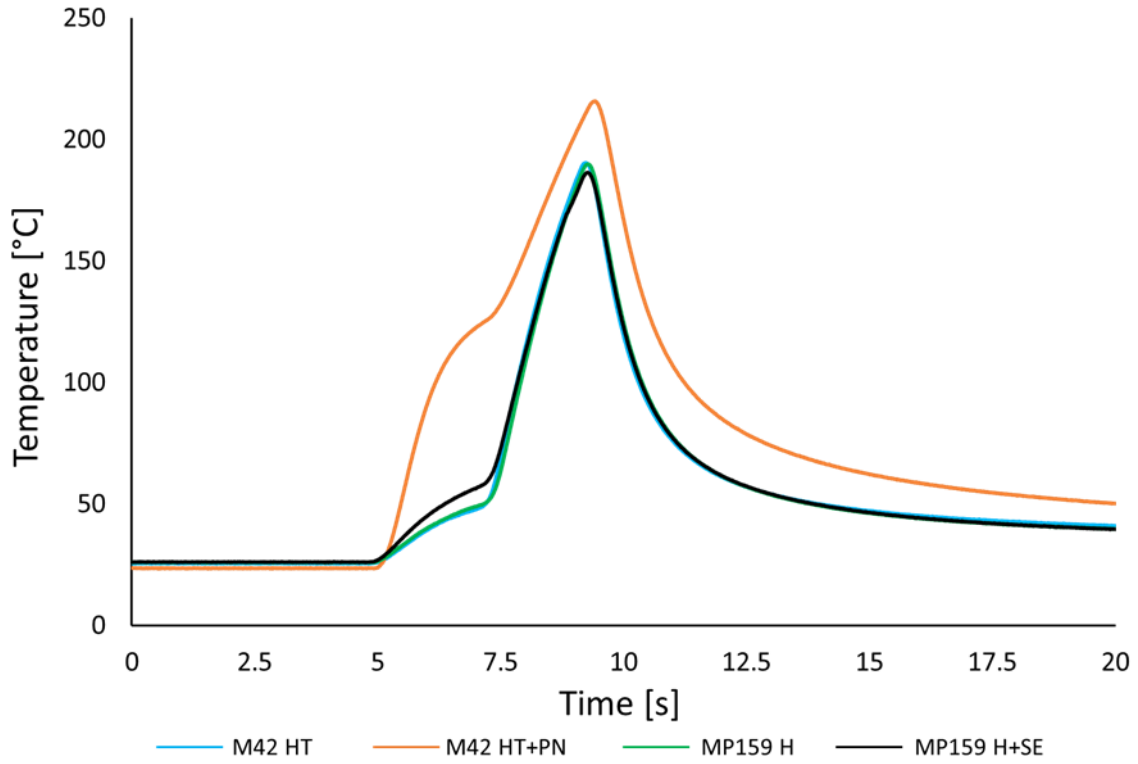

Figure 4.8 - Temperature measurement plot for the single spot specimen.

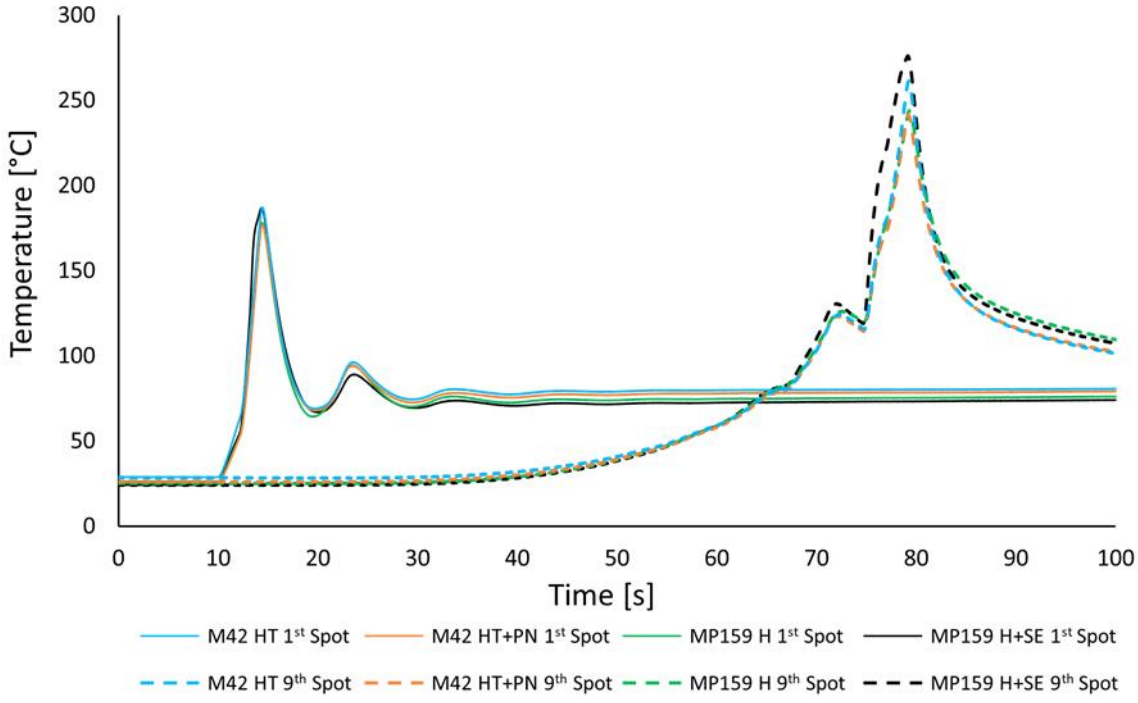

Figure 4.9 - Temperature measurement plot for the multiple spot specimen.

One explanation for this observation, as described by Threadgill et al. (2009), can be the fact that the heat generation in FSW relies on the interaction of various factors, including the process

parameters, the parent material and the tool design. The same reasoning is valid for the multiple variants of the process, like RFSSW. This makes the calculation of the effective heat input a complex task, compared to processes using an external heat source. Nevertheless, considering this scenario where the setup for each tool material was nearly identical between experiments, a more reasonable explanation could be the short plunge cycle times which limits the actual interaction of the tool surface with the base material. This observation coupled with a varying stick-slip contact condition between the tool surface and the base material, limits the peak temperature of the weld cycle and maintains a self-stabilising behaviour.

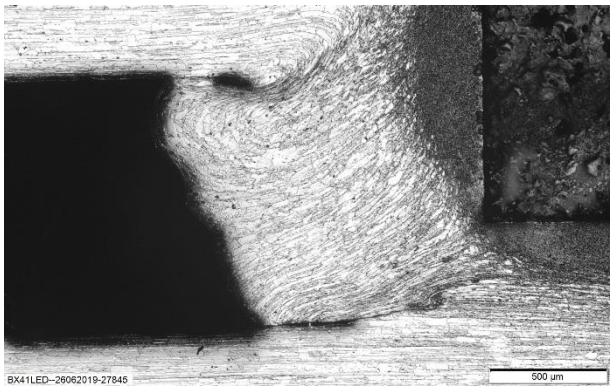

Figure 4.10 - Collapsed thermocouple hole in the M42 HT+PN single spot specimen.

4.3.4. Wear characterization of shoulder component

Monitoring tool wear is an essential task for all FSW process variants to ensure consistency in tool performance and weld quality. Severe tool wear can lead to internal defects, such as inclusions of solid particles from the tool body, which can compromise weld integrity and surface quality (Farias et al. 2013; Lacki, Więckowski and Wieczorek 2015). This has been observed by various researchers while producing FSW joints in abrasive parent materials (Fernandez and Murr 2004; Prado et al. 2003; Shindo, Rivera and Murr 2002; Wang et al. 2014), leading to a "self-optimisation" of the tool profile. "Self-optimisation" is a term introduced by the previous authors describing a stage of the tool life when, after an initial period of wear, the new tool geometry experiences negligible wear rates. If this condition is not achieved, as reported by Montag et al. (2014), the continuous wear of the tool can lead to increase in process temperature, deviation from the zeroing-reference point and lead to surface defects such as burrs at the periphery of the tool area. Additionally, the reduction in radius increases the clearance-fit between the tool components, leading to material entrapment in this area.

The wear measurements recorded during the plunge trials on the tool material specimens are shown in Figure 4.11. A reduced set of data points is presented for both surface treatment specimens due to persistent clogging. Despite the similar wear performance, a marginally higher reduction in radius was observed on the MP159 H tool specimen in comparison with the M42 HT tool specimen. This was an unexpected result considering that MP159 is commonly used in FSW as the probe tool material due to its stable material properties and wear resistance under high temperature and pressure conditions. However, similar observations were also reported in the study conducted by Więckowski et al. (2019). Despite the limited sample points, a tool geometry self-optimisation trend was not observed in the current study as continuous wear on both tool specimens was measured.

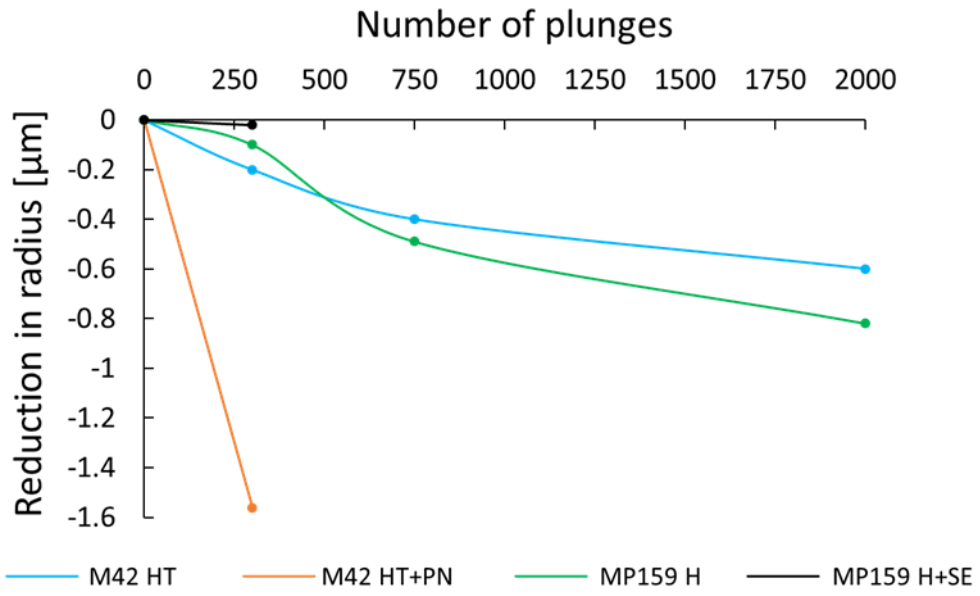

Figure 4.11 - Plot of wear measurements of the tool material specimens.

The SEM analysis of the M42 HT tool specimen after 300 and 2000 plunges is shown in Figure 4.12 and Figure 4.13, respectively. The specimens from this material initially presented remnants of turning marks on the surface, as observed in Figure 4.12.D) and Figure 4.13.D). After 300 plunges, signs of sliding wear can be observed in Figure 4.12.B) by the smooth surface close to the bottom of the specimen. This effect becomes greater after 2000 plunges with some tool surface degradation as observed in Figure 4.13.B). Figure 4.12.C) shows the bottom edge of the tool specimen which is in contact with the highest temperature region during the plunge cycle. This area shows minor outward deformation, commonly referred to as “mushrooming”, which is likely caused by tool material over-tempering leading to a local reduction of the original hardness value.

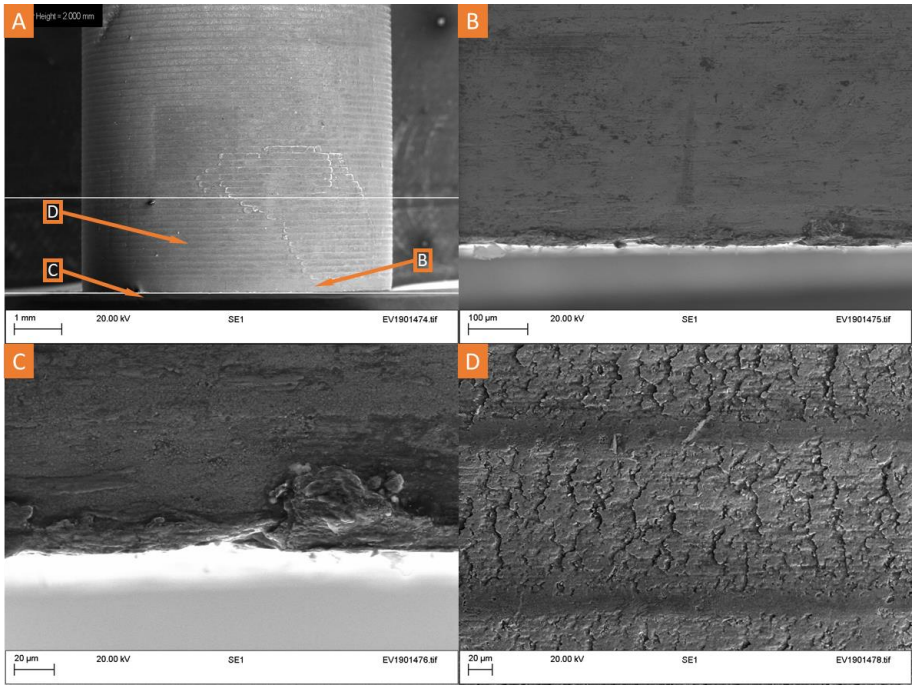

Figure 4.12 - SEM analysis of M42 HT specimen after 300 plunges;
A) Contact surface of the tool specimen;
B) High magnification region – location shown in Figure 4.12.A);
C) High magnification region – location shown in Figure 4.12.A);
D) High magnification region – location shown in Figure 4.12.A).

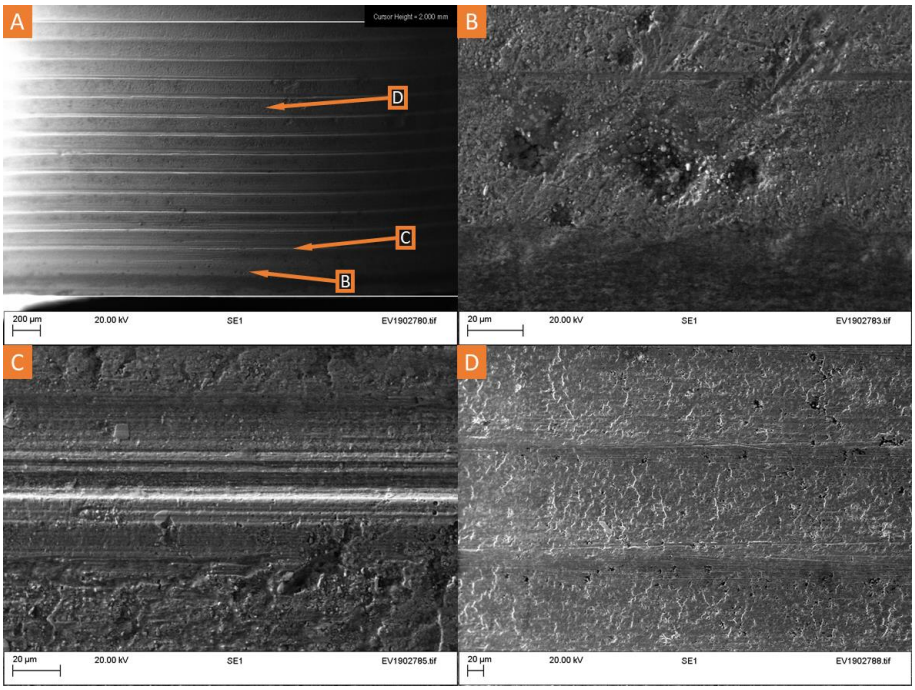

Figure 4.13 - SEM analysis of M42 HT specimen after 2000 plunges;
A) Contact surface of the tool specimen;
B) High magnification region – location shown in Figure 4.13.A);
C) High magnification region – location shown in Figure 4.13.A);
D) High magnification region – location shown in Figure 4.13.A).

The SEM analysis of the MP159 H tool specimen after 300 and 2000 plunges is shown in Figure 4.14 and Figure 4.15, respectively. In this tool material, a small discoloration can be seen in Figure 4.14.A) at the contact surface area. This allied with the smooth surfaces are signs of sliding wear in this area. No cracks or severe tool degradation were visually identified during the course of this investigation as opposed to the M42 HT tool specimen. This could be related to the multiphase crystalline structure present in this material which impedes the motion of dislocations and provides its high strength properties (Davis 2000).

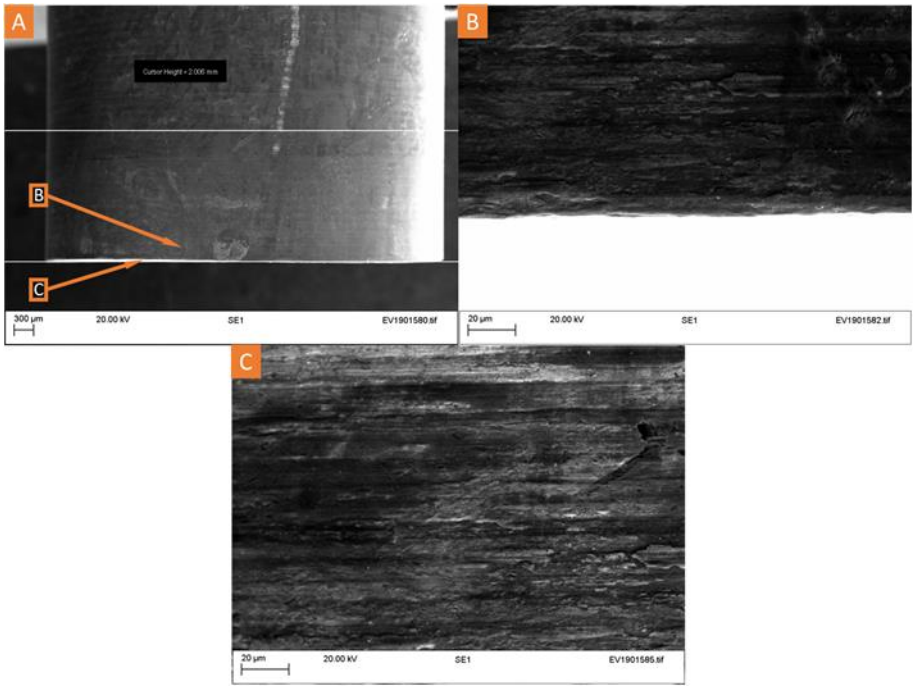

Figure 4.14 - SEM analysis of MP159 H specimen after 300 plunges;
A) Contact surface of the tool specimen;
B) High magnification region – location shown in Figure 4.14.A);
C) High magnification region – location shown in Figure 4.14.A);

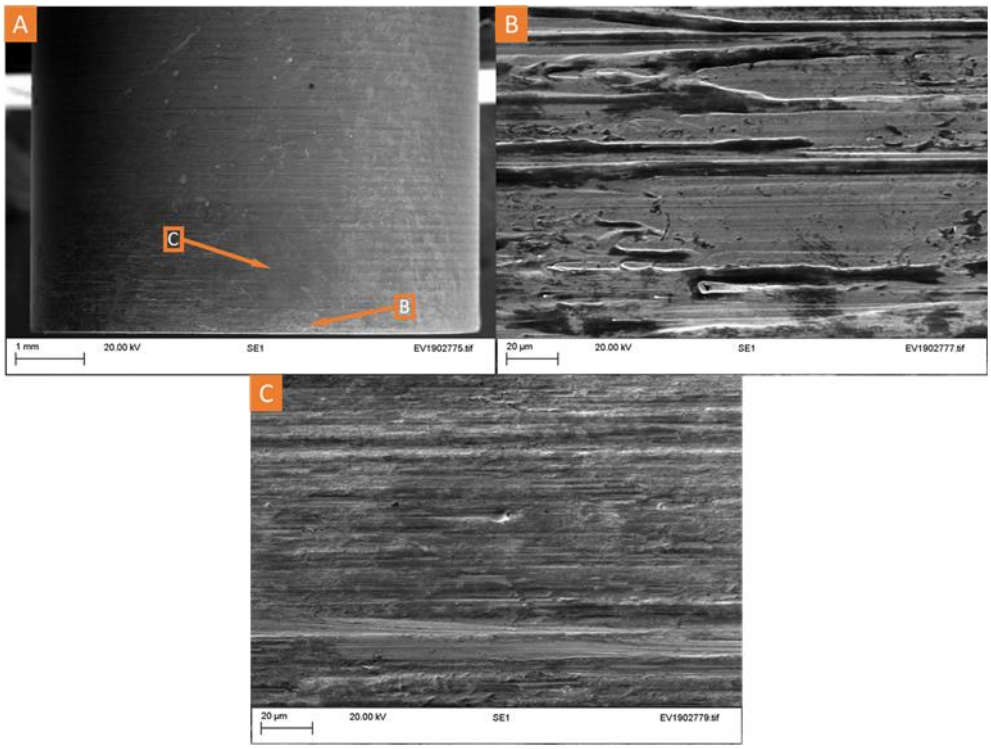

Figure 4.15 - SEM analysis of MP159 H specimen after 2000 plunges;
A) Contact surface of the tool specimen;
B) High magnification region – location shown in Figure 4.15.A);
C) High magnification region – location shown in Figure 4.15.A);

4.4 Conclusions

The aim of this investigation was to identify alternative tool material candidates for RFSSW. Rod specimens of M42 high speed steel, MP159 multiphase alloy and silicon nitride were selected considering their suitability for FSW. Plunge trials were conducted using a conventional FSW machine to simulate the stresses on the tool during service conditions. Performance and microstructural analysis coupled with thermal and wear measurements were carried out to evaluate the suitability of each material for RFSSW. The following conclusions can be drawn from the present investigation:

- Due to the poor reliability and short life observed in the silicon nitride tool specimens, this material cannot be considered as a suitable alternative for RFSSW tooling components. Additionally, the high material costs and special production considerations could potentially make this material less viable economically for in a production scenario.
- During the plunge trials, tool fracture was only observed for the silicon nitride specimens. The catastrophic failure of both tool specimens occurred in a predominantly brittle fracture, as expected given the nature of the material.

- Surface treatments on the metallic specimens increased the affinity between the tool specimens and the base material, leading to the more frequent occurrence of clogging. Due to extra cost of the treatment and the detrimental effect on performance, further investigation was not performed to explain this phenomenon.
- The protruding features produced by the different tool materials exhibited similar grain morphology and alignment. The plastic deformation and temperature gradient in different areas of the feature evidenced the presence of different microstructural regions and material flow patterns during the plunging phase.
- Temperature measurements were performed for all metallic tool material candidates in a single and multiple spot specimen analysis. Similar temperature profiles and values were observed across all specimens, despite the difference in thermal conductivity properties.
- Wear measurements were performed on all metallic tool materials, with limited data on the surface treated specimens due to persistent clogging. M42 HT and MP159 exhibited similar performance, with M42 HT displaying greater wear resistance.
- SEM analysis showed signs of sliding wear on both tools, with small tool degradation on the surface of the M42 HT specimen.
- M42 high speed steel in hardened and tempered condition and MP159 multiphase alloy in hardened condition presented similar levels of performance and should both be considered as alternative materials to be used as tooling components for RFSSW.

A summary of the performance for each tool material based on industrially relevant and operational criteria for RFSSW is presented in Table 4.10. From this table, it can be observed that M42 high speed steel in the hardened and tempered condition is the most promising tool material for RFSSW. Although MP159 in the hardened condition presented similar promising results and is extensively used in other friction welding technologies, M42 is a more economically viable and widely available material. For this reason, this material will be used in the following chapter.

Table 4.10 - Tool material evaluation based on industrially relevant and operational criteria for RFSSW.

Tool Material	M42 High Speed Steel		MP159 Co-Ni-Cr alloy		Si_3N_4
Surface Treatment	Hardened and tempered	Hardened, tempered and Plasma Nitriding	Hardened	Hardened and Surface Treated	As received
Affordability	★★★★★	★★★★	★★★	★★	★
Availability	★★★★★	★★★★★	★★★	★★	★
Machinability	★★★★★	★★★★★	★★★★★	★★★★★	★
Inert to Workpiece	★★★★★	★★★★★	★★★★★	★★★★★	★★★★★
Wear Resistance	★★★★	★	★★★	★★★★	N/A
Microstructure	★★★★★	★★★★★	★★★★★	★★★★★	★★★★★
Susceptibility to Clogging	★★★★★	★	★★★★★	★	N/A
Score	1st	3rd	2nd	4th	5th
Legend: ⋆ - Very poor; ⋆⋆ - Poor; ⋆⋆⋆ - Average; ⋆⋆⋆⋆ - Good; ⋆⋆⋆⋆⋆ - Very good					

Chapter 5

Influence of tool material and profile on RFSSW joints

The influence of the process parameters in the weld microstructure and mechanical properties using standard RFSSW tool was addressed in Chapter 3. From Chapter 4, a suitable tool material that could withstand the cyclic loads and frictional wear during RFSSW was identified. In this chapter, the effect of different tool materials and profiles on the mechanical and microstructural properties of RFSSW joints was investigated.

5.1 Introduction

As stated in the work of Montag et al. (2014) and most recently highlighted in the RFSSW review by Feng et al. (2019), there is a lack of published experimental data regarding RFSSW tool design. Although the welding tool plays a critical role in the process, the impact of different tool profiles as well as different materials on the process has not been studied. This fact was also highlighted in chapter 2. The investigation conducted in this chapter aims to provide an understanding of the influence of different tool materials and profiles on the mechanical performance and microstructural properties on RFSSW joints.

5.2 Materials and methods

5.2.1. Base materials

This investigation employed the same base materials which were used in Chapter 3. The chemical compositions and mechanical properties of the alloys are presented in Table 5.1 and Table 5.2, respectively.

Table 5.1 - Chemical composition of the base material.

Element [Weight %]	Si	Fe	Cu	Mn	Mg	Zn	Cr	Ti	Al
AA5754-H24	0.1	0.4	0.02	0.30	2.73	< 1.0	0.05	0.01	
AA2024-T3	0.9	0.11	4.3	0.52	1.5	0.1	0.01	0.04	remainder
AA7075-T6	0.07	0.17	1.5	0.03	2.4	5.9	0.2	0.03	

Table 5.2 - Mechanical properties of the base material.

	Yield stress $\sigma_{0.2\%}$ [MPa]	Ultimate tensile stress σ_{UTS} [MPa]	Elasticity modulus [GPa]	Poisson ratio [ν]	Elongation [%]	Hardness [HV0.2]
AA5754-H24	206.0 ± 2.4	264.1 ± 2.7	73	0.33	11.7 ± 0.6	77.0 ± 1.9
AA2024-T3	343.0 ± 3.0	473.0 ± 5.0			18.0 ± 1.0	137.0 ± 4.9
AA7075-T6	512.0 ± 2.0	580.0 ± 1.0			13.0 ± 0.7	177.0 ± 4.3

5.2.2. Welding equipment

The work was carried out using TWI's RFSSW system, shown in Figure 3.1. The RFSSW system at TWI consists of a 6-axis articulated robot with a 300kg payload capacity from KHI, which has been fitted with a C-frame RFSSW gun. An extensive description of the technical data and recordable process parameters has been provided in Chapter 3.

5.2.3. Tool material and design

Two different tool materials and two different profiles were selected for this investigation. M42 High Speed Steel and a metal matrix composite of tungsten carbide particles imbedded in cobalt (WC-Co) were use as tool materials. These materials were selected based on the results obtained from Chapter 4 and from the equipment manufacturer, respectively. The physical properties of the tool material are displayed in Table 5.3.

Table 5.3 - Tool material properties

	M42	WC-Co
Density [Kg/m^3]	7.9	14.4
Modulus of Elasticity [kN/mm^2]	200.0	580.0
Thermal Conductivity [W/m °C]	28.0	105.0

To determine the influence of a different tool material on the RFSSW process and weld properties, a tool set was manufactured by combining (i) the most promising tool material candidate proposed in Chapter 4 with (ii) the RFSSW tool design supplied by KHI, assessed in Chapter 3. The tool provided by KHI (Tool 1) was used as the reference for comparison against the new tool set, which will be referred hereinafter as Tool 2. The geometry of the tool components on both tool sets was cylindrical without any features on any of the surfaces as shown in Figure 3.2.

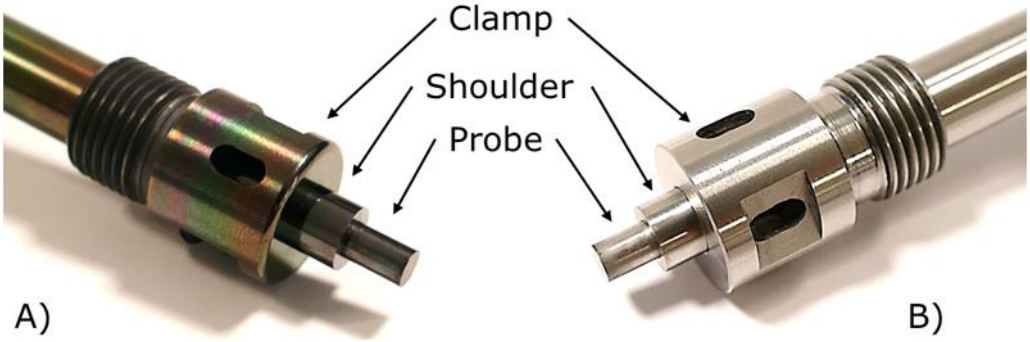

Figure 5.1 - A) RFSSW tool components of Tool 1 and B) the RFSSW tool components of Tool 2 made from M42 high-speed steel.

To determine the influence of different shoulder profiles on the RFSSW process and weld properties, a second tool set was manufactured utilising the same material as in Tool 1, while incorporating a grooved feature on the external surface of the shoulder. This tool design will be referred hereinafter as Tool 3. The use of a left-hand groove, in relation to the right-hand grip rule, on the external surface of the shoulder has been widely used by other researchers when

welding using the shoulder-plunge variant, as reported in Chapter 2. This external surface feature is reported to enhance the stirring action and improve the material flow during the plunging stage. However, a direct comparison between RFSSW tool profiles and materials has not been previously reported in literature.

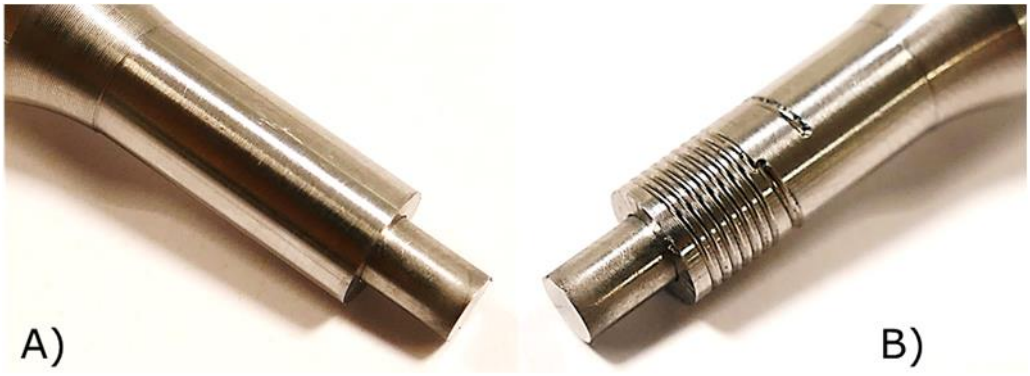

Figure 5.2 - Shoulder and probe design for A) Tool 2 and B) Tool 3 RFSSW tool sets.

The different materials and profiles used in this investigation are summarised in Table 5.4. Both the clamp and probe profiles were identical on all the tool sets and were based on the KHI design (Tool 1). This was deliberate as the welding trials were performed using the shoulder-plunge variant of the process and the designs of the probe and clamp were considered to have a neglectable influence on the weld cycle or material flow.

Table 5.4 - RFSSW tool materials and profiles.

	Tool material	Shoulder design
Tool 1	WC-Co	Featureless
Tool 2	M42	Featureless
Tool 3	M42	Left-hand grooved

The general dimensions of the tool components are provided in Table 3.4 while detailed technical drawings of the tool components are presented in Appendix A2.

Table 5.5 - RFSSW tool dimensions

	Probe	Shoulder	Clamp
External diameter [mm]	Ø 4	Ø 7	Ø 16
Internal diameter [mm]	n/a	Ø 4	Ø 7

5.2.4. Welding sequence

Sheet interface surfaces were manually cleaned with acetone to remove contaminants prior to welding. Similar material and single spot RFSSW specimens were produced using the shoulder-plunge variant of RFSSW Figure 2.5.A, operating in force-control mode. The best performing

process parameter combination determined in Chapter 3 for each aluminium alloy was used in the present investigation, as shown in Table 3.5.

Table 5.6 - RFSSW process parameters

RFSSW Process parameters	
Rotation Speed [rev/min]	1000
Plunge Depth [mm]	
AA5754-H24	2.2
AA2024-T3 and AA7075-T6	2.4
Stage 1 Dwell time [s]	
AA5754-H24	1.0
AA2024-T3 and AA7075-T6	2.0
Shoulder plunge force [kN]	
AA5754-H24	13.5
AA2024-T3 and AA7075-T6	14.5
Clamp force [kN]	7.0

5.2.5. Microstructural and mechanical characterisation

Metallographic specimens were sectioned, polished and etched with Keller's reagent for microstructural analysis. Optical microscopy was conducted using an OLYMPUS GX71 inverted geometry optical microscope with a Colorview III camera. Weld static strength was evaluated via lap shear testing using an INSTRON 8502 tensile machine with a displacement rate of 1 mm/min at room temperature. The geometry of the specimens for lap shear testing were produced in accordance with BS EN ISO 18785-4:2018 with the sheet rolling direction perpendicular to the loading direction, as shown in Figure 3.3. Three specimens were tested for each aluminium alloy and each tool design variants. Fracture surfaces were inspected under SEM using a Zeiss EVO LS15.

As a common practice in the aerospace industry, the effect of the presence of an interfacial sealant on the mechanical strength and microstructural properties was also investigated. This investigation was performed for the high strength alloys AA2024-T3 and AA7075-T6 with all tool design variants. The sealant and application method used in Chapter 3 were also applied in this investigation.

Mechanical characterisation of specimens was conducted four weeks after welding in order to ensure consistency in specimen aging time between the testing of specimens with interfacial sealant and in bare condition, as performed in Chapter 3. However, on the aforementioned chapter, a longer wait period was applied (seven weeks). This means that a new base line comparison was established with a new set of mechanical specimens produced using Tool 1.

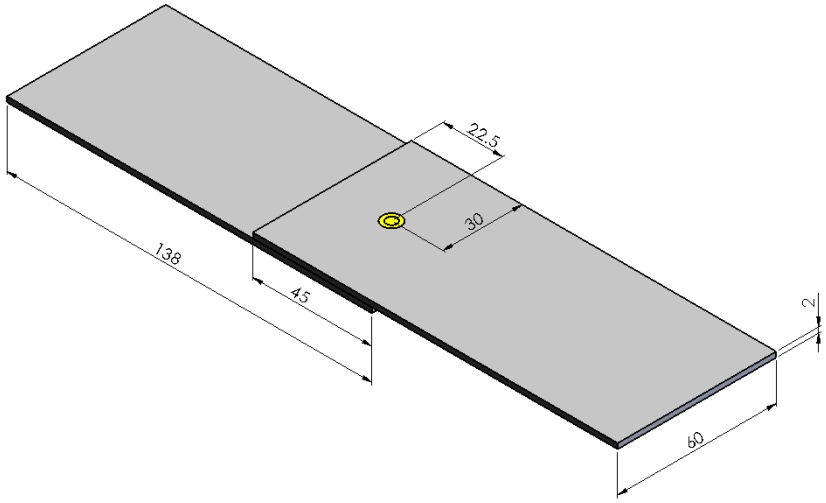

Figure 5.3 - Lap shear test specimen geometries.

5.2.6. Temperature measurements

For each tool design, temperature measurements were performed to record the thermal history of the weld cycle and measure the peak temperature. As performed in Chapter 4, a block measuring 150 x 50 x 20 mm of AA7050-T7451 was used as the base material using the process parameters from Table 3.5. The first spot-weld was distanced 25 mm from the edges. A spacing of 50 mm between each spot-weld along the length was applied, as shown in Figure 5.4.

For this investigation, a calibrated 1 mm diameter Type K shielded thermocouple was placed at a depth of 2 mm from the top surface and 20.5 mm from the side. Temperature measurements were recorded using a calibrated Ni 9213 digital acquisition module and processed using Ni Express 2015 software. A 100 Hz frequency of acquisition was used.

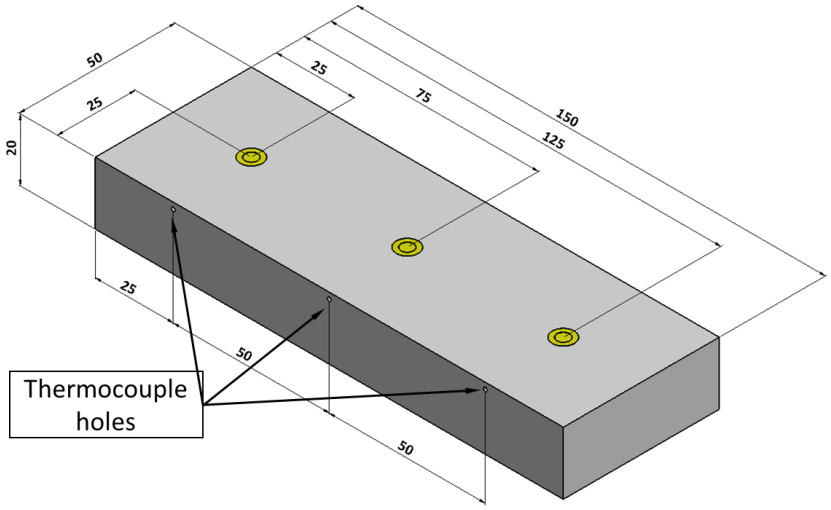

Figure 5.4 - Schematic drawing of temperature measurement block with three thermocouple holes.

5.2.7. Tool failure analysis

To estimate the life expectancy of Tool 2 and 3 under RFSSW service conditions, one specimen of each tool design was used to perform rows of consecutive welds. Similar to the procedure described in Section 4.2.4 from Chapter 4, an AA7050-T7451 25 mm thick plate was used as the base material. The first weld was located 15 mm from the edge of the plate. The subsequent welds were separated by 20 mm intervals. This procedure, along with a compressed air-cooling period of 15 seconds between each weld, was continuously repeated until tool fracture. The fracture surfaces of the tools were inspected under SEM using a Zeiss EVO LS15.

5.3 Results and discussion

5.3.1. Temperature measurements

Figure 5.5 shows the thermal history of the welds performed with the various tool designs under consideration. Tool 1 presented the highest peak temperature of all the welds experimented in this study. This result can be explained by the longer cycle time, which increases the processing time between the tool and the base material leading to a higher temperature. The RFSSW equipment used in this study, as described in Chapter 3, works in force control-mode, with a constant applied plunge force. Under certain welding conditions, this can lead to a variable plunge rate that is dependent on the rate and extent of material softening from the heat generated by the tool.

As described in Section 5.2.3, Tool 1 was produced by the equipment manufacturer using a featureless design. This design provides low downward acceleration to the base material, as stated in the study by Ji et al. (2017-B). Also, the material used to manufacture this tool has a significantly higher thermal conductivity than the alternative candidate tool material, M42. This means that the heat generated by frictional contact between the base material and the bottom of the tool can dissipate quicker along the full length of the tool body, potentially narrowing the region of plasticised base material ahead of the tool. The development of this plasticised base material zone is crucial to produce consolidated welds as observed in other friction welding technologies (Vairis and Frost 2000; Thomas and Nicholas 1997).

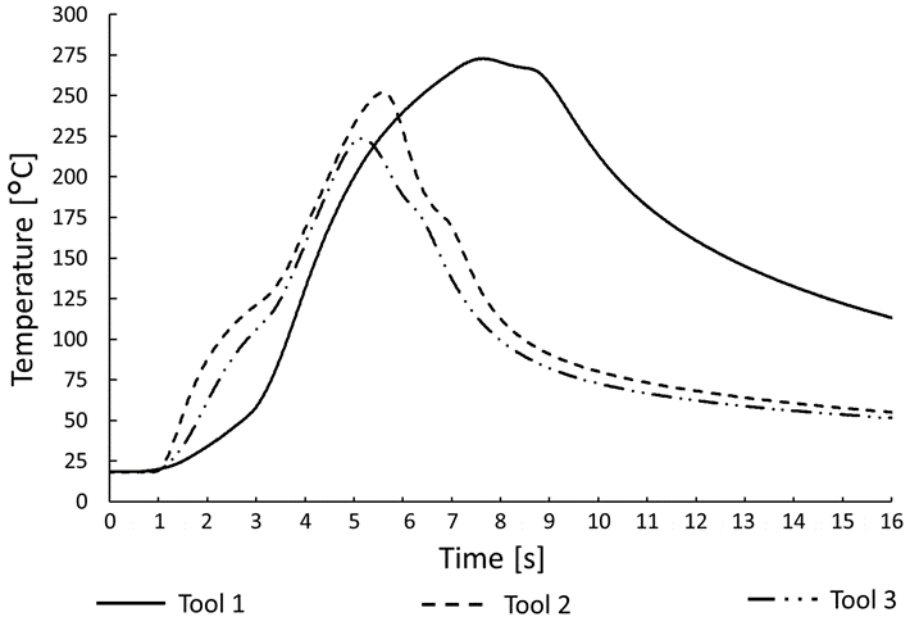

Figure 5.5 - Temperature measurement plot of Tool 1, 2 and 3.

Figure 5.6.A) and B) present the tool position during the weld cycle for Tool 1 and 2, respectively. The numbers in the graph relate to the stages of the process, as described in Chapter 2. It can be seen that, during stage 2, a much quicker and consistent plunge rate can be achieved with Tool 2. This leads to a shorter weld cycle, which limits the exposure time of the rotating tool to the base material, delivering a lower heat input to the weld.

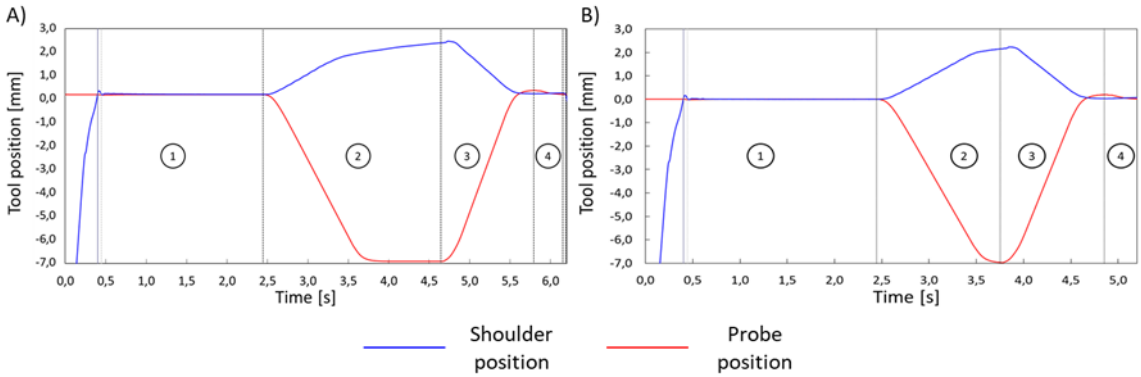

Figure 5.6 - Shoulder and probe position during the four stages of the RFSSW cycle for A) Tool 1 and B) Tool 2 during the weld cycle relative to the reference point (top surface of the base material).

Both Tools 2 and 3 show a lower weld peak temperature, as well as a shorter weld cycle compared to that of Tool 1. The significant differences between Tool 1 and 2 are their raw material and surface treatment. The low friction coating prevents the base material from adhering to the surface of the tool as well as the tool components from joining together under service conditions. This is accomplished by reducing the static friction coefficient between the contact surfaces. For

comparison, the surface coating used provides a friction coefficient varying between 0.04 and 0.08 (Wallwork 2020), while the values between steel and aluminium typically range between 0.47 and 0.61 (Avallone 2007). From a tribological perspective, the frictional interaction between the base material and the uncoated tool will generate a higher degree of heat. As previously mentioned, using a material with a lower thermal conductivity reduces the heat loses via conduction through the tool body. This in turn, increases the parent material softening rate and extends the plasticised material region ahead of the tool, thereby enabling faster plunge rates. Considering the conclusions gathered from Chapter 3, it is likely that Tools 2 and 3 would produce welds with greater mechanical performance.

The influence of different tool profiles on the weld peak temperature can be determined by comparing the thermal history of Tool 2 and 3. The presence of an external groove promotes the downward material flow and the plasticisation of more weld material. The resistance to the shoulder plunging motion would be expected to increase, thus increasing the weld cycle time and the weld peak temperature. However, it can be seen from the thermal plot that the opposite was observed. Building on the hypothesis presented in the previous paragraph, it is possible that the increase in mechanical stirring promoted further material softening around and ahead of the tool direction. This translated into an increase in plunge rate and a shorter interaction time between the tool and the weld material.

5.3.2. Lap shear strength analysis

5.3.2.1. Influence of tool material

In this investigation, the effect of different tool materials on the mechanical performance of the weld can be determined by comparing the lap shear testing results between Tool 1 and 2 (i.e. both tools have the same design and dimensions but are made from different tool materials). Figure 5.7 shows the results of lap shear testing of bare specimens for all the alloys used in this study. For each alloy, the minimum lap shear strength value specified by AWS D17.2/D17.2M:2019 for resistance spot welding as well as the shear strength design for a 1/4" MS20426DD AA2024-T31 solid rivet, specified by MMPDS-04 (2008), are presented in the bar chart. Similar to what was observed in section , all welds surpassed the minimum value set by AWS D17.2/D17.2M:2019 yet none of the welds exceeded the strength requirements specified by MMPDS-04 (2008). The difference between the strength values however is negligible, in particular for the AA2024-T3.

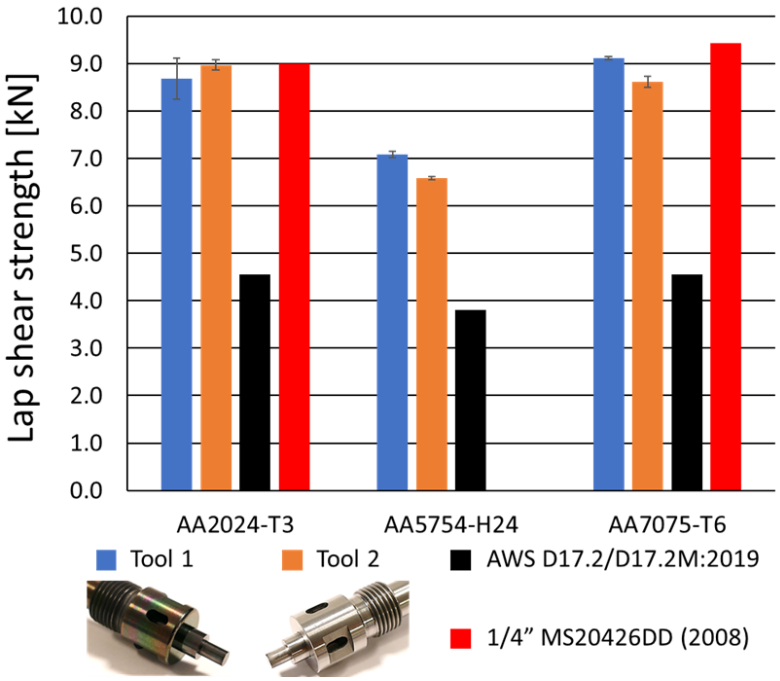

Figure 5.7 - Influence of different tool materials on the lap shear strength results of bare specimens.

The choice of tool material impacts the frictional heat generation rate, the tool mechanical properties and weld thermal cycle (Chandrashekar, Kumar and Reddappa 2015). For FSW, researchers have reported a clear influence in the weld mechanical performance and microstructure with the change of tool material (Bozkurt and Boumerzoug 2018; Jayaseelan et al. 2019; Khaliq and Bharti 2015 and Withers et al. 2012). Certain tool material properties, as mentioned in the previous chapter, ultimately dictate which materials can be welded using RFSSW. Oliveira et al. (2011) attributed the improvement in weld quality and strength to the lower thermal conductivity of a titanium tool when joining thermoplastics using RFSSW.

From the data presented in Figure 5.7, contrary to the predictions from the previous section, it can be seen that similar lap shear strength values between welds performed with Tool 1 and 2 were measured. Comparing the static strength from Tool 2 with Tool 1, the values ranged between a decrease of 7 % and an increase of 3 % in lap shear strength. This observation suggest that for the tool geometry under consideration, the choice of tool material did not have a clear impact on the joint mechanical properties. This suggests that a more cost-effective material alternative can be used, without compromising the performance of the joint. This result was also observed by other authors for FSW (Çevik, Özçatalbaş, and Gülenç 2016; Singarapu, Adepu and Arumalle 2015)

In this study, three different failure modes were observed: shear fracture through the nugget (Figure 5.8), shear fracture through the interface (Figure 5.9) and shear through the plug on the top sheet (Figure 5.10). An explanation for the crack initiation and propagation for each failure mode has been provided in Sections 3.3.1 and 3.3.3. Shear fracture through the interface and shear through the plug on the top sheet were observed on RFSSW of AA5754-H24 and AA7075-T6, respectively. These failure modes were observed for both tools across all the tested specimens. For RFSSW AA2024-T3, shear fracture through the nugget was observed for welds performed with Tool 1 whilst shear fracture through the interface was predominantly observed for welds performed with Tool 2.

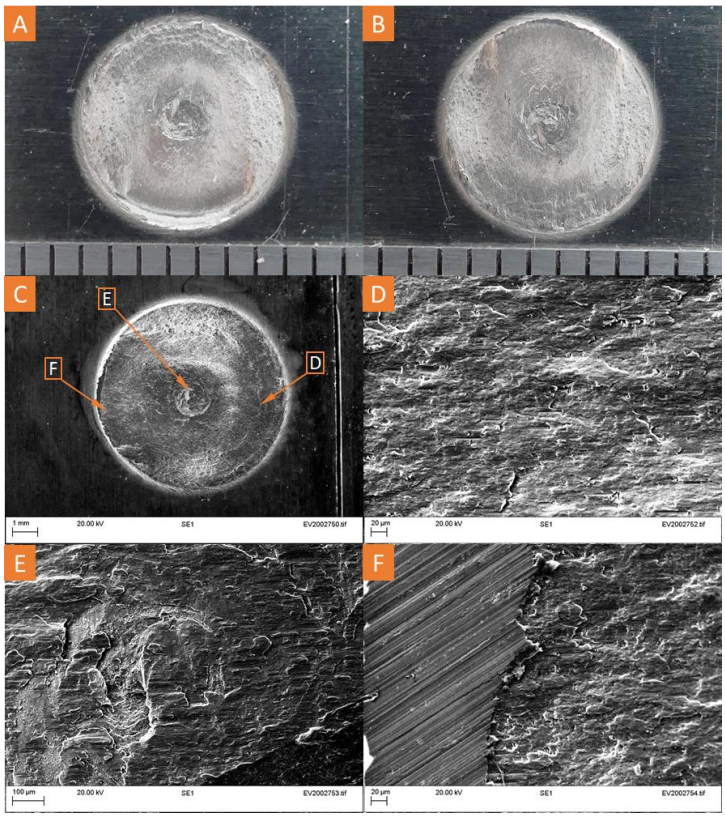

Figure 5.8 - Fracture surfaces of RFSSW AA2024-T3 using Tool 1:
A) Top sheet;
B) Bottom sheet;
C) SEM fractography;
D) High magnification region – location shown in Figure 5.8.C);
E) High magnification region – location shown in Figure 5.8.C);
F) High magnification region – location shown in Figure 5.8.C).

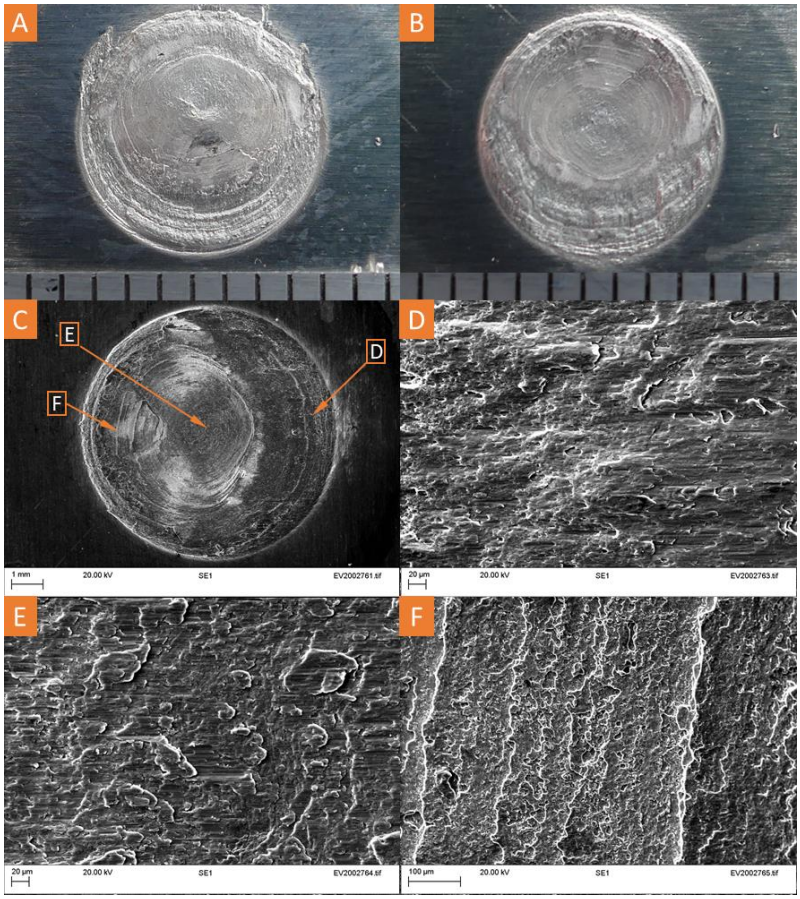

Figure 5.9 - Fracture surfaces of RFSSW AA5754-H24 using Tool 2:
A) Top sheet;
B) Bottom sheet;
C) SEM fractography;
D) High magnification region – location shown in Figure 5.9.C);
E) High magnification region – location shown in Figure 5.9.C);
F) High magnification region – location shown in Figure 5.9.C).

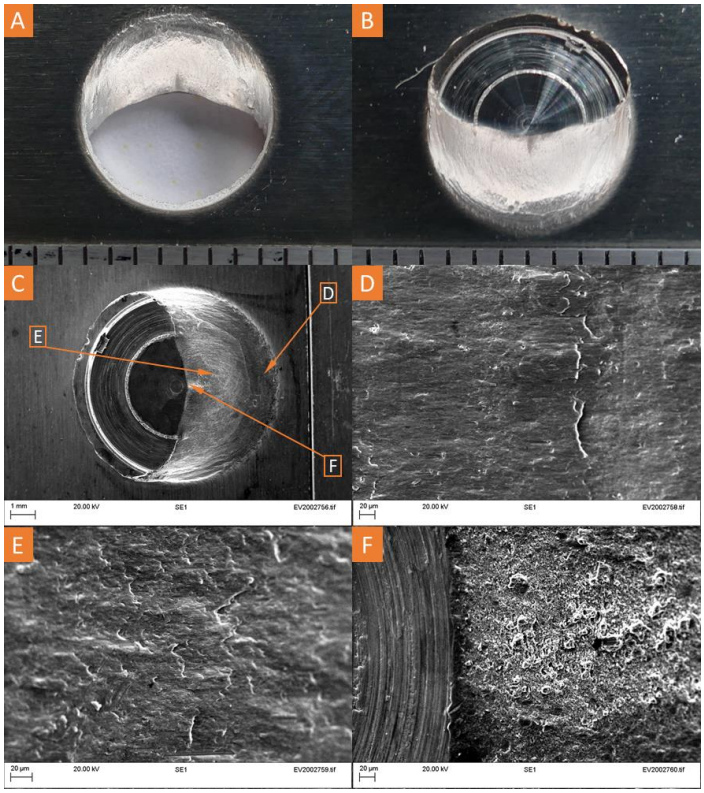

Figure 5.10 - Fracture surfaces of RFSSW AA7075-T6 using Tool 1:
A) Top sheet;
B) Bottom sheet;
C) SEM fractography;
D) High magnification region – location shown in Figure 5.10.C);
E) High magnification region – location shown in Figure 5.10.C);
F) High magnification region – location shown in Figure 5.10.C).

Figure 5.11, Figure 5.12 and Figure 5.13 present the cross-sections of RFSSW AA2024-T3, AA5754-H24 and AA7075-T6, respectively, performed using Tool 2. An extensive description of the microstructural regions of the weld has been provided in Section 3.3.4. The geometry of the welds are nearly identical to the ones produced by Tool 1, which suggest that the change in the tool material has a negligible effect on the weld microstructure. No internal defects were observed on any of the cross-sections, which supports the hypothesis that the tool external profile has a greater influence on the microstructure and quality of the weld. Also, these observations confirm the correct choice of process parameters which can be used with tools made from different materials with the same design. As observed in Section 3.3.4, the surface oxides present in AA5754-H24 can be seen at the joint line remnant (Figure 3.40.D) and on the contact area between the probe and the surface of the top sheet (Figure 3.40.C). This is due to the higher melting temperature of the films formed by this alloy.

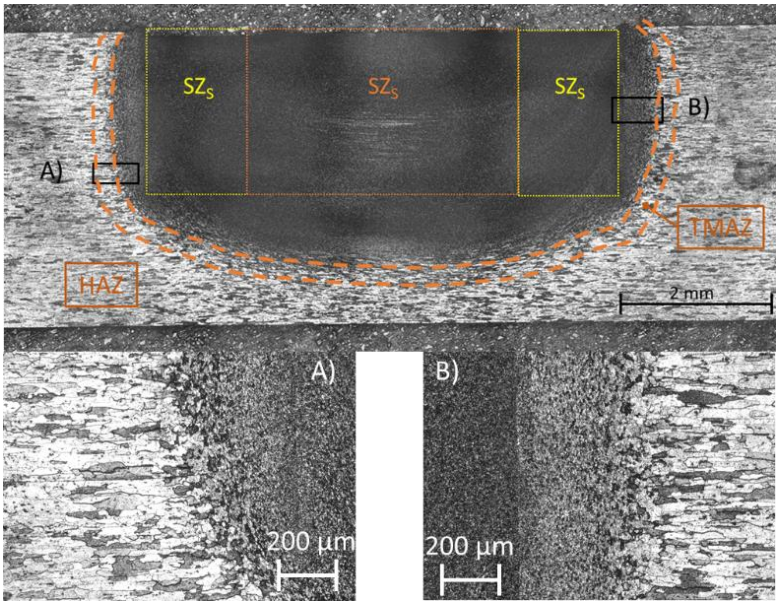

Figure 5.11 - Cross-section of RFSSW AA2024-T3 using Tool 2 in bare condition:
A) SZ/TMAZ interface;
B) Hook region.

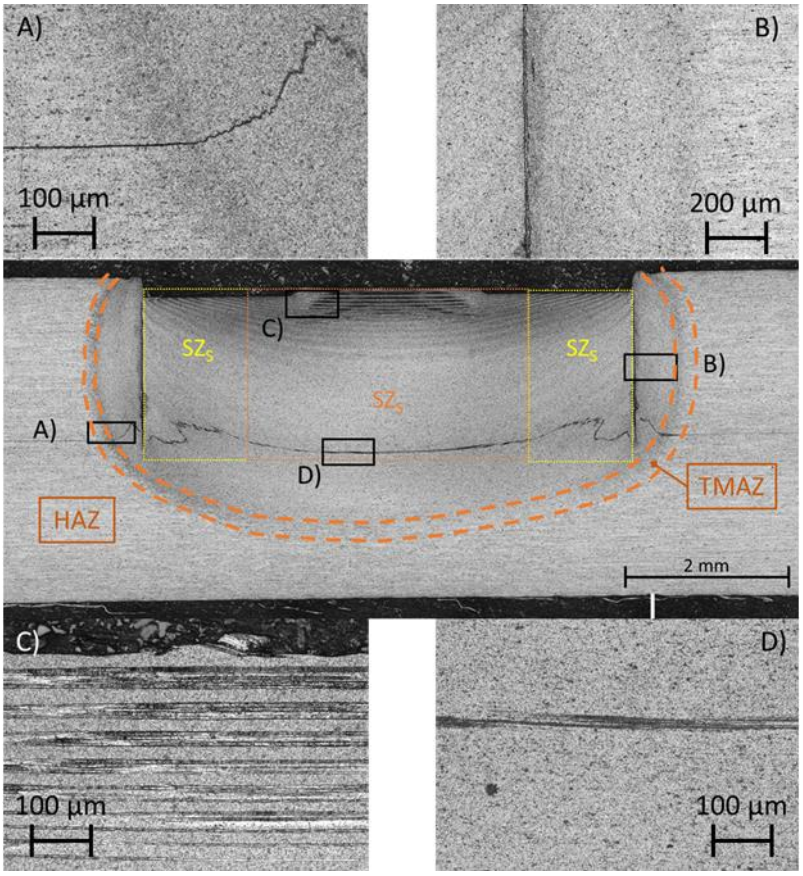

Figure 5.12 - Cross-section of RFSSW AA5754-H24 using Tool 2 in bare condition:
A) SZ/TMAZ interface;
B) Hook region;
C) Probe contact region;
D) Joint line remnant.

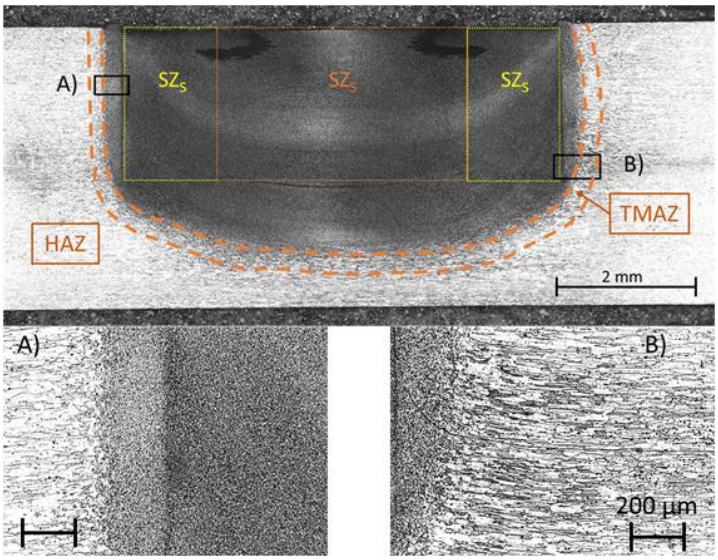

Figure 5.13 - Cross-section of RFSSW AA7075-T6 using Tool 2 in bare condition:
A) SZ/TMAZ interface;
B) Hook region.

As performed in Section 3.3.1, the impact of an interfacial aerospace sealant on the mechanical strength and microstructural properties of RFSSW welds produced with tools from different materials was investigated. Figure 5.14 shows the results of lap shear testing of specimens with interfacial sealant for AA2024-T3 and AA7075-T6, along with the shear strength requirements specified by AWS D17.2/D17.2M:2019 and MMPDS-04 (2008). All welds surpassed the minimum value set by AWS D17.2/D17.2M:2019 and only the RFSSW AA2024-T3 specimen produced with Tool 2 did not exceeded the shear strength requirement for a riveted joint.

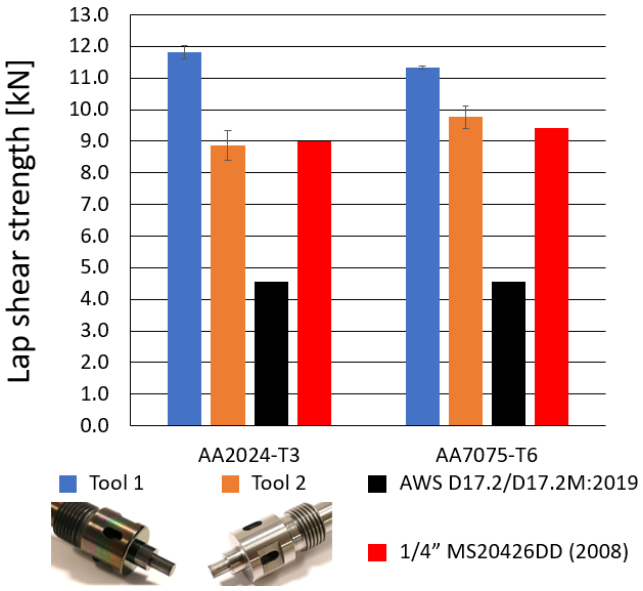

Figure 5.14 - Influence of different tool materials on the lap shear strength results of specimens with interfacial sealant.

In contrast to what was observed for the bare specimen testing, the tool material properties can have a significant impact on the mechanical strength of the welds with interfacial sealant. Comparing the lap shear strength values obtained for Tool 2 with Tool 1, a decrease in shear strength ranging between 14 and 25 % was observed. The explanation for this phenomenon can be attributed to a higher temperature of the edge of the shoulder in Tool 2, due the differences in tool material conductivity. As observed by Zhao et al. (2016), the contact area between the edge of the shoulder and the base material is where the peak welding temperature is observed. The peak temperature at the tool contact area depends on multiple factors, including the rate of heat loss in the weld due to conduction through the tool body. These losses are related to the tool and base material physical properties, in particular the thermal conductivity. Considering the same base material, the tool material used in Tool 2 has a lower thermal conductivity coefficient, which leads to smaller heat losses through the tool body. Despite that being a positive factor in producing a faster weld cycle, it can also lead to severe overheating and degradation of the sealant, as well as the pre-cured areas around the weld. Whoever further testing and analysis would be required to confirm this hypothesis.

For the AA2024-T3 welds performed with Tool 2, shear fracture through the nugget and through the interface failure modes were observed. This can be linked to the unpredictable flow of the interfacial sealant in the weld area and the similarity in the crack propagation mechanism of these failure modes. The welds produced with Tool 1 produced consistent Shear through the plug on the top sheet failure modes for RFSSW AA7075-T6 and Shear fracture through the nugget for RFSSW AA2024-T3. The fracture surfaces are identical to the ones presented for the bare specimens and in Section 3.3.1.

The cross-sections of RFSSW AA2024-T3 and AA7075-T6 with interfacial sealant performed using Tool 2 are shown, respectively, in Figure 5.15 and Figure 5.16. Similar to the cross-section on the bare specimens, no internal defects were observed, which further supports the greater influence of the tool design on the microstructure and quality of the weld, compared to tool material choice. Comparing the cross-sections produced using Tool 1 in Section 3.3.4, the cross-sections produced with Tool 2 only show a thin layer of sealant at the centre of the joint line remnant. This is particularly evident for the RFSSW AA7075-T6 as observed in Figure 5.16.C). In spite of this, strong bonding was obtained at the centre of the weld nugget as shown by the shear through the plug failure mode.

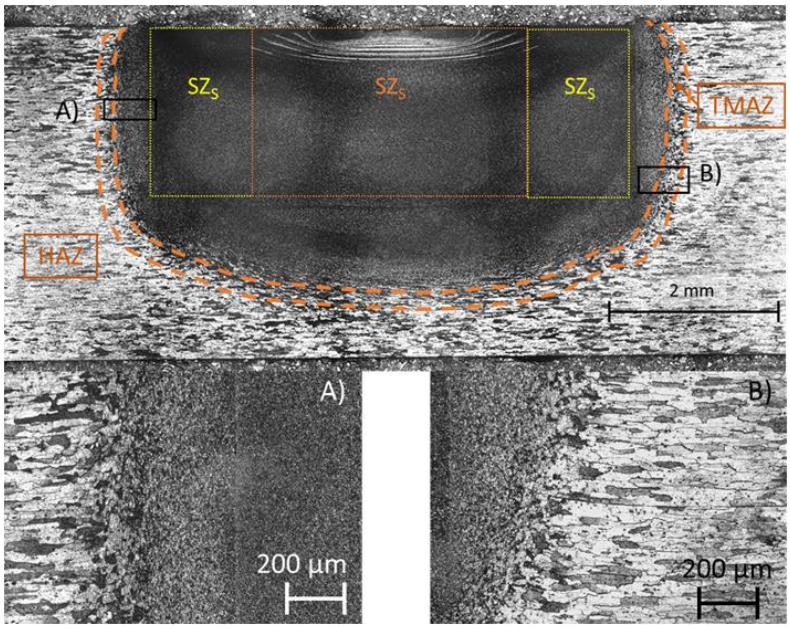

Figure 5.15 - Cross-section of RFSSW AA2024-T3 using Tool 2 with interfacial sealant:
A) SZ/TMAZ interface;
B) Hook region.

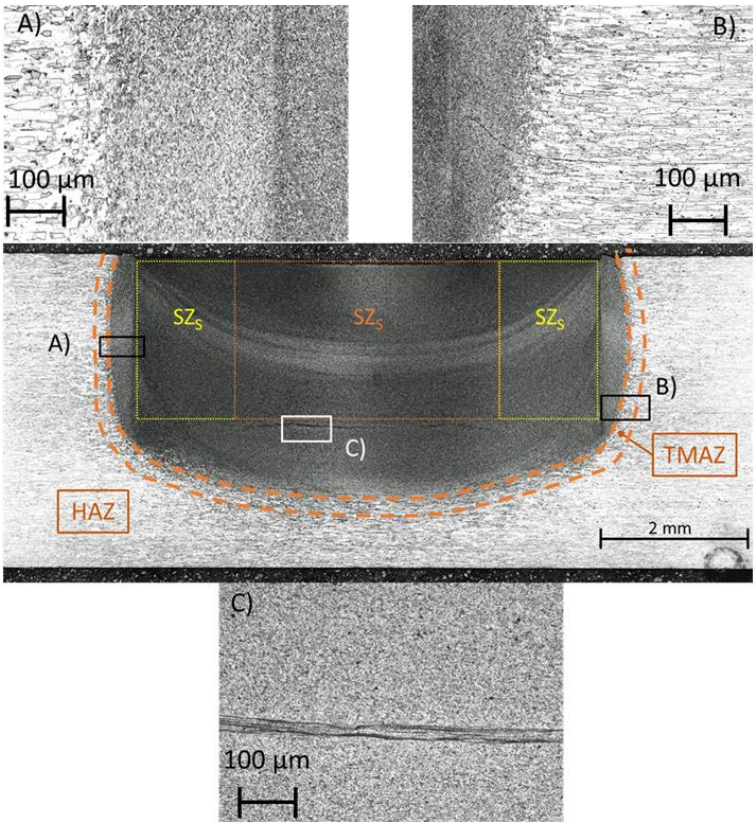

Figure 5.16 - Cross-section of RFSSW AA7075-T6 using Tool 2 with interfacial sealant:
A) SZ/TMAZ interface;
B) Hook region;
C) Joint line remnant.

5.3.2.2. Influence of tool profile

In FSW, the profile of the tool plunging component has a great impact on the flow of plasticised material, heat generation and weld properties (Rai et al 2011). Multiple researchers have acknowledged the importance and need for further research in this topic, with many of them studying the effect of the probe profile with the weld mechanical performance and microstructure (Khodaverdizadeh, Heidarzadeh and Saeid 2013; Mohanty et al. 2012; Palanivel et al. 2012; Ullegaddi, Murthy and Harsha 2017). For the RFSSW process, limited studies have been published on the influence of different tool profiles on the weld microstructure, mechanical performance and quality. Shen et al. (2018 and 2020) achieved greater dissimilar intermixing between dissimilar RFSSW of AA6022-T4 and AA7075-T6 by adding grooves on the bottom surface of the shoulder.

The effect of different tool profiles on the mechanical performance of the weld can be determined by comparing the lap shear testing results between Tool 2 and 3. Both tools have the same dimensions and are made from the same material but feature different profiles. These experiments aimed to further understand the relationship between RFSSW tool profile with the weld mechanical performance and microstructural features. Figure 5.17 shows the results of lap shear testing of bare specimens for all the alloys used in this study.

In comparison with Tool 2, adding a profile to Tool 3 allowed to improve the joint shear strength from 2 to 24 % depending on the material welded. Shear through the plug on the top sheet failure mode was observed for all welds performed with Tool 3, suggesting adequate bonding conditions at the weld interface. The presence of the left-hand thread on the profile of the tool increases the downward flow of material, improving the consolidation of material in this area. This positive outcome highlights the importance and the need for further research in this topic.

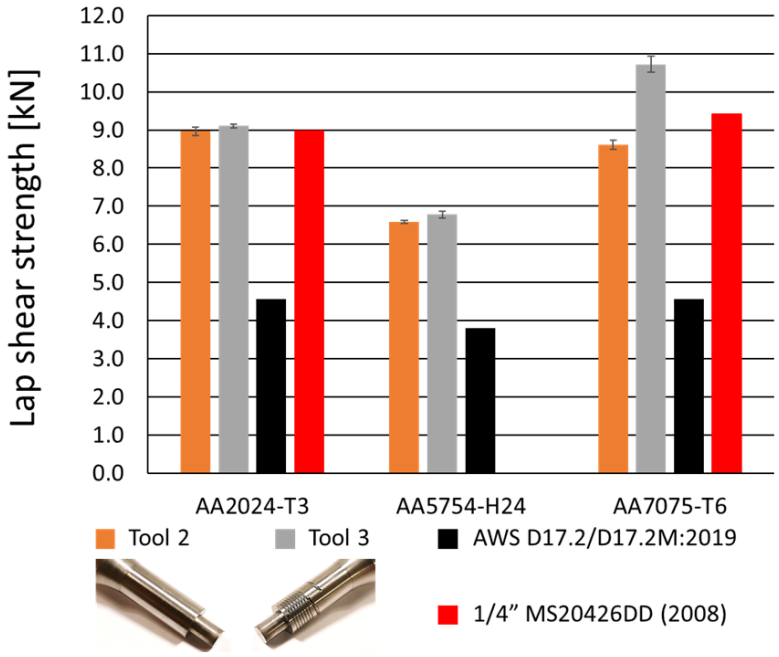

Figure 5.17 - Influence of different tool profiles on the lap shear strength results of bare specimens.

The weld cross-sections of RFSSW AA2024-T3, AA5754-H24 and AA7075-T6 performed using Tool 3 are presented in Figure 5.18, Figure 5.19 and Figure 5.20, respectively. In comparison with the shape of the welds for the previous section, the cross-section of the welds produced with Tool 3 present an enlarged area at the bottom edge of the weld. This is particularly noticeable on the cross-section of RFSSW AA2024-T3 and AA7075-T6, however it was not observed for AA5754-H24. In fact, for this alloy, the cross-sections from all tools tested in this investigation are nearly identical, with the difference of a noticeable oxide alignment at the edge of the stir zone matching the threaded profile of the shoulder [Figure 5.19.B)]. These observations, along with the similar shear strength observed from the lap shear testing, seem to suggest that this alloy is more sensitive to changes in the process parameters than the tooling material and profile. Similar weld cross-section shape was observed by Suhuddin et al. (2015) when joining the same alloy using RFSSW.

When using a threaded tool profile, Shen et al. (2013 and 2014) and Kluz et al. (2019) observed internal voids and lack of fill defects. The authors have attributed these defects to poor metallurgical bonding, residual heat stress after welding and insufficient flow of material during refill, which directly relate to the tool profile as well as process parameters. However, Adamus, J and Adamus, K (2019) considered the loss of material during the plunging stage to be the cause of voids in the weld, this being corrected by a slight surface compression at the end of the cycle. This would cause a characteristic indent. In this study however, no internal defects were observed

on any of the cross-sections, which confirms the correct choice of process parameters which can be used with tools of different materials and profiles.

In the simulation work carried out by Ji et al. (2017-B), the author analysed the material flow of RFSSW using different tool profiles and dimensions. Based on the observations in this study, it was suggested that a featureless profile (Tool 1 and 2) may be able to reduce or even eliminate the hook defect. This is ideal as other authors have suggested a correlation between hook heights and poor lap shear strength (Cao et al 2017; Santana et al. 2017; Zhao et al. 2014). However, this relationship is not verified consistently, as some authors did not find an evident relationship (De Castro et al. 2018-A; Shen et al. 2014; Zhou et al. 2017). As observed in Table 5.7, the welds produced using Tool 2 showed to have higher hook height than the welds produced with Tool 3.

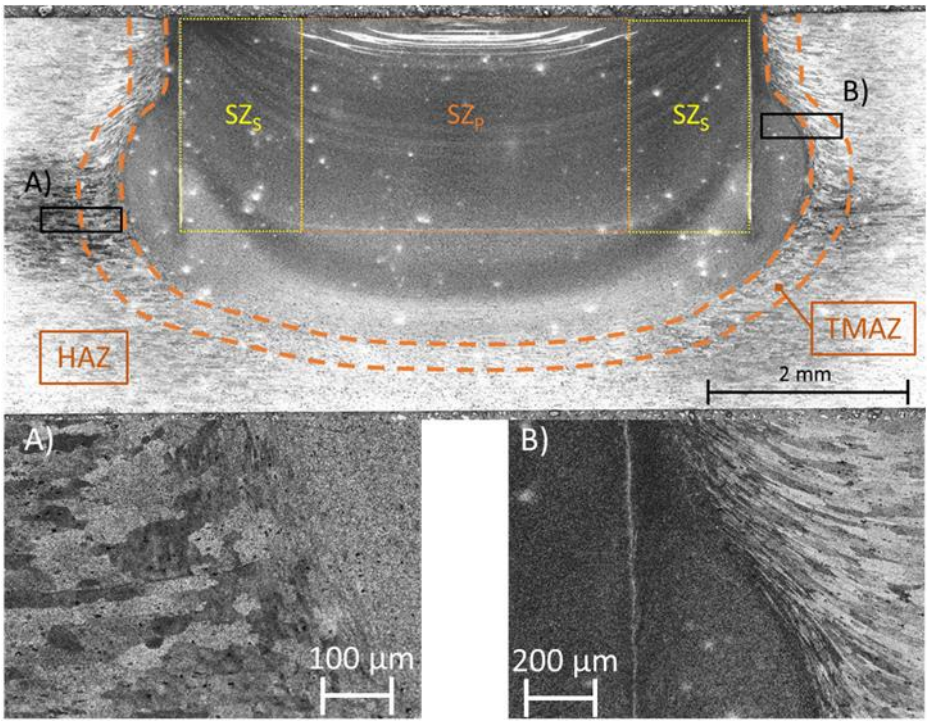

Figure 5.18 - Cross-section of RFSSW AA2024-T3 using Tool 3 in bare condition:
A) Hook region;
B) SZ/TMAZ interface.

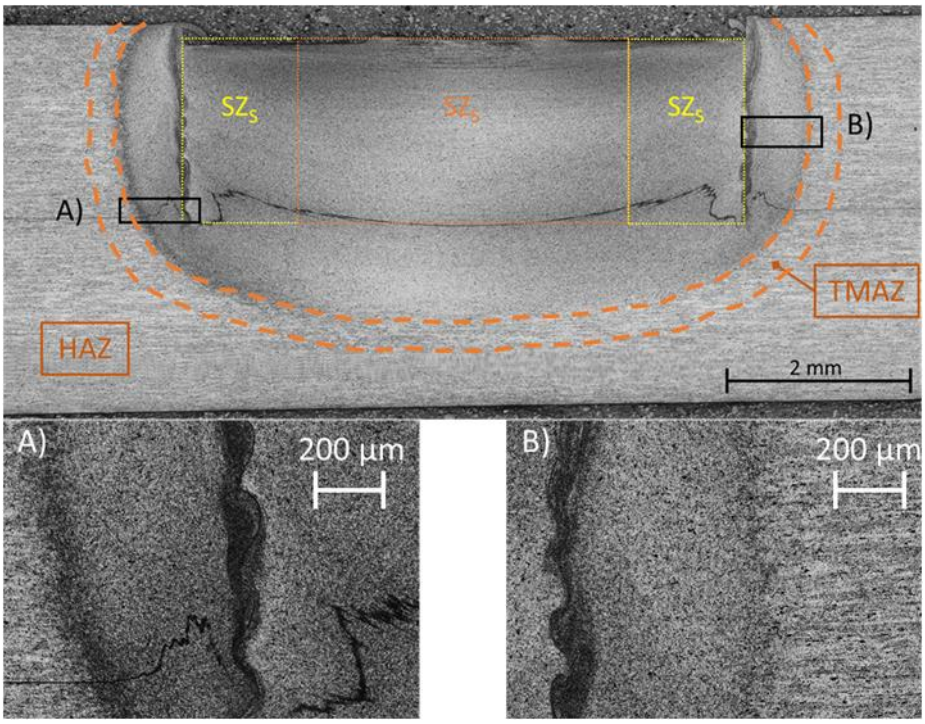

Figure 5.19 - Cross-section of RFSSW AA5754-H24 using Tool 3 in bare condition:
A) SZ/TMAZ interface;
B) Hook region;

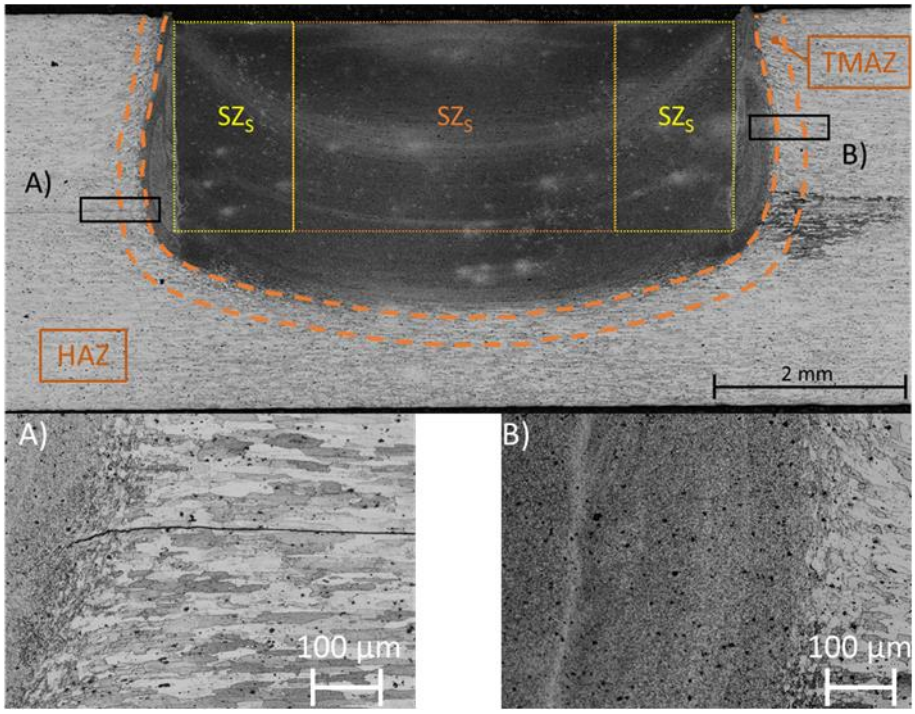

Figure 5.20 - Cross-section of RFSSW AA7075-T6 using Tool 3 in bare condition:
A) Hook region;
B) SZ/TMAZ interface.

Table 5.7 - Hook height for RFSSW AA2024-T3, AA5754-H24 and AA7075-T6 welds using Tool 2 and 3.

Aluminium Alloy	Welding Condition	Tool ID	Hook Height [µm]
AA2024-T3	Bare	Tool 2	48.75
		Tool 3	58.75
	with sealant	Tool 2	73.10
		Tool 3	50.30
AA5754-H24	Bare	Tool 2	49.75
		Tool 3	34.65
AA7075-T6	Bare	Tool 2	108.70
		Tool 3	49.75
	with sealant	Tool 2	193.65
		Tool 3	47.80

The impact of an interfacial aerospace sealant on the mechanical strength and microstructural properties of RFSSW welds produced with tools with different profiles was investigated. Figure 5.21 shows the results of lap shear testing of specimens with interfacial sealant for AA2024-T3 and AA7075-T6, along with the shear strength requirements specified by AWS D17.2/D17.2M:2019 and MMPDS-04 (2008). All welds produced with Tool 3 surpassed the minimum value set by AWS D17.2/D17.2M:2019 and the shear strength requirement for a riveted joint. This can be attributed to a more efficient material flow promoted by the threaded profile of the shoulder and a more even distribution of the sealant around the weld area.

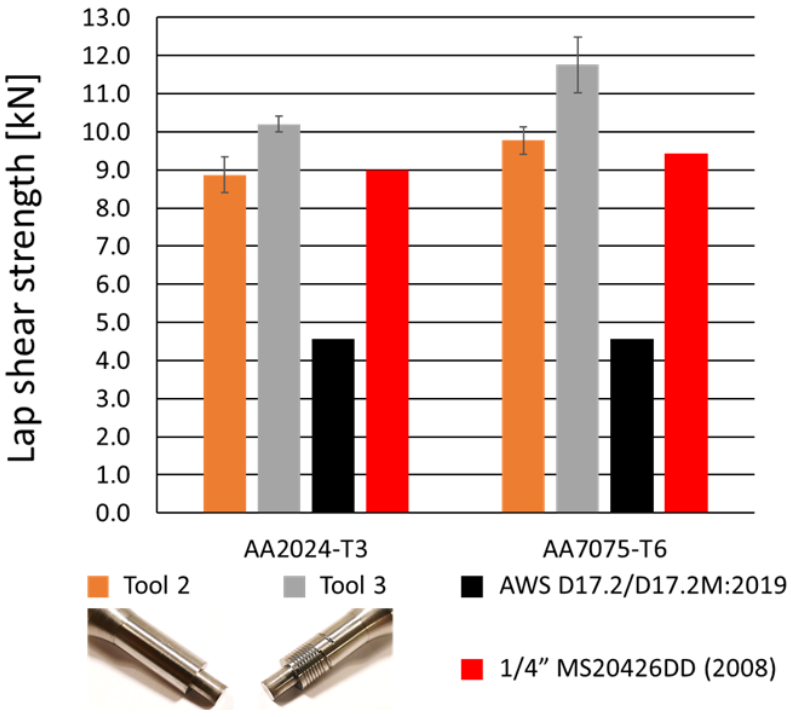

Figure 5.21 - Influence of different tool profiles on the lap shear strength results of specimens with interfacial sealant.

Figure 5.22 and Figure 5.23 show the cross-sections of RFSSW AA2024-T3 and AA7075-T6, respectively, with interfacial sealant performed using Tool 3. Similar to the cross-section on the bare specimens, no internal defects were observed. However, in comparison to the cross-section of the welds from the bare specimens, the joint line remnant is noticeable at the centre of the weld. This could be explained by a lower temperature due to the volatilisation of the sealant solvent, which acts as a thermal barrier leading to an incomplete dispersion of the oxide films.

In this study, shear fracture through the interface was mainly observed for the RFSSW AA7075-T6 welds. This result was expected considering the strong presence of oxide films on the joint line remnant, as shown in Figure 5.23.C). The oxide films provided poor consolidation in this area and promoted the crack propagation from the hook through the weld interface. The opposite is true for the RFSSW AA2024-T3 welds where shear through the plug on the top sheet was mainly observed.

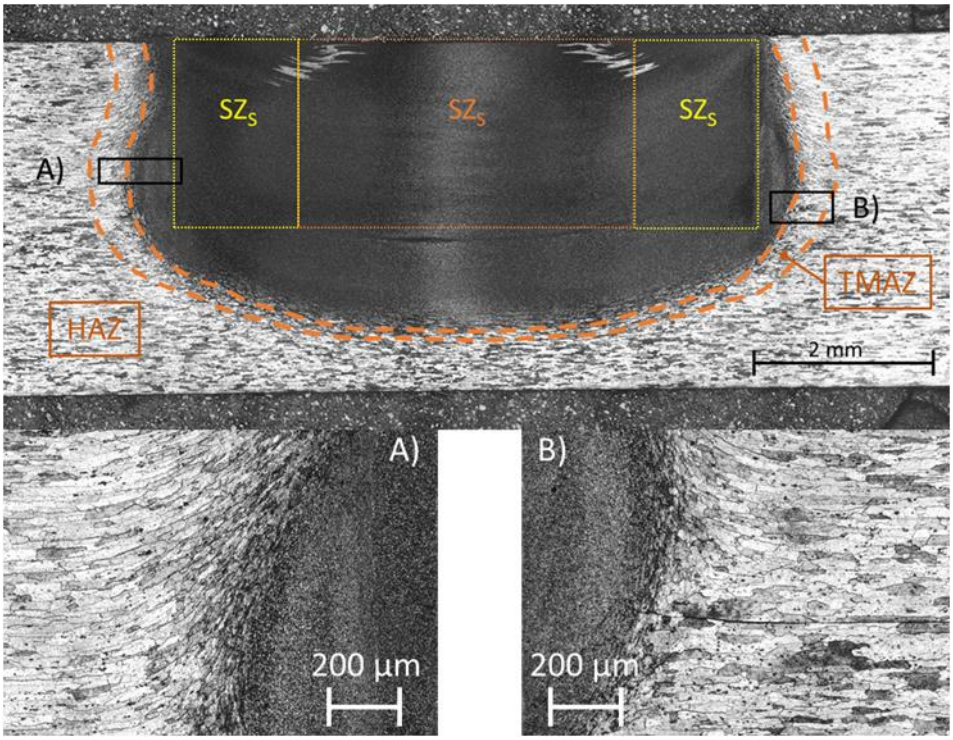

Figure 5.22 - Cross-section of RFSSW AA2024-T3 using Tool 3 with interfacial sealant:
A) SZ/TMAZ interface;
B) Hook region.

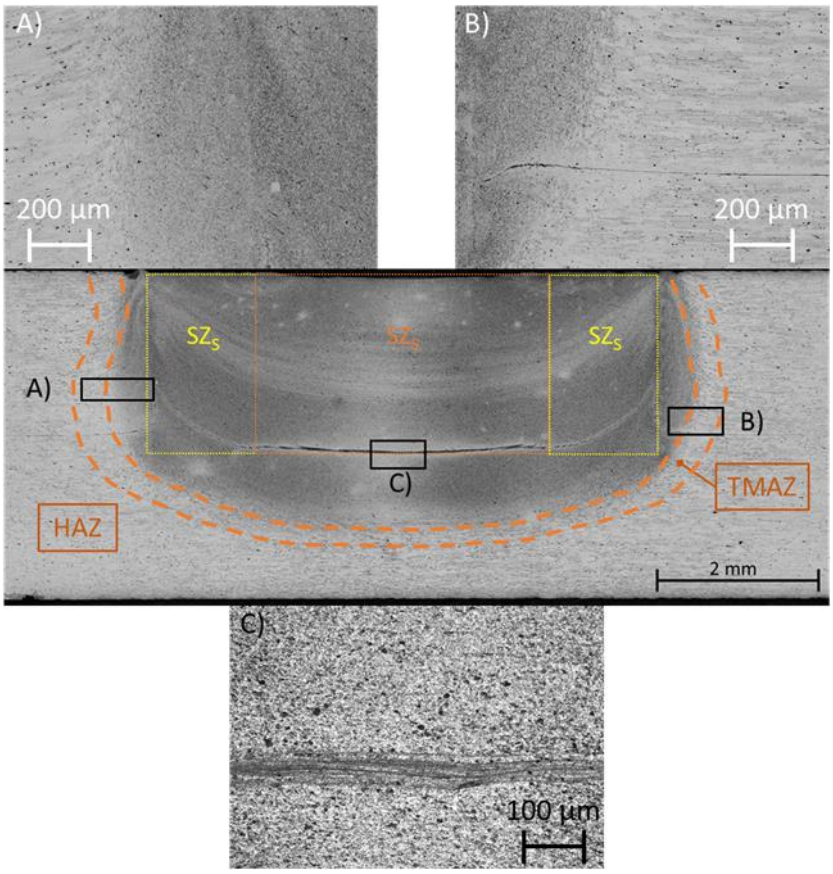

Figure 5.23 - Cross-section of RFSSW AA7075-T6 using Tool 3 with interfacial sealant:
A) SZ/TMAZ interface;
B) Hook region;
C) Joint line remnant.

5.3.3. Tool fracture analysis

As described in Section 5.2.7, the life of RFSSW Tool 2 and 3 was determined by producing multiple welds on an AA7075-T7451 plate. This activity was performed without tool inter-cleaning and until tool fracture occurred. Tool 2 fractured after 92 welds while Tool 3 fractured after 55 welds. The fracture surfaces of the tool components from Tool 2 and 3 are presented in Figure 5.24 and Figure 5.25, respectively. Both tool failures occurred on the probe component, with the fracture being located on the 4 mm side of the transition radius region. The type of fracture observed in this study originates from rotating-bending fatigue conditions commonly observed in axles, as well as medical devices (de Freitas et al. 2011; Yan, Yang and Qi 2006)

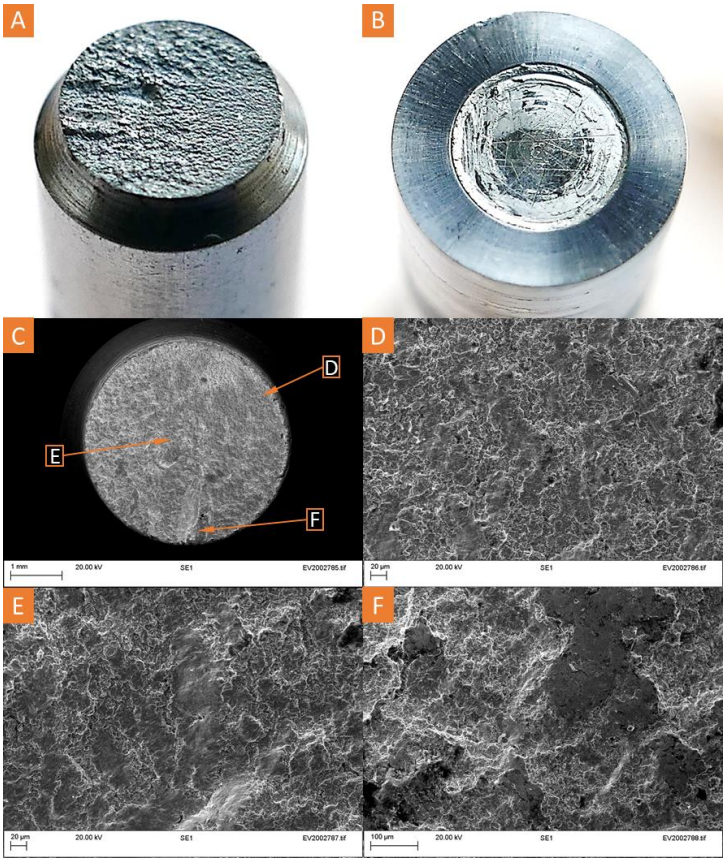

Figure 5.24 - Fracture surface of the components from Tool 2 after 92 welds:
A) Probe;
B) Shoulder, with fractured portion of probe;
C) SEM fractography of the probe component;
D) High magnification region – location shown in Figure 5.24.C);
E) High magnification region – location shown in Figure 5.24.C);
F) High magnification region – location shown in Figure 5.24.C).

Considering that the probe component has vertical independent movement whilst concentrically assembled with the shoulder, the external surfaces of both components, as well as the internal surface of the shoulder require a ground finish. This operation ensures that, after the hardening and tempering process, the diameter of these surfaces is within the tolerance specified in the drawing and the total runout is minimised. The maximum total radial runout for the probe is 40 µm as specified by the component drawing in the Appendices (Figure A0.3). This tolerance was determined considering the clearance between the probe and the shoulder, 60 µm, aiming to reduce the likelihood of interference.

However, when assembling the tool components, a total runout of 80 µm was observed whilst rotating the probe component. This superior value means that, under service conditions with both components rotating at the same speed and direction, the probe would have intermittent

contact with the inside surface of the shoulder and experiencing bending stresses. The continuous contact between these two components can lead to the development of microcracks at the surface of the component ultimately resulting in failure. This phenomenon can be seen in Figure 5.24.A) and Figure 5.25.A) by the difference in striation appearance, where the smoother surface indicates cyclic and continuous crack propagation while the rougher surface with river markings is indication of a predominantly brittle fracture mode. The crack initiation point is consistent with the location of the highest runout value on the probe component.

Another cause for the premature failure if the tools could be the weld material entrapment between the components. Once the probe failure occurred, the broken portion of this component was stuck to the inside of the shoulder, as seen in Figure 5.24.B). and Figure 5.25.B). Figure 5.25.B) exhibited a layer of intermetallic compounds of noticeable thickness while a considerable amount of accumulated material between the components can be observed in Figure 5.24.B). As mentioned in Chapter 4, this entrapment of material could restrict the motion of the tool components during welding, producing a sudden fracture. The continuous build-up of aluminium intermetallic compounds on a H13 steel RFSSW toolset was also observed in the study conducted by Larsen, Hunt and Hovanski (2020). In their study, the experimented tools had considerably short tool life (53 and 48 welds for different process parameter combinations) as to what would be required in high-volume production. The authors showed that the affinity between the steel tool and the aluminium workpiece promoted the continuous intermetallic compound growth outward from surface of the probe and inward from the surface of the shoulder. The estimation by the authors suggest that this layer can reach more than a third of the clearance between the two components, leading to the seizing of the tool components.

Finally, the location of the fracture can be attributed to the design of the probe component and the transition radius region in the main body. Due to the difference in diameters of the probe component, the presence of this transition region presents a stress concentration area and a highly probable area for the component to fracture. Considering that both RFSSW tools fractured in this region, this suggests that a redesign of this component is required.

The premature and unexpected failure of these components can be attributed to the interaction of three distinct causes presented in this section. To potentially increase the life expectancy of the RFSSW tooling, these points should be addressed and complimented with further research

into manufacturing routes as well as effective coatings to prevent material entrapment and prevent joining of tool components during welding.

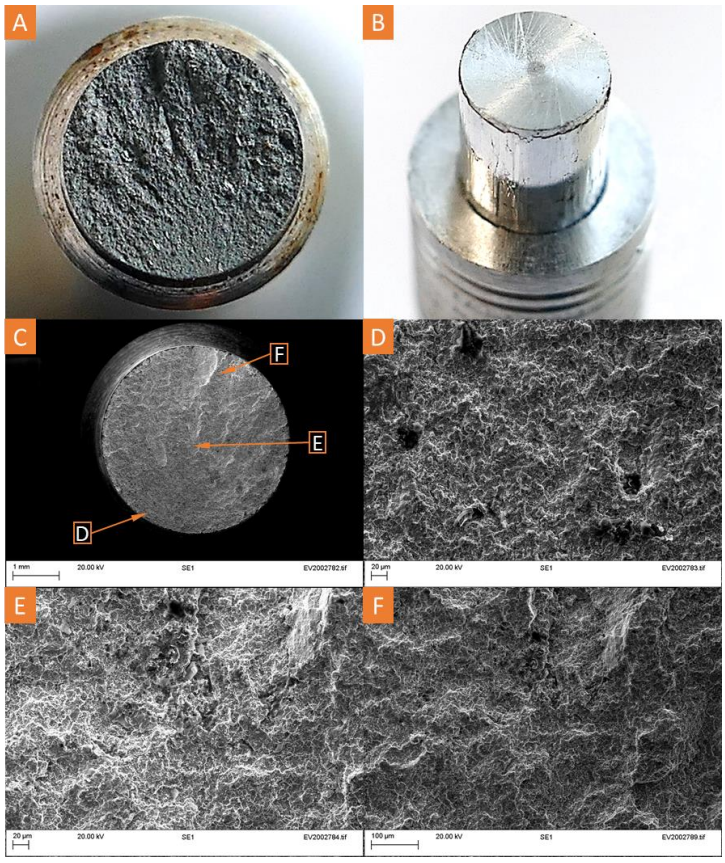

Figure 5.25 - Fracture surface of the components from Tool 3 after 55 welds:
A) Probe;
B) Shoulder, with fractured portion of probe;
C) SEM fractography of the probe component;
D) High magnification region – location shown in Figure 5.25.C);
E) High magnification region – location shown in Figure 5.25.C);
F) High magnification region – location shown in Figure 5.25.C).

5.4 Conclusions

The relationship between RFSSW tool design and material with the weld mechanical performance and microstructure was addressed. M42 high speed steel in hardened and tempered condition was used to manufacture RFSSW with different profiles and compare its performance against a conventional RFSSW tool. Lap shear tests were performed to quantify the mechanical strength of welds produced with various tool material and design combinations. Cross-section analysis was conducted to understand the influence of different tool profiles and materials on the weld microstructure. The following conclusions can be drawn from the present investigation:

- The highest weld peak temperature was measured for Tool 1. The featureless design and higher thermal conductivity of the material lead to an increase of the weld cycle time, increasing the processing time between the tool and base material.
- RFSSW lap shear strength values in bare condition varied between 8.69 and 9.10 kN for AA2024-T3 welds, 6.58 to 7.09 kN for AA5754-H24 and between 8.62 and 10.72 kN for AA7075-T6 welds. These results surpassed the minimum strength requirements for resistance spot welding defined by AWS D17.2/D17.2M:2013.
- RFSSW lap shear strength values in bare condition of AA2024-T3 and AA7075-T6 performed with Tool 3 surpassed the shear strength requirements for an equivalent AA2024-T31 solid rivet.
- Using the best performing process parameters from Chapter 3, all tool material and design variants produced fully consolidated welds with the typical microstructure and metallurgical features of RFSSW. Tool 3 produced larger weld areas due to the increased stirring action from the external tool features. This design also produced welds with small hook heights, contributing to the increase in lap shear performance.
- For the same tool material, a threaded shoulder profile (Tool 3) produced welds with stronger shear strength values. This result highlights the need for further research in this topic, by testing various tool profiles.
- Similar strength results observed for the tools made from different materials with the same profile. This suggests that the tool profile has a greater influence on the mechanical strength of the weld compared to the choice of material.
- M42 high speed steel in hardened and tempered condition can be used as a reliable alternative tool material for RFSSW. However, a considerable material entrapment inside the shoulder was observed which emphasises the need for further investigation into effective coating techniques.
- Both Tool 2 and 3 experienced a failure on the transition radius on the probe component due to cyclic rotating-bending stresses. Additional to the recommendations presented in the previous point, improvements to the fabrication route, component design and tolerances could potentially increase tool life expectancy.

RFSSW of AA2024-T3 and AA7075-T6 in the presence of an aerospace grade sealant was performed for all tool material and design variants. This specimen variant was used to determine

the impact of an interfacial sealant on the tool performance and weld properties. From the present investigation the following conclusions can be drawn:

- Fully consolidated welds were produced for both alloys using all tool variants. Similar microstructure to the bare condition was observed, with more noticeable surface oxides at the centre of the stir zone due to reduced plastic deformation in this area.
- The disparity between the RFSSW shear strength values of Tool 1 and 2 suggests that a correct choice of tool material is imperative to maximise the weld mechanical performance. However, the threaded shoulder design produced stronger welds for the same tool material.
- The presence of an interfacial sealant improved the shear strength of AA7075-T6 welds performed with all tool variants, maintaining the same trend observed for the bare condition. The explanation for this improvement is analogous to the reason presented in Chapter 3.
- The same trend observed for the bare conditions was not observed for the welds with interfacial sealant on AA2024-T3. Despite the similar behaviour under lap shear conditions, welds produced with Tool 1 and 3 displayed an increase in shear strength, whilst no improvement was noticed for welds performed with Tool 2.

Chapter 6

Thesis conclusions and recommendations for further research

This chapter presents a summary of the work performed in this thesis as well as the main conclusions of each chapter. Finally, based on the knowledge gathered from this work, several research topics are recommended for further investigation.

6.1 Thesis Summary

Based on the findings and recommendations from Chapter 2, the aim of this thesis was to further understand the relationship between RFSSW tool design and material with the mechanical performance and microstructural features of the joint produced.

In Chapter 3, a design of experiments approach was used to investigate the effect of RFSSW process parameters on the mechanical performance and microstructure of AA2024-T3, AA5754-H24 and AA7075-T6. In addition to this topic, the impact of an interfacial sealant on RFSSW joints was also investigated. Furthermore, fatigue testing and residual stress measurements were performed on all alloys. The results suggest that plunge depth had the greatest impact on weld mechanical strength on all alloys tested, while welding conditions promoting lower heat input tended to improve the shear strength. The use of sealant did not affect the weld cycle and increased the shear strength of the specimen by preventing out-of-plane bending. The peak residual stress was measured at the centre of the spot-weld and its value to be dependent on the nature of the alloy as well as the number of spot-welds in the specimen.

In Chapter 4, various tool material and surface modification combinations were selected to determine the most promising tool material candidates for RFSSW based on industrially relevant criteria (e.g. process repeatability, tool life, joint mechanical properties). In this investigation, five tool material and surface modification combinations were tested under RFSSW service conditions. M42 high speed steel without surface modifications was determined to be a suitable RFSSW tool material candidate due to a consistent performance under service conditions, low surface wear and cost-effective solution. This tool material was used to manufacture RFSSW tools to test in Chapter 5

In Chapter 5, the effect of different tool materials and geometries on the mechanical performance was investigated. Three RFSSW tools made from different combinations of tool materials and designs were used to produce lap shear testing specimens. Shear strength results showed that on all alloys the addition of an external groove feature on the shoulder component led to an improvement of the mechanical strength of the weld, with and without the presence of an interfacial sealant. This design also produced bigger weld areas. The use of M42 high speed steel material on a simple RFSSW tool design showed to have a detrimental effect on the mechanical performance, leading to the conclusion that tool material should be regarded as a key design consideration to maximise weld performance.

This thesis contributed to the further development of RFSSW, establishing both a theoretical and technical basis for new researchers or industrial users searching for alternative single point joining methods. The results from this research are novel and have significant, practical implications to aid further industrial development and implementation of RFSSW.

6.2 Recommendations for Further Research

The research that has been described in this thesis contributed significantly to expand the knowledge of RFSSW process. Despite this knowledge advancement, many research topics remain to be addressed. Using this thesis as a baseline for further research, further research into the previously and newly identified research topics will facilitate the industrialisation of the RFSSW process.

Some recommended areas for future work are:

- **Further research on tool designs and materials:** In the course of this investigation, a limited selection of tool materials and designs were investigated. The outcome of the investigation highlighted the potential for further research in this field, with various tool materials, coatings and designs to explore. The outcome from further research in this field as well as a more in-depth analysis of the fatigue cycle for each tool set, could lead to improvements on weld mechanical performance as well as a better understanding of the material flow on different tool materials and designs. Furthermore, an increase in tool life expectancy and the development of more cost-effective tooling solutions could be achieved, which would provide crucial data for preventive maintenance and process control.
- **Development of further mechanical performance data:** The outcome of the testing performed in Chapter 5 confirmed that the tool material and design used in RFSSW influence the weld mechanical and microstructural properties. Understanding the effect of different tool materials and designs on the joint mechanical performance will require further mechanical testing, performed under service conditions, along with residual stress measurements. The outcome of this research would provide the data to predict failure loads along with the locations in a component under service conditions. Predicting fracture modes as well as modelling the stress distribution in large assemblies would also allow design engineers to better design components.
- **Extended testing on samples with sealant:** The investigation conducted in Chapter 3 provided a deeper understanding of the weld properties than in Chapter 5, as mentioned in the

previous point. However, more conclusive results on the residual stress distribution are required. This can be addressed by comparison with other residual stress measurement techniques. A further understanding of the impact of residual stress distribution on the joint performance is also a key topic of study to expand the current understanding of the RFSSW process. Further studies into the corrosion behaviour of bare and samples with sealant are also pertinent to better understand and improve the RFSSW process. The effect of interfacial sealant in the residual stress distribution of a multiple spot-weld component is also a topic of industrial relevance.

- Compare with established technologies: When assessing the suitability of the RFSSW process to replace traditional processes used in industry (e.g. spot-welding and fastening processes), it is vital to compare the mechanical performance results following the same standards. However, the information from the standards generally provides a minimum threshold and (to the best of the author's knowledge) a study directly comparing the aforementioned technologies using the same material and procedures has not been published. Such a study would provide a benchmark of mechanical performance, as well as an analysis on the advantages and shortcomings of each technology.
- RFSSW on anodised materials: Oxide films formed by anodizing processes produce materials that have better mechanical performance, as well as, improved corrosion and abrasion resistance. This is a common practice in the aerospace industry since that aircraft structures operate in extremely variable environmental conditions. However, the oxide layer produced during anodizing can generate defects in the weld if not dispersed effectively. The same principle applies to other corrosion protection treatments such as paints. Future work in this area could consider the effect of different tool designs aimed at promoting a more even dispersion of these films, without a detrimental effect on the joint mechanical performance.

References

Adamus, J. and Adamus, K., (2019). The analysis of reasons for defects formation in aluminum joints created using RFSSW technology. *Manufacturing Letters*, *21*, pp.35-40.

Ahmad, B., van der Veen, S.O., Fitzpatrick, M.E. and Guo, H., (2018). Measurement and modelling of residual stress in wire-feed additively manufactured titanium. *Materials Science and Technology*, *34*(18), pp.2250-2259.

Ahn, B.W., Choi, D.H., Kim, D.J. and Jung, S.B., (2012) Microstructures and properties of friction stir welded 409L stainless steel using a Si3N4 tool. *Materials Science and Engineering: A*, *532*, pp.476-479.

Akhtar, S.S., Arif, A.F.M. and Yilbas, B.S., (2012) Influence of multiple nitriding on the case hardening of H13 tool steel: experimental and numerical investigation. *The International Journal of Advanced Manufacturing Technology*, *58*(1-4), pp.57-70.

Amancio-Filho, S. T., Bueno, C., Dos Santos, J. F., Huber, N., & Hage Jr, E. (2011-A). On the feasibility of friction spot joining in magnesium/fiber-reinforced polymer composite hybrid structures. *Materials Science and Engineering: A*, *528*(10-11), 3841-3848.

Amancio-Filho, S. T., Camillo, A. P., Bergmann, L., Dos Santos, J. F., Kury, S. E., and Machado, N. G. (2011-B) Preliminary Investigation of the Microstructure and Mechanical Behaviour of 2024 Aluminium Alloy Friction Spot Welds. *Materials Transactions* 52 (5), 985-991

Amini, A., Asadi, P., and Zolghadr, P. (2014) 15-Friction Stir Welding Applications in Industry. in Givi, M. K. B. and Asadi, P., *Advances in Friction-Stir Welding and Processing*., Woodhead Publishing, 671-722

Andres, J., Wrońska, A., Gałaczyński, T., Luty, G., & Burek, R. (2018). Effect of Process Parameters on Microstructure and Mechanical Properties of RFSSW Lap Joints of Thin Al7075-T6 Sheets. *Archives of Metallurgy and Materials*, *63*.

ASM International Handbook Committee (1989) *ASM Handbook, Volume 16-Machining*. ASM International.

Automation, A., (2005). Mazda develops world's first steel and aluminium joining technology using friction heat. Vol. 25, No. 4

Avallone, E.A., (2007). *Marks' standard handbook for mechanical engineers*. The McGraw-Hill Companies, Inc.

AZoM (2001) *Silicon Nitride (Si3N4) Properties and Applications* [online] available from <https://www.azom.com/article.aspx?ArticleID=53> [2nd June 2020]

Barnes, S.J., Bhatti, A.R., Steuwer, A., Johnson, R., Altenkirch, J. and Withers, P.J., (2012). Friction stir welding in HSLA-65 steel: Part I. Influence of weld speed and tool material on microstructural development. *Metallurgical and Materials Transactions A*, *43*(7), pp.2342-2355.

Boldsaikhan, E., Fujimoto, M., Kamimuki, K., Okada, H., Duncan, B., Bui, P. and Handyside, A. (2016). Refill Friction Stir Spot Joining Rivet Replacement Technology (No. 2016-01-2130). *SAE Technical Paper.*

Boldsaikhan, E., Fukada, S., Fujimoto, M., Kamimuki, K. and Okada, H., (2019). Refill friction stir spot welding of surface-treated aerospace aluminum alloys with faying-surface sealant. *Journal of Manufacturing Processes*, *42*, pp.113-120.

Boldsaikhan, E., Fukada, S., Fujimoto, M., Kamimuki, K., Okada, H., Duncan, B., Bui, P., Yeshiambel, M., Brown, B., and Handyside, A. (2017) Refill Friction Stir Spot Joining for Aerospace Aluminum Alloys. in Hovanski Y., Mishra R., Sato Y., Upadhyay P., Yan D. ed*, Friction Stir Welding and Processing IX*., 237-246

Bond technologies (2018) *Refill Friction Stir Spot Welding Machine: Discreet solid state bonding system* [online] available from < https://bondtechnologies.net/products/friction-stir-welding-machines/refill-spot-welding/> [6th July 2020]

Buffa, G., Fratini, L., Micari, F. and Settineri, L., (2012). On the choice of tool material in friction stir welding of titanium alloys. *Proceedings of NAMRI/SME*, *40*.

Camilo, A., Pieta, G., Brzostek, R., Suhuddin, U., Goushegir, S., Amancio, S., and dos Santos, J. (2014) *A Review on Microstructure and Properties of Friction Stir Spot Welds (Refill) in Aircraft Aluminium Alloys* Boeing Longacres Customer Centre Renton, WA

Campanelli, L. C., Alcântara, N. G. d., and Santos, J. F. d. (2011) Solid State Spot Welding of Lightweight Alloys. *Soldagem & Inspeção* 16 (3), 301-307

Campanelli, L. C., Antonialli, A. Í. S., Alcântara, N. G. D., Bolfarini, C., Suhuddin, U. F. H., & Santos, J. F. D. (2013-A). Lap shear test of a magnesium friction spot joint: numeric modeling. *Tecnologia em Metalurgia, Materiais e Mineração*, *10*(2), 97.

Campanelli, L. C., Suhuddin, U. F. H., Antonialli, A. Í. S., Dos Santos, J. F., De Alcantara, N. G., & Bolfarini, C. (2013-B). Metallurgy and mechanical performance of AZ31 magnesium alloy friction spot welds. *Journal of Materials Processing Technology*, *213*(4), 515-521.

Campanelli, L. C., Suhuddin, U. F. H., Santos, J. F. D., & Alcântara, N. G. D. (2012). Parameters optimization for friction spot welding of AZ31 magnesium alloy by Taguchi method. *Soldagem & Inspeção*, *17*(1), 26-31.

Cao, J.Y., Wang, M., Kong, L. and Guo, L.J., (2016). Hook formation and mechanical properties of friction spot welding in alloy 6061-T6. *Journal of Materials Processing Technology*, *230*, pp.254-262.

Cao, J.Y., Wang, M., Kong, L., Zhao, H.X. and Chai, P., (2017). Microstructure, texture and mechanical properties during refill friction stir spot welding of 6061-T6 alloy. *Materials Characterization*, *128*, pp.54-62.

Cao, J.Y., Zhang, C.C., Xing, Y.F. and Wang, M., (2020). Pin plunging reinforced refill friction stir spot welding of Alclad 2219 to 7075 alloy. *Journal of Materials Processing Technology*, p.116760.

Cardillo, M. E., Shen, J., de Alcântara, N. G., Afonso, C. R., & dos Santos, J. F. (2018). Effect of friction spot welding parameters on the joint formation and mechanical properties of Al to Cu. *Welding in the World*, 1-9.

Carl Zeis AG (2013). *CONTURA® G2 Specifications.* Germany

Çevik, B., Özçatalbaş, Y. and Gülenç, B., (2016). Effect of tool material on microstructure and mechanical properties in friction stir welding. *Materials Testing*, *58*(1), pp.36-42.

Chandrashekar, A., Kumar, B.A. and Reddappa, H.N., (2015). Friction Stir Welding: Tool Material and Geometry. *Akgec Internatıonal Journal of Technology*, *6*(1-4), pp.16-20.

Chen, K., Liu, X. and Ni, J., (2017). Keyhole refilled friction stir spot welding of aluminum alloy to advanced high strength steel. *Journal of Materials Processing Technology*, *249*, pp.452-462.

Chen, Y., Chen, J., Shalchi Amirkhiz, B., Worswick, M. J., & Gerlich, A. P. (2015). Microstructures and properties of Mg alloy/DP600 steel dissimilar refill friction stir spot welds. *Science and Technology of Welding and Joining*, *20*(6), 494-501.

Colligan, K. (2010) The Friction Stir Welding Process: An Overview. in Lohwasser, D. and Chen, Z. ed. - *Friction stir welding from basics to applications*, 1st ed. Woodhead Publishing Limited, 2010, 15-41

da Silva, A. A. M., dos Santos, J. F., Rosendo, T. R., Ramos, F. D., Mazzaferro, C. C. P., Tier, M. A. D. and Strohaecker, T. R. (2007-A). Performance evaluation of 2-mm thick alclad AA2024 T3 aluminium alloy friction spot welding (No. 2007-01-3812). *SAE Technical Paper*.

Da Silva, A.M., Tier, T.R., Ramos, F.D., Mazzaferro, C., Mazzaferro, J., Bergmann, L., Strohaecker, T.R. and dos Santos, J.F., (2007-B). Friction spot and friction stir spot welding processes–a literature review. *Bulletin of National R&D Institute for Welding and Material Testing*, *3*, pp.36-44.

Davis, J.R. (ed.) (2000) *Nickel, cobalt, and their alloys*. ASM international.

De Backer, J., & Bolmsjö, G. (2013). Thermoelectric method for temperature measurement in friction stir welding. *Science and Technology of Welding and Joining*, *18*(7), 558-565.

de Castro, C. C., Plaine, A. H., Dias, G. P., de Alcântara, N. G., & dos Santos, J. F., (2018-B). Investigation of geometrical features on mechanical properties of AA2198 refill friction stir spot welds. *Journal of Manufacturing Processes*, *36*, pp. 330-339.

de Castro, C.C., Plaine, A.H., de Alcântara, N.G. and dos Santos, J.F., (2018-A). Taguchi approach for the optimization of refill friction stir spot welding parameters for AA2198-T8 aluminum alloy. *The International Journal of Advanced Manufacturing Technology*, *99*(5-8), pp.1927-1936.

De Freitas, M., Reis, L., Da Fonte, M. and Li, B., (2011). Effect of steady torsion on fatigue crack initiation and propagation under rotating bending: Multiaxial fatigue and mixed-mode cracking. *Engineering Fracture Mechanics*, *78*(5), pp.826-835.

Deng, L., Li, S., Ke, L., Liu, J. and Kang, J., (2019). Microstructure and fracture behavior of refill friction stir spot welded joints of AA2024 using a novel refill technique. *Metals*, *9*(3), p.286.

Derlatka, A. and Kasza, P., (2014a). Numerical analysis of aluminium cellular beams with cells of different diameters. In *Advanced Materials Research* (Vol. 1020, pp. 151-157). Trans Tech Publications.

Derlatka, A. and Kasza, P., (2014b). Numerical analysis of aluminum cellular beams with cells of different arrangement. In *Advanced Materials Research* (Vol. 1020, pp. 158-164). Trans Tech Publications.

Ding, Y., Shen, Z., and Gerlich, A. (2017) Refill Friction Stir Spot Welding of Dissimilar Aluminum Alloy and AlSi Coated Steel. *Journal of Manufacturing Processes* 30, 353-360

Effertz, P. S., Infante, V., Quintino, L., Suhuddin, U., Hanke, S., & Dos Santos, J. F. (2016). Fatigue life assessment of friction spot welded 7050-T76 aluminium alloy using Weibull distribution. *International journal of fatigue*, *87*, 381-390.

Effertz, P., Quintino, L., and Infante, V. (2017) The Optimization of Process Parameters for Friction Spot Welded 7050-T76 Aluminium Alloy using a Taguchi Orthogonal Array. *The International Journal of Advanced Manufacturing Technology* 91 (9-12), 3683-3695

Esteves, J., Goushegir, S., Dos Santos, J., Canto, L., Hage Jr, E., and Amancio-Filho, S. (2015) Friction Spot Joining of Aluminum AA6181-T4 and Carbon Fiber-Reinforced Poly (Phenylene Sulfide): Effects of Process Parameters on the Microstructure and Mechanical Strength. *Materials & Design* 66, 437-445

Farias, A.D., Batalha, G.F., Prados, E.F., Magnabosco, R. and Delijaicov, S., (2013). Tool wear evaluations in friction stir processing of commercial titanium Ti–6Al–4V. *Wear*, *302*(1-2), pp.1327-1333.

Feng, X.S., Li, S.B., Tang, L.N. and Wang, H.M., (2020). Refill Friction Stir Spot Welding of Similar and Dissimilar Alloys: A Review. *Acta Metallurgica Sinica (English Letters)*, *33*(1), pp.30-42.

Fernandez, G.J. and Murr, L.E., (2004). Characterization of tool wear and weld optimization in the friction-stir welding of cast aluminum 359+ 20% SiC metal-matrix composite. *Materials Characterization*, *52*(1), pp.65-75.

Frankel, P., Preuss, M., Steuwer, A., Withers, P.J. and Bray, S., (2009). Comparison of residual stresses in Ti–6Al–4V and Ti–6Al–2Sn–4Zr–2Mo linear friction welds. *Materials Science and Technology*, *25*(5), pp.640-650.

Fu, B (2019) 'Texture development of a modified refill friction stir spot weld of AM50 magnesium alloy'. 6th International Conference on Scientific and Technical Advances on Friction Stir Welding & Processing. Held 11th-13th September 2019 at Université catholique de Louvain - Belgium

Fukada, S., Ohashi, R., Fujimoto, M., & Okada, H. (2014). Refill friction stir spot welding of dissimilar materials consisting of A6061 and hot dip zinc-coated steel sheets. In *Proceedings of the 1st international joint symposium on joining and welding* (pp. 183-187).

Fuller, C. B. (2007) Friction Stir Tooling: Tool Materials and Designs. *Friction Stir Welding and Processing*, 7-36

Gerlich, A., Yamamoto, M. and North, T.H., (2008). Local melting and tool slippage during friction stir spot welding of Al-alloys. *Journal of materials science*, *43*(1), pp.2-11.

Gonçalves, J. (2015) Soldagem Pontual Por Fricção (FSpW) De Poliamida 6 MSc Thesis Universidade Federal de São Carlos

Gonçalves, J., dos Santos, J. F., Canto, L. B., & Filho, S. T. A. (2016). Improvement of friction spot welding (FSpW) to join polyamide 6 and polyamide 66/carbon fibre laminate. *Welding international*, *30*(4), 247-254.

Gonçalves, J., dos Santos, J., Canto, L., and Amancio-Filho, S. (2015) Friction Spot Welding of Carbon Fiber-Reinforced Polyamide 66 Laminate. *Materials Letters* 159, 506-509

Goushegir, S., Dos Santos, J., and Amancio-Filho, S. (2015) Influence of Process Parameters on Mechanical Performance and Bonding Area of AA2024/carbon-Fiber-Reinforced Poly (Phenylene Sulfide) Friction Spot Single Lap Joints. *Materials & Design* 83, 431-442

Goushegir, S., Dos Santos, J., and Amancio-Filho, S. (2016) Failure and Fracture Micro-Mechanisms in Metal-Composite Single Lap Joints Produced by Welding-Based Joining Techniques. *Composites Part A: Applied Science and Manufacturing* 81, 121-128

Gründer, M. (2014) Duales Studium bei Premium AEROTEC (Teil 2) Vielfältige Karriereaussichten. *Flug Revue* [online]. Available from https://www.flugrevue.de/jobs/luftfahrtberufe/duales-studium-bei-premium-aerotec-vielfaeltige-karriereaussichten/542996?seite=2 [21st March 2018]

Hameister, H. and Bock, M., (2011). Solid-State Spot Welding (Friction Spot Welding and Friction Stir Spot Welding) as a Bonding Technique to Replace the Process of Riveting within the Aircraft Industry? (No. 2011-01-2499). *SAE Technical Paper*.

Hameister, H., (2013). Increasing Competitiveness and Sustainability in Structural Assembly by Using Friction Spot Welding (No. 2013-01-0835). *SAE Technical Paper*.

Horie, S., Shinozaki, K., Yamamoto, M., North, T.H. and Gerlich, A., (2010). Effect of microstructure on liquation cracking during AZ91 friction stir spot welding. *Science and Technology of Welding and Joining*, *15*(8), pp.671-675.

Huang, Y., Meng, X., Xie, Y., Lv, Z., Wan, L., Cao, J., & Feng, J. (2018). Friction spot welding of carbon fiber-reinforced polyetherimide laminate. *Composite Structures*, *189*, 627-634.

Infante, V. and Vidal, C. (2014) 5 - Tool and Welding Design. in *Advances in Friction-Stir Welding and Processing*. ed. by Givi, M. K. B. and Asadi, P., Woodhead Publishing, 199-240

Itapu, S.K. and Muci-Küchler, K.H., (2006). Visualization of Material Flow in the Refill Friction Stir Spot Welding Process (No. 2006-01-1206). *SAE Technical Paper.*

Iwashita, T., Mazda Motor Corp, (2003). *Method and apparatus for joining*. U.S. Patent 6,601,751

Jadhav, G. and Dalu, R. (2014) Friction Stir Welding–Process Parameters and its Variables: A Review. *International Journal of Engineering and Computer Science* 3, 6325-6328

Ji, S., Li, Z., Wang, Y., Ma, L., and Zhang, L. (2017-A) Material Flow Behavior of Refill Friction Stir Spot Welded LY12 Aluminum Alloy. *High Temperature Materials and Processes* 36 (5), 495-504

Ji, S., Wang, Y., Li, Z., Yue, Y., and Chai, P. (2017-B) Effect of Tool Geometry on Material Flow Behavior of Refill Friction Stir Spot Welding. *Transactions of the Indian Institute of Metals* 70 (6), 1417-1430

Kalagara, S. and Muci-Küchler, K. (2007) 'Numerical Simulation of a Refill Friction Stir Spot Welding Process'. *Friction Stir Welding and Processing IV*, 369-378

Khaliq, A. and Bharti, P.K., (2015). Influence of tool material on mechanical properties of AA6061-O during the friction stir welding process. *IOSR J. Mech. Civ. Eng., e-ISSN*, pp.2278-1684.

Khodaverdizadeh, H., Heidarzadeh, A. and Saeid, T., (2013). Effect of tool pin profile on microstructure and mechanical properties of friction stir welded pure copper joints. *Materials & Design*, *45*, pp.265-270.

Kim, Y.G., Kim, I.J., Kim, J.S. and Park, J.H., (2014) Mechanical properties and tool life of friction-stir-welded DP590 using the Si3N4 tool. *Materials Transactions*, *55*(10), pp.1557-1563.

Klender, J., (2020) *Tesla leverages SpaceX welding technique in Model Y components* [online] available from <https://www.teslarati.com/tesla-model-y-spacex-welding-technique-analysis-video/> [9 July 2020]

Kluz, R., Kubit, A., Trzepiecinski, T., Faes, K. and Bochnowski, W., (2019). A weighting grade-based optimization method for determining refill friction stir spot welding process parameters. *Journal of Materials Engineering and Performance*, *28*(10), pp.6471-6482.

Krishnan, K.N., (2002). On the formation of onion rings in friction stir welds. *Materials science and engineering: A*, *327*(2), pp.246-251.

Kubit, A., Bucior, M., Wydrzyński, D., Trzepieciński, T., & Pytel, M. (2018-A). Failure mechanisms of refill friction stir spot welded 7075-T6 aluminium alloy single-lap joints. *The International Journal of Advanced Manufacturing Technology*, *94*(9-12), 4479-4491.

Kubit, A., Kluz, R., Trzepieciński, T., Wydrzyński, D., & Bochnowski, W. (2018-B). Analysis of the mechanical properties and of micrographs of refill friction stir spot welded 7075-T6 aluminium sheets. *Archives of Civil and Mechanical Engineering*, *18*(1), 235-244.

Kubit, A., Trzepiecinski, T., Faes, K., Drabczyk, M., Bochnowski, W. and Korzeniowski, M., (2019-A). Analysis of the effect of structural defects on the fatigue strength of RFSSW joints using C-scan scanning acoustic microscopy and SEM. *Fatigue & Fracture of Engineering Materials & Structures*, *42*(6), pp.1308-1321.

Kubit, A., Trzepiecinski, T., Święch, Ł., Faes, K. and Slota, J., (2019-B). Experimental and numerical investigations of thin-walled stringer-stiffened panels welded with RFSSW technology under uniaxial compression. *Materials*, *12*(11), p.1785.

Kwee, I., De Waele, W. and Faes, K., (2019). Weldability of high-strength aluminium alloy EN AW-7475-T761 sheets for aerospace applications, using refill friction stir spot welding. *Welding in the World*, *63*(4), pp.1001-1011.

Lacki, P. and Derlatka, A. (2016) Experimental and Numerical Investigation of Aluminium Lap Joints made by RFSSW. *Meccanica* 51 (2), 455-462

Lacki, P. and Derlatka, A. (2017) Strength Evaluation of Beam made of the Aluminum 6061-T6 and Titanium Grade 5 Alloys Sheets Joined by RFSSW and RSW. *Composite Structures* 159, 491-497

Lacki, P. and Derlatka, A. (2018) 'Influence of PU Foam Reinforcement of I-Beam on Buckling Resistance'. *Composite Structures*

Lacki, P., Więckowski, W. and Wieczorek, P., (2015). Assessment of joints using friction stir welding and refill friction stir spot welding methods. *Archives of Metallurgy and Materials*, *60*(3), pp.2297-2306.

Lage, S. B. M., Campanelli, L. C., de Bribean Guerra, A. P., Shen, J., dos Santos, J. F., da Silva, P. S. C. P., and Bolfarini, C. (2018). A study of the parameters influencing mechanical properties and the fatigue performance of refill friction stir spot welded AlMgSc alloy. *The International Journal of Advanced Manufacturing Technology*, 1-10.

Larsen, B., Hunt, J. and Hovanski, Y., (2020). Investigating steel tool life in the RFSSW process. *Journal of Manufacturing Processes*, *58*, pp.637-645.

Larsen, B. and Hovanski, Y., (2020). Reducing Cycle Times of Refill Friction Stir Spot Welding in Automotive Aluminum Alloys (No. 2020-01-0224). *SAE Technical Paper*.

Leggatt, R.H., (2008). Residual stresses in welded structures. *International Journal of Pressure Vessels and Piping*, *85*(3), pp.144-151.

Li, Z., Ji, S., Ma, Y., Chai, P., Yue, Y., & Gao, S. (2016). Fracture mechanism of refill friction stir spot-welded 2024-T4 aluminum alloy. *The International Journal of Advanced Manufacturing Technology*, *86*(5-8), 1925-1932.

Lienert, T., Stellwag Jr, W., Grimmett, B., and Warke, R. (2003) Friction Stir Welding Studies on Mild Steel. *Welding Journal-New York*- 82 (1), 1-S

Liu, C. and Yi, X., (2013). Residual stress measurement on AA6061-T6 aluminum alloy friction stir butt welds using contour method. *Materials & Design*, *46*, pp.366-371.

Liu, F.C., Hovanski, Y., Miles, M.P., Sorensen, C.D. and Nelson, T.W., (2018). A review of friction stir welding of steels: Tool, material flow, microstructure, and properties. *Journal of Materials Science & Technology*, *34*(1), pp.39-57.

Liu, Z., Yang, K. and Yan, D., (2019). Refill Friction Stir Spot Welding of Dissimilar 6061/7075 Aluminum Alloy. *High Temperature Materials and Processes*, *38, pp.69-75.*

Łogin, W., Śliwa, R.E., Ostrowski, R. and Andres, J., (2019). The Influence of Tool Geometry for Refill Friction Stir Spot Welding (RFSSW) on Weld Properties During Joining Thin Sheets of Aluminum Alloys. *Archives of Metallurgy and Materials*, *64*.

Maggiolino, S. and Schmid, C. (2008) Corrosion Resistance in FSW and in MIG Welding Techniques of AA6XXX. *Journal of Materials Processing Technology* 197 (1-3), 237-240

Mandal, N.R., (2001). *Aluminium welding*. Woodhead publishing.

Mazzaferro, J. A. E., Rosendo, T. d. S., Mazzaferro, C. C. P., Ramos, F. D., Tier, M. A. D., Strohaecker, T. R., and Santos, J. F. d. (2009) Preliminary Study on the Mechanical Behavior of Friction Spot Welds. *Soldagem & Inspeção* 14 (3), 238-247

Mehta, M., Arora, A., De, A. and DebRoy, T., (2011). Tool geometry for friction stir welding—optimum shoulder diameter. *Metallurgical and Materials Transactions A*, *42*(9), pp.2716-2722.

Mohanty, H.K., Mahapatra, M.M., Kumar, P., Biswas, P. and Mandal, N.R., (2012). Effect of tool shoulder and pin probe profiles on friction stirred aluminum welds—a comparative study. *Journal of Marine Science and Application*, *11*(2), pp.200-207.

Montag, T., & Wulfsberg, J. (2014). Use of the Refill Friction Stir Spot Welding (RFSSW) Process as a Technology for bonding of Aluminum and fibre reinforced plastics. *Proceedings of Euro Hybrid Materials and Structures*.

Montag, T., Wulfsberg, J., Hameister, H., and Marschner, R. (2014) Influence of Tool Wear on Quality Criteria for Refill Friction Stir Spot Welding (RFSSW) Process. *Procedia CIRP* 24, 108-113

Mouritz A P, (2012): *Introduction to aerospace materials*. Cambridge: Woodhead Publishing Limited

Muci-Küchler, K. H., Kalagara, S., and Arbegast, W. J. (2010) Simulation of a Refill Friction Stir Spot Welding Process using a Fully Coupled Thermo-Mechanical FEM Model. *Journal of Manufacturing Science and Engineering* 132 (1), 014503

Muci-Küchler, K.H., Itapu, S.K., Arbegast, W.J. and Koch, K.J., (2005b). *Visualization of material flow in friction stir spot welding* (No. 2005-01-3323). SAE Technical Paper.

Muci-Küchler, K.H., Kakarla, S.S.T., Arbegast, W.J. and Allen, C.D., (2005a). *Numerical simulation of the friction stir spot welding process* (No. 2005-01-1260). SAE Technical Paper.

Nandan, R., DebRoy, T., and Bhadeshia, H. (2008) Recent Advances in Friction-Stir welding–process, Weldment Structure and Properties. *Progress in Materials Science* 53 (6), 980-1023

Nasiri, A. M., Shen, Z., Hou, J. S. C., and Gerlich, A. P. (2018) Failure Analysis of Tool used in Refill Friction Stir Spot Welding of Al 2099 Alloy. *Engineering Failure Analysis* 84, 25-33

Ojo, O.O., Taban, E. and Kaluc, E., (2015). Friction stir spot welding of aluminum alloys: A recent review. *Materials Testing*, *57*(7-8), pp.609-627.

Okada, H., Kamimuki, K., and Fujimoto, M. (2013) Assembly Study of Refill FSSW. *SAE International Journal of Aerospace* 6 (2013-01-2310), 299-304

Okada, H., Kashiki, H., Fukuhara, K. and Fujimoto, M., Kawasaki Jukogyo KK, (2015). *Friction stir spot welding device and friction stir spot welding method*. U.S. Patent 8,950,650.

Oliveira, P. (2012) 'Estudo das propriedades e desempenho mecânico de juntas soldadas por fricção pontual de poli (metacrilato de metila) (PMMA)' MSc thesis Universidade Federal de São Carlos

Oliveira, P. H. F. D., Amancio Filho, S. D. T., Santos, J. F. D., & Hage Junior, E. (2012). Feasibility study of the Friction Spot Welding (FSpW) process in thermoplastics. *Soldagem & Inspeção*, *17*(2), 96-103.

Oliveira, P., Amancio Filho, S., dos Santos, J., and Hage Jr, E. (2011) Influence of the Tool Material on the Microstructure and Mechanical Properties of Pmma Lap Joints Welded by Friction Spot. *Proc.: ANTEC-2011, Society of Plastics Engineers, 3rd may*, 1821-1825

Padhy, G.K., Wu, C.S. and Gao, S., (2018). Friction stir based welding and processing technologies-processes, parameters, microstructures and applications: A review. *Journal of Materials Science & Technology*, *34*(1), pp.1-38.

Palanivel, R., Mathews, P.K., Murugan, N. and Dinaharan, I., (2012). Effect of tool rotational speed and pin profile on microstructure and tensile strength of dissimilar friction stir welded AA5083-H111 and AA6351-T6 aluminum alloys. *Materials & Design*, *40*, pp.7-16.

Pan, T.Y., (2007). Friction stir spot welding (FSSW)-a literature review (No. 2007-01-1702). *SAE Technical Paper.*

Patnaik, A., Koch, K., Arbegast, W. and Allen, C., (2006). Static properties of "refill" friction spot welded skin stiffened compression panels (No. 2006-01-0967). *SAE Technical Paper*.

Paz, G., Blaga, L., Goushegir, S., Abibe, A., dos Santos, J., Mazzaferro, J., and Amancio-Filho, S. (eds.) (2014) *21st CBECiMat, Brazilian Congress of Materials Science and Engineering, Congresso Brasileiro De Engenharia e Ciencia Dos Materiais*. 'Numerical Simulation of the Mechanical Behavior of Polymer-Metal Joints'

Peel, M.J., Steuwer, A., Withers, P.J., Dickerson, T., Shi, Q. and Shercliff, H. (2006) Dissimilar friction stir welds in AA5083-AA6082. Part I: process parameter effects on thermal history and weld properties. *Metallurgical and Materials Transactions A*, *37*(7), pp.2183-2193.

Persson, A., Hogmark, S., & Bergström, J. (2005). Thermal fatigue cracking of surface engineered hot work tool steels. *Surface and Coatings Technology*, *191*(2-3), 216-227.

Pieta, G., dos Santos, J., Strohaecker, T., and Clarke, T. (2014) Optimization of Friction Spot Welding Process Parameters for AA2198-T8 Sheets*. Materials and Manufacturing Processes* 29 (8), 934-940

Plaine, A. H., Gonzalez, A. R., Suhuddin, U. F. H., Dos Santos, J. F., & Alcântara, N. G. (2015). The optimization of friction spot welding process parameters in AA6181-T4 and Ti6Al4V dissimilar joints. *Materials & Design*, *83*, 36-41.

Plaine, A., Gonzalez, A., Suhuddin, U., dos Santos, J., and Alcântara, N. (2016) Process Parameter Optimization in Friction Spot Welding of AA5754 and Ti6Al4V Dissimilar Joints using Response Surface Methodology. *The International Journal of Advanced Manufacturing Technology* 85 (5-8), 1575-1583

Plaine, A., Suhuddin, U., Alcântara, N., and dos Santos, J. (2017) Microstructure and Mechanical Behavior of Friction Spot Welded AA6181-T4/Ti6Al4V Dissimilar Joints*. The International Journal of Advanced Manufacturing Technology* 92 (9-12), 3703-3714

Prado, R.A., Murr, L.E., Soto, K.F. and McClure, J.C., (2003). Self-optimization in tool wear for friction-stir welding of Al 6061+ 20% Al2O3 MMC. *Materials science and engineering: A*, *349*(1-2), pp.156-165.

Prime, M.B., (2001). Cross-sectional mapping of residual stresses by measuring the surface contour after a cut. *Journal of engineering materials and technology*, *123*(2), pp.162-168.

Qiao, F., Cheng, K., Wang, L., and Guo, L. (2016) An Experimental Investigation on the Dissimilar Joining of AA6061 and 1Cr18Ni9Ti by Refill Friction Stir Spot Welding and its Mechanical Properties. *Proceedings of the Institution of Mechanical Engineers, Part B: Journal of Engineering Manufacture* 230 (4), 779-785

Rai, R., De, A., Bhadeshia, H., and DebRoy, T. (2011) Friction Stir Welding Tools. *Science and Technology of Welding and Joining* 16 (4), 325-342

Reimann, M., Gartner, T., Suhuddin, U., Göbel, J., and dos Santos, J. F. (2016) Keyhole Closure using Friction Spot Welding in Aluminum Alloy 6061–T6. *Journal of Materials Processing Technology* 237, 12-18

Reimann, M., Goebel, J., & dos Santos, J. F. (2018). Microstructure Evolution and Mechanical Properties of Keyhole Repair Welds in AA 2219-T851 Using Refill Friction Stir Spot Welding. *Journal of Materials Engineering and Performance*, 1-7.

Reimann, M., Goebel, J., and dos Santos, J. F. (2017) Microstructure and Mechanical Properties of Keyhole Repair Welds in AA 7075-T651 using Refill Friction Stir Spot Welding. *Materials & Design* 132, 283-294

Reimann, M., Goebel, J., Gartner, T. M., and dos Santos, J. F. (2017) Refilling Termination Hole in AA 2198–T851 by Refill Friction Stir Spot Welding. *Journal of Materials Processing Technology* 245, 157-166

Reynolds, A.P., Tang, W., Gnaupel-Herold, T. and Prask, H., (2003). Structure, properties, and residual stress of 304L stainless steel friction stir welds. *Scripta Materialia*, *48*(9), pp.1289-1294.

Rosendo, T., Parra, B., Tier, M., Da Silva, A., Dos Santos, J., Strohaecker, T., and Alcântara, N. (2011) Mechanical and Microstructural Investigation of Friction Spot Welded AA6181-T4 Aluminium Alloy. *Materials & Design* 32 (3), 1094-1100

Rosendo, T., Tier, M., Mazzaferro, J., Mazzaferro, C., Strohaecker, T. R., & Dos Santos, J. F. (2015). Mechanical performance of AA6181 refill friction spot welds under Lap shear tensile loading. *Fatigue & Fracture of Engineering Materials & Structures*, *38*(12), 1443-1455.

Santana, L., Suhuddin, U., Ölscher, M., Strohaecker, T., and dos Santos, J. (2017) Process Optimization and Microstructure Analysis in Refill Friction Stir Spot Welding of 3-mm-Thick Al-mg-Si Aluminum Alloy. *The International Journal of Advanced Manufacturing Technology* 92 (9-12), 4213-4220

Santos, T., Vilaça, P., dos Santos, J., and Quintino, L. (2009) Computational Tools for Modelling FSW and an Improved Tool for NDT. *Welding in the World* 53 (5-6), R99-R108

Schilling, C. and dos Santos, J., Gkss-Forschungszentrum Geesthacht GmbH, (2004). *Method and device for joining at least two adjoining work pieces by friction welding*. U.S. Patent 6,722,556.

Schmal, C., Meschut, G. and Nico, B.U.H.L., (2019). Joining of high strength aluminum alloys by refill friction stir spot welding (III-1854-18). *Welding in the World*, *63*(2), pp.541-550.

Schmidt, H.B. and Hattel, J.H., (2008). Thermal modelling of friction stir welding. *Scripta Materialia*, *58*(5), pp.332-337.

Seaman, J., Namola, K., and Gould, J. (2016) Refill Friction Stir Spot Welding Development *17th Sheet Metal Welding Conference*, 19-20 October 2016, Livonia, Michigan

Senkara, J.A.Z.H. and Zhang, H., (2000). Cracking in spot welding aluminum alloy AA5754. *WELDING JOURNAL-NEW YORK-*, *79*(7), pp.194-s – 201-s.

Shen, J., Lage, S.B., Suhuddin, U.F., Bolfarini, C. and Dos Santos, J.F., (2018). Texture development and material flow behavior during refill friction stir spot welding of AlMgSc. *Metallurgical and Materials Transactions A*, *49*(1), pp.241-254.

Shen, Z., Chen, J., Ding, Y., Hou, J., Shalchi Amirkhiz, B., Chan, K., and Gerlich, A. (2017) Role of Interfacial Reaction on the Mechanical Performance of Al/steel Dissimilar Refill Friction Stir Spot Welds. *Science and Technology of Welding and Joining*, 1-16

Shen, Z., Chen, Y., Hou, J. S. C., Yang, X., & Gerlich, A. P. (2015). Influence of processing parameters on microstructure and mechanical performance of refill friction stir spot welded 7075-T6 aluminium alloy. *Science and Technology of Welding and Joining*, *20*(1), 48-57.

Shen, Z., Ding, Y. and Gerlich, A.P., (2019). Advances in friction stir spot welding. *Critical Reviews in Solid State and Materials Sciences*, pp.1-78.

Shen, Z., Ding, Y., Gopkalo, O., Diak, B. and Gerlich, A.P., (2018). Effects of tool design on the microstructure and mechanical properties of refill friction stir spot welding of dissimilar Al alloys. *Journal of Materials Processing Technology*, *252*, pp.751-759.

Shen, Z., Hou, J., Chan, K., Scotchmer, N., Zhou, N., and Gerlich, A. (eds.) (2016) *SWMC XVII Conference*. 'Spot Welding Aluminum 6022-T4 to Galvanized DP600 Sheet by Refill Friction Stir Spot Welding'

Shen, Z., Li, W.Y., Ding, Y., Hou, W., Liu, X.C., Guo, W., Chen, H.Y., Liu, X., Yang, J. and Gerlich, A.P., (2020). Material flow during refill friction stir spot welded dissimilar Al alloys using a grooved tool. *Journal of Manufacturing Processes*, *49*, pp.260-270.

Shen, Z., Yang, X., Yang, S., Zhang, Z., & Yin, Y. (2014). Microstructure and mechanical properties of friction spot welded 6061-T4 aluminum alloy. *Materials & Design (1980-2015)*, *54*, 766-778.

Shen, Z., Yang, X., Zhang, Z., Cui, L., & Li, T. (2013). Microstructure and failure mechanisms of refill friction stir spot welded 7075-T6 aluminum alloy joints. *Materials & design*, *44*, 476-486.

Shi, Y., Yue, Y., Zhang, L., Ji, S., and Wang, Y. (2018) 'Refill Friction Stir Spot Welding of 2198-T8 Aluminum Alloy'. *Transactions of the Indian Institute of Metals* 71 (1), 139-145

Shindo, D.J., Rivera, A.R. and Murr, L.E., (2002). Shape optimization for tool wear in the friction-stir welding of cast AI359-20% SiC MMC. *Journal of materials science*, *37*(23), pp.4999-5005.

Silva, A. C. F., De Backer, J., & Bolmsjö, G. (2017). Temperature measurements during friction stir welding. *The International Journal of Advanced Manufacturing Technology*, *88*(9-12), 2899-2908.

Silva, B.H., Zepon, G., Bolfarini, C. and dos Santos, J.F., (2020). Refill friction stir spot welding of AA6082-T6 alloy: Hook defect formation and its influence on the mechanical properties and fracture behavior. *Materials Science and Engineering: A*, *773*, p.138724.

Singarapu, U., Adepu, K. and Arumalle, S.R., (2015). Influence of tool material and rotational speed on mechanical properties of friction stir welded AZ31B magnesium alloy. *Journal of Magnesium and Alloys*, *3*(4), pp.335-344.

Skorupa, A. and Skorupa, M., (2012). Design Parameters Influencing the Fatigue Behaviour of Riveted Lap Joints. In *Riveted Lap Joints in Aircraft Fuselage* (pp. 101-114). Springer, Dordrecht.

Song, X.Q., Takahashi, Y., He, W.M., Ihara, T., (2017) On the Formation Mechanisms of Adhering Layer during Machining Metal Material. Key Engineering Materials 749, 39–45.

Staron, P., Kocak, M. and Williams, S., 2002. Residual stresses in friction stir welded Al sheets. *Applied Physics A*, *74*(1), pp.s1161-s1162.

Suhuddin, U. F. H., Fischer, V., Kostka, A., & dos Santos, J. F. (2017). Microstructure evolution in refill friction stir spot weld of a dissimilar Al–Mg alloy to Zn-coated steel. *Science and Technology of Welding and Joining*, *22*(8), 658-665.

Suhuddin, U., Fischer, V., Kroeff, F., & Dos Santos, J. F. (2014). Microstructure and mechanical properties of friction spot welds of dissimilar AA5754 Al and AZ31 Mg alloys. *Materials Science and Engineering: A*, *590*, 384-389.

Suhuddin, U., Gera, D., Alcantara, N. and dos Santos, J., 2019. Welding Multilayer Materials by Refill Friction Stir Spot Welding. In *Friction Stir Welding and Processing X* (pp. 245-253).

Suhuddin, U., Kroeff, F. & dos Santos, J. F., (2011). *Dissimilar Friction Spot Welding of Al/Mg Alloys.* Manchester, UK, Challenges for Joining Lightweight Dissimilar Materials for Automotive Applications Conference.

Suhuddin, U.F.H., Fischer, V. and Dos Santos, J.F., (2013). The thermal cycle during the dissimilar friction spot welding of aluminum and magnesium alloy. *Scripta Materialia*, *68*(1), pp.87-90.

Thibault, D., Bocher, P., Thomas, M., Gharghouri, M. and Côté, M., (2010). Residual stress characterization in low transformation temperature 13% Cr–4% Ni stainless steel weld by neutron diffraction and the contour method. *Materials Science and Engineering: A*, *527*(23), pp.6205-6210.

Thomas, W.M., Nicholas, E.D., Needham, J.C., Murch, M.G., Templesmith, P. and Dawes, C.J., Friction Stir Butt Welding (1991), *International Patent Application No. PCT/GB92/02203 and GB Patent Application No. 9125978.8, U.S. Patent No. 5,460,317*

Threadgill, P., Leonard, A., Shercliff, H., and Withers, P. (2009) Friction Stir Welding of Aluminium Alloys. *International Materials Reviews* 54 (2), 49-93

Tier, M. D., dos Santos, J. F., Olea, C. W., Rosendo, T., Mazzaferro, C. P., Mazzaferro, J. A. E. and Isakovic, J. T. (2008). The influence of weld microstructure on mechanical properties of alclad AA2024-T3 friction spot welded (No. 2008-01-2287). *SAE Technical Paper.*

Tier, M., Rosendo, T., dos Santos, J., Huber, N., Mazzaferro, J., Mazzaferro, C., and Strohaecker, T. (2013) 'The Influence of Refill FSSW Parameters on the Microstructure and Shear Strength of 5042 Aluminium Welds'. *Journal of Materials Processing Technology* 213 (6), 997-1005

TRA-C, (2020) *TRA-C Industrie expert in metal work* [online] available from <http://www.tra-c.com/download/publications/TRA_C_GB.pdf> [9 July 2020]

Uematsu, Y., Tokaji, K., Tozaki, Y., Kurita, T. and Murata, S., (2008). Effect of re-filling probe hole on tensile failure and fatigue behaviour of friction stir spot welded joints in Al–Mg–Si alloy. *International Journal of Fatigue*, *30*(10-11), pp.1956-1966.

Ullegaddi, K., Murthy, V. and Harsha, R.N., (2017). Friction Stir Welding Tool Design and Their Effect on Welding of AA-6082 T6. *Materials Today: Proceedings*, *4*(8), pp.7962-7970.

UNITED STATES, & BATTELLE MEMORIAL INSTITUTE. (2008). *MMPDS-04: Metallic materials properties development and standardization (MMPDS)*. [Washington, D.C.], Federal Aviation Administration.

Vairis, A. and Frost, M., (2000). Modelling the linear friction welding of titanium blocks. *Materials Science and Engineering: A*, *292*(1), pp.8-17.

Venukumar, S., Yalagi, S.G., Muthukumaran, S. and Kailas, S.V., (2014). Static shear strength and fatigue life of refill friction stir spot welded AA 6061-T6 sheets. *Science and Technology of Welding and Joining*, *19*(3), pp.214-223.

Verastegui, R. N., Esmerio Mazzaferro, J. A., Petry Mazzaferro, C. C., Strohaecker, T. R., & Dos Santos, J. F. (2014). Welding of Aluminum to DP600 Steel Plates by Refill Friction Stir Spot Welding Process (Refill FSSW): Preliminary Results. *Advanced Materials Research*, *1082*.

Wallwork Heat Treatment Ltd (2020) *Diamolith DLC* [online] available from <https://www.wallworkht.co.uk/content/diamolith_dlc/> [11 June 2020]

Wang, J., Su, J., Mishra, R.S., Xu, R. and Baumann, J.A., (2014). Tool wear mechanisms in friction stir welding of Ti–6Al–4V alloy. *Wear*, *321*, pp.25-32.

Xu, Z., Li, Z., Ji, S., & Zhang, L. (2018). Refill friction stir spot welding of 5083-O aluminum alloy. *Journal of Materials Science & Technology*, *34*(5), 878-885.

Yan, X.J., Yang, D.Z. and Qi, M., (2006). Rotating–bending fatigue of a laser-welded superelastic NiTi alloy wire. *Materials characterization*, *57*(1), pp.58-63.

Yang, X., Fu, T., and Li, W. (2014) 'Friction Stir Spot Welding: A Review on Joint Macro-and Microstructure, Property, and Process Modelling'. *Advances in Materials Science and Engineering* 2014

Yue, Y., Shi, Y., Ji, S., Wang, Y., and Li, Z. (2017) Effect of Sleeve Plunge Depth on Microstructure and Mechanical Properties of Refill Friction Stir Spot Welding of 2198 Aluminum Alloy. *Journal of Materials Engineering and Performance* 26 (10), 5064-5071

Zhao, Y., Liu, H., Chen, S., Lin, Z., and Hou, J. (2014) Effects of Sleeve Plunge Depth on Microstructures and Mechanical Properties of Friction Spot Welded Alclad 7B04-T74 Aluminum Alloy. *Materials & Design (1980-2015)* 62, 40-46

Zhao, Y., Liu, H., Yang, T., Lin, Z., and Hu, Y. (2016) Study of Temperature and Material Flow during Friction Spot Welding of 7B04-T74 Aluminum Alloy. *The International Journal of Advanced Manufacturing Technology* 83 (9-12), 1467-1475

Zhao, Y., Wang, C., Dong, C., Deng, J., & Tan, J. (2018-A). Numerical study on a thermal process in friction spot welding of Al-Zn-Mg-Cu alloy. *Welding in the World*, 1-9.

Zhao, Y., Wang, C., Li, J., Tan, J. and Dong, C., (2018-B) Local melting mechanism and its effects on mechanical properties of friction spot welded joint for Al-Zn-Mg-Cu alloy. *Journal of Materials Science & Technology*, *34*(1), pp.185-191.

Zhou, L., Luo, L. Y., Wang, R., Zhang, J. B., Huang, Y. X., & Song, X. G. (2018). Process Parameter Optimization in Refill Friction Spot Welding of 6061 Aluminum Alloys Using Response Surface Methodology. *Journal of Materials Engineering and Performance*, *27*(8), 4050-4058.

Zhou, L., Luo, L., Zhang, T., He, W., Huang, Y., and Feng, J. (2017) Effect of Rotation Speed on Microstructure and Mechanical Properties of Refill Friction Stir Spot Welded 6061-T6 Aluminum Alloy. *The International Journal of Advanced Manufacturing Technology* 92 (9-12), 3425-3433 .

Appendices

A1 - Reported RFSSW material combinations

Table A1 - Similar material combinations successfully welded/joined by RFSSW.

Material properties				Process parameters					LSS [kN]	Reference
Base material	Thickness [mm]	Overlapped area [mm²]	Surface treatments	Shoulder geometry	Probe geometry	Rotation speed [rev/min]	Plunge Depth [mm]	Welding time [s]		
Aluminium - 2XXX series										
AA 2024-T3	2.00	46x60	Alclad (100µm)	9 mm threaded	5.2 mm grooved	1900 (plunge) 1700 (retract)	2.5	3.8	9.0 ± 1.90	da Silva et al. (2007-A)
AA 2024-T3	2.00	46x60	Alclad (100µm)	9 mm threaded	5.2 mm grooved	1900	2.5	4.8	10.68±0.66	Tier et al. (2008)
AA 2024-T3	2.00	46x60	n/a	9 mm threaded	6 mm grooved	1900	2.5	6.8	10.3±0.1	Amancio-Filho et al. (2011-B)
AA 2024-T4	1.5 (top) 2.0 (bottom)	50x60	Alclad	9 mm threaded	5 mm grooved	1000 800 (Dwell ST2)	1.8	6	9.25±0.1	Li et al. (2016)
AA 2198-T8	1.6	46x35	n/a	9 mm threaded	6 mm grooved	1500	2.8	3	7.95±0.35	de Castro et al. (2018-A)
Aluminium - 5XXX series										
AA 5042-O	1.5	50x60	n/a	9 mm threaded	5.2 mm grooved	900	1.55	2.04	6.31±0.16	Tier et al. (2013)
AA 5083-O	2	40x30	n/a	9 mm threaded	5.2 mm grooved	2300	2.4	3.5	7.72	Xu et al. (2018)
Aluminium - 6XXX series										
AA 6061-T4	2	40x40	n/a	9 mm threaded	5 mm grooved	1500	2.2	4	7.12	Shen et al. (2014)
AA 6181-T4	1.7	45x60	n/a	9 mm threaded	5.2 mm grooved	2400	1.75	3	6.8±0.17	Rosendo et al. (2015)
AA 6061-T6	2	25x25	n/a	9 mm threaded	5 mm grooved	1500	2	2.1	9.1±0.24	Cao et al. (2016)
AA 6061-T6	2	25x25	n/a	9 mm threaded	5.3 mm grooved	1500	2.5	n/a	7.98	Zhou et al. (2018)
Aluminium - 7XXX series										
AA 7075-T6	2	40x40	n/a	9 mm threaded	5 mm grooved	1500	n/a	4	7.03	Shen et al. (2013)
AA 7075-T6	0.8	25x25	Alclad	9 mm threaded	6 mm grooved	2100	1.1	3.5	4.7	Shen et al. (2014)

AA 7050-T76	2	46x60	n/a	9 mm threaded	6 mm grooved	2600	2.6	2.2	11.27±0.33	Effertz et al. (2016)
AA 7075-T6	1.6 (top) 0.8 (bottom)	30x20	n/a	9 mm threaded	5.2 mm grooved	2400	1.5	3.5	7.58	Kubit et al (2018-A)
AA 7075-T6	0.8	30x30	n/a	9 mm threaded	5.2 mm grooved	3000	1.7	2.5	6.48	Kubit et al (2018-B)
AA 7075-T6	1.6 (top) 0.8 (bottom)	n/a	Alclad (100µm)	9 mm threaded	5.2 mm grooved	2000	1.7	2 (PT)	5.87	Andres et al. (2018)
Aluminium - AlMgSc Alloys										
KO 8542	1.6	25.4x25.4	n/a	9 mm threaded	6 mm grooved	1000	1.4	1 (PT)	9.34 ± 0.23	Lage et al. (2018)
Magnesium alloys										
AZ31-H24	2	46x60	n/a	9 mm threaded	6 mm grooved	3000	3	n/a	4.74 ± 0.19	Campanelli et al. (2012)
Polymers and reinforced polymers										
CF-Polyethylenimine	2	n/a	n/a	9 mm threaded	6 mm grooved	1200	2.2	n/a	1.6	Huang et al. (2018)
PMMA	3	25x25	n/a	n/a	n/a	500	4	5.5	(8.3 ± 1.2) MPa	Oliveira et al. (2012)

Table A2 - Dissimilar material combinations successfully welded/joined by RFSSW.

Material properties					***Process parameters***					**LSS [kN]**	**Reference**
Top sheet material	**Bottom sheet material**	**Thickness [mm]**	**Overlapped area [mm²]**	**Surface treatments**	**Shoulder geometry**	**Probe geometry**	**Rotation speed [rev/min]**	**Plunge Depth [mm]**	**Welding time [s]**		
AA 7075-T6	AA 2024-T3	1.27 (Top) 1.6 (Bottom)	38x40	n/a	7 mm featureless	4 mm featureless	1400	1.56	n/a	6.33±0.14	Boldsaikhan et al. (2016)
AA 6061-T6	AA 7075-T6	3	50x50	N/A	9 mm threaded	5 mm grooved	1600	3.6	n/a	12.89	Liu, Yang and Yan (2018)
AA 6082-T6	PA6-GF30	2 (Top) 10 (Bottom)	30x30	n/a	9 mm threaded	6.4 mm grooved	3100	0.8	n/a	3.71	Montag and Wulfsberg (2014)
AA 5083	Cu-DHP	2	n/a	n/a	9 mm threaded	6 mm grooved	1200	2	n/a	6.72	Cardillo et al. (2018)
AA AA6181-T4	Carbon steel	1 (Top) 1.2 (Bottom)	30x30	Zn Coating (steel)	6 mm featureless	3.5 mm featureless	1600	0.7	n/a	3.5	Fukada et al. (2013)
AA 6061-T7	DP600	1.5	n/a	Without Zn coating	n/a	n/a	900	1.45	8	6.58±0.16	Verestegui et al. (2015)
				With Zn coating			1500	1.3	4	6.36±0.19	
Al-Mg-Mn alloy	HSLA-GI	3 (Top) 2 (Bottom)	n/a	Zn Coating (steel)	9 mm threaded	6 mm grooved	1600	2.8	4	7.8	Suhuddin et al. (2017)
AA 5754-H24	AZ31	2	n/a	n/a	9 mm threaded	6 mm grooved	1900	1.8	4	n/a	Suhuddin et al. (2014)
AA 6181-T4	Ti6Al4V	1.5	25.4x25.4	n/a	9 mm threaded	6.4 mm grooved	2500	1.4	n/a	6.449 ± 0.55	Plaine et al. (2015)
AA 5754	Ti6Al4V	2 (Top) 2.5 (Bottom)	25.4x25.4	n/a	9 mm threaded	6.4 mm grooved	2000	1.8	2	7.4	Plaine et al. (2016)
AZ31-O	PPS-GF	2 (Top) 8 (Bottom)	n/a	Mechanical abrasion before welding	9 mm threaded	6 mm grooved	3000	0.25	8	2.3	Amancio-Filho et al. (2011-A)
	PPS-CF	2 (Top) 2.1 (Bottom)	n/a				1950			1.5	
ZEK100	DP600-GI	1.53 (Top) 1 (Bottom)	25x25	Acetone cleaning before welding	10 mm threaded	6.3 mm grooved	1800	1.5	3	4.7	Chen et al. (2015)
PA6	CF-PA66	4 (Top) 2 (Bottom)	25.4x25.4	n/a	n/a	n/a	1500	3.8	8	2.2	Goncalves et al. (2016)

A2 - Drawings of RFSSW tool components

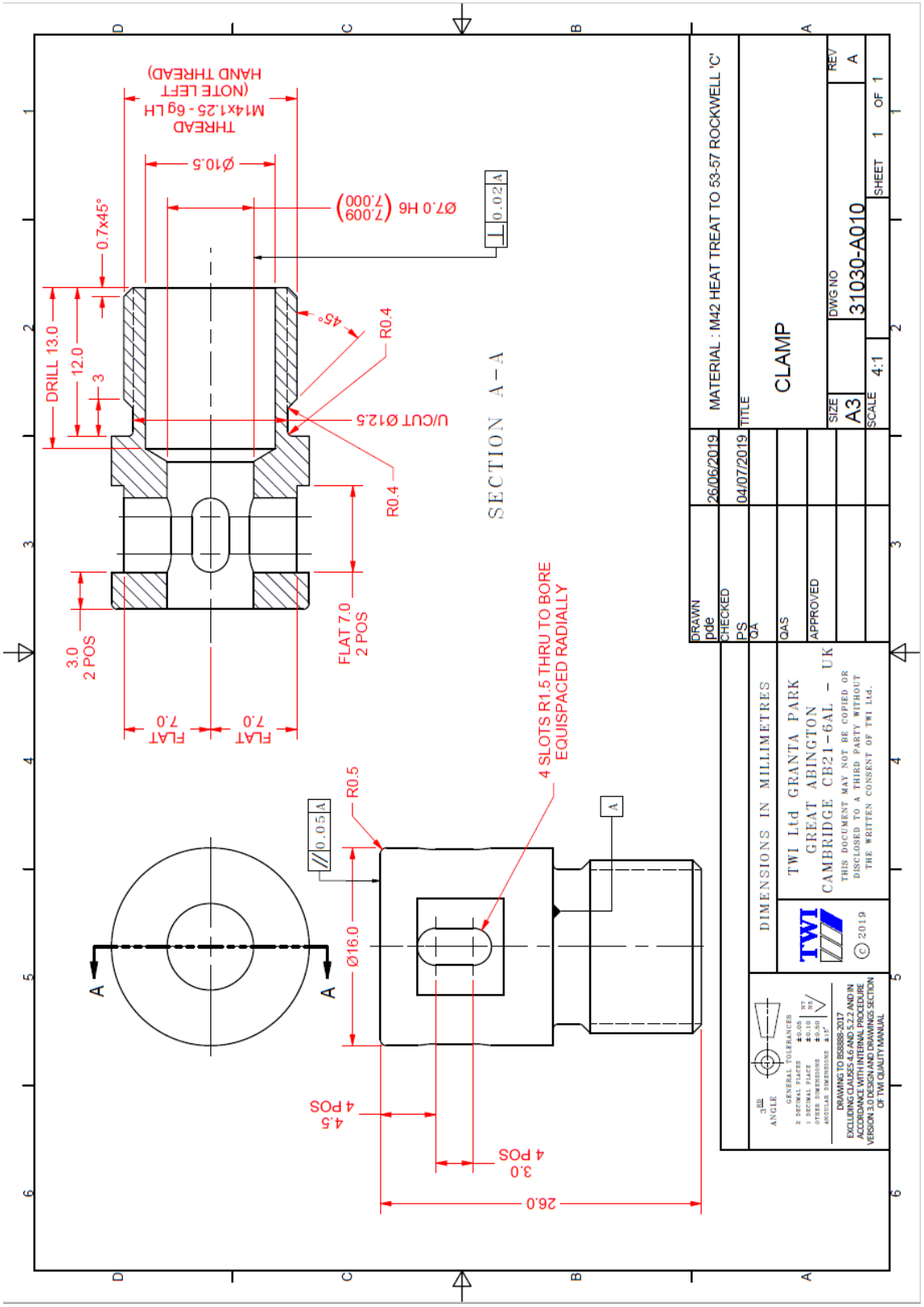

Figure A0.1 - Technical drawing of the RFSSW clamp component.

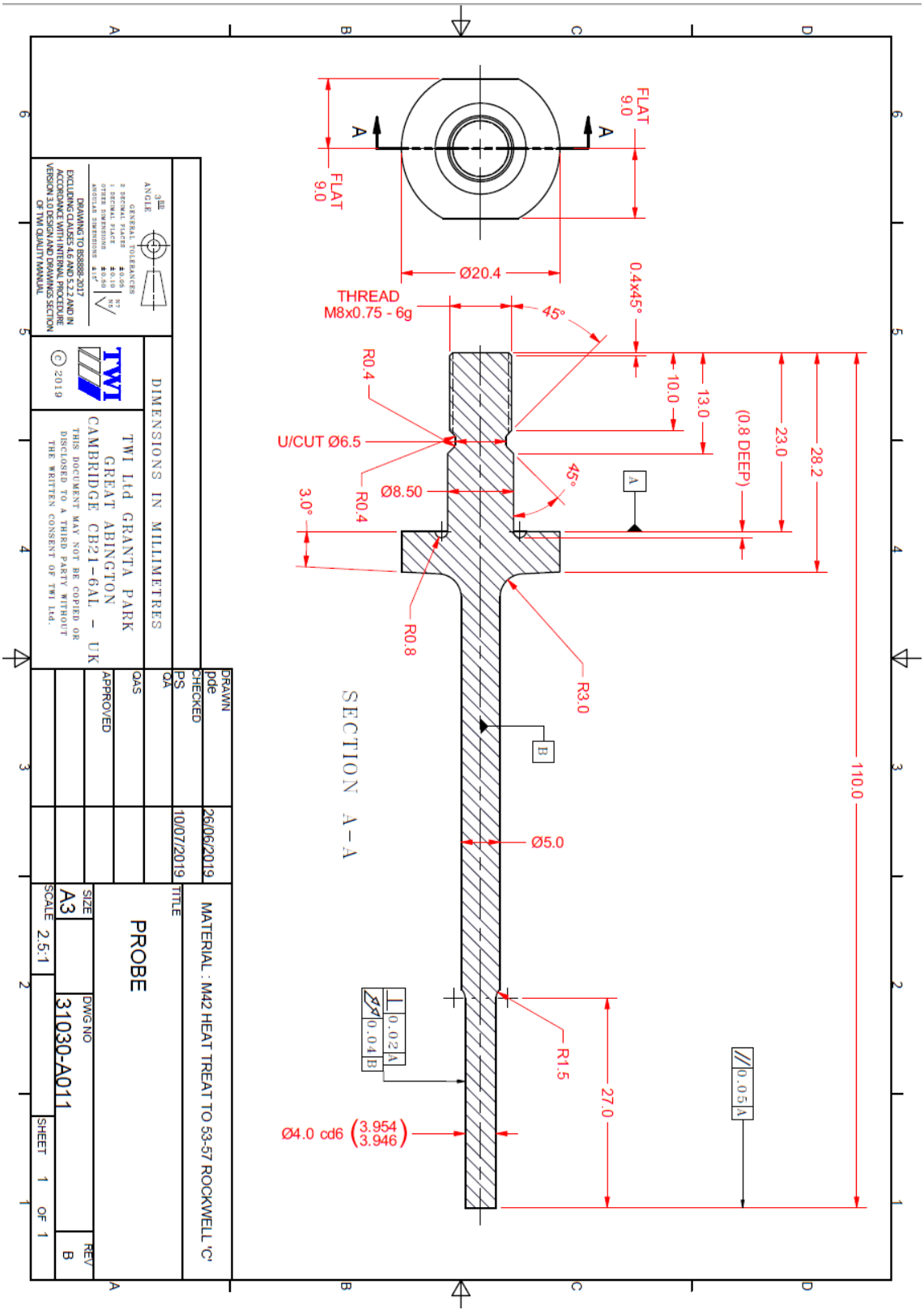

Figure A0.2 - Technical drawing of the RFSSW probe component.

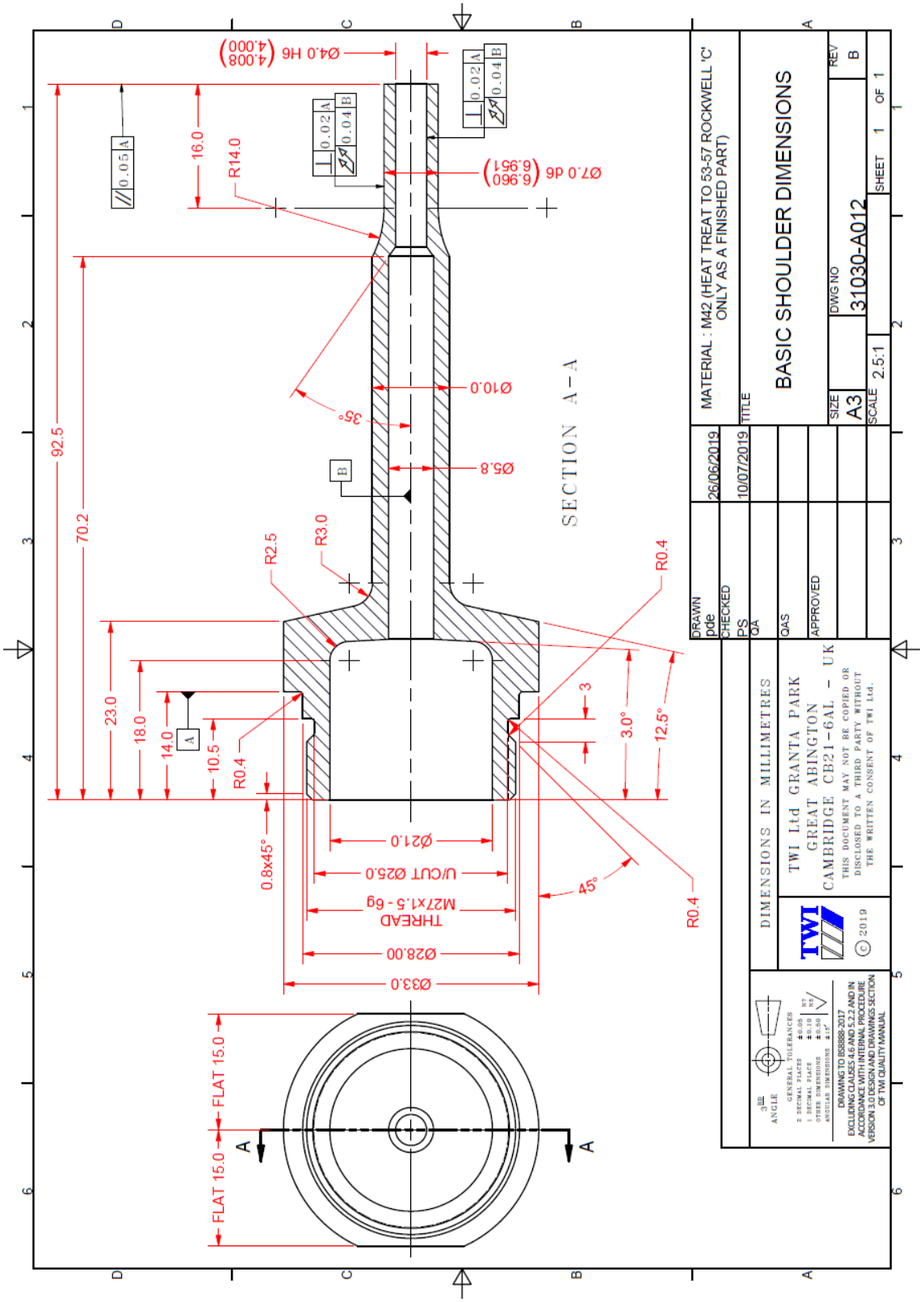

Figure A0.3 - Technical drawing of the RFSSW featureless shoulder component. (Tool 2)

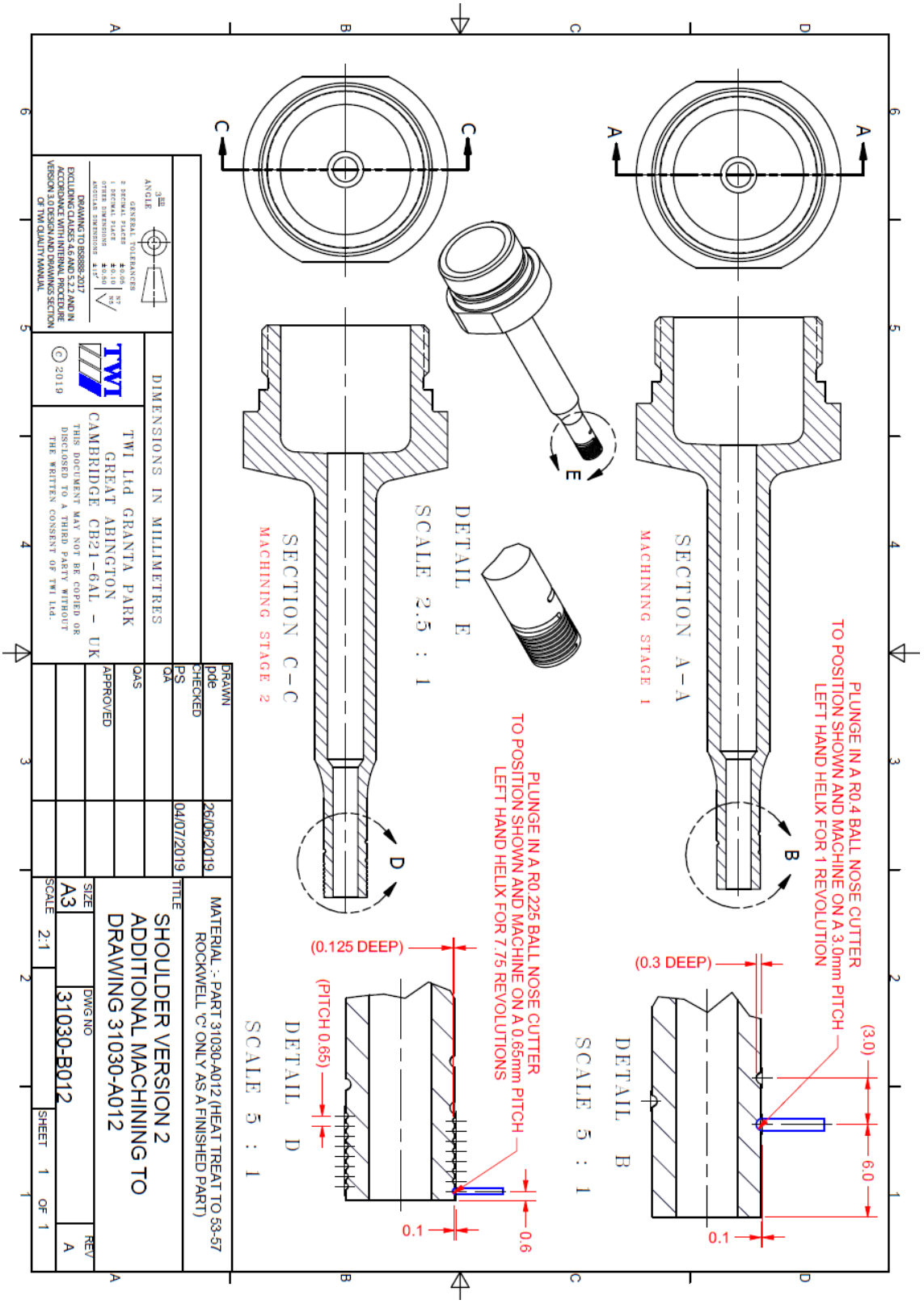

Figure A0.4 - Technical drawing of the RFSSW threaded shoulder component. (Tool 3)